From Sm1-xGdxAl2 electronic properties to magnetic tunnel junctions based on Sm1-xGdxAl2 and/or [Co/Pt] electrodes: Towards the integration of Zero Magnetization ferromagnets in spintronic devices

Mathias Bersweiler

UNIVERSITÉ DE LORRAINE

Ecole doctorale EMMA

THÈSE

Pour l'obtention du titre de :

DOCTEUR de L'UNIVERSITÉ DE LORRAINE

Spécialité: *Physique*

Présentée par :

BERSWEILER Mathias

From $Sm_{1-x}Gd_xAl_2$ electronic properties to magnetic tunnel junctions based on $Sm_{1-x}Gd_xAl_2$ and/or [Co/Pt] electrodes: Towards the integration of Zero Magnetization ferromagnets in spintronic devices

---

Thèse soutenue publiquement le 22 octobre 2014 à Nancy devant le jury composé de :

M. Olivier Fruchart	Directeur de recherche, Institut Néel	Rapporteur
M. Coriolan Tiusan	Professeur, Technical University of Cluj-Napoca	Rapporteur
M. Henri Jaffrès	Chargé de recherche, Unité mixte de Physique CNRS Thales	Examinateur
M. Patrick Le Fèvre	Chargé de recherche, Synchrotron SOLEIL	Examinateur
M. Yannick Fagot-Revurat	Professeur, Université de Lorraine	Examinateur
M. Michel Hehn	Professeur, Université de Lorraine	Directeur de thèse
Mme. Karine Dumesnil	Chargé de recherche, Université de Lorraine	Co-directrice de thèse

Institut Jean Lamour – UMR 7198 – Département P2M – Equipe 101-
Faculté des Sciences et Technologies – Campus Victor Grignard – BP 70239 – 54506 Vandœuvre-lès-Nancy Cedex

Université de Lorraine – Pôle M4 : matière, matériaux, métallurgie, mécanique

Remerciements

Au moment où j'écris ces lignes, je suis sur le point de fermer toute une page de ma vie et une autre ne demande qu'à être écrite…La thèse fut pour moi avant tout une belle aventure où j'ai fait la rencontre de personnes humainement formidables et donc que je tiens à remercier. Dans la longue liste des remerciements, je tiens tout d'abord à remercier les membres de mon jury qui ont accepté de lire tout mon tapuscrit ci-après !

Merci à **Yannick Fagot-Revurat** d'avoir accepté de présider le jury. De plus je tiens à te remercier pour l'aide et les conseils précieux que tu m'as fournis lors du dépouillement des résultats ARPES. Je tiens aussi à te remercier pour ta disponibilité malgré un emploi du temps chargé… Il faut le reconnaitre je ne m'en serais jamais sorti sans ton aide, je te dois donc une fière chandelle...
Je tiens ensuite à remercier **Oliver Fruchard** et **Coriolan Tiusan** de m'avoir fait l'honneur d'accepter d'être mes rapporteurs. Cori nous t'avions confié une lourde et difficile tâche avec les calculs de structure de bande électroniques à l'aide du code Wien2k…Alors merci pour tout, car les résultats extraits ont permis d'avoir une meilleurs compréhension de la physique qui se cache derrière notre système. Merci également à **Henri Jaffrès** et **Patrick Lefèvre** d'avoir accepté d'être les examinateurs de mon travail de thèse. Patrick, je me souviendrai longtemps de nos run synchrotrons avec toi sur CASSIOPEE, ta bonne humeur malgré le fait que l'on te fasse revenir à 2h du matin pour transférer les échantillons, les fou rires et discussions que l'on a pu avoir durant le temps d'acquisition des datas.

Attaquons nous maintenant aux remerciements pour les personnes avec qui l'aventure de la thèse fut avant tout une aventure humaine.

Mes premiers remerciements vont évidement à **Karine Dumesnil** avec qui cette aventure a commencé depuis plusieurs années (3ans et 6 mois avec le stage de master). Il faut dire qu'il s'en est passé des choses… Entre ton année aux Etats-Unis et nos longues conversations Skype, le fait de se lancer dans la folle aventure des mesures ARPES qui peut se résumer en une phrase culte : «une mort certaine, une faible chance de succès…mais qu'attendons-nous ! »…, la MBE qui a fonctionné que 6 mois, cette thèse ne fut pas de tout repos, il faut le dire ! Cependant je tiens à te remercier pour la patience, la disponibilité, l'écoute dont tu as fait preuve durant ces derniers mois lors de la correction du tapuscrit, la large autonomie que j'ai eue lors de ma thèse (sauf pour le choix des couleurs lors de mes présentations), la possibilité que tu m'as donnée de participer à de nombreuses conférences ainsi que la rigueur que tu as essayé de me transmettre durant ces 3 ans et 6 mois (promis je serai plus ordonné à l'avenir). Il ne fait aucun doute que si je suis devenu le scientifique que je suis aujourd'hui c'est grâce à toi et je t'en serai éternellement reconnaissant. Ce fut un plaisir de travailler avec toi. Mes remerciements vont ensuite à **Michel Hehn**, qui m'a toujours écouté, sorti de mauvais pas lorsque la physique coinçait et qui est l'artisan des calculs micromagnétiques et des nombreux échantillons [Co/Pt] et jonctions magnétiques tunnel réalisés par pulvérisations. Un des faits qui m'a le plus marqué est ma demande d'une série de 5 échantillons pour des mesures complémentaires, le lendemain je les trouve sur mon bureau…un service digne d'un 5*… Je te remercie aussi pour ta disponibilité ainsi que de la patience dont tu as fait preuve durant toute cette thèse. Je dois néanmoins avouer que sur la fin de thèse, j'ai cru que nous allions te perdre avec les 2 répétitions par semaines planifiées et les discussions pour préparer les questions...Quoiqu'il en soit j'ai adoré travailler avec toi. Reformer un trio comme nous l'avons formé avec Karine et toi va être très dur, vous avez mis la barre très haute…Je tiens également à remercier **Daniel Lacour** qui a participé à nos réunions au 3ème apportant un regard extérieur à mon travail et avec qui j'ai partagé de nombreux verres lors de nos virées dans les bars de Nancy après les soutenances de thèses ou repas d'équipe. Je te souhaite aussi bonne chance avec tes expositions imageries magnétiques qui sont vraiment cool.

Mes remerciements vont ensuite à toutes les personnes avec qui j'ai collaboré ingénieurs, technicien et chercheurs: **Yannick, Cori** et **Patrick** je vous ai déjà remercié avant…Sans vous les mesures ARPES et leurs traitements n'auraient jamais été possibles… Il va de soi que je remercie les autres collaborateurs qui ont contribué aux mesures de photoémissions résolues en angles et en spins : **François Bertran** (toujours disponible pour répondre à des questions de photoémissions résolues en spin) et **Amina Taleb**. Merci à **François Montaigne** pour m'avoir fait découvrir le monde de la recherche en L3 et d'avoir participé et apporté un regard extérieur sur les mesures de transports. Merci à **Thierry Gourieux** pour les quelques discussions que l'on a pu avoir pour les mesures XPS. Il ne faut pas que j'oublie de remercie le « boss » de l'équipe 101 **Stéphane Mangin** avec qui j'ai pu découvrir les joies de l'animation scientifique sur la supraconductivité. Personnellement, je ne sais pas comment tu fais pour gérer toutes tes activités mais pour moi tu es un Dieu vivant. Mes remerciement vont ensuite à **Olivier Lenoble** qui m'a proposé le monitorat de physique sur Epinal. Merci à **Sylvie Robert** qui m'a initié à la réflectométrie et à la diffraction aux grand angles et avec qui nous avons eu de longues conversation sur des sujets divers et variés et qui m'a toujours sorti d'un mauvais pas…Promis je me ferais désenvoûter un jour… J'ai aussi une pensée pour **Pascal Boulet** et **Thomas Hauet** (camarade Meusien), respectivement les responsables des CC X-gamma et magnétisme. Merci à **Danielle Pierre** qui m'a initié à la croissance de film mince par MBE, **Stéphane Suire** qui m'a toujours sorti d'un mauvais pas quand le SQUID ou le VSM ne fonctionnait pas et rempli quelques dizaines de bidon d'hélium et d'azote… Un grand merci à **Alexandre Bouché** autre camarade meusien et voisin sur le « bébé » tube pour sa bonne humeur et les nombreux fou rires que nous avons pu avoir lors de la croissance de nos échantillons. Merci également à **Yuan Lu** avec qui j'ai passé de nombreuses heures et que j'ai fait revenir très tard les soirs ou pendant le weekend en salle MPGA afin de préparer nos échantillons... Un grand merci à **Gwladys Lengaigne** pour la nanostructuration des jonctions magnétique tunnel même si parfois les délais étaient très serrés ! Merci à toi **Sebastient Petit-Watelot** pour les pauses thés…

Je tiens ensuite à remercier les personnes qui sont devenues pour moi une seconde famille : **Hanna Riahi** et son mari **Cédric Moll** avec qui j'ai a partagé de nombreuses aventures, restaurant, moments de joie (mariage, déménagement, naissance). Vous serez les meilleurs parents au monde pour le petit **Aaron**...**Christel Berthelot** avec qui aussi j'ai passé de nombreuses aventures (plus ou moins alcoolisées. Et je dois dire monter une armoire en kit à minuit passé et en étant fortement inhibés d'alcool restera notre fait d'arme le plus marquant. Je tiens ensuite à remercier **Amina Neggache** qui a débuté sa thèse en même temps que moi et avec qui j'ai passé de nombreux moments de rigolades et de discussion beaucoup plus sérieuse sur la physique (évidement). On aura aussi vécu pas mal de chose ensemble et oui tu as le mauvais œil au-dessus de toi… **Yong Xu**… tu m'épateras toujours… Désolé de n'avoir pu répondre à certaines de tes questions sur la langue française… Ensuite il faut que je remercie **Guillaume Vasseur** qui m'a plus d'une fois sorti d'un mauvais pas pour les traitements de photoémission grâce à ses macros IGOR… Un grand merci à mon illustre prédécesseur **Mathieu Da Silva** avec qui nous avons bien rigolé, bu et discuté. Pour toutes les soirées et restaurants ayant pour but de ressouder les liens entre doctorants et nouveaux entrants doctorant ou non, je tiens donc à exprimer ma gratitude à toutes les personnes qui ont toujours répondu présentes à cette initiative: **Jennifer Weimmerskirch**, **Marion Lavenanant-Jambert**, **Damien Louis** (mon jeune padawan, la force je te transmettrais et tu transmettras), **Florent Hilde**, **Mohamed Salah Elhadri**, **Melissa Fauchard, Emmanuel Schaal**, **Guillaume Salah**, **Ludovic Pasquier**, **Tom Ferte**, **Vincent Polewczyk** (mon successeur, rends-moi fier), **Robert Tolley**, **Arlensiu Celis**. Je n'oublie pas les anciennes et anciens avec qui j'ai pu faire quelques sorties nocturnes: **Emilie Steveler**, **Amandine Duluard**, **Stéphanie Girod**, **Matthias Gottwald** et **Sylvain Le Gall.** Il va de soi que je remercie les illustres membres de la «**Team pokemon**».

Bref à tous ceux qui j'ai pu croiser durant cette thèse ou avec qui j'ai travaillé mais que je n'ai pas cités, MERCI pour tout !

La
dédicace
de ce tapuscrit
est partagée
en sept :
pour Gäelle et Fluffy,
pour mes Parents,
pour Antoine,
pour Hanna,
pour Christel,
pour Amina
et pour vous,
si vous m'avez
soutenu jusqu'à
la toute
fin.

Introduction

Conventional electronics uses and manipulates the electric charge of the electrons to make passive and active devices, ignoring the existence of the spin of the electron. However, since the pioneer work of N.F. Mott[1], it is known that the scattering probability of electrons in ferromagnetic materials is spin-dependent and that spin plays a role in electronics if magnetic materials are inserted in electronic devices. The combination of materials with controlled magnetic response at nanoscale was however limited before the development of deposition technics like sputtering, thermal evaporation or molecular beam epitaxy which permit the elaboration of metallic, semiconductor or insulating thin films with a control of thickness and roughness at the atomic scale.

The role of the spin of the electrons has then become a field of high interest for fundamental research as well as for the development of new electronic devices with the discovery of the Giant Magneto Resistance (GMR) in 1988 by A. Fert[2] and P. Grünberg[3]. Indeed, they showed that the resistance of a multilayer alternating magnetic and non-magnetic few nanometers thick films strongly depends on the relative orientation of consecutive magnetizations. Since this discovery, many other related effects have been highlighted, such as the spin torque effect predicted by L. Berger[4] and J. Slonczewski[5] in 1996: It has been shown that a spin-polarized current transports angular momentum that can be transferred to the magnetization of a magnetic nanostructure. Its magnetization can thus be excited and reversed or excited to steady state precessions. Those high frequency precessions are actually studied to build up agile and integrated oscillators. Magnetic materials were also combined with new promising materials like graphene[6], nanotubes[7] or molecular materials[8] to take the best from the associated materials and possibly give rise to new functionalities. All those related effects are gathered in a new field of condensed matter called spintronics.

In spintronics, the manipulation of both the charge and the spin of electrons provides new phenomena, new capabilities and functionalities. Spintronics offers the possibility of a new generation of electronic devices with low power consumption, higher density of computation and storage. Today, everybody has already used a spintronic device since the read heads of the hard discs use the GMR phenomenon in order to read the magnetic information stored in the hard disc.

The use of magnetic materials has however revealed several difficulties, mostly related to the magnetic interactions between two magnetic elements (inside a nanostructure between two magnetic layers or between first neighbor nanostructures like in MRAM) and/or to the formation of domains structure in the magnetic material at the remanent state. The grail would be the development of materials which would exhibit both 100% spin polarization and very small or zero-magnetization. The combination of these two interesting properties in a single material presents several advantages: such materials would not generate magnetic dipole fields, they would be insensitive to the applied field but they could nevertheless be very efficient spin analyzers or polarizers and would thus constitute ideal compounds for various spintronics devices. With respect to the magnetization decrease, antiferromagnets, ferrimagnets or ferromagnets without magnetization appear for now to be the best candidates.

The magnetic properties of antiferromagnetic compounds are generally used in antiferromagnetic/ferromagnetic (AF/F) systems, in order to pin the magnetization of a ferromagnetic layer via the exchange coupling. As detailed in Ref[9], the spin dependent transport studies with AF is still in its infancy but has been identified as a very promising way since (i) the spin penetration depth in the AF would be much longer than in the F and (ii) the use of AF doesn't generate stray fields and would permit a new generation of electronic devices with low power consumption and ultimate reduced sizes. This new research area with AF is starting to yield

encouraging results with the determination for the first time of critical penetration depths and absorption mechanisms of spin currents in $Ir_{20}Mn_{80}$ and $Fe_{50}Mn_{50}$ heterostructures[9].

On the other hand, classical ferrimagnetic compounds have already been used. Gd-Tb alloys have been integrated as electrodes in magnetic tunnel junctions (MTJs) and have permitted to observe a finite Tunnel MagnetoResistance value at the magnetic compensation of the two magnetization sub lattices[10]. In these MTJs, the spin polarization at the magnetic compensation has been explained as the consequence of much higher polarization of the tunneling current from the Transition Metal (TM) lattice as compared to the opposite Rare Earth (RE) one.

Beyond classical RE/TM ferrimagnets, an interesting archetype of zero-magnetization ferromagnet based on a Rare Earth- Non-magnetic intermetallic ($Sm_{1-x}Gd_xAl_2$) has been synthetized for the first time in 1999 by A. Adachi *et al*[11] and then as epitaxial thin film by our group[12]. It has been shown that $Sm_{1-x}Gd_xAl_2$ exhibits both a zero-magnetization and a long range ferromagnetic order where all the spin contributions point in the same direction[13] and thus appears as the best candidate in the development of spin polarizer. Recently, $Sm_{1-x}Gd_xAl_2$ has been successfully integrated in MTJs where a finite value of TMR has been observed at the magnetic compensation, thus giving the first proof that such zero-magnetization material can spin-polarize a current[14].

The main goals of this PhD work were to extend and strengthen the investigation of (i) surface/interface magnetic and electronic properties in $Sm_{1-x}Gd_xAl_2$ and (ii) $Sm_{1-x}Gd_xAl_2$-and/or [Co/Pt] multilayers-based MTJs. The manuscript is divided in seven chapters:

Chapter 1 is devoted to the magnetic properties of Sm and Sm-based compounds. The concept of ferromagnetic without magnetization is introduced and the main results obtained on bulk and epitaxial thin films of $Sm_{1-x}Gd_xAl_2$ are given, as well as on $Sm_{1-x}Gd_xAl_2$-based heterostructures. Those permit to precise the objectives of this work and to explain the research strategy that has been followed.

Chapter 2 introduces the physics of angle and spin-resolved photoemission spectroscopies and gives the specificities of the CASSIOPEE beamline where the study of the electronic band structure of $Sm_{1-x}Gd_xAl_2$ has been performed.

These experimental results are presented, discussed and compared with electronic band structure calculations (Wien2k code) in chapter 3.

Chapter 4 details the different contributions to the magnetic anisotropy in a thin layer or multilayer and the effects of roughness and/or intermixing. The results on [Co/Pt] multilayers found in the literature are then introduced.

The results obtained on [Co/Pt] multilayers and [Co/Pt]-based MTJs during this PhD are presented and discussed in chapters 5 and 6, respectively.

Chapter 7 presents the spin polarization dependence on Pt thickness and temperature in [Co/Pt]-based MTJs. The results concerning SGA-based MTJs using either an AlO_x or MgO tunnel barrier are then presented and discussed.

References

[**1**] N.F. Mott, Proc. R. Soc. A **156**, 368 (1936).
[**2**] M.N. Baibich *et al*., Phys. Rev. Lett. **61**, 2472 (1988).
[**3**] G. Binasch *et al*., Phys. Rev. B **39**, 4828 (1989).
[**4**] L. Berger, Phys. Rev. B **54**, 9353 (1996).
[**5**] J.C. Slonczewski , J. Magn. Magn. Mater. **159**, L1 (1996).
[**6**] A. Candini *et al*., Nano Lett. **11**, 2634 (2011).
[**7**] K. Tsukagoshi *et al*., Lett. to Nat. **401**, 572 (1999).
[**8**] N.J. Tao *et al*., Nat. Nanotechnol. **1**, 173 (2006).
[**9**] P. Merodio *et al*., Appl. Phys. Lett. **104**, 032406 (2014).
[**10**] C. Kaiser *et al*., Phys. Rev. Lett. **95**, 047202 (2005).
[**11**] H. Adachi *et al*., Nature **401**, 148 (1999).
[**12**] A. Avisou *et al*., J. Magn. Magn. Mater. **316**, 317 (2007).
[**13**] A. Avisou *et al*., J. Phys. Condens. Matter **20**, 265001 (2008).
[**14**] M. Da Silva *et al*., Appl. Phys. Lett. **98,** 232504 (2011)

Content

Chapter 1: $Sm_{1-x}Gd_xAl_2$, a recent story 1

I. From Sm^{3+} to $SmAl_2$ 3
I.A. Localized magnetism in Lanthanide metals 3
I.B. Sm multiplets mixing in a metallic matrix 4
I.C. $SmAl_2$, a self-ferrimagnet 5
II. $Sm_{1-x}Gd_xAl_2$, a zero-magnetization ferromagnet 7
II.A. First evidence of the zero-magnetization state 7
II.B. Ferromagnetic order at T_{comp} 8
III. SGA as epitaxial films 9
III.A. Epitaxial growth and structural properties 10
III.B. Magnetic properties 11
III.B.1. Perpendicular anisotropy and giant coercivity 12
III.B.2. 5d spin polarization and long-range ferromagnetic order 13
IV. SGA epitaxial films in magnetic heterostructures 13
IV.A. Exchange-coupled bilayers 14
IV.B. Magnetic Tunnel Junctions 17
V. Summary and purpose of this thesis 18
References 20

Chapter 2: Photoemission spectroscopy 21

I. Generalities on photoemission spectroscopy 23
I.A. Photoemission and the photoelectric effect 23
I.B. The three-steps model 24
I.B.1. Optical excitation of one electron in the solid 24
I.B.2. Propagation of the photoelectron to the surface 25
I.B.3. Escape of the photoelectron from the solid to the vacuum 26
I.C. Photoemission and dipole selection rules 27
II. Angle Resolved PhotoEmission Spectroscopy (ARPES) 28
II.A. Geometry of the ARPES experiment 28
II.B. Information provided by ARPES experiments 29
III. Spin-Resolved PhotoEmission Spectroscopy 30
IV. CASSIOPEE beamline 32
V. Conclusion 33
References 34

Chapter 3: Electronic properties of (111)$Sm_{1-x}Gd_xAl_2$ surface and interface ... 35

I. Literature review 37
I.A. Electronic band structure in Rare Earth dialuminides 37
I.B. Valence stability in Sm metal and $SmAl_2$ 38
I.C. Electronic surface state in Lanthanide elements 39
II. (111) SGA surface preparation and characterization 40
II.A. Chemical analysis 40
II.B. Structural analysis of the Nb-free surface 41
II.C. Electronic analysis 43
III. Electronic structure of (111) SGA surface 44
III.A. Samarium 4f multiplets 45
III.B. Valence band analysis (ARPES) 46
III.B.1 In-plane wave vector measurements 47
III.B.2 Out-of-plane wave vector measurements 54
III.B.3 Discussion on the nature of observed electronic states 57

III.C. Spin Resolved analysis....63
IV. Electronic structure of (111)SGA/MgO 65
IV.A. Interface oxidation....65
IV.B. Samarium 4f multiplets 66
IV.C. Valence band analysis....67
V. Conclusion 68
References....69

Chapter 4: Overview of the magnetic anisotropy in [Co/Pt] multilayers.....70

I. Introduction to the magnetic anisotropy 72
I.A. Origin of magnetic anisotropy in thin magnetic films 72
I.A.1. Shape anisotropy....72
I.A.2. Magneto-crystalline anisotropy....73
I.A.3. Surface or interface anisotropy 73
I.A.4. Magneto-elastic anisotropy....74
I.B. Effect of the roughness and interface alloy 75
I.C. Experimental determination of Keff 75
I.D. Stoner-Wohlfarth model 76
II. Perpendicular Magnetic Anisotropy in [Co/Pt] multilayers....77
II.A. Influence of the crystallographic orientation and preparations....78
II.B. Deviation from the linear behavior 79
III. Conclusion....80
References....81

Chapter 5: Magnetic and structural properties in [Co/Pt] multilayers 82

I. Description of the [Co/Pt] multilayers....84
II. Structural properties of the [Co/Pt] multilayers 85
II.A. Generalities on X-ray diffraction 85
II.B. Experimental setup 86
II.C. Growth direction in the sputtered [Co/Pt] multilayers 88
II.D. Reflectometry analysis on [Co/Pt] multilayers 89
II.D.1. Co and Pt thicknesses 92
II.D.2. Co and Pt roughnesses....93
III. Magnetic properties in the [Co/Pt] multilayers....93
III.A. Experimental setup 93
III.B. Experimental results 94
III.B.1 Effective anisotropy 97
III.B.2. Saturation magnetization 99
III.B.3. Influence of temperature....102
IV. Conclusion 103
References....105

Chapter 6: Magnetic Tunnel Junctions with [Co/Pt]-based electrodes.....106

I. Introduction....108
I.A. MTJ's structure....108
I.B. Micromagnetic simulations and magnetic parameters of the materials 109
II. Magnetic properties in MTJs full stack....111
II.A. Magnetization reversal 111
II.B. Magnetic configurations....114
II.B.1. Influence of the applied magnetic field....114
II.B.2. Influence of the temperature 117
II.B.3. Calculated (H,T) phase diagram for the hard electrode 118
III. Transport properties in nano-patterned MTJs 119
III.A. Common features in perpendicular MTJs....119
III.A.1. Tunnel characteristics 119

III.A.2. R(H) characteristics 122
III.B. Phase diagrams in nano-patterned MTJs 124
III.B.1. Duplication of domains from the hard to the soft electrode 126
III.B.2. Spring magnet and exchange bias behavior 130
III.C. Coupling through the MgO barrier 131
IV. Conclusion 134
References 135

Chapter 7: Spin-polarization in [Co/Pt]- and SGA- based magnetic tunnel junctions 136

I. TMR and effective polarization in [Co/Pt] based-MTJs 138
I.A. Effective polarization of [Co/Pt]: more than an interface phenomenon? 138
I.B. Bloch low and Curie temperature 141
II. TMR and spin-polarization in SGA/AlO_x/[Co/Pt] MTJs 143
II.A. Tunnel characteristic 143
II.B. Finite magneto-resistance tunnel at the magnetic compensation 144
II.C. Discussion 146
III. Preliminary results on SGA/MgO/[Co/Pt] MTJs 146
III.A. SGA surface preparation 148
III.B. Common features in perpendicular SGA-based MTJs 149
III.B.1. Tunnel conductance versus voltage 149
III.B.2. Tunnel conductance versus temperature 150
III.B.3. Resistance versus applied field characteristics 151
III.C. Discussion 151
IV. Conclusion 152
References 153

General conclusion and future projects 154

Chapter 1
$Sm_{1-x}Gd_xAl_2$, a recent story

I. From Sm^{3+} to $SmAl_2$ 3
I.A. Localized magnetism in Lanthanide metals 3
I.B. Sm multiplets mixing in a metallic matrix 4
I.C. $SmAl_2$, a self-ferrimagnet 5
II. $Sm_{1-x}Gd_xAl_2$, a zero-magnetization ferromagnet 7
II.A. First evidence of the zero-magnetization state 7
II.B. Ferromagnetic order at T_{comp} 8
III. SGA as epitaxial films 9
III.A. Epitaxial growth and structural properties 10
III.B. Magnetic properties 11
III.B.1. Perpendicular anisotropy and giant coercivity 12
III.B.2. 5d spin polarization and long-range ferromagnetic order 13
IV. SGA epitaxial films in magnetic heterostructures 13
IV.A. Exchange-coupled bilayers 14
IV.B. Magnetic Tunnel Junctions 17
V. Summary and purpose of this thesis 18
References 20

This first chapter is divided in five parts. The first part gives a brief overview of the magnetic properties from the Sm^{3+} free ion to the $SmAl_2$ intermetallic compound. These elements are necessary to further explain how it is possible to slightly tune the $SmAl_2$ magnetic characteristics and generate an original magnetic compensated state. The second part is devoted to the unusual magnetic properties of bulk $Sm_{1-x}Gd_xAl_2$ (called SGA in the following), a zero-magnetization ferromagnet. The third part presents the properties of SGA as epitaxial films. The fourth part summarizes the various studies that have been undertaken in SGA-based heterostructures, such as exchange-coupled bilayers and Magnetic Tunnel Junctions (MTJs). In view of this general context, the fifth part explains the main objectives of this PhD work and gives a schematic view of the manuscript.

A magnetic compensated state is defined as a magnetic state where the magnetization is equal to zero. Such zero-magnetization states are already well-known in a wide variety of materials: in antiferromagnets (for instance NiO) where the two opposite magnetic sublattices belong to the same chemical sublattice (Ni), in some pure metals (for instance Cr or Dy) that exhibit a modulated magnetic phase, in ferrimagnets (for instance TbCo) where the two opposite magnetic sublattices belong to different chemical sublattices (Tb and Co). In the two first cases, the zero-magnetization state exists over an extended temperature range while it is limited to a given temperature (the so-called compensation temperature) in the third case. The compensation temperature is the temperature where the two magnetic sublattices perfectly cancel each other, i.e. the temperature where the thermal dependences of the magnetization associated to each magnetic sublattice cross each other.

The $Sm_{1-x}Gd_xAl_2$ compound is the first example of a new type of materials exhibiting a magnetic compensated state. Beyond antiferromagnetic metals and compounds, beyond compensated ferrimagnets, this material can be defined as a *zero-magnetization ferromagnet*. This original property, achieved at a given compensation temperature (T_{comp}), is counterintuitive since a ferromagnet usually exhibits a spontaneous magnetization with no applied field. In the case of SGA, we will see how the compensated state is generated by substituting a small quantity of Sm atoms by Gd atoms in a ferromagnetic $SmAl_2$ matrix.

In order to understand the physics and the mechanisms behind this ferromagnetic compensated state, some generalities about the magnetism of lanthanide elements and more especially of the Sm^{3+} ion which drives the magnetic properties of $SmAl_2$, are briefly introduced in the next section. Complementary informations can also be found in the PhD work of A. Avisou[1].

I. From Sm^{3+} to $SmAl_2$

I.A. Localized magnetism in Lanthanide metals

The magnetism in the Lanthanide family, to which belongs the Samarium, is mainly driven by the 4f electrons. The spatial extension of the 4f orbitals being weak, the 4f electrons are localized close to the atomic nucleus and as a result don't contribute to the interatomic bonds. Consequently, the magnetism in the Lanthanide metals is defined as localized, contrarily to the 3d metals whose magnetism can be well described by the itinerant electrons model. Two distinct cases must be considered in the Lanthanide family: the case of light Rare Earth (called RE in the following) where the 4f shell is less than half-filled (n < 7) and the case of heavy RE where the 4f shell is more than half-filled (n > 7). The magnetic moment in both cases can be calculated by the so-called Hund's rules (see below) which permit to determine the 4f spin and orbital moments, respectively defined as S and L.

Hund rules:

- The electrons occupy the free orbitals in order to maximize S, which corresponds to the minimization of the Coulomb interaction. In the case of light RE, S = n/2 whereas in the case of heavy RE, S = (14-n)/2, where n corresponds to the number of 4f electrons.
- The electrons occupy the free orbitals in order to maximize L.

Taking the spin-orbit coupling between **L** and **S** into account leads to the total angular momentum $\boldsymbol{J} = \boldsymbol{L} + \boldsymbol{S}$. From the spin-orbit coupling arise new energy levels, the so-called multiplets. The lowest energy level (fundamental multiplet) is J=L-S for light RE (anti-parallel coupling between ***L*** and ***S***) whereas J=L+S for heavy RE (parallel coupling between ***L*** and ***S***).

In the case of the Sm^{3+} ion, with an electronic configuration $[Xe]4f^5 5d^1 6s^2$, the Hund's rules give S = 5/2 and L = 5. The fundamental state is characterized by J=L-S=5/2, where Spin and Orbital moments are antiparallel. This low value for J leads to a particularly small energy difference between the fundamental and first excited multiplets (J=7/2): it is only of the order of 0.13 eV whereas it is close to 1 eV in most of other rare earth metals[2].

I.B. Sm multiplets mixing in a metallic matrix

In Sm-based metallic compounds, the main interactions between the Sm^{3+} ions and the crystal are the crystalline and the exchange fields. The former results from the electrostatic interactions between the charge distribution in the crystal and the 4f orbitals of the Sm^{3+} ions; the latter describes the indirect exchange interaction between the 4f moments (the so-called RKKY coupling[3], mediated by direct exchange between 4f moments and conduction electrons).

The resulting total Hamiltonian can thus be written in the case of zero applied field by:

$$H = \lambda \boldsymbol{L}.\boldsymbol{S} + H_{CF} - 2\mu_B J_{ff} \langle \boldsymbol{S} \rangle . \boldsymbol{S} \qquad \textbf{(I-1)}$$

where **L** and **S** are the orbital and spin moments, $\lambda \boldsymbol{L}.\boldsymbol{S}$ is the spin-orbit coupling, H_{CF} is the crystalline field Hamiltonian and $2\mu_B J_{ff} \langle \boldsymbol{S} \rangle . \boldsymbol{S}$ is the exchange energy, with J_{ff} the exchange interaction between 4f spins.

Note: *in the presence of an external field, it is necessary to add two Zeeman terms which correspond to the interaction of the external field with the total 4f moment and with the spin of conduction electrons.*

Figure 1 presents the energy levels resulting from the total Hamiltonian diagonalization in the case of Sm^{3+} free ion (left part) and in the presence of crystal and exchange fields (right part).

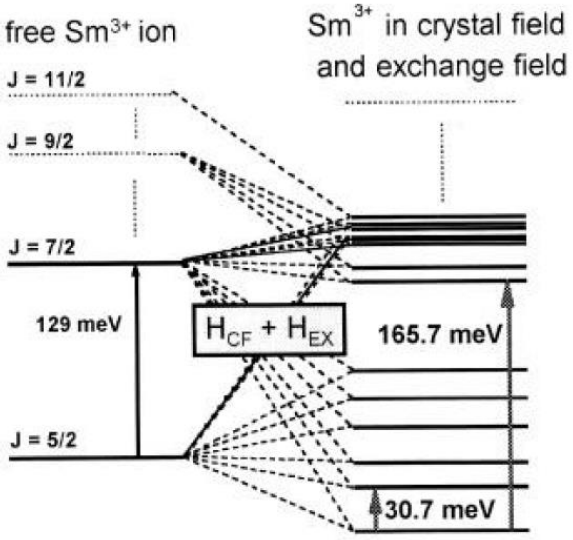

Figure 1: Sketch of the energy levels for free Sm^{3+} (Left) and for Sm^{3+} ion in $SmCo_5$ (right), where one can see the effects of crystal and exchange fields: lift of degeneracy and mixing of multiplets (from[4]).

The diagonalization of H not only lifts the degeneracy of the Sm^{3+} multiplets, but also leads to a mixing of these multiplets. Because the lowest energy levels are particularly close to each other, as mentioned in the previous paragraph, the new energy levels are indeed linear combinations of the fundamental and first excited states, as illustrated in figure 1.

This multiplets mixing plays a significant role in the magnetic properties of Sm-based ferromagnetic compounds: it mainly affects the value of the saturation magnetization (largely reduced compared to the $0.71\mu_B$ of the free ion) and the temperature dependence of the magnetic moment, as it is described in the specific case of $SmAl_2$ in the following paragraph.

I.C. $SmAl_2$, a self-ferrimagnet

$SmAl_2$ belongs to the dialuminide family ($REAl_2$) and crystallizes in cubic so-called "Laves phase" structure (space group $Fd\bar{3}m$ - N° 227) sketched in figure 2. The Samarium atoms (in red) form a diamond structure where half of the tetragonal sites are occupied by Sm atoms, the other half being occupied by regular tetrahedron of Aluminum atoms (in blue). The $SmAl_2$ lattice constant is equal to 7.943 Å at room temperature (JCPDS source).

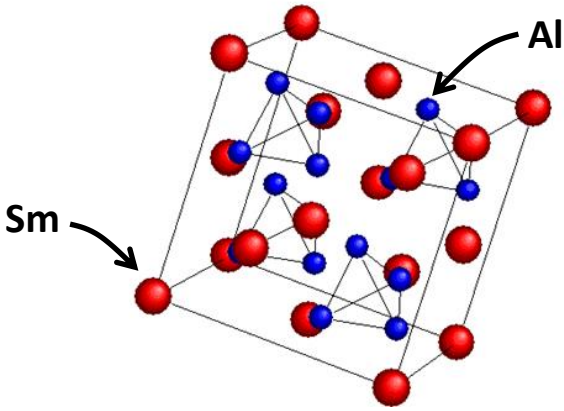

Figure 2: Sketch of the cubic Laves phase structure in the case of $SmAl_2$.

$SmAl_2$ is a ferromagnetic compound with a Curie temperature of 127K[5] and an easy magnetization axis parallel to the (111) direction[5],[6]. As it has been briefly mentioned previously, in this ferromagnetic Sm-based compound, the effect of crystal and exchange fields is to lift the degeneracy of Sm multiplets and to give rise to new energy levels that result from the mixing of ground and first excited states.

The two main consequences of the multiplets mixing on the $SmAl_2$ magnetic properties are the following:

(i) *Reduction of the magnetic moment*.

Taking the multiplets mixing into account permits to calculate a 4f magnetic moment of 0.5 μ_B/Sm, i.e. reduced by 30% compared to the value in the free ion ($0.71\ \mu_B$). This effect is however not large enough to explain the experimental value of $0.26\ \mu_B/Sm$ measured at 2K in $SmAl_2$. The negative contribution of conduction electrons (calculated -$0.24\mu_B/Sm$) is not negligible compared to the small 4f contribution and also contributes to drastically decrease the total moment (values calculated by H. Adachi *et al.*[5]). The sum of both 4f and conduction electrons calculated contributions is in good agreement with the experimental value of $0.26\ \mu_B/Sm$ at 2K.

(ii) *Different temperature dependences for the 4f spin and orbital moments*.

The diagonalization of the Hamiltonian (I-1) taking the mixing between 5/2 and 7/2 states into account highlights a slight difference in the temperature dependences of the calculated 4f orbital ($\boldsymbol{L}_{4fSm}$) and spin ($\boldsymbol{S}_{4fSm}$) moments (figure 3 (a)). Below the Curie temperature (127K), the orbital moment $\boldsymbol{L}_{4fSm}$ is larger than the spin moment $\boldsymbol{S}_{4fSm}$ over the whole temperature range, and the small spin polarization of conduction electrons ($\boldsymbol{S}_{ecSm}$) contribute positively to the total Sm spin moment (confirmed by Compton-scattering experiments[7]), as it is sketched in figure 3 (b). As a consequence, the total moment results from the sum of a small 4f contribution, dominated by the orbital part, and an antiparallel contribution of conduction electrons, of the same order of magnitude but still smaller over the entire temperature range.

$$\boldsymbol{M}_{total} = \boldsymbol{L}_{4fSm} - \boldsymbol{S}_{4fSm} - \boldsymbol{S}_{ecSm} \qquad \text{(I-2)}$$

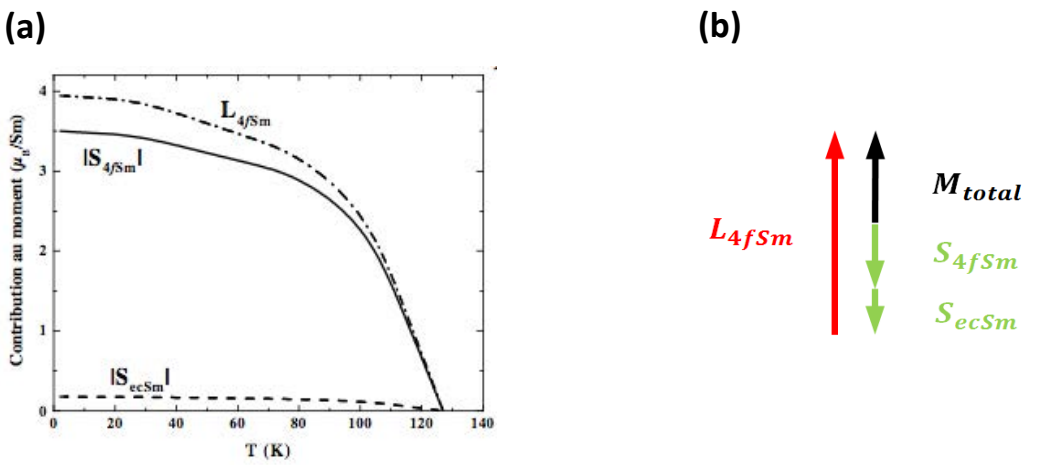

Figure 3: (a) Calculated temperature dependences of the Samarium 4f spin (black lines) and orbital (dash-dot) contributions and of the conduction electrons contribution (dash line) in $SmAl_2$[1] (b) Sketch of the different contributions to the total magnetic moment in $SmAl_2$.

Since the $SmAl_2$ magnetization results from antiparallel magnetic contributions that exhibit different temperature variations but that all originate from the Sm element, this compound can be interestingly considered as a *self-ferrimagnet*. Figure 4 presents two sketches to compare a "classical" ferrimagnetic compound, such as a CoTb alloy where antiparallel magnetic contributions belong to the Co and Tb magnetic sub-lattices, and the $SmAl_2$ "self-ferrimagnet", as it has been previously discussed.

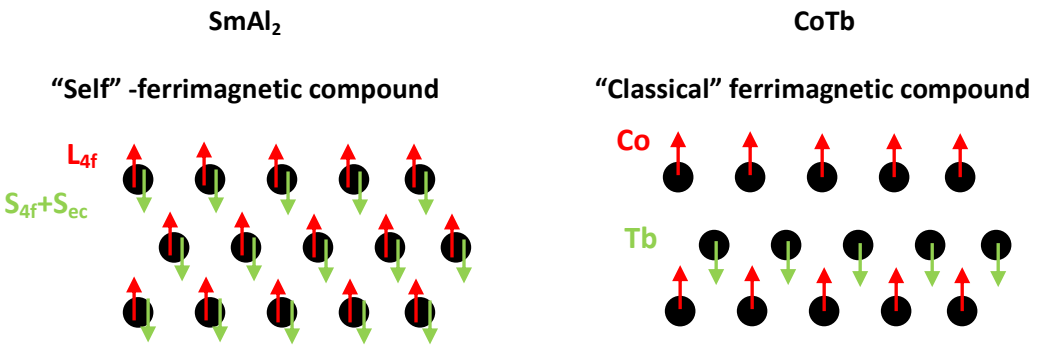

Figure 4: Sketches of the orientation of the magnetic contributions in the case of $SmAl_2$ a "self-ferrimagnet" (left) and in the case of a "classical" ferrimagnet (right).

The main difference is that the ferrimagnetic character in $SmAl_2$ originates from the specific properties of Sm ions and not from the occurrence of two magnetic species on two sublattices. Antiparallel contributions are orbital and spin moments, with long range parallel order for both orbital and spin contributions.

In contrast to some ferrimagnetic compounds, $SmAl_2$ doesn't exhibit a magnetic compensated state where its magnetization drops to zero. The curves for spin and orbital thermal variations do not cross each other and the orbital part remains dominant over the entire temperature range. However, the equation **(I-2)** suggests that slightly increasing the spin part (either from 4f or conduction electrons) would enable us to generate a magnetic compensation. Such a compensated state would be thus particularly original since it will coexist with the long range parallel order of all spin contributions in the magnetic system.

II. $Sm_{1-x}Gd_xAl_2$, a zero-magnetization ferromagnet

The first strategy to generate a magnetic compensation in the $SmAl_2$ compound was to try to modify the contribution of conduction electrons in changing the s-f exchange or the density of states at the Fermi level. Those changes could theoretically be achieved via modification of the lattice constant. The substitution of Sm atoms in $SmAl_2$ by non-magnetic Sc, Y or La (effect of chemical pressure) resulted in the reduction of ordering temperature but no compensated state could be observed[8].

The second attempt was to modify the 4f contribution, i.e. to increase the 4f spin contribution. Given the magnetic coupling between lanthanides elements (ferromagnetic coupling between spin moments), replacing a small quantity of Sm atoms by other Lanthanide atoms would yield a total moment that is the average of the 4f spin and orbital moments of each RE element. The strategy developed by Adachi *et al.*[8] was to substitute Gd atoms to Sm ones, to synthetize the $Sm_{1-x}Gd_xAl_2$ (SGA) compound. This choice has been strongly motivated by the S character of Gd ions that will only contribute to the spin moments via both 4f and conduction electrons contributions.

The goal of this section is to give an overview of the magnetic properties investigated in bulk SGA and more especially of the various analysis devoted to the original magnetic compensated state, coexisting with long-range parallel (i.e. ferromagnetic) spin and orbital orders.

II.A. First evidence of the zero-magnetization state

The magnetic compensation via the tuning of the 4f contribution in bulk $SmAl_2$ has been demonstrated by H. Adachi *et al.*[8] and achieved by substituting a small quantity of Gd atoms by Samarium atoms. Given the Gd^{3+} electronic configuration ($[Xe]4f^7 5d^1 6s^2$), the Hund's rules lead to $\boldsymbol{L} = 0$ in order to maximize $\boldsymbol{S}$ and its total angular momentum is thus a pure spin moment. Previous results of hyperfine studies on SGA alloys[9] have reported the parallel coupling between the Gd and Sm spin contributions. Gd is thus expected to contribute positively to the spin part of the net moment providing two new spin contributions $\boldsymbol{S}_{4fGd}$ and $\boldsymbol{S}_{ecGd}$. The net moment defined by equation **(I-2)** can be rewritten as:

$$\boldsymbol{M}_{total} = \boldsymbol{L}_{4fSm} - \boldsymbol{S}_{4fSm} - \boldsymbol{S}_{ecSm} - \boldsymbol{S}_{4fGd} - \boldsymbol{S}_{ecGd} \qquad \textbf{(II-1)}$$

Figure 5 presents the temperature dependence of the magnetization in bulk $SmAl_2$ and in two SGA compounds corresponding to different Gd concentrations. While a monotonously decreasing M(T) curve is measured for $SmAl_2$ (decrease of L and S with L > S in the whole temperature range), the substitution of Gd atoms in the $SmAl_2$ matrix yields a magnetic compensation, occurring at 81K and 64K for respectively 1.8% and 2.6% Gd contents. The authors suggest that the ferromagnetic spin

order should be kept in the compensated state. No definitive proof is however provided by these macroscopic measurements.

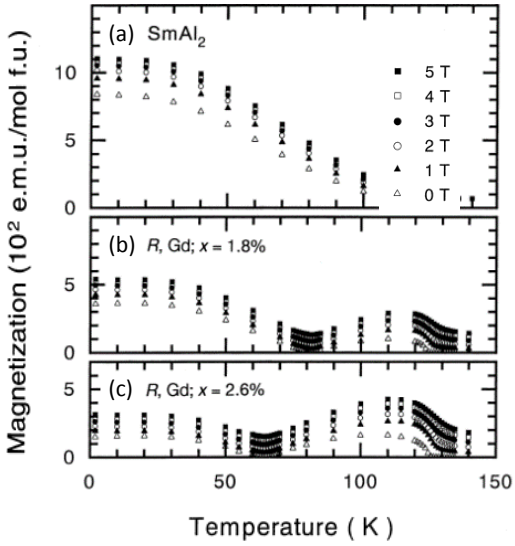

Figure 5: Temperature dependence of magnetization in bulk $SmAl_2$ (a) and in bulk SGA for different Gd concentrations (b) and (c) (from[8]).

II.B. Ferromagnetic order at T_{comp}

Following the observation of a zero-magnetization state in bulk SGA by Adachi *et al.*[8], several groups have tried to clearly identify the underlying mechanism and confirm the co-existing ferromagnetic spin order. A variety of techniques has been used, which enabled to explore the system from different angles and to separately probe the different contributions to the magnetic moment.

The Magnetic Compton scattering[10], based on the interaction between the spin moment ($\boldsymbol{S}_{ec} + \boldsymbol{S}_{4f}$) and the helicity of light, has brought the first proof of the spin ferromagnetic order via the observation of a finite signal at T_{comp}. By changing the thermal history (measurements at T_{comp} coming from high or low temperature side), the authors report on opposite spin polarizations, implying a positive (negative) spin contribution to the total moment above (below) T_{comp}.

Non-resonant X-ray Magnetic Scattering[11], based on the interaction between the photon and the spin and orbital 4f moments, has been used to investigate separately the thermal dependences of the 4f spin and 4f orbital moments under an applied field of 1T. These measurements have especially confirmed the dominant character of orbital contribution below compensation and the dominant character of spin contributions above compensation. In the same study, measurements of specific heat show no anomaly at the compensation, implying no magnetic transition and suggesting the persistence of the ferromagnetic order.

Six years after their first report on the SGA magnetic compensation, Adachi *et al.*[8] unambiguously prove the spin and orbital long-range orders at compensation. Using X-Ray Magnetic Circular Dichroism (XMCD)[12], based on the difference in absorption by a magnetic material when it is excited by a left or a right circularly polarized light, they could separately probe the Gd and Sm 4f contributions ($M_{4,5}$ edge). Taking advantage of the sum rules, they could extract the spin and orbital contributions, as it is reported in figure 6 (a). The net resulting magnetizations for the Sm, Gd and conduction electrons are compared to the net magnetization of $SmAl_2$ in figure 6 (b).

These results prove the monotonic decrease of the Sm 4f spin moment and its finite value at compensation, in agreement with a remaining long-range ferromagnetic order. They confirm the

anti-parallel coupling between Sm orbital and spin contributions and the dominant L contribution over the entire temperature range, as expected from the calculation presented in figure 3. Consequently, the compensated state cannot be achieved by only the Sm 4f electrons; the Gd spin moment and the conduction electron polarization (ferromagnetically coupled to the Sm 4f spin contribution) must be taken into account to cancel the surplus of orbital moment of the Sm^{3+} ions.

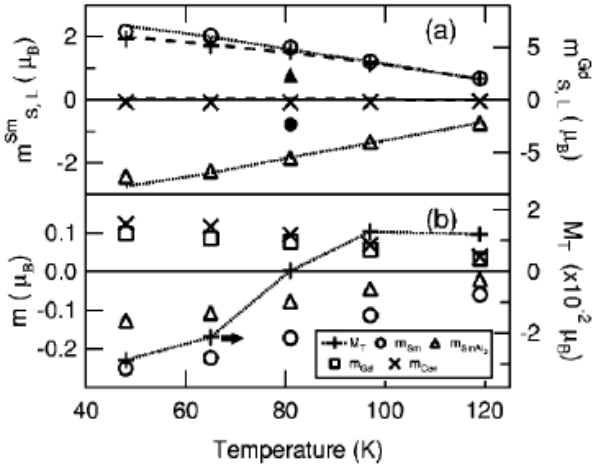

Figure 6: (a) Experimental values of m_S^{Sm}(○), m_S^{Gd}(+), m_L^{Sm}(Δ) and m_L^{Gd}(x) when the sample was magnetized at 110K (open symbols) and at 43K (filled symbols). The dashed and dotted lines correspond to the theoretical value of the 4f spin and orbital moments of Gd and Sm (respectively). (b) Net magnetization (+) for the Sm (○), Gd (□) and conduction electrons (x) compared to the net magnetization of $SmAl_2$ (Δ) (from[12]).

The different studies mentioned in this section have contributed to the definition of bulk SGA compound as a zero-magnetization ferromagnet. These unusual properties make it very attractive for specific fundamental studies as well as for various types of applications.

Because of its zero-magnetization, such a compound doesn't indeed generate any dipolar field and is insensitive to an external applied field: these characteristics should permit to achieve a uniform magnetic state, without formation of magnetic domains, that doesn't induce magnetic perturbation for neighboring elements and is magnetically very stable. However, as a ferromagnet, it must be able to spin-polarize or spin-analyze an electrical current.

The combination of these usually antagonist properties would be particularly interesting for applications dealing with the control and/or manipulation of the electron spin, such as magnetic tips for spin-polarized tunnel microscopy or as a component in some spintronic devices. These potential developments have strongly motivated the studies undertaken by our group in Institute Jean Lamour to achieve the growth of SGA epitaxial films, to investigate their structural, magnetic and electronic properties and to further integrate them in more complex hybrid systems. Indeed, these properties should be conserved in thin films used in spintronics devices as spin-valves or magnetic tunnel junctions.

III. $Sm_{1-x}Gd_xAl_2$ as epitaxial films

The first paragraph briefly summarizes the growth conditions and structural characteristics of SGA epitaxial films. The second paragraph presents their magnetic properties, investigated by the combination of SQUID magnetometry and XMCD experiments.

III.A. Epitaxial growth and structural properties

Our group in IJL has been the first to achieve the growth of single crystalline epitaxial SGA films by Molecular Beam Epitaxy (MBE)[13],[14]. The experimental process is based on the co-deposition at 510°C of Sm, Gd and Al atoms on a Nb buffer (50 nm thick) covering a $(11\bar{2}0)$ sapphire substrate. The different fluxes are previously calibrated by a quartz microbalance at the substrate position in order to get the desired stoichiometry.

Figure 7 presents typical (a) Reflection High Energy Electron Diffraction (RHEED) patterns along two azimuthal directions collected during the SGA growth and (b) large angle X-ray diffraction patterns (specular analysis along the growth direction and rocking curve across the (111)SGA Bragg peak) measured with a PanAnalytical X'Pert Pro diffractometer working at the Cu K_α wavelength.

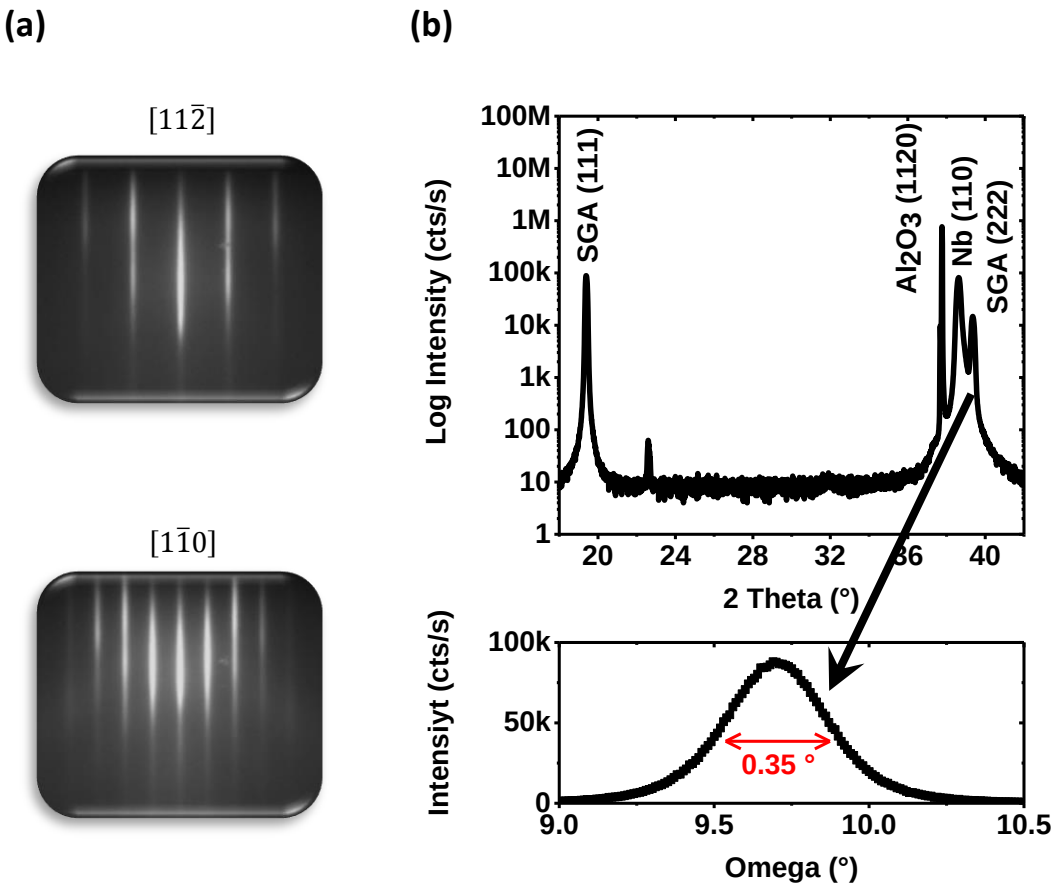

Figure 7: (a) RHEED patterns along two azimuthal directions ($[11\bar{2}]$ and $[1\bar{1}0]$) after the deposition of 300 nm of SGA (b) X-ray diffraction patterns collected at high angles for a SGA epitaxial film. Top: specular analysis and bottom: rocking curve across the (111)SGA Bragg peak) (from[15]).

Those results attest for the epitaxial growth of SGA along the [111] direction of the Laves phase structure. The RHEED patterns for both directions exhibit very thin, continuous and contrasted streaks revealing a smooth (111)SGA surface of high crystalline quality. The large angle X-ray scattering pattern permits to identify the (111) SGA diffraction peak with its second order at higher angle values. The full width at half maximum (0.35°) of the rocking curve across the (111) SGA Bragg peak attests for the small mosaïcity, i.e. a reduced dispersion of the [111] directions around the growth axis. Further details can be found in the references [13],[14].

III.B. Magnetic properties

The magnetic properties of SGA epitaxial films have been first explored by A. Avisou *et al.*[16], using the combination of macroscopic magnetization measurements (SQUID magnetometry, ±7T) and element- and shell- selective technique (XMCD at the Sm and Gd $L_{2,3}$ absorption edges, ±7T). Some complementary XMCD measurements have been performed during this PhD work in order to extend the field range of investigation to ±17T[17]. Such high field XMCD studies have been made possible on the ID12 beamline at the European Synchrotron Radiation Facility (ESRF), in collaboration with F. Wilhelm and A. Rogalev.

The magnetic field was applied perpendicular to the film surface and parallel to the direction of the incident X-ray beam. XMCD spectra were recorded by flipping the helicity of incoming X-rays and keeping the direction of the magnetic field fixed. The degree of circular polarization of the monochromatic X-ray beam was estimated to be in excess of 85%. The spectra were recorded in the total fluorescence detection mode. Measurements at the L edges of rare earth probe the transition from *2p* core levels to *5d* empty states ; they permit to determine the projection of the *5d* spin momentum along the quantification axis, i.e. either parallel or antiparallel to the direction of applied magnetic field. Due to the so-called breathing effect[18], a negative (positive) signal measured at the L_2 (L_3) edge results from a positive projection of *5d* spin polarization along the quantification axis (i.e. parallel to the positive field direction)[19].

It was verified that the shapes of the XMCD spectra do not change with the applied field intensity and that they exhibit a maximum for the same energy values. As an example, figure 8 presents two XMCD spectra recorded at the Sm L_2 edge at 20K and +7T (blue curve) and at 115K and +17T (green curve) for a SGA layer. To record element-selective hysteresis loops, the energy of the incident X-ray photons was thus tuned to the maximum of the XMCD signal either at the Sm L_2 edge (7.316 keV) or at the Gd L_3 edge (7.247 keV).

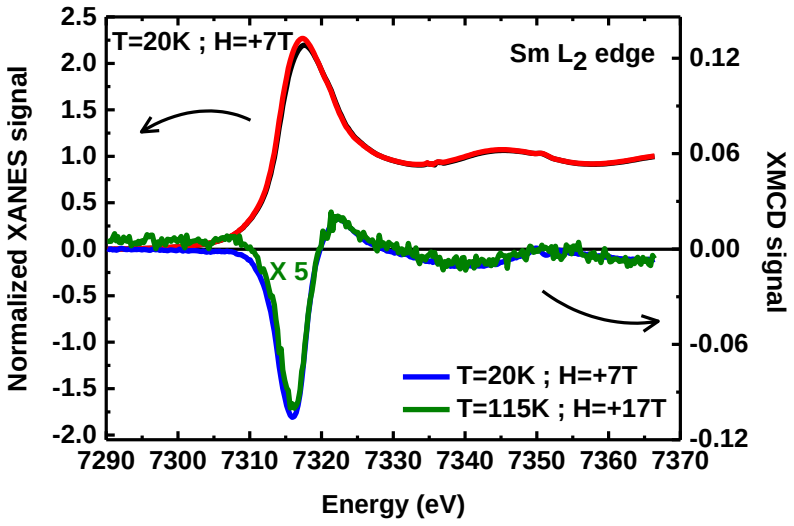

Figure 8: Normalized x-ray absorption near edge structure curves (for both incident photons polarizations) and normalized x-ray magnetic circular dichroic signals at the Sm L_2 edge for a 300nm thick single crystalline $Sm_{0.0972}Gd_{0.028}Al_2$ layer. XANES measurements and corresponding blue XMCD curve have been measured at 20K and under +7T. The XMCD signal measured at 115K and +17T (green curve, intensity multiplied by a factor of 5) has been added for comparison.

The main results are summarized in figure 9 and discussed in the following paragraphs.

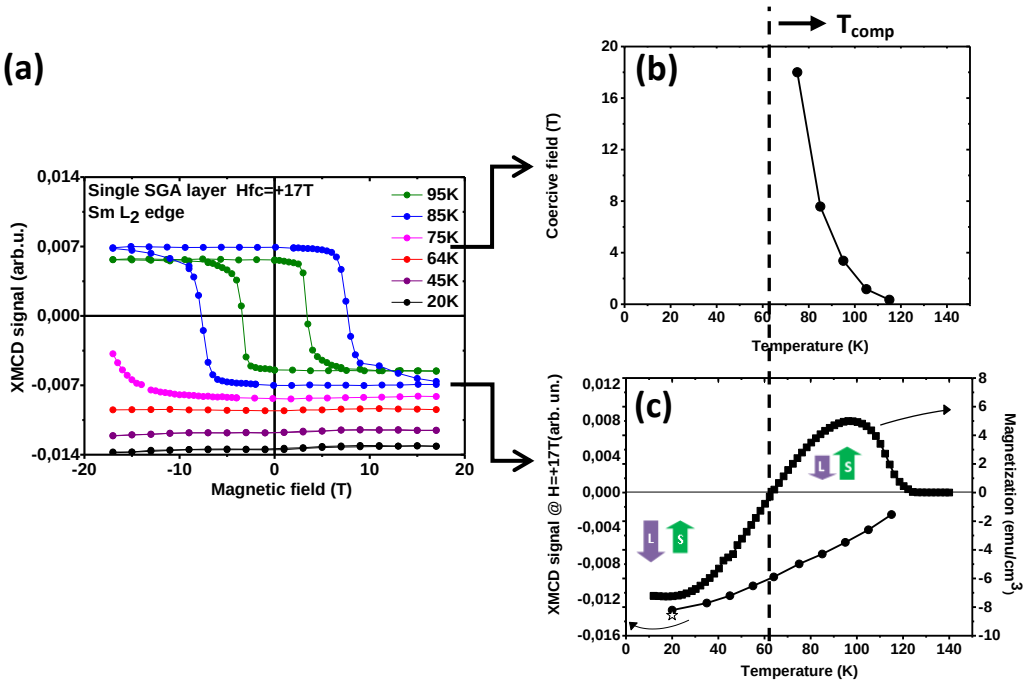

*Figure 9: (a) XMCD loops recorded at the Sm L_2 edge after a +17T field cooling for the 300 nm-thick $Sm_{0.0972}Gd_{0.028}Al_2$ epitaxial film. (b) Temperature dependence of the coercive field values extracted from the XMCD loops. (c) Temperature dependence of the XMCD signal (dots) compared to the magnetization measured by SQUID (squares) after a +7T cooling field. The magnetic **L** and **S** configurations are sketched with the purple and green arrows respectively (from*[17]*).*

III.B.1. Perpendicular anisotropy and giant coercivity

The hysteresis loops measured at 95K and 85K (i.e. above the compensation temperature T_{comp}=64K) for an external field applied perpendicular to the sample surface (figure 9 (a)) are characteristics of a perpendicular easy magnetization axis, as previously reported by Avisou *et al.*[14],[16]. It has been suggested that the perpendicular anisotropy in Sm based compound would result from magneto-elastic effects related to the compressive strain observed along the growth direction[20].

The XMCD signal recorded below T_{comp} is almost constant in the ±17T field range. The coercive field can be properly determined only down to 85K (i.e. approximately 20K above T_{comp}). Its temperature dependence is given in figure 9 (b). The strong divergence when approaching the compensation point is expected from the vanishing magnetization: the magnetization becoming small, the Zeeman energy becomes also small and as a result the magnetic field required to reverse the magnetization increases drastically. It is a common feature in usual ferrimagnetic compounds[21],[22]. However, in ferrimagnetic compounds, the coercive field decreases when further decreasing the temperature away from the compensation. This is obviously not the case in SGA epitaxial films below T_{comp} despite the increase of magnetization at low temperature. The giant coercivity is thus not related to the small magnetization value but to other features becoming dominant at low temperatures. The persistence of a huge coercivity below the compensation temperature in SGA epitaxial films also differs from the behavior reported in bulk SGA (for example 0.2T at 10K from[11]). The reasons for such a large coercive field and the specific role of structural characteristics (antiphase boundaries, microstructure) in SGA epitaxial films still remain to be clarified.

III.B.2. 5d spin polarization and long-range ferromagnetic order

The negative XMCD signal measured at the Sm L_2 edge for the maximum +17T field (figure 9(a)) reveals a positive projection of the 5d spin polarization, i.e. the spin contribution point towards the positive field direction. This configuration (L-down and S-up), sketched by the respective purple and green arrows in figure 9 (c), is favored by the Zeeman interaction above T_{comp} where S contributions are dominant. Above T_{comp}, the magnetization reversal in SGA epitaxial film is driven by the flipping of the dominant S contribution towards the negative field direction (L-up configuration), thus yielding a positive signal at the Sm L_2 edge as observed in figure 9 (a). Below T_{comp}, the signal measured in the SGA epitaxial film remains negative over the entire ±17T field range. Despite the dominant L contributions in this temperature range, the smaller S component still point towards the positive field direction: the S-up configuration is stabilized during the cooling process from above T_{comp} and persists down to low temperature due to the diverging coercive field, as previously discussed.

The temperature dependence of the XMCD signal recorded at 17T is reported in figure 9 (c), in comparison with SQUID measurements (black squares). It reflects the variation of the 5d spin polarization that monotonically decreases when increasing the temperature. This variation is in good agreement with the one for 4f Sm and Gd spin contributions measured in bulk SGA at the $M_{4,5}$ edge[12] and confirms the close correlation between the 4f and 5d spin contributions. Two main points have to be noted in figure 9 (c): (i) the Curie temperature can be extrapolated to 126K, in good agreement with the Curie temperature obtained from SQUID measurements and with the bulk $SmAl_2$ Curie temperature, (ii) the 5d spin polarization exhibits a finite value at T_{comp}, confirming the persisting long-range ferromagnetic order in the compensated state, as reported previously by Avisou *et al.*[16].

In order to analyze the possible existence of domains after the cooling process towards below compensation, a specific cooling procedure has been used to specifically prevent the formation of L-up domains: the cooling field has been reversed from +17T to -17T at T_{comp} thus "following" the dominant magnetic contribution. The resulting 5d polarization at 20K (star symbol in figure 9 (c)) is very close to the one measured after the +17T usual cooling, which suggests a homogeneous S-up magnetic configuration after the +17T field cooling. A high external field up to 17T does not permit inducing any "Zeeman-favored" L-up domains.

IV. $Sm_{1-x}Gd_xAl_2$ epitaxial films in magnetic heterostructures

Beyond the epitaxial growth of (111)SGA epitaxial films, the group in Nancy undertook a few years ago the investigation of magnetic SGA-based heterostructures:

(i) *Exchange-coupled bilayers*, where the highly coercive SGA compound acts as a magnetically hard pinning layer[23].The investigation of exchange coupling in SGA-based bilayers is first a powerful way to probe the interface magnetic properties of SGA. At the SGA compensation point, SGA/SA bilayers can also be interestingly compared to conventional AFM/FM exchange-bias systems, where the zero-magnetization AFM is responsible for the biased reversal of the FM layer. Despite its zero-magnetization state, as it is the case in AFM, the remaining ferromagnetic order in SGA has however the strong advantage to enable the exploration of its magnetic behavior by specific techniques such as XMCD, as it has been shown for single SGA layers in section II.B.2.

(ii) *Magnetic tunnel junctions*, where SGA could constitute an original electrode capable to spin polarize a current in its zero magnetization state[15]. The investigation of SGA-based magnetic tunnel junctions permits to directly probe the possibility for zero-magnetization SGA to spin-polarize a current and is also a good way to probe interface magnetic and electronic properties. Moreover,

the general context of this study is the exploration of the tunnel properties in magnetic systems where the electrodes are not conventional ferromagnets, as it is the case in the large majority of magnetic tunnel junctions. An intense research activity namely aims at designing materials that would permit to get a perfectly stable spin-polarized electrode. The idea is to eliminate interactions with other magnetic elements and external field and for this purpose, ideal compounds would be half-metallic antiferromagnets or ferrimagnets with 100% spin polarization and very small or zero magnetization. Up to now, these materials however still remain theoretical objects. Conventional ferrimagnetic alloys (RE-TM) have been already used as electrode in MTJ's[24] and a finite tunnel spin polarization could be measured at the magnetic compensation point. The use of SGA permits to go a step further with a material for which the zero magnetization state coexists with a "true" ferromagnetic state where all spin contributions point towards the same direction.

IV.A. Exchange-coupled bilayers

Exchange-coupled bilayers have been fabricated by the successive epitaxial growth of SGA and $SmAl_2$ (SA) layers. As detailed in section I.C., SA can be considered as a self ferrimagnet where the magnetic contributions are antiparallel spin and orbital moments. Those contributions exhibit different temperature dependences but never perfectly cancel each other, which explains the absence of magnetic compensation temperature. The orbital part is the dominant contribution over the entire temperature range. In SGA/SA systems, the SA layer thus plays the role of a soft ferromagnetic layer.

The investigation of the SGA/SA bilayer magnetic properties by SQUID magnetometry (figure 10) has confirmed the exchange coupling occurring at the interface, attested by the biased reversal of the softer SA layer. Most interesting was the observation of this SA biased reversal at the SGA compensation temperature (64K). This is a consequence of the persisting long range ferromagnetic order in compensated SGA and a proof that this order is maintained at the SGA surface since exchange bias effects are mostly sensitive to surface/interface properties. As mentioned previously, SGA/SA bilayers can thus be interestingly compared to conventional AFM/FM exchange-bias systems where the zero-magnetization AFM is responsible for the biased reversal of the FM layer.

Given the element- and electronic shell- selectivity of XMCD, it was possible to investigate the magnetic properties of SGA in SGA/SA bilayers and especially to analyze the influence of the SA reversal on SGA, which is a challenging task in conventional AFM/FM exchange-bias systems. XMCD experiments have shown that the SA reversal induces the partial reversal of SGA (figure 11). This SGA reversal is achieved via exchange coupling at the interface, as proved by the observation of a partial SGA reversal even at the compensation (64K) where its magnetization drops to zero and thus doesn't interact with the external magnetic field. The relatively large amount of rotatable SGA moments suggests the coexistence of domains with opposite orientation in the SGA layer: those will constitute pinned and rotatable components.

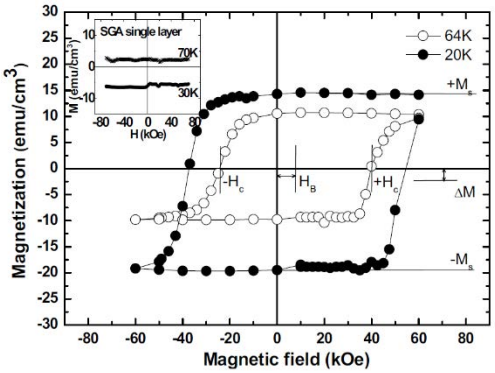

Figure 10: Magnetization measurements of $Sm_{0.972}Gd_{0.028}Al_2/SmAl_2$ bilayer performed at 20K (filled circles) and 64K (empty circles) with the magnetic field applied perpendicular to the sample surface (prior to measurements, the system has been field cooled from 150K in 6T). Inset: similar measurements performed on the single SGA layer at 70K and 30K (from[23]).

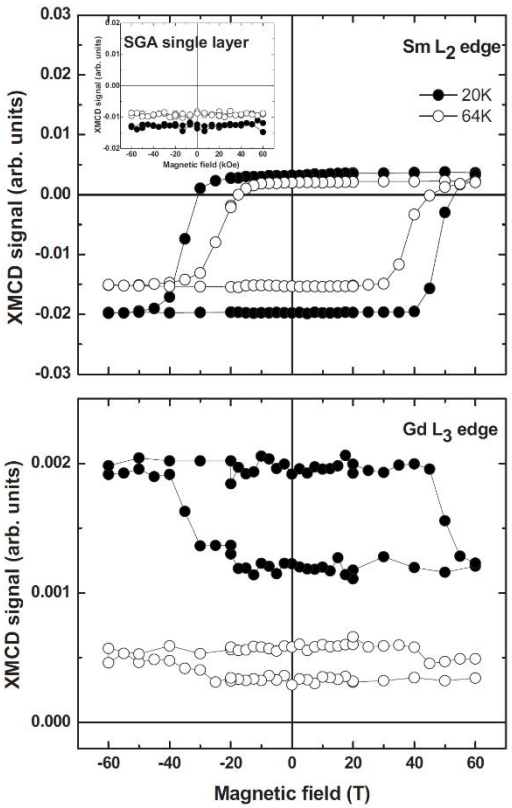

Figure 11: XMCD loop for the $Sm_{0.972}Gd_{0.028}Al_2/SmAl_2$ bilayer recorded at 20K (filled circles) and 64K (empty circles), for incident photon energy tuned to the Sm L_2 edge (top curves) and Gd L_3 edge (bottom curves) (prior each measurement, the system has been field cooled from 150K in 6T). Inset: XMCD measurements performed at the Sm L_2 edge for the same temperature and in the same conditions for $Sm_{0.972}Gd_{0.028}Al_2$ uncovered single layer (from[23]).

Part of this PhD work has been devoted to the further exploration of this phenomenon, the investigation of the SGA magnetic configuration and magnetic behavior in SGA/SA bilayers. The idea was to study the formation of these domains in the SGA layer and to analyze the role of the cooling field in the large ±17T field range available at the ID12 beamline (ESRF). In this manuscript, we have chosen to only briefly summarize this study (as it has been done above for previous studies on SGA epitaxial films and heterostructures) since this part is not directly connected to the main objectives of the PhD work. More informations can be found in reference[17].

Element-specific hysteresis loops have been measured at the Sm and Gd $L_{2,3}$ absorption edges, the latter giving specific information on the SGA magnetic configuration and behavior under field. +7T and +17T cooling fields have been used before measurements at the SGA compensation temperature. The results suggest that, after the cooling process, different domains with opposite orientations coexist in SGA of the SGA/SA system (figure 12, top right), in contrast to the homogeneous configuration stabilized in the single SGA layer (figure 12, top left). Despite the extraordinary large coercivity in SGA, the exchange coupling at the interface drives the formation of L-up domains (proportion x), parallel to the L-up configuration in SA. Part of those domains (proportion αx) is driven to reverse during the SA reversal under magnetic field (figure 12, bottom right). Pinned domains are responsible for the SA biased reversal and the proportion of pinned domains can satisfactorily account for the bias field value.

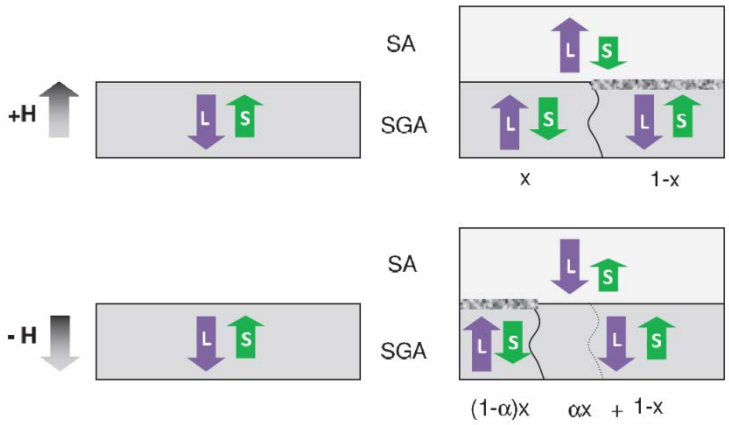

Figure 12: Sketches of the magnetic configuration below the SGA compensation temperature in the single SGA layer (left) and in the SGA/SA bilayer (right) for positive (top) and negative (bottom) fields. In the SGA/SA bilayer, x corresponds to the proportion of L-up domains for the positive field, αx is the proportion of L-up domains that reverses toward L-down for the negative field (from[17]).

An interesting observation is that the proportion x of L-up domains increases with increasing the cooling field (17% for +7T and 36% for +17T). This is surprising since the Zeeman energy doesn't favor this L-up orientation, neither at the compensation (where the magnetization vanishes), nor during the cooling process (where the S contribution is dominant over the orbital one). This result suggests that the effect of exchange coupling, which favors the L-up orientation in SGA, is strengthened when increasing the cooling field. In order to explain this phenomenon, we have suggested an original mechanism, based on the effect of the cooling field on the interface domain walls during the cooling process. Because of the decreasing SGA magnetization when decreasing temperature from above compensation, the field-cooling process would push interface domain walls towards SGA to keep most of the SA magnetization towards the field. The larger the field, the larger the driving force to push domain walls in SGA. Those domain walls then only represent a cost in energy, which leads to their annihilation and formation of L-up domains.

Via this indirect process, the applied field permits controlling the magnetic configuration in the zero-magnetization SGA. Its role is rather counterintuitive since it basically favors the magnetic orientation that opposes Zeeman interaction during the cooling process. This phenomenon may occur in other systems with low-magnetization materials and may be of more general interest to control the magnetic configuration in zero-magnetization ferromagnets.

IV.B. Magnetic tunnel junctions (MTJ)

SGA-based magnetic tunnel junctions have been fabricated by capping a SGA epitaxial film with a 2nm thick Al layer before the exposure to the air for natural oxidation, followed by the sputtering of a $[Co(0.2nm)/Pt(0.65nm)]_5$ stacking that exhibits a perpendicular to the surface easy magnetization axis. The full film has been patterned into micron-sized square-shaped MTJs using standard lithography and ion etching techniques, which allow perpendicular tunnel transport measurements across the insulating AlO_x barrier.

Measurements performed at low temperature (15K) in the ±0.15T field range (figure 13) have shown (i) the reversal of the softer [Co/Pt] magnetization while the highly coercive SGA remains unaffected and (ii) the simultaneous abrupt change in resistance of the MTJ. This phenomenon has been unambiguously attributed to a Tunnel Magneto Resistance effect of approximately +0.2% ($[R(+0.14T) - R(-0.14T)]/R(+0.14T)$) in this SGA-based MTJ.

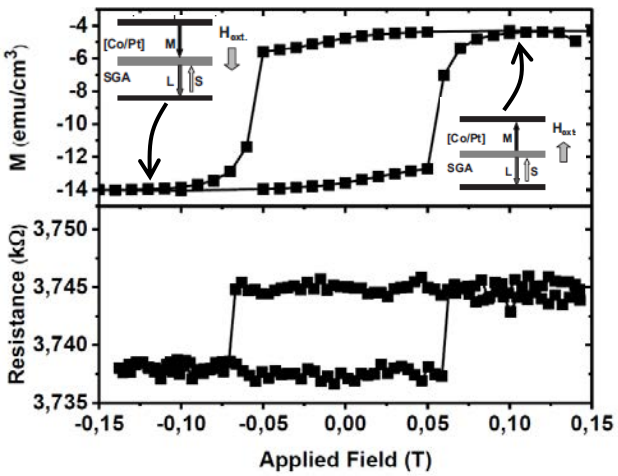

Figure 13: Minor magnetization (top sketch) and resistance loop (bottom sketch) versus the magnetic applied field measured at 10 mV and at 15 K after a 0.14T field-cooling on a SGA/AlO_x/$[Co/Pt]_5$ magnetic tunnel junction. The top sketches represent the parallel and anti-parallel spin orientation for both electrodes.

The investigation of the temperature dependence of TMR (figure 14) has proved that the TMR decreases when increasing temperature and vanishes in the vicinity of the SGA Curie temperature (125K). These transport properties, intimately related to the SGA/AlOx interface, thus reveal an interface magnetic ordering temperature close to the core of the SGA layer, a strong indication of the quality of the interface. Of paramount interest is the observation of a finite TMR at the SGA magnetic compensation (72K), a proof that SGA can simultaneously exhibit zero magnetization and significant polarization of conduction electrons, to give rise to a spin-polarized current. This study has also highlighted that the TMR is related to the relative orientation of spin contributions, and not of magnetization of both electrodes (since TMR is always positive while the SGA magnetization changes sign at compensation).

Finally, the observation of a larger resistance when SGA and [Co/Pt] spin contributions are parallel than when they are antiparallel, and considering the positive polarization of the Co electrode in our system, implies that the SGA tunnel polarization should be negative.

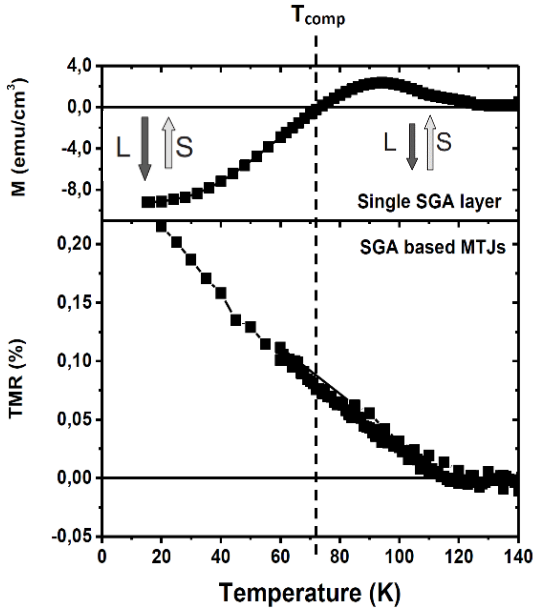

*Figure 14: Top: Magnetization of a SGA single layer versus temperature, in increasing temperature under zero-applied field after field-cooling under +7 T. The magnetic **L** and **S** configurations in the SGA epitaxial layer are sketched with the dark and light grey arrows respectively. Bottom: TMR of a SGA/AlO_x/$[Co/Pt]_5$ MTJ versus temperature.*

V. Summary and purpose of this thesis

The experimental report of a zero-magnetization ferromagnet has been achieved by Adachi *et al.*[8] who succeeded in engineering a magnetic compensation point via the increase of the spin contribution in the "self-ferrimagnet" $SmAl_2$ compound. This Gd-substituted compound has been the focus of several research groups who contributed to the clarification and confirmation of the mechanism at the origin of this unusual compensated long range ferromagnetic spin order.

Our group has been pioneer in achieving the SGA growth as epitaxial thin films. XMCD measurements at the Sm and Gd $L_{2,3}$ edges have confirmed the long-range ferromagnetic order persisting at the magnetic compensation via the observation of a finite XMCD signal. Its dependence versus field reveals that this compound exhibits a giant coercivity, exceeding 17T below T_{comp}.

Taking advantage of the possibility to obtain high quality SGA epitaxial films that exhibit such unusual zero-magnetization ferromagnet characteristics, various studies have been undertaken towards SGA-based heterostructures. Those aimed both at investigating original and relevant properties (exchange bias effects and magnetic behavior in the zero-magnetization pinning layer, magneto-tunnel properties in the case of a zero-magnetization electrode…), but also at going further into the analysis of SGA specific properties. Beyond XMCD investigations of SGA single layers that probed the 5d polarization in the whole film, the exploration of exchange-coupled bilayers has provided information on the persisting spin polarization *at the interface*. The transport properties in MTJs, especially the finite TMR at compensation, have proved that this interface spin polarization is also efficient *at the Fermi level*, and thus capable to generate a spin-polarized current.

The main initial goal of this PhD work was to extend and strengthen the investigation of surface/interface magnetic and electronic properties in SGA and SGA-based Magnetic Tunnel Junctions. Following the first encouraging measurements on SGA-based MTJs (summarized in this chapter and developed in more details in chapter 7 devoted to SGA-based MTJs), our objective was (i) to explore the SGA surface electronic properties that must be closely related to transport properties in MTJs (ii) to analyze transport properties in SGA-based MTJs in connection with SGA electronic properties and to try to quantify the SGA polarization, especially in the compensated state.

Two main directions have been followed to achieve these goals. The first one was to undertake an X-ray Photoemission Spectroscopy study to analyze the electronic properties of (111)SGA epitaxial films. This has been mainly performed using synchrotron-based XPS (beamline Cassiopée at SOLEIL) where the tunable incident photon energy and the available angle resolution allow the investigation of electronic structure along various directions and in the vicinity of the Fermi level. Beyond the angle-resolved study, spin-resolved experiments have been developed in an attempt to directly quantify the spin polarization at the Fermi level, and especially in the magnetically compensated state. Those results are presented in the first part of this manuscript (chapters 2 and 3).

In parallel to this direct spectroscopic approach, we have followed an indirect one, consisting in the investigation of transport properties in SGA-based MTJs. The ideas were to get a quantitative estimation of the SGA tunnel polarization and to try to correlate these transport properties with the SGA electronic structure.

A first essential step was the characterization and optimization of the second electrode, i.e. the [Co/Pt] stacking. An extensive study has been devoted to this point, with a particular focus on the influence of Pt thickness, bottom and capping layers (which play the role of the insulating barrier in MTJs architectures) on the structural and magnetic properties. Those results are presented in the second part of this manuscript (Chapters 4 and 5).

The objective of quantifying the SGA tunnel polarization from the TMR in MTJs requiring the quantification of the [Co/Pt] tunnel polarization as well, a specific investigation of MTJs where both electrodes are similar [Co/Pt] stackings has been undertaken. Beyond the determination of the [Co/Pt] polarization, the analysis of magneto-tunnel transport properties appears to be a very powerful probe of the interface magnetic configuration and behavior under field. This has permitted to highlight some original properties in these [Co/Pt] MTJs and analyze the influence of the Pt thickness and temperature, in combination with micromagnetic simulations. The results concerning [Co/Pt] MTJ's are gathered in the third part of the manuscript (chapter 6).

The last chapter (chapter 7) presents the results concerning the effective spin polarization dependence on the Pt thickness and temperature in [Co/Pt]-based MTJs and the results obtained on the SGA-based MTJs, using either an AlO_x or MgO tunnel barrier. Details are first given on the transport properties measured in SGA/AlO_x/[Co/Pt], in connection with SGA electronic properties. The choice of exploring the MTJs with a MgO barrier has been then motivated by (i) the results obtained for [Co/Pt] stacking grown on MgO, (ii) the electronic structure calculation performed for the SGA surface and (iii) the ARPES measurements on a MgO capped SGA film. The various attempts to observe a TMR effect in SGA/MgO/[Co/Pt] MTJs are presented.

References

[**1**] A. Avisou, thesis, (2006).
[**2**] J.H. Van Vleck, "*The Theory of Electric and Magnetic Susceptibilities*", Oxford University Press, England, (1932).
[**3**] M.A. Ruderman *et al.*, Phys. Rev. B **96**, 72 (1954).
[**4**] P. Tils *et al.*, J. Alloys Compd. **289**, 28 (1999).
[**5**] H. Adachi *et al.*, Phys. Rev. B **59**, 445 (1999).
[**6**] N. Kaplan *et al.*, Phys. Rev. B **7**, 40 (1971).
[**7**] H. Adachi *et al.*, Phys. Rev. B **56**, 5744 (1997).
[**8**] H. Adachi *et al.*, Nature **401**, 148 (1999).
[**9**] A.K Grover *et al.*, J. Appl. Phys. **50**, 7501 (1979).
[**10**] H. Adachi *et al.*, Phys. Rev. Lett. **87**, 127202 (2001).
[**11**] J. Taylor *et al.*, Phys. Rev. B **66**, 161319 (2002).
[**12**] S. Qiao *et al.*, Phys. Rev. B **70**, 134418 (2004).
[**13**] A. Avisou *et al.*, J. Cryst. Growth **297**, 239 (2006).
[**14**] A. Avisou *et al.*, J. Magn. Magn. Mater. **316**, 317 (2007).
[**15**] M. Da Silva *et al.*, Appl. Phys. Lett. **98**, 232504 (2011).
[**16**] A. Avisou *et al.*, J. Phys. Condens. Matter **20**, 265001 (2008).
[**17**] M. Bersweiler *et al.*, Phys. Rev. B **88**, 054411 (2013).
[**18**] X. Wang *et al.*, Phys. Rev. B **47**, 9087 (1993).
[**19**] J.C. Parlebas *et al*. Phys. Rep. **431**, 1 (2006).
[**20**] A. Avisou *et al.*, J. Appl. Phys. **103**, 07E135 (2008).
[**21**] T. Wu *et al.*, J. Appl. Phys. **73**, 1368 (1993).
[**22**] F. Hellman *et al.*, Appl. Phys. Lett. **59**, 2757 (1991).
[**23**] M. Ungureanu *et al.*, Phys. Rev. B **82**, 174421 (2010).
[**24**] C. Kaiser *et al.*, Phys. Rev. Lett. **95**, 047202 (2005).

Chapter 2
Photoemission spectroscopy

I. Generalities on photoemission spectroscopy 23
I.A. Photoemission and the photoelectric effect 23
I.B. The three-steps model 24
I.B.1. Optical excitation of one electron in the solid 24
I.B.2. Propagation of the photoelectron to the surface 25
I.B.3. Escape of the photoelectron from the solid to the vacuum 26
I.C. Photoemission and dipole selection rules 27
II. Angle Resolved PhotoEmission Spectroscopy (ARPES) 28
II.A. Geometry of the ARPES experiment 28
II.B. Information provided by ARPES experiments 29
III. Spin-Resolved PhotoEmission Spectroscopy 30
IV. CASSIOPEE beamline 32
V. Conclusion 33
References 34

The objective of this chapter is first to give some general basic informations on the physical processes underlying the photoemission spectroscopy. Then, more specific details are given on the Angular- and Spin-Resolved Photoemission Spectroscopy (ARPES and SRPES) to underline the fundamental information these techniques can provide on the bulk and surface/interface electronic structures. Finally, the CASSIOPEE beamline (synchrotron SOLEIL), where the photoemission studies have been performed, is described. Results will be presented and discussed in the next chapter.

I. Generalities on photoemission spectroscopy

I.A. Photoemission and the photoelectric effect

The photoemission is based on the photoelectric effect. When excited by an electromagnetic radiation of energy hν, a solid emits photoelectrons in all directions in vacuum; the photoelectrons are characterized by a kinetic energy (E_K) and a momentum **K**. In the case of direct optical transitions, which is experimentally the most common case, the conservation of energy (figure 1) leads to the following relation between the kinetic energy of the emitted photoelectrons and the binding energy (E_B) of the excited state:

$$E_K = h\upsilon - \phi - E_B \qquad \textbf{(I-1)}$$

where Φ, the work function, is a characteristic constant of the sample surface and corresponds to the minimum energy required to eject an electron out of the crystal. As a result, the photon energy must be larger than Φ to overcome this energy and emit photoelectrons. The order of magnitude for Φ is generally of a few eV (4-5 eV for metals). In this chapter, the following formalism will be used to describe the energy for the initial (i) and final states (f):

$$E_i = -E_B \text{ and } E_f = E_K + \phi$$

The relation **(I-1)** becomes: $E_f = h\upsilon + E_i$ **(I-2)**

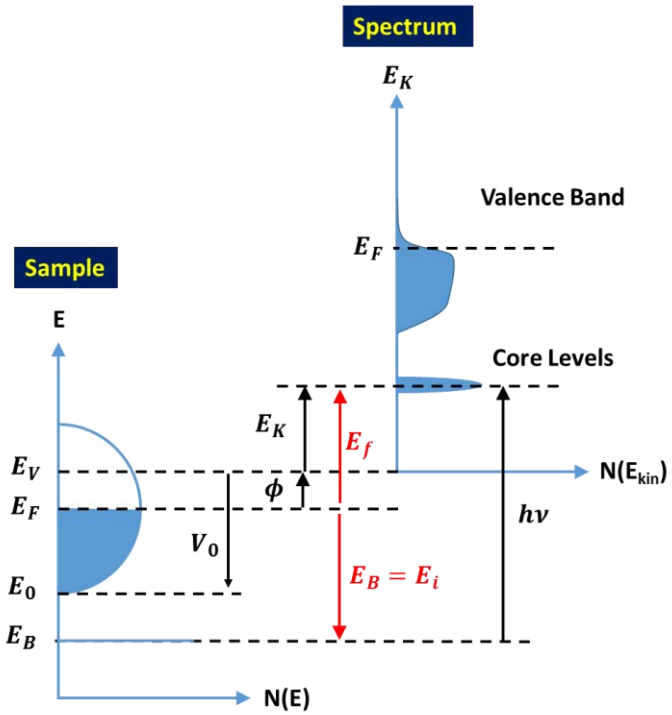

Figure 1: Energy conservation in a photoemission process. If the photon energy is higher than the work function ϕ, the photoelectrons are emitted in the vacuum and measured as a function of their kinetic energy (Right). Note: it is more practical to work with the binding energy E_B (left) when we refer to the density of state in the solid. (At the Fermi level E_B = 0 eV). $V_0 = E_V - E_0$ is the inner potential measured between the vacuum level E_V and the bottom of the band E_0.

I.B. The three-steps model

The rigorous way to describe the photoemission process is to treat the photon absorption, the electron removal and detection as a single coherent system[1],[2] (one-step model sketched in the right part of the figure 2). However, due to the complexity of such a treatment, a common hypothesis is to consider only one electron in the so-called three-steps model (sketched in the left part of the figure 2).

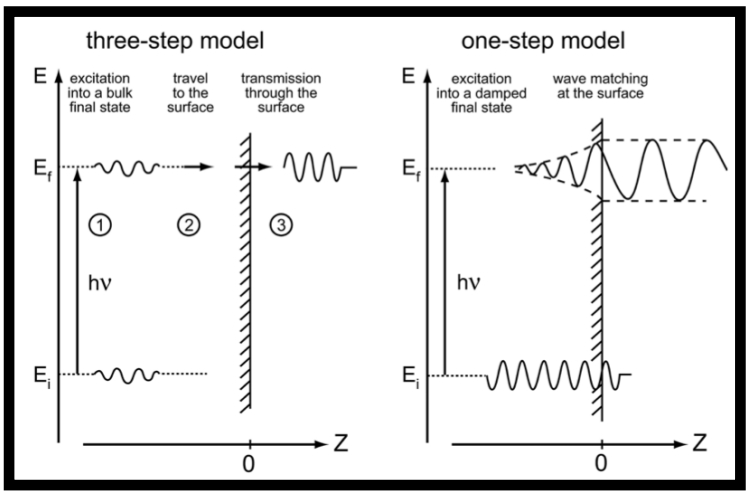

Figure 2: Illustration of the three steps model (left) and the one step model (right) from Ref[3].

The three steps model has been introduced by C.N. Berglund and W.E Spicer[4] in order to describe in a simple way the photoemission process. It is a purely phenomenological model within which the case of one electron is treated and the photoemission process is subdivided into three independent and sequential steps: (i) optical excitation of one electron in the solid (ii) propagation of the photoelectron to the surface (iii) escape of the photoelectron from the solid to the vaccum.

I.B.1. Optical excitation of one electron in the solid

When the photon radiation of energy $h\upsilon$ excites the solid, an electron absorbs a photon and an optical transition of this electron from the initial ground state $|\Psi_i\rangle$ to the final ground state $|\Psi_f\rangle$ occurs. The transition probability $P_{i\to f}$ of the photoelectron can be approximated by the Fermi gold rules:

$$P_{i\to f} = \frac{2\pi}{\hbar}\left|\langle\Psi_f|H_{int}|\Psi_i\rangle\right|^2\delta(E_f - E_i - h\nu) \qquad \text{(I-3)}$$

H_{int} defines the interaction Hamiltonian between the photon and the electron:

$$H_{int} = \frac{e}{2mc}(\boldsymbol{A}\cdot\boldsymbol{p} + \boldsymbol{p}\cdot\boldsymbol{A}) - \frac{e}{m}\boldsymbol{S}\cdot\boldsymbol{B} + \frac{\boldsymbol{e^2}}{\boldsymbol{2m}}\boldsymbol{A}^2 \qquad \text{(I-4)}$$

where **p** is the electronic momentum operator, **A** the electromagnetic vector potential, $\boldsymbol{S}\cdot\boldsymbol{B}$ the interaction between the spin and the magnetic field. The commutation relation $[\boldsymbol{p},\boldsymbol{A}] = -i\hbar\nabla\cdot\boldsymbol{A}$ and the dipole approximation (i.e. **A** constant over atomic dimensions (**A**(r,t) = $\mathbf{A_0}$) and therefore $\nabla\cdot\boldsymbol{A} = 0$ which holds in the ultraviolet) have been used. In the case of optical linear regime, the

quadratic term in $\mathbf{A}^2$ can be neglected due to the weak intensity of the electromagnetic radiation. Besides working with low electromagnetic radiation like ultraviolet or soft X-ray, the interaction between the spin (**S**) and the magnetic field (**B**) can be also neglected. Based on these two assumptions, the interaction Hamiltonian between the photon and the electron can be re-written as:

$$H_{int} \simeq \frac{e}{2mc} \boldsymbol{A_0} \cdot \boldsymbol{p} \qquad \text{(I-5)}$$

During the optical transition, all the information on the electronic structure of the system is conserved. The energy conservation described in the previous section leads to the equation **(I-2)**; as a result of the translation symmetry in the crystal, the momentum of the emitted photoelectron is conserved and given by $\boldsymbol{k_f} = \boldsymbol{k_i} + \boldsymbol{G}$ where **G** is a vector of the reciprocal space. This leads to $\boldsymbol{k_f} = \boldsymbol{k_i}$ when considering the projection of the dispersion relations in the first Brillouin Zone.

I.B.2. Propagation of the photoelectron to the surface

During this second step, the photoelectron travels to the surface under the shape of a wave package. As a result of the interaction between the photoelectron and other photoelectrons, phonons or impurities in the crystal (which are not negligible), the photoelectron can be inelastically scattered to the surface. In this particular case, the photoelectrons have lost the initial information about the kinetic energy and consequently contribute to the inelastic background spectrum. The escape probability for the photoelectron elastically scattered in the vacuum is strongly dependent on the inelastic mean free path λ defined as the distance over which an electron can travel through a solid between two inelastic collisions. As a result, the inelastic mean free path determines the surface sensitivity of the photoemission process. The universal inelastic mean free path curve versus the electron kinetic energy is given in figure 3 for a few metals.

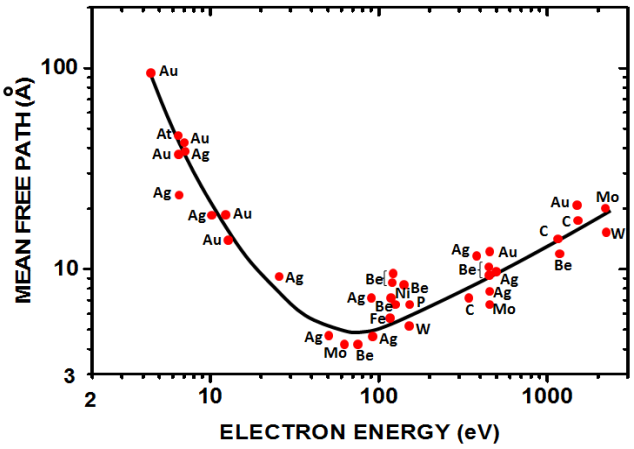

Figure 3: Inelastic mean free path for a few metals versus the kinetic energy from 2 to 2000 eV (Ref[3]).

Figure 3 obviously shows that electronic information on the solid's surface can be preferentially obtained by photoemission with exciting radiation in the range [10-100] eV where the inelastic mean free path is only a few atomic planes; this is the Ultra-violet regime (UPS) which is suitable to investigate valence states. Working with higher energy in the X-ray regime (XPS) permits to probe deeper in the volume (a few nanometers) and to study the core levels.

I.B.3. Escape of the photoelectron from the solid to the vacuum

Making the assumption that the electron in the final state E_f can be described by the nearly-free electron model, a photoelectron can escape out of the crystal to the vacuum only if the following condition is satisfied:

$$\frac{\hbar^2 k_\perp^2}{2m} \geq V_0 \qquad \text{(I-6)}$$

Where $V_0 = E_V - E_0$ is the inner potential measured between the vacuum level E_V and the bottom of the band E_0 (figure 1).

Due to the translation symmetry in the crystal, and in the case where bulk and surface have the same periodicity, the parallel component $k_{//}$ of the momentum **k** for the photoelectron emitted in the vacuum is conserved. However, due to the discontinuity of potential in the direction perpendicular to the surface, the perpendicular component $k_\perp$ is not conserved. This property is sketched in figure 4.

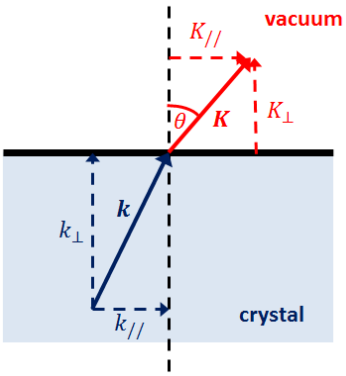

Figure 4: Refraction of the photo-electron from the crystal to the vacuum.

The determination of the momentum components in the vacuum and inside the crystal thus requires certain assumptions regarding the electronic final states.
The final state in the vacuum is a pure free electron with an energy:

$$E_K = \frac{\hbar^2}{2m} K^2 = \frac{\hbar^2}{2m}\left(K_{//}^2 + K_\perp^2\right) \qquad \text{(I-7)}$$

Inside the crystal, the final states are supposed to belong to a nearly-free electron band with the following dispersion relation:

$$E_f = \frac{\hbar^2 k^2}{2m} - V_0 + \phi = \frac{\hbar^2}{2m}\left(k_{//}^2 + k_\perp^2\right) - V_0 + \phi \qquad \text{(I-8)}$$

Given the relation $E_f = E_K + \phi$, one can calculate the components of the momentum inside the crystal:

$$k_{//} = K sin\theta = \left(\frac{2mE_K}{\hbar^2}\right)^{1/2} sin\theta \quad \text{(I-9)}$$

$$k_{\perp} = \left(\frac{2m(E_K cos^2\theta + V_0)}{\hbar^2}\right)^{1/2} \quad \text{(I-10)}$$

In conclusion, this three-steps model constitutes an approximation of the accurate underlying physical mechanism that permits to largely simplify the analysis of Photoemission Spectroscopy (PES) data. From the measurements of the detected photoelectron kinetic energy (E_K) and momentum direction in the vacuum (θ), it is possible to calculate the initial energy and momentum in the crystal. PES appears to be thus a powerful tool to determine the dispersion relations E(**k**) of the electronic states.

I.C. Photoemission and dipole selection rules

It has been shown previously that the dipole element matrix for an optical transition of the photoelectron from the initial ground state $|\Psi_i\rangle$ to the final ground state $|\Psi_f\rangle$ is proportional to $\langle\Psi_f|\boldsymbol{A}.\boldsymbol{p}|\Psi_i\rangle$. The dipole element matrix can be re-written as $\langle\Psi_f|\boldsymbol{E}.\boldsymbol{r}|\Psi_i\rangle$ where **E** is the electric dipole operator of the incoming light and **r** defines the radial vector operator (the direction of **E** defines the polarization of the incoming light). The conditions for which the dipole matrix element is non-zero are usually called "dipole selection rules" whereas the dipole matrix elements which do not obey these selection rules are usually called "forbidden transitions".

In the case of a single electron in a central potential (the simplest system which can be excited is the hydrogen atom), the "dipole selection rules" are given by:

$$\Delta l = l_f - l_i = \pm 1 \quad \text{(I-11)}$$
$$\Delta m = m_f - m_i = 0, \pm 1 \quad \text{(I-12)}$$

where l and m are the quantum numbers which characterize the eigenstates of the $\hat{\boldsymbol{L}}^2$ and $\hat{\boldsymbol{L}}_z$ operators. Considering that the Hamiltonian only affects the spatial part of the wave function and not the spin, a third rule must be considered and is given by:

$$\Delta s = s_f - s_i = 0 \quad \text{(I-13)}$$

where s is the spin quantum number. More details about the "dipole selection rules" demonstration can be found in Ref[5].

Following these selection rules, the dipole matrix element vanishes if the initial and final states both have zero angular momentum. If $\Delta m = 0$, only the electric dipole operator **E** with a polarization component along z will stimulate a transition between the initial and final states; if $\Delta m = \pm 1$, only the electric dipole operator **E** with a polarization component in the (x,y) plane will stimulate the transition between both states. Finally, $\Delta s = 0$ involves that the transition between two states with different spin multiplicity is forbidden.

In the solid, the "dipole selection rules" are governed by the symmetry of the crystal due to the periodic potential. As a result of the "conservation" of the quantum number m for the atomic orbitals by reflection symmetry in the mirror planes, as illustrated in F. Bonell's PhD[6], the "dipole selection rules" can be applied for crystals with a periodic potential.

Because of the boundaries conditions of the final state in the crystal which must be compatible with outgoing plane wave (i.e. time-reversed LEED state), the final state must be totally symmetric with respect to all symmetry operations. For the case of photoelectron emission with the detector located in a mirror plane, the final state wavefunction has to be even with respect to the incident mirror plane. For an initial state of either even (+) or odd (-) symmetry with respect to the mirror plane, the polarization condition on the electric dipole operator for which $\langle \Psi_f | \boldsymbol{E}.\boldsymbol{r} | \Psi_i \rangle \neq 0$ can be given by:

- For Ψ_i even, $\Longrightarrow \langle + | + | + \rangle \Longrightarrow \boldsymbol{E}$ even
- For Ψ_i odd, $\Longrightarrow \langle + | - | - \rangle \Longrightarrow \boldsymbol{E}$ odd

As a result of the optical transition for the photoelectron governed by the Fermi gold rules, only the initial states with the same symmetry as the electromagnetic field **E** can be excited and detected by photoemission. An appropriate choice of the polarization of the incoming photon beam in a photoemission experiment could thus permit determining the symmetry of electronic bands in the crystal.

II. Angle Resolved PhotoEmission Spectroscopy (ARPES)

As it has been shown in the previous section, and theoretically developed by C.N. Berglund and W.E Spicer[4], photoemissions experiments can provide information about the band structure in the studied material. Experimentally, the electronic band structure could be mapped from the angle and energy dependence of the photoemission spectra. Since the first angle resolved photoemission measurements performed by Neville V. Smith *et al.* on 1T-$TaSe_2$ compound[7], the ARPES is the most powerful and most commonly used spectroscopy technique to directly probe the electronic structure of a solid. The goals of this section are (i) to describe the ARPES geometry and its link with the initial momentum **k** in the crystal (ii) to explain how ARPES data are usually presented and, more importantly, which information can be extracted.

II.A. Geometry of the ARPES experiment

A schematic drawing of an ARPES experiment is shown in figure 5.

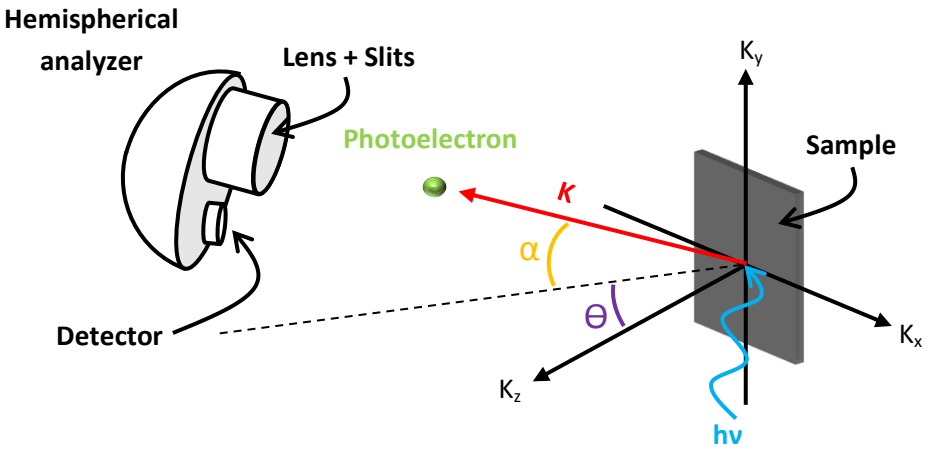

*Figure 5: Geometry of the ARPES measurements. The red arrow illustrates the momentum **K** of the photoelectron emitted in the vacuum after being excited by a monochromatic photon radiation (blue undulated arrow) with an energy hv.*

In order to avoid inelastic collisions and to guaranty the conservation of the electronic properties (i.e. energy and momentum of the electrons), ARPES experiments require Ultra High Vacuum (UHV) environment, in a typically range of [10^{-10}-10^{-11}] mbar. The photon radiation necessary for the excitation of the electrons in the solid can be generated by a gas-discharge lamp working with specific radiation of elements (the most common radiations used in laboratories for ARPES studies being the He I and He II radiations) or by using a synchrotron light. The synchrotron light presents the advantage of having access to a wide continuous energy range from the soft to the hard X-ray (e.g. [1 eV-50 keV] for the French synchrotron SOLEIL). Besides using a synchrotron radiation enables to change the polarization of the light which can provide fundamental information about the symmetry of the electronic states in the crystal as detailed in the previous section. Other advantages of a synchrotron light are the high intensity level in photoemission spectra, small photon spot or the possibility to perform time-resolved measurements.

If the photon energy is larger than the inner potential, photoelectrons emitted in the vacuum in all directions are collected by a 2D-hemispheric analyzer with a finite acceptance angle in the vertical direction. The analyzer's role is to filter the kinetic energy of the photoelectrons for a given emission direction. Thanks to the application of an electric potential on the external and internal hemispheres of the analyzer, only the photoelectrons with the desired kinetic energy are measured by the detector while the other photoelectrons strike the wall of the analyzer. Beyond the possibility to get angle resolution via the analyzer acceptance angle along the vertical direction (α), the sample can rotate around the vertical K_y axis, which provides angle resolution in the (K_x;K_z) incidence plane (θ).

Given the geometry of the ARPES experiment (figure 5) and the relations (I-9) and (I-10) deduced from the conservations of energy and momentum, the measurements of the kinetic energy and emission angles (Θ and α) of the photoelectron in vacuum thus enable the determination of the three components of the initial momentum **k** in the crystal:

$$k_x = \left(\frac{2mE_K}{\hbar^2}\right)^{1/2} sin\theta\, cos\alpha \qquad \textbf{(II-1)}$$

$$k_y = \left(\frac{2mE_K}{\hbar^2}\right)^{1/2} sin\alpha \qquad \textbf{(II-2)}$$

$$k_Z = \left(\frac{2m\left(E_K cos^2\theta cos^2\alpha + V_0\right)}{\hbar^2}\right)^{1/2} \qquad \textbf{(II-3)}$$

Measuring the intensity versus the kinetic energy for various detection angles, various orientation of the sample and various incident photon energies would thus enable to access to the dispersion of electronic bands along various high symmetry directions of the Brillouin Zone.

II.B. Information provided by ARPES experiments

ARPES experiments provide directly an image of the electronic band structure of material in the reciprocal space and thus give essential information about both binding energy and **k**-vector of electrons inside the material. Besides, as previously mentioned, by an appropriate choice of the polarization and energy range of the incoming photon beam, ARPES experiments can provide information about the symmetries of the band structure and can investigate the electronic states localized at the surface as well as deeper in the volume.

The ARPES data are generally collected as intensity maps $I(E_K,\alpha)$ for different θ angles, directly measured and delivered by the 2D-detector. In order to extract electronic band dispersions, $I(E_B, k_x)$ and $I(E_B, k_y)$ maps can be calculated using the expressions **(II-1)** and **(II-2)**. An example of

$I(E_B, k_x)$ map, measured for hv = 20 eV along the ΓK direction of the Brillouin Zone (BZ) of $YbAl_2$, is shown in figure 6 (a). Several dispersive and non-dispersive bands can be observed.

In equivalent way, the electronic band dispersion can be represented by the compilation of several line shape profiles of the intensity as a function of the binding energy at constant momentum called Energy Dispersion Curves (EDCs). The plot of EDCs along the ΓK direction of the $YbAl_2$ BZ are shown in figure 6 (b). The intense peak localized at 0.17 eV corresponds to the non-dispersive $4f_{7/2}$ contribution of $YbAl_2$.

Finally, "cuts" at constant energy (so-called iso-energetic maps) permit to explore the electronic band structure in various planes of the Brillouin Zone. Iso-energetic maps obtained for E_B = 0 eV are Fermi surface mapping, as shown for example in the (k_x, k_z) and (k_x, k_y) planes of $YbAl_2$ Brillouin Zone in figures 6 (c) and (d) respectively.

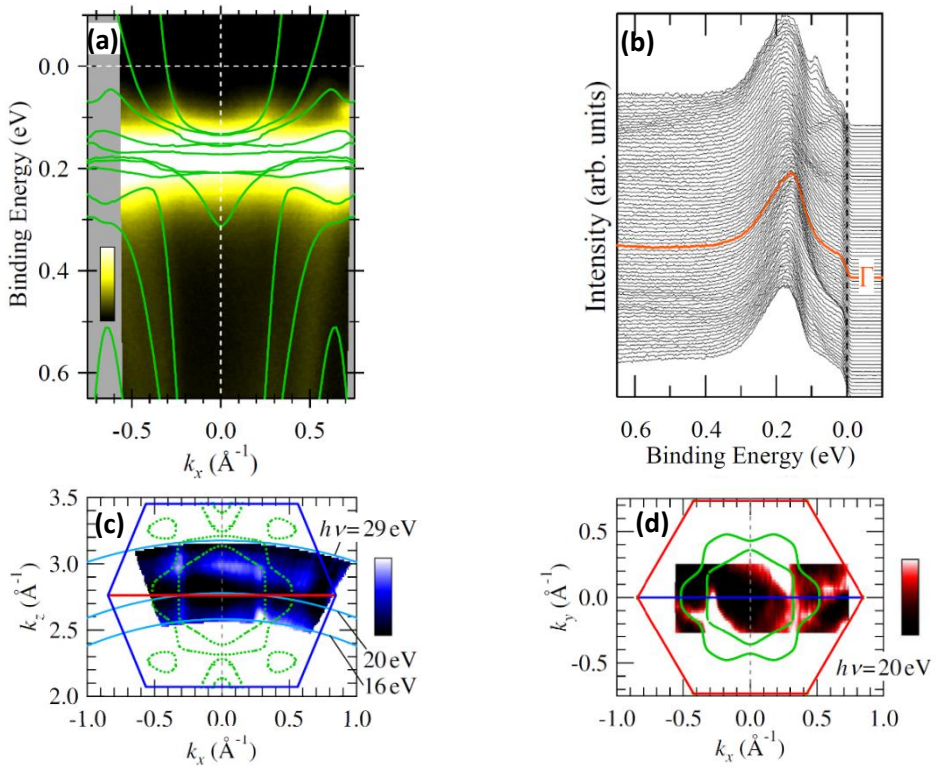

Figure 6: (a) $I(E_B, k_x)$ map of $YbAl_2$ along the ΓK direction. (b) EDC obtained from (a). (c) and (d) Iso-energetic cuts at E_B = 0 eV (Fermi surface mapping) in (k_x,k_z) and (k_x,k_y) planes respectively. The green dotted and solid lines indicate the electronic band and Fermi Surface obtained by the LDA calculation (from[8]).

III. Spin-Resolved PhotoEmission Spectroscopy

This section briefly explains how essential information on the spin-polarization of the material can be additionally extracted from photoemission experiments.

The basis of Spin Resolved Photoemission Spectroscopy (SRPES) is to analyze the spin of emitted photoelectrons. The spin detection can be achieved by interaction with a solid target, using either the scattering of photoelectrons by atomic nucleus (Mott scattering) or their interaction with spin polarized electrons in a ferromagnetic thin film (asymmetric absorption or reflection). The Mott scattering is commonly used for spin detection in spectroscopy experiments.

The Mott scattering corresponds to the asymmetric scattering of the electron (depending on its spin) on an atomic nucleus. It results from the spin-orbit interaction. During its scattering, the

electron gains an angular momentum **L** which is parallel or anti-parallel to its spin **S**, as sketched in figure 7. The spin-orbit coupling favors the parallel alignment between **L** and **S**, i.e. the scattering probability is greater towards +Θ than towards -Θ. This asymmetric scattering is characterized by the Sherman function S: $\sigma_1 = \sigma_0 (1+S)$ and $\sigma_2 = \sigma_0 (1-S)$ are the scattering cross sections for a spin up respectively towards +Θ and towards -Θ.

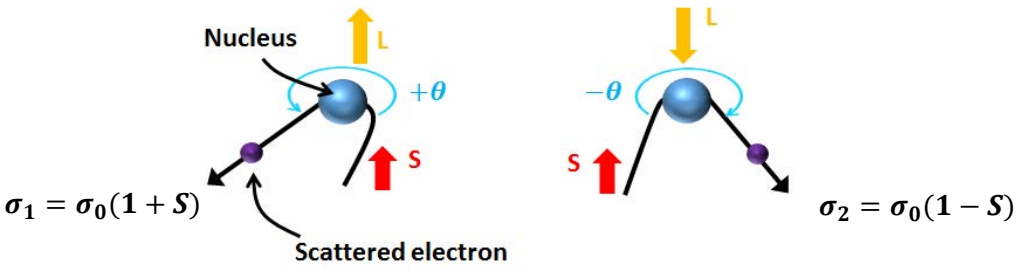

*Figure 7: Mott scattering on a heavy nucleus. The spin-orbit coupling favors the parallel alignment of the spin electron momentum **S** with its kinetic orbital momentum **L** sketched by the red and orange arrows respectively. σ_1 and σ_2 are the cross sections of the spin up diffusion in the left and right directions respectively.*

The scattering asymmetry being larger at high energies, the electrons are accelerated to tens of keV. Besides, the spin orbit coupling being proportional to the nucleus charge Z, heavy elements are generally chosen to constitute the solid target. In most cases, Au targets are used and the maximum asymmetry is obtained for Θ = ± 120°. The scattered electrons are collected by two detectors positioned at ± 120° from the target, which permits to measure one component of the polarization. Another couple of detectors is generally added to measure a second component of the polarization. Because of the poor efficiency of the spin analyzers (10^{-3}), such spin-resolved measurements require a very intense excitation source such as the one provided on synchrotron beamlines.

In the ideal case where both detectors are perfectly similar, the scattering asymmetry A is directly proportional to the spin polarization P and is given by:

$$A = \frac{I_1 - I_2}{I_1 + I_2} = \text{SP} \qquad \textbf{(III-1)}$$

where I_1 and I_2 are the intensities measured by the two detectors localized at ± 120° from the Au target, and S is the Sherman function.

However, the real case is significantly different since the detectors are never perfectly identical; there might be several issues leading to instrumental asymmetries: different sensitivities, imperfect alignment in the analyzer, asymmetries in the acceleration voltages. The solution to get rid of these differences between the detectors is to perform two sets of measurements where the roles of both detectors would be exchanged: either in reversing the sample magnetization or in switching the incident photon beam polarization. In the case where the detectors don't exhibit any offset, it can be shown that:

$$\tilde{A} = \frac{\sqrt{I_1^+ I_2^-} - \sqrt{I_1^- I_2^+}}{\sqrt{I_1^+ I_2^-} + \sqrt{I_1^- I_2^+}} = \text{SP} \qquad \textbf{(III-2)}$$

where I_1^+, I_2^+ are the intensities measured in both detectors for the up magnetization and I_1^-, I_2^- for the down magnetization.

Figure 8 (F. Bonell thesis[6]) gives an example of a spin polarization measurement versus the binding energy for a (001) Fe surface at its remanent state (room temperature and 60 eV incident photon energy). Spin-resolved photoelectrons have been collected for up and down magnetized states and the spin polarization has been calculated from the geometrical average of the measured intensities **(III-2)**.

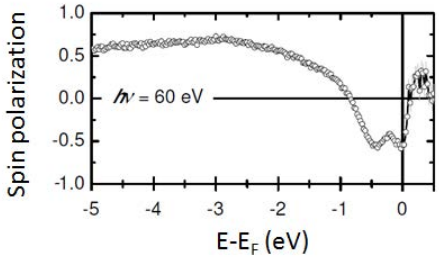

Figure 8: Spin polarization of (001) Fe surface measured at room temperature and for an incident photon energy of 60 eV.

IV. CASSIOPEE beamline

The CASSIOPEE beamline at the French synchrotron SOLEIL is a soft X-ray beamline dedicated to the study of the electronic structure of the matter by photoemission spectroscopies. Some pictures of the beamline are given in figure 9.

`

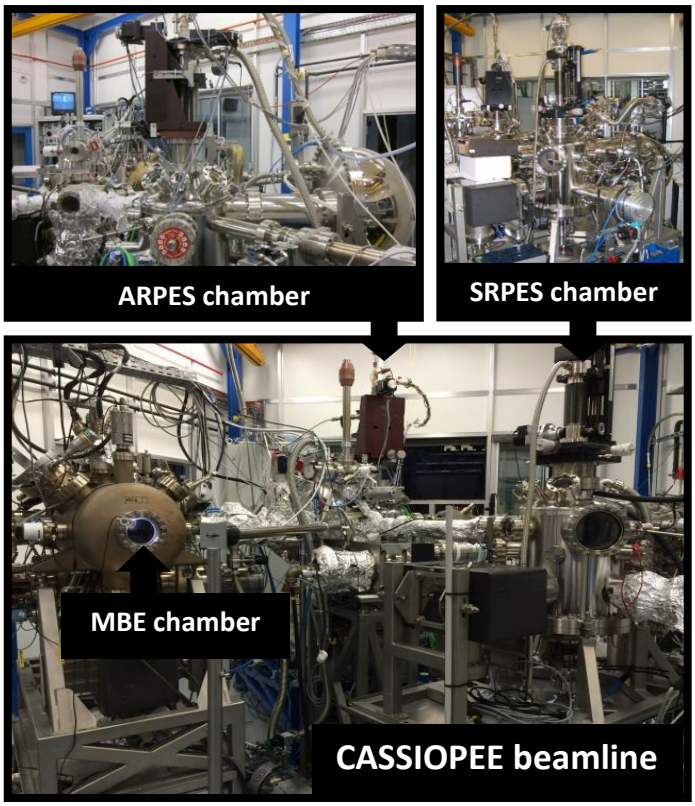

Figure 9: Pictures of the CASSIOPEE beamline (courtesy of Synchrotron SOLEIL).

Two spectroscopy chambers are respectively devoted to high resolution ARPES and SRPES measurements. Both chambers are connected to a MBE preparation chamber for (i) sample growth,

(ii) surface preparation by etching and annealing and (iii) surface characterization by Auger, RHEED and Low Electron Energy Diffraction (LEED). The sample can be transferred under Ultra High Vacuum from one chamber to another, which is an essential prerequisite for such measurements that are extremely sensitive to surface properties. The pressure in the ARPES and SRPES chambers are typically kept in a range of [10^{-11}-10^{-10}] mbar.

The beamline characteristics are the followings: the incident beam is a monochromatic photon radiation the linear polarization of which can be either s- or p-type. For s-polarization, the electrical field is perpendicular to the incidence plane (the plane defined by the direction of incident photon beam and the normal to the surface), i.e. parallel to the surface. For p-polarization, the electrical field is in the incidence plane. The wide energy range available (8eV-1500eV) allows both surface and bulk electronic studies of the condensed matter.

In the case of ARPES (SRPES) measurements, the emitted photoelectrons are collected by a hemispherical analyzer SCIENTA R4000 (SES 2002 coupled to a Mott detector for the spin analysis) through a vertical (horizontal) slit with an acceptance angle α of ±15° (±8°). The SRPES measurements are performed in the remanent state but the sample can be first magnetized under an external magnetic field up to ±1200 Oe. The sample can be cooled down to 4K (25K) in the ARPES (SRPES) chamber.

The binding energy resolution (typically better than 10 meV) is given by the monochromatic radiation resolution (typically 5 meV), the Pass Energy used and the size of the vertical or horizontal slits. Whereas the angular resolution on the parallel ($k_{//}$) and perpendicular ($k_{\perp}$) components of the **k** momentum vector are in the order of magnitude of the angle and energy step used during photoemission experiments (approximately 10^{-2} Å^{-1} and 10^{-4} Å^{-1} respectively).

V. Conclusion

To summarize this chapter, photoemission spectroscopies are based on the photoelectric effect and in a simple approach can be satisfactorily described by the three-steps model: (i) optical excitation of one electron in the solid, (ii) propagation of the photoelectron to the surface and (iii) escape of the photoelectron from the solid to the surface. Due to the high-resolution and continuous progress in synchrotron sources, the ARPES and SRPES are the most powerful spectroscopies to investigate the electronic band structure of the matter. Indeed, given the different degrees of freedom available in the synchrotron-ARPES geometry (rotation of the sample, acceptance angle of the detector and tunable photon energy), it is possible to have access to the three components of the electron's momentum inside the solid. So, ARPES experiments provide directly an image of the electronic band structure of material in the reciprocal space and thus give essential information about both binding energy and **k**-vector of electrons inside the material. Besides, by an appropriate choice of the polarization and energy range of the incoming photon beam, ARPES experiments provide information about the symmetries of the band structure and investigate the electronic states localized at the surface as well as deeper in the volume. Generally the ARPES results are presented as $I(E_B, k_{//})$ mapping where a cut at $k_{//}$ permits to plot the EDC spectra at a particular point of the SBZ and a cut at constant binding energies called iso-energetic map summarizes the electronic band structure in the (k_x, k_y) or (k_x, k_z) plan. The spin analysis of photoelectrons, based on the Mott scattering of the electrons by heavy nucleus, brings complementary information on the surface/interface electronic structure. The measurements of spin up and spin down densities of state enable the determination of the spin polarization, especially at the Fermi level where it is a key parameter for transport properties in spintronic systems. Experimentally, the CASSIOPEE beamline at the French synchrotron SOLEIL is a state-of-the-art instrument gathering growth/preparation/characterization and analysis chambers (high resolution ARPES and SRPES) to explore the bulk and surface/interface electronic structures.

References

[**1**] G.D. Mahan *et al.*, Phys. Rev. B **2**, 4334 (1970).
[**2**] A. Bansil *et al.*, Phys. Rev. Lett. **83**, 5154 (1999).
[**3**] S. Hüfner *et al.*, Springer - Verlag Berlin (1995).
[**4**] C.N. Berglund *et al.*, Phys. Rev. B **136**, A1030 (1964).
[**5**] C. Cohen-Tannoudji *et al.*, *Mecanique Quantique*, Herman (1973).
[**6**] F. Bonell, thesis (2009).
[**7**] N. V Smith *et al.*, Solid State Commun. **15**, 211 (1974).
[**8**] M. Matsunami *et al.*, Phys. Rev. B **87**, 165141 (2013).

Chapter 3
Electronic properties of $(111)Sm_{1-x}Gd_xAl_2$ surface and interface

I. Literature review 37
I.A. Electronic band structure in Rare Earth dialuminides 37
I.B. Valence stability in Sm metal and $SmAl_2$ 38
I.C. Electronic surface state in Lanthanide elements 39
II. (111) SGA surface preparation and characterization 40
II.A. Chemical analysis 40
II.B. Structural analysis of the Nb-free surface 41
II.C. Electronic analysis 43
III. Electronic structure of (111) SGA surface 44
III.A. Samarium 4f multiplets 45
III.B. Valence band analysis (ARPES) 46
III.B.1 In-plane wave vector measurements 47
III.B.2 Out-of-plane wave vector measurements 54
III.B.3 Discussion on the nature of observed electronic states 57
III.C. Spin Resolved analysis 63
IV. Electronic structure of (111)SGA/MgO 65
IV.A. Interface oxidation 65
IV.B. Samarium 4f multiplets 66
IV.C. Valence band analysis 67
V. Conclusion 68
References 69

This chapter is focused on the photoemission experiments that have been performed mostly on the (111)SGA surface, but also on MgO-covered SGA. Angle-Resolved PhotoEmission (ARPES) and Spin-Resolved PhotoEmission (SRPES) experiments have been performed on the beamline CASSIOPEE at the synchrotron SOLEIL (described in chapter 2), in collaboration with P. Le Fèvre, F. Bertran and A. Taleb.

This chapter is divided in four main parts. The first part is devoted to a literature review on some RE and RE dialuminides electronic properties. The second part describes an essential and difficult step before any ARPES analysis, i.e. the preparation of the (111)SGA surface with optimum quality. The experimental data collected on the (111)SGA surface are gathered in the third section. The analysis of the Sm valence stability via the measurements of 4f multiplets is first presented. The main part concerns then the exploration of the valence band, where 3D-ARPES measurements with different photon beam polarization have been performed to observe and study various electronic states. Electronic band structure calculations (collaboration with C. Tiusan) have been developed to help unraveling the nature of these various contributions. Finally, SRPES experiments have been undertaken to probe the SGA spin-polarization at the Fermi level. The fourth and last section is devoted to the study of MgO-covered SGA, a relevant system in the context of magnetic tunnel junctions where the SGA electrode is covered by an oxide insulating barrier. The main goal was to analyze the effect of the MgO cover on the surface oxidation, the Sm valence and the electronic states described in the previous section.

I. Literature review

Before the presentation and discussion of the experimental results obtained on $Sm_{1-x}Gd_xAl_2$ during this PhD work, it is worth mentioning some important features previously reported on the electronic properties of RE dialuminides and of RE metals. These will give an overview of the current knowledge on these complex compounds and may help in the analysis and interpretation of the SGA ARPES experiments.

I.A. Electronic band structure in Rare Earth dialuminides

Rare Earth dialuminides compounds have attracted particular interest because they show variety of unusual physical properties, such as Kondo effect, superconductivity etc…Various studies have been thus undertaken to explore their electronic properties, mostly via electronic band structure calculations and photoemission spectroscopy experiments.

Electronic band structure calculations have been especially reported for $LaAl_2$[1], YAl_2[2] and, more recently, $SmAl_2$[3] compounds. In these first two compounds, A. Hasegawa *et al.* used a self-consistent Augmented Plane Wave (APW) method, taking relativistic effects into account for $LaAl_2$.They show that the first seven bands are fully occupied and the next three bands partially occupied, resulting in complex Fermi surfaces consisting of various sheets with some specific features: The $LaAl_2$ eighth band has small hole pockets around L points ; The $LaAl_2$ and YAl_2 tenth bands have a large closed electron sheet centered at the Γ point, with small electron pockets around L points in YAl_2. In the case of $SmAl_2$, H.J. Gotsis *et al.*[3] performed band structure calculations in both the local spin-density approximation (LSDA) and the LSDA+U (U is the Hubbard parameter) incorporating spin-orbit coupling. They used the general potential Linearized Augmented Plane Wave (LAPW) method, as implemented in the WIEN2K code. The electronic band structure of $SmAl_2$ extracted from[3] is presented in figure 1. Because of the localized nature of *f* electrons, the authors showed that the Hubbard parameter has to be taken into account to properly describe the $SmAl_2$ properties (*f* electron occupancy, spin and orbital moments, position of *4f* bands). A physically meaningful calculation is obtained with a U parameter between 0.5 and 0.6Ry.

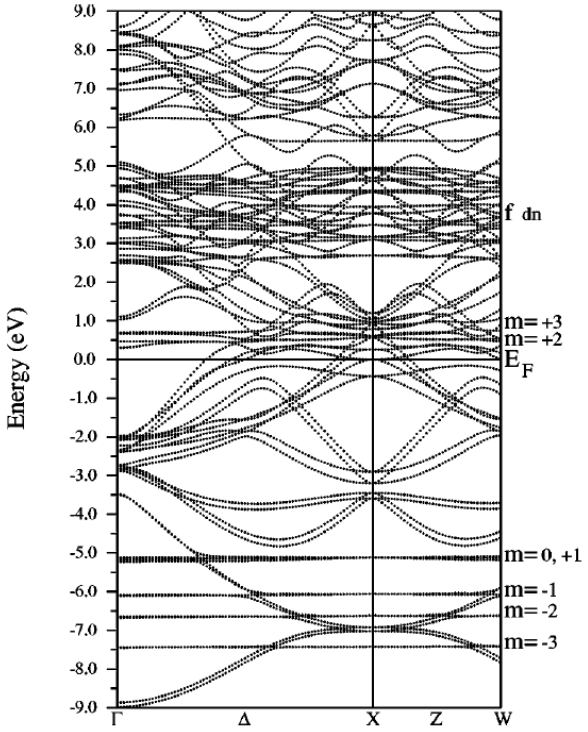

Figure 1: Calculated electronic band structure of $SmAl_2$ using the LDA+U method[3].

No specific indication about the nature of the bands can be found in[3], but from the comparison with other calculations performed on $LaAl_2$[4], it appears that the lowest bands (binding energy larger than 4eV) are likely due to the Al s like states while the region up to the Fermi level shows the hybridized character of Sm-d and Al-p like states.

A recent paper by D. Paudyal *et al.*[5] also highlights the crucial role of the Hubbard parameter to properly locate the occupied and unoccupied 4f states below and above the Fermi level, respectively, and to describe the 4f Crystal Field splitting. The authors calculated the Density Of States for different $REAl_2$ (R=Ho, Dy, Er, $Er_{0.75}Dy_{0.25}$, $Er_{0.25}Dy_{0.75}$), using the LSDA+U method implemented in the tight binding linear muffin tin orbital (TB-LMTO) approach. They could evaluate the exchange and crystal field splitting, important for the understanding of low temperature properties in pure and mixed Rare Earth dialuminides.

From the experimental point of view, high-resolution photoemission experiments have been carried out almost thirty years ago to investigate different $REAl_2$ compounds (RE=Lu, Gd, Dy, Er, Tm, Eu and Sm)[6]. The aim was mainly to analyze the stability of the 4f configurations, i.e. the surface effects on the 4f and 5p binding energies as well as on the valence state, as it is described in the following section.

More recently, a three-dimensional ARPES study of $YbAl_2$, one of the prototypical valence fluctuation systems, has been published by M. Mastunami *et al.*[7]. They could observe band dispersions around the Γ point and Fermi surfaces that are well described by the LDA calculation. They also highlighted a strongly c-f hybridized and dispersive Kondo resonance peak, suggesting the coexistence between the coherent Kondo state and the unrenormalized band structure in $YbAl_2$.

I.B. Valence stability in Sm metal and $SmAl_2$

G.K. Wertheim *et al.*[8], performing XPS measurements as a function of the take-off angle, were the first to demonstrate that a divalent component of the spectrum originated from Sm atoms in the surface layer. B. Johansson[9] then showed that this result was consistent with general cohesive properties of metal surfaces. Based on the difference between energies for divalent and trivalent bulk configurations, this author used general properties of the surface tension of metals to determine the surface stable valence configuration in Rare Earth metals. The surface valence transition results from the decrease in cohesive energy caused by the reduction of atoms coordination at the surface. A. Rosengren *et al.*[10] then further investigated the valence instability at the Sm surface within a pair bonding model, confirming a favored divalent surface. They also compared the calculated positions of the surface divalent samarium level relative to the Fermi energy in the cases where a divalent surface covers a trivalent crystal (0.65eV) and where isolated divalent Sm atoms are surrounded by trivalent atoms at the surface (0.26eV). They concluded that the surface is composed of only divalent atoms.

Following these early papers, several groups have studied the surface character of the divalent contributions e.g. as a function of the oxygen exposure[11] or the Sm coverage[12],[13].

C. Laubschat *et al.*[14] have reported on the valence stability in Rare Earth compounds, and in particularly in RE dialuminides. They have analyzed surface effects on the valence state by high-resolution photoemission experiments and extended the work by B. Johansson[9] to determine the stability diagram for the RE dialuminide compounds (figure 2). Their approach was to consider the measured binding energies as identical to the stability energies of Johansson's scheme.

In this diagram, the horizontal lines denote the relative position of the Fermi level in the bulk (E_F^b) and at the surface (E_F^S). The data above both E_F^S and E_F^b reveal a stable trivalent configuration in bulk and at the surface. The data below both E_F^S and E_F^b reveal a stable divalent configuration in

bulk and at the surface, as it is the case for $EuAl_2$ and $YbAl_2$. For $SmAl_2$, comprised between E_F^S and E_F^b, the divalent configuration is stable at the surface and the trivalent configuration is stable in the bulk.

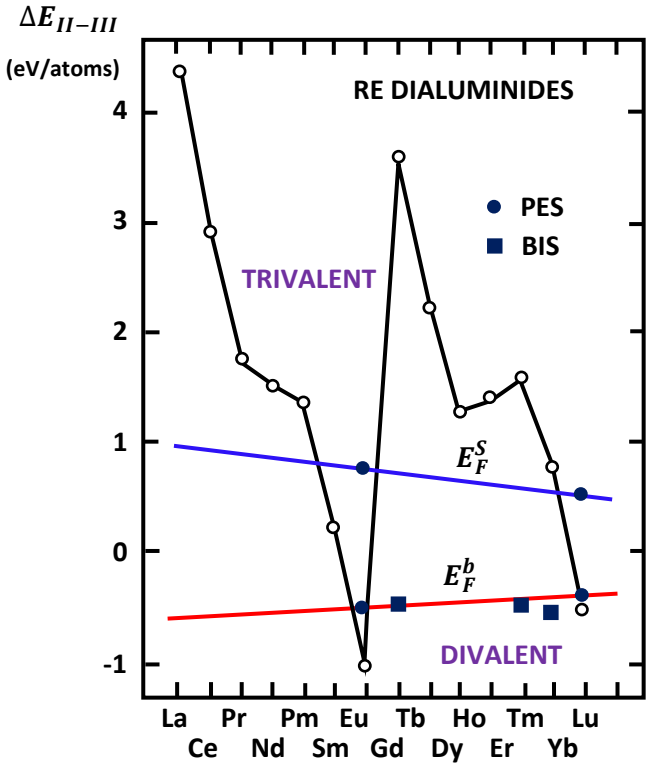

Figure 2: Stability diagram of the divalent and trivalent configurations for the RE dialuminide compounds extracted from PES (blue circles) and BIS (blue squares) experiments. The horizontal lines correspond to the relative position of the Fermi level in the bulk E_F^b (red line) and at the surface (blue line)[14].

I.C. Electronic surface state in Lanthanide elements

In the electronic structure of the matter, some electronic states specifically develop at the surface. They can be identified by photoemission-based spectroscopies, especially via their non-dispersive character along the direction perpendicular to the surface and their strong sensitivity to any surface contaminants.

An occupied surface state has been first predicted[15] and experimentally observed[16] for (0001) Gd crystal. Surface states have been then observed for various Lanthanide elements, mostly by PhotoEmission Spectroscopy (PES) or by Scanning Tunneling Spectroscopy (STS) (Table 1).

Lanthanide Metal	Gd	La	Lu	Dy	Ho	Er	Eu	Sm	Tb	Tm	Yb
Technics used	PES	STS	STS-PES	PES	PES	PES	PES	STS	PES	PES	PES
Surface			(0001)				(110)		(0001)		(111)
References	[16],[17]	[18]	[18][19]	[19]	[19]	[19]	[19]	[20]	[21]	[22]	[22]

Table 1: Experimental evidence of surface states for Lanthanide elements using Photoemission Spectroscopy (PES) and Scanning Tunneling Spectroscopy (STS)

From Table 1, it appears that the occurrence of a surface state is a common property of Lanthanide metals surfaces. The surface state appears as a sharp peak by PES or STS and is localized near the Fermi level around the $\bar{\Gamma}$ point (for Lu, La, Gd, Tb, Tm and Yb). It exhibits only small binding energy dispersion with respect to the parallel component $k_{//}$ whereas no dispersion is observed with respect to the component perpendicular to the surface $k_{\perp}$ [16],[21]. These surface states for lanthanide metals were characterized as d-like surface state[19] (e.g. d- like surface state in the case of (0001) Tm and (111) Yb surface[22]) in agreement with the first experimental observation and prediction realized on (0001) Gd surface[15],[16].

To our knowledge, no surface state has been reported up to now in Rare Earth dialuminide compounds.

II. (111) SGA surface preparation and characterization

Getting a smooth and high crystal quality (111) SGA surface without oxygen (O), nitrogen (N) or carbon (C) contamination is a crucial step to perform relevant ARPES experiments. As it has been described in the previous chapter, ARPES is indeed a highly surface sensitive technique since only the electrons close to the surface can escape and be detected.

As described in the chapter 1, (111) SGA epitaxial films are grown by molecular beam epitaxy at the Institute Jean Lamour in Nancy[23]. They are covered with a 25nm thick niobium, in order to protect them from oxidation in air. A preparation process has thus been developed to obtain a Nb-free SGA surface with required quality. For this purpose, preliminary experiments have been first carried out in the IJL (in collaboration with Y. Fagot). Experimental conditions have been then adjusted in the CASSIOPEE preparation chamber.

The (111) SGA surface preparation finally consists in two successive steps: (i) *Removal of the Nb cover layer by Ar sputter etching*. The energy was chosen at 2 keV and reduced to 600 eV in the final part of the etching process, close to the SGA surface. This step was regularly monitored by Auger measurements; (ii) *Annealing of the SGA surface.* A “flash heating” at high temperature (above 550°C) during 15 min aimed at desorbing residual impurities, as well as rearranging and smoothing the surface. The procedure of short etching (15 min at 600 eV) and annealing has been repeated between each ARPES experiments in order to “refresh” the SGA surface which is rather unstable likely due to the high affinity of Sm and Al to oxygen.

Several techniques of surface characterization (Auger measurements, RHEED, LEED and photoemission experiments) have been used to confirm the quality and the crystal order of the (111) SGA surface, and thus valid the preparation process.

II.A. Chemical analysis

Figure 3 presents the Auger spectra collected during and at the end of the Nb etching process, around the Al, Sm and Nb contributions and at higher kinetic energies around the oxygen peak.

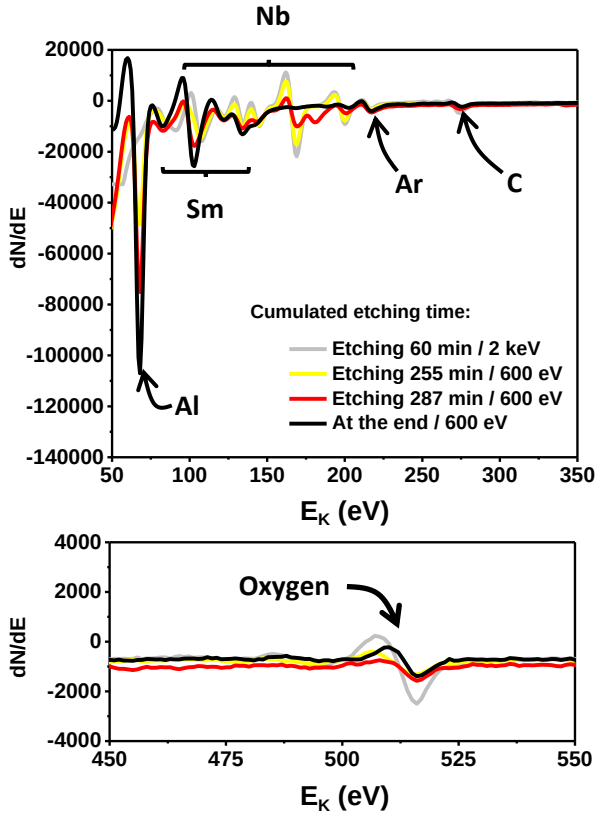

Nb Auger peaks (eV)	Sm Auger peaks (eV)
	80
105	100
121	118
132	133
142	
167	
197	

Figure 3: Left: Auger spectra collected during and at the end of the etching process of the(111) SGA epitaxial film. Right: Auger peaks positions for Nb and Sm (Handbook of Auger electron spectroscopy).

The Nb being a heavy element and the current density during the etching being weak, several hours (approximately 5 hours) have been necessary to remove the Nb cover. The etching process has been followed up via the measurements of the Nb peaks localized at 169 eV and 200 eV, i.e. outside of the range where Sm peaks are expected (figure 3 right). The decrease of the Nb peak intensity with time attests for its progressive etching and the absence of Nb residual peak at the end of the process confirms the Nb-free surface. Moreover, the Al and Sm peaks are clearly identified in figure 3. Nevertheless, the persistence of weak oxygen, carbon and argon contributions are observed. The argon contribution results from the argon implantation during etching. The persistence of an oxygen peak (not observed after a similar process in IJL) is attributed to the Auger gun in the CASSIOPEE MBE chamber (confirmed by XPS experiments). In order to avoid this contamination, no Auger analysis has been performed after the final “refreshing” short etching and annealing steps.

II.B. Structural analysis of the Nb-free surface

The symmetry and roughness of the surface have been probed by LEED and RHEED experiments. Both techniques are based on the electrons diffraction. In the case of the LEED (RHEED), the electrons are accelerated at low (high) voltage and impact the surface perpendicularly (with a small angle). The reflection of the electrons is observed on a phosphorescent screen. The RHEED and LEED patterns are extremely sensitive to the surface geometry and permit to determine the symmetry and crystalline structure of the surface, and to identify possible surface reconstructions. Moreover, the RHEED patterns permit to analyse the surface roughness with the

observation of thin and continuous diffraction streaks in the case of a smooth surface, or more or less intense diffraction spots in the case of a rough surface.

Figure 4 presents the RHEED patterns collected along the $[11\bar{2}]$ azimuthal direction before (a) and after (b) the annealing of the Nb-free SGA surface. The RHEED pattern obtained at the IJL after the initial growth is shown in figure 4 (c).

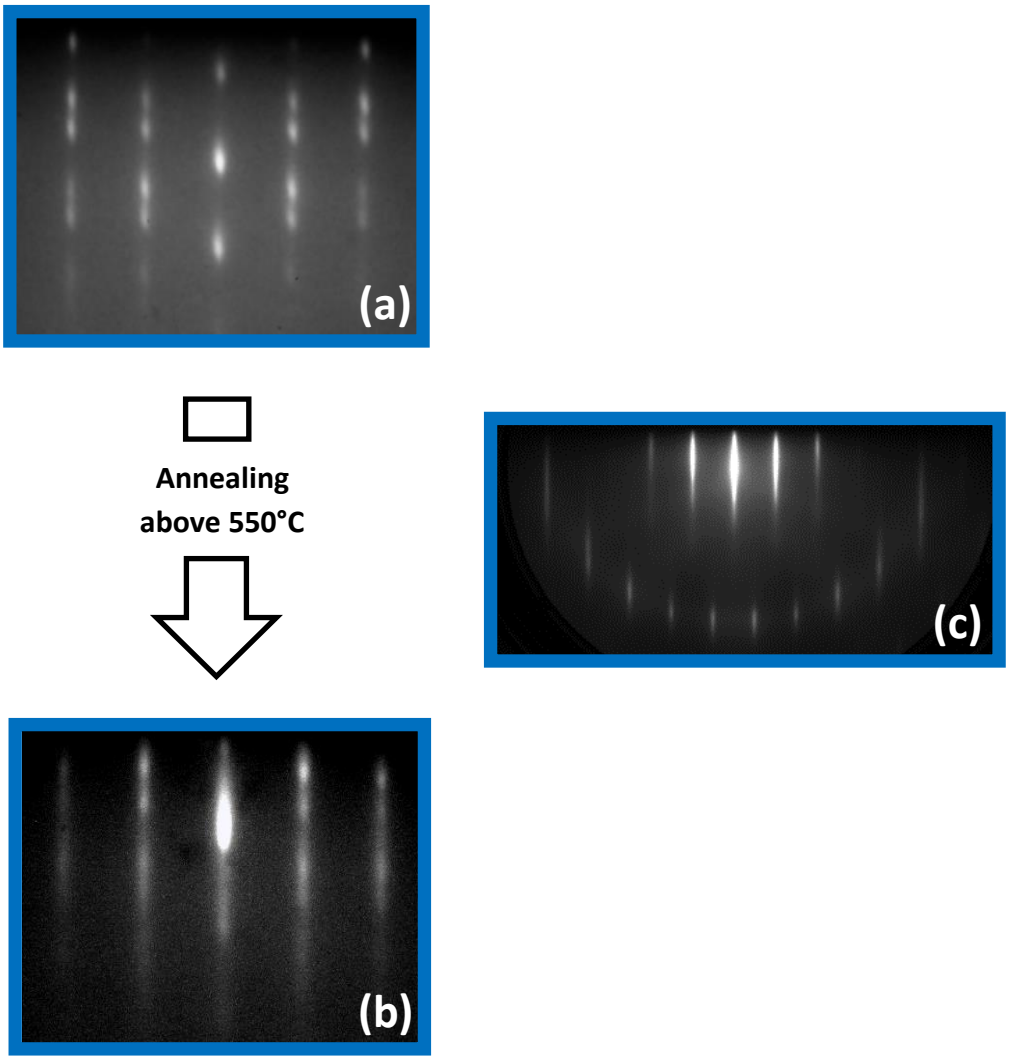

Figure 4: RHEED patterns collected in the CASSIOPEE MBE chamber along the $[11\bar{2}]$ azimuthal direction of the Nb-free SGA layer (a) before and (b) after the annealing at a temperature higher than 550°C. (c) RHEED pattern collected in the IJL MBE chamber after the initial growth.

Figure 4 (a) first shows that the crystal order has been preserved after the etching process, but the surface is significantly rougher than it was just after the initial growth (figure 4 (c)). The short high temperature annealing improves, i.e. smooth, the SGA surface as attested by the observation of more continuous streaks in figure 4 (b). The annealed surface has been further analysed via the LEED patterns collected for several electron energies (figure 5). The (111) plane of $SmAl_2$ (direct lattice) is shown in the black box (upper right).

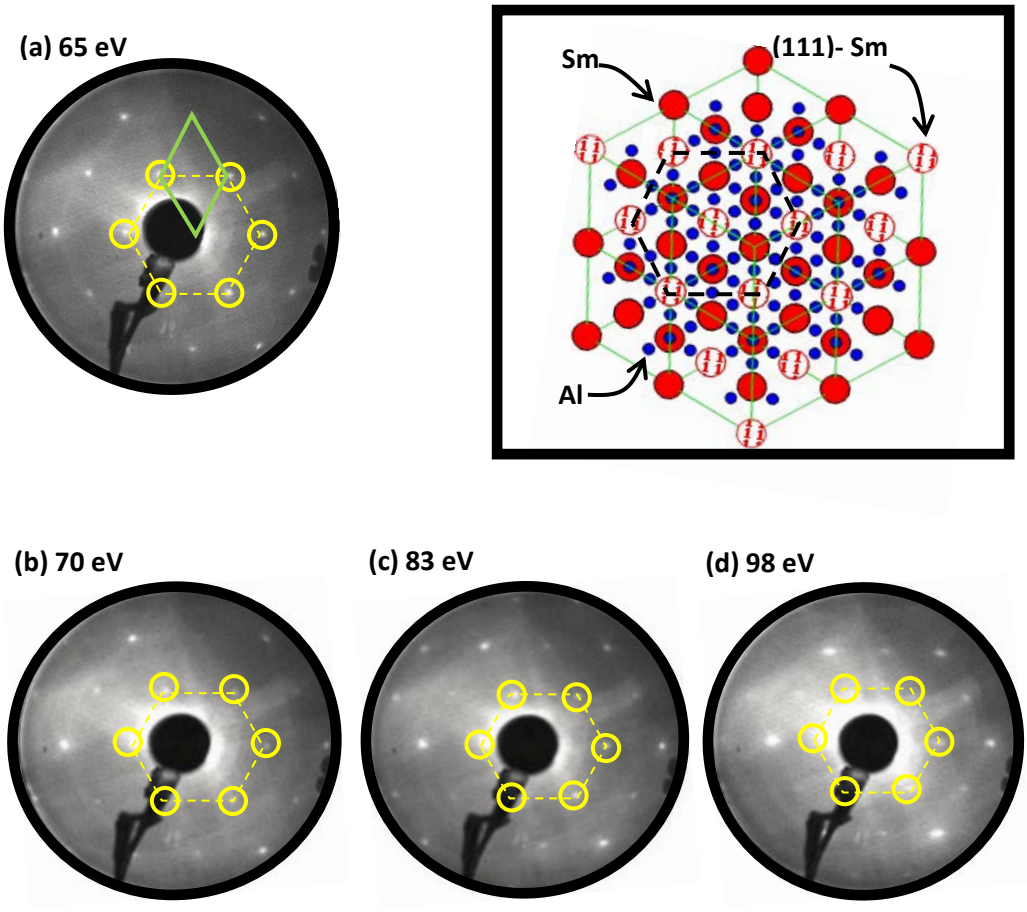

Figure 5: LEED patterns collected at 65 eV (a), 70 eV (b), 83 eV (c) and 98 eV (d) on (111)SGA surface. The elementary mesh of SGA is sketched by the green diamond. Upper right: (111) $SmAl_2$ plane, as obtained from the software CaRIne.

The different LEED patterns exhibit several intense diffraction spots. The spots surrounded by the yellow rings and linked by the yellow dotted lines in figure 5 define the 1x1 hexagonal pattern of (111)SGA surface in the reciprocal space and permit to extract the elementary mesh of SGA (green diamond in figure 5 (a)). The external diffraction spots correspond to higher order. This hexagonal symmetry for the (111)SGA surface is consistent with as-grown properties of SGA epitaxial films and with the symmetry expected for the $SmAl_2$ (111) plane.

Finally, the spots' intensities don't depend on the incident electron energy (65 eV, 70 eV, 83 eV and 98 eV) which reveal the absence of surface reconstruction.

II.C. Electronic analysis

Photoemission spectroscopy, as described in the previous chapter, was systematically used to provide complementary information on the surface quality, and especially on its possible oxidation, by the exploration of the Al core levels. The spectra were collected at 4K and for an incident photon energy of 100 eV around the Aluminum 2p multiplets. Figure 6 presents typical examples obtained for a "clean" SGA surface (open symbols) and for a "partially oxidized" SGA surface (filled symbols).

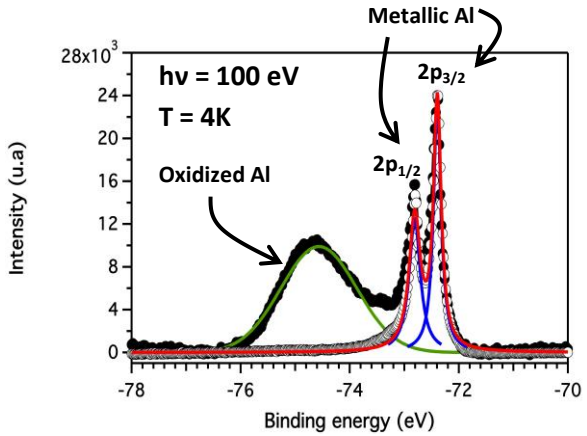

Figure 6: Photoemission measurements of the Aluminum 2p contributions performed at 4K and for an incident photon energy of 100 eV for a "clean" (111)SGA surface (open circles) with its fit (red curve) and an "oxidized" (111) SGA surface (filled circles - signal multiplied by a factor 4.8). The metallic contributions are well fitted by two Lorentzian peaks (blue curve) whereas the oxidized contribution is fitted by a Gaussian (green curve).

In both cases, the $2p_{1/2}$ and $2p_{3/2}$ multiplets of the metallic aluminium are clearly visible and well fitted by two Lorentzians separated by a spin-orbit coupling of 0.4 eV, in agreement with the literature[24]. For optimal preparation conditions (in particular without any final Auger analysis after the etching and annealing processes), only those multiplets are observed. In the other cases, a supplementary contribution at higher binding energy, attributed to oxidized Al, is observed. The photoemission signal is by the way strongly reduced (by a factor 4.8 in this example).

This PE analysis of Al 2p core levels appears to be very sensitive to the surface preparation and a good probe of the SGA surface quality. Such measurements have been thus systematically performed before each ARPES experiment and only SGA surfaces without oxidized Al contribution have been studied.

In conclusion, the combination of complementary characterization experiments confirms that the specifically developed preparation process is suitable to provide a clean (111)SGA surface with good crystalline quality. Although the quality is likely still lower than for as-grown SGA epitaxial films, especially regarding the surface roughness, the (111)SGA surface prepared in the CASSIOPEE MBE chamber gathers satisfactory properties to perform relevant ARPES experiments.

It has to be underlined that, although the optimal preparation conditions have been clearly identified, the surface preparation has remained a tough part in this study and required a lot of time. The MBE base pressure is namely another crucial parameter, especially during the annealing process, since pressures in the low 10^{-9} mbar range during annealing were required to get a clean SGA surface. These drastic conditions may be difficult to reach in a synchrotron MBE, where successive users groups work in the same MBE chamber and may evaporate various types of elements.

III. Electronic structure of (111) SGA surface

This section gathers the ARPES data collected on the (111) SGA surface: around the Sm 4f contributions to analyze the Sm valence stability and, for smaller incident energies, to probe the various electronic states in the valence band area. All the data have been collected at low temperature (4K) and for a p- or s- polarization of the incident photon beam. The data analysis and interpretation have benefited from electronic band structure calculations (collaboration with C. Tiusan). First SRPES results are presented at the end of this section.

III.A. Samarium 4f multiplets

The various samarium 4f contributions have been analyzed by PhotoEmission Spectroscopy for incident photon energy in the [130eV-150eV] range. Figure 7 (a) presents the Energy Dispersion Curve (EDC) at $\bar{\Gamma}$ point for two particular incident photon energies hv = 140 eV (black curve) and hv = 134 eV (grey curve).

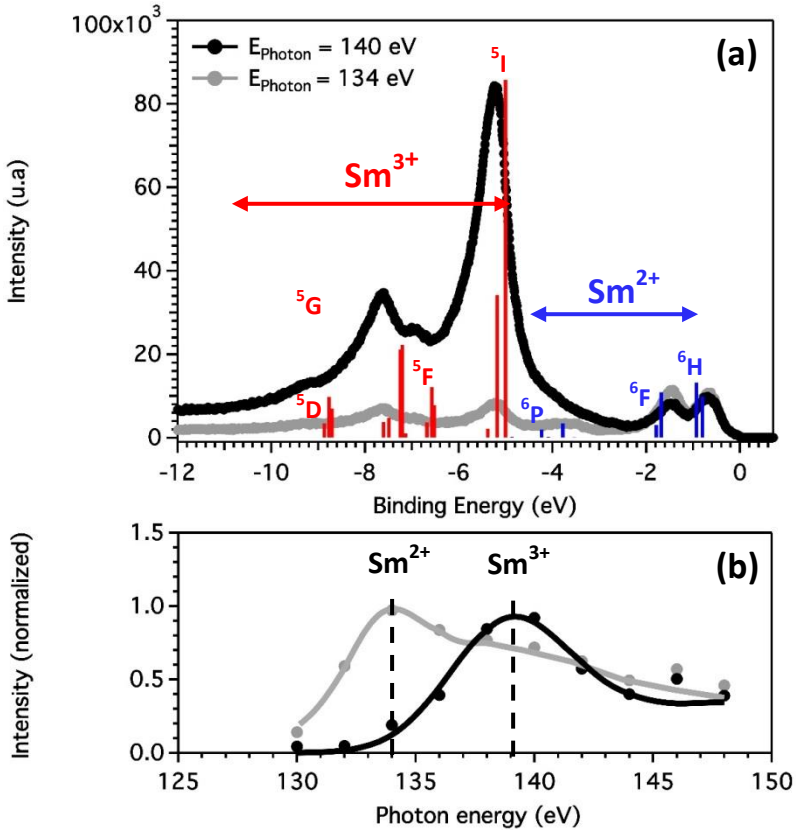

Figure 7: (a) Intensity versus the binding energy at $\bar{\Gamma}$ point and around the Sm 4f contributions for the (111)SGA surface. The Sm^{3+} and the Sm^{2+} multiplets weight and binding energy positions[25] are normalized by the ^5I and ^6F intensity and indicated by the vertical red and blue bars respectively. (b) Normalized intensity versus the incident photon energy for the ^5I (black) and ^6F (grey) Sm multiplets. The black and grey lines are guide for the eyes.

The photoemission spectra around the Sm 4f contributions show two separate groups: near the Fermi level up to approximately 3 eV in binding energy, and beyond for larger binding energies.

These two main contributions can be characterized by resonant photoemission where the emission from 4f levels is resonantly enhanced for incident photon energy tuned to the $4d \rightarrow 4f$ energy threshold. The resonant photoemission process for the Sm^{2+} and Sm^{3+} can be summarized by the following equations **(III-1)** and **(III-2)** respectively:

$$Sm4d^{10}4f^6 + h\nu \rightarrow [Sm4d^9 4f^7]^* \longrightarrow Sm4d^{10}4f^5 + e^- \qquad \textbf{(III-1)}$$

$$Sm4d^{10}4f^5 + h\nu \rightarrow [Sm4d^9 4f^6]^* \longrightarrow Sm4d^{10}4f^4 + e^- \qquad \textbf{(III-2)}$$

where * denotes the excited character of the state. This process is similar to an Auger decay process. An electron of the 4d core level is promoted to the 4f level generating a 4d core hole. The system being in an excited and unstable state relaxes by filling the core hole with one electron from the

upper 4f level. This transition is accompanied by the emission of an electron which can be detected in the photoemission experiment.

The resonant analysis is presented in figure 7 (b) for the contributions localized at 1.4 eV and 5.2 eV. These two contributions exhibit a maximum for an incident photon energy of 134 eV and 140 eV respectively. These values are in agreement with the resonance photon energy for the divalent Sm^{2+} (134 eV) and trivalent Sm^{3+} (140 eV), as determined by resonant photoemission[26] and absorption measurements[27] on a Sm single layer.

Moreover, several peaks resulting from the $4f^5$ and $4f^4$ final state multiplets are identified in figure 7 (a): final states (^6H, ^6F, ^6P) of initial Sm^{2+} ($^7F_0$) and final states (^5I, ^5F, ^5G, ^5D) of initial Sm^{3+} ($^6H_{5/2}$), as allowed by selection rules. Their weights and intensity ratios are in perfect agreement with the Sm^{2+} and Sm^{3+} multiplets structure calculated by Gerken *et al*. in Sm metal[25] and presented by the vertical bars (normalized with the ^6F and ^5I intensity respectively). However, a negative (positive) chemical shift is observed for the Sm^{3+} (Sm^{2+}), probably due to the different chemical environment. The divalent and trivalent contributions are separated by 4.5 eV in binding energy which is in agreement with the Coulomb correlation energy value determined on polycrystalline $SmAl_2$ by C. Laubschat *et al*.[6].

To summarize this section, photoemission experiments for incident photon energies in the [130eV-150eV] range enabled the exploration of 4f spectrum for the (111)SGA and the analysis of valence stability. The superposition of the multiplets originating from the Sm^{2+} and Sm^{3+} contributions could be observed, in agreement with calculations made using different formalism e.g. intermediate coupling[25] or Hubbard-I-formalism[28] in Sm metal. The trivalent and divalent contributions have been unambiguously identified by the resonant experiments and the multiplets positions relative to the Fermi level.

No specific investigation has been carried out to localize the divalent atoms. However, from the previous theoretical and experimental studies performed on Sm metal as well as on $SmAl_2$, the divalent contributions are most likely related to surface atoms. The position of divalent multiplets, i.e. 0.68eV and 1.47eV, are by the way consistent with a *divalent surface covering a trivalent crystal*, as calculated by A. Rosengren *et al.*[10].

Let's finally mention that Gd multiplets are also expected for this SGA surface. They should be localized near 8.6eV[29], but, due to the weak Gd concentration and the proximity with Sm multiplets, they are likely embedded in the Sm signal and consequently not detected by photoemission.

III.B. Valence band analysis (ARPES)

Beyond the analysis of the 4f contributions, photoemission spectroscopy with photon of low energy has been used to investigate the SGA electronic properties of the valence band. Angle Resolved experiments have been performed at 4K, for s- and p- polarizations and different incident photon energies.

As mentioned in the section II.B., the LEED patterns have permitted to confirm the hexagonal symmetry of the SGA surface. The (111) SGA Surface Brillouin Zone (SBZ) is presented in figure 8 on the LEED pattern, together with a sketch showing the first bulk Brillouin Zone for the fcc crystal with its projection along [111]. High symmetry directions are $(\overline{\Gamma K})$ and $(\overline{\Gamma M})$ with $|\overline{\Gamma K}|$ = 0.74 Å^{-1} and $|\overline{\Gamma M}| = 0.64$ Å^{-1}.

Taking advantage of the analyzer acceptance angle α along the vertical direction, of the sample rotation θ around the vertical K_y axis (Chapter 2, section II.A. figure 5), and of the tunable incident photon energy $h\nu$, it was possible to explore electronic states along different directions of

the BZ, for in-plane and out-of-plane wave vector measurements, as sketched in figures 9 (a) and (b) respectively.

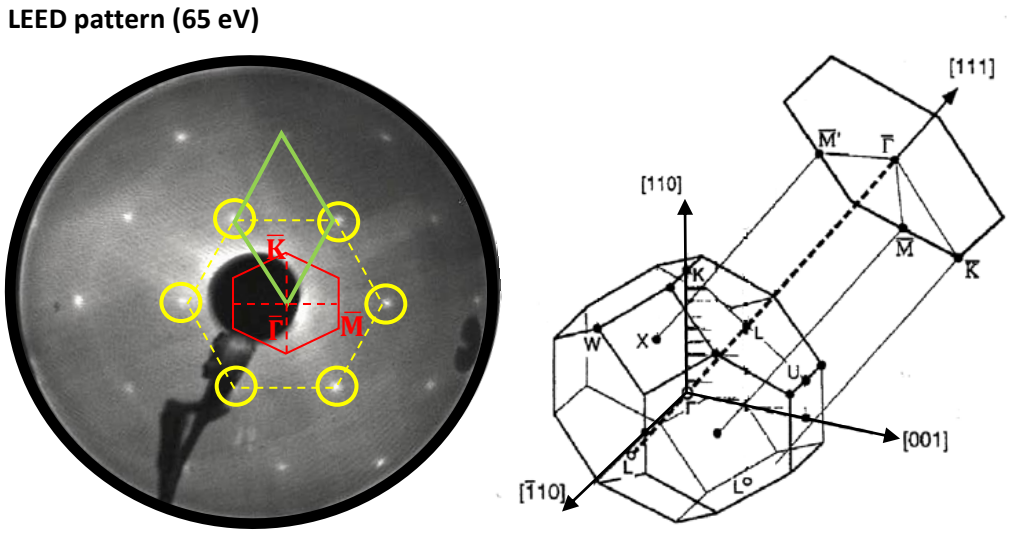

Figure 8: Left: LEED pattern of (111) SGA surface taken at 65 eV. The (111)-SGA Surface Brillouin Zone (SBZ) is delimited by the red hexagon and two high symmetry directions $\overline{\Gamma K}$ and $\overline{\Gamma M}$ are indicated by the red dotted lines. Right: first bulk Brillouin zone for fcc crystal with its projection along the [111] direction.

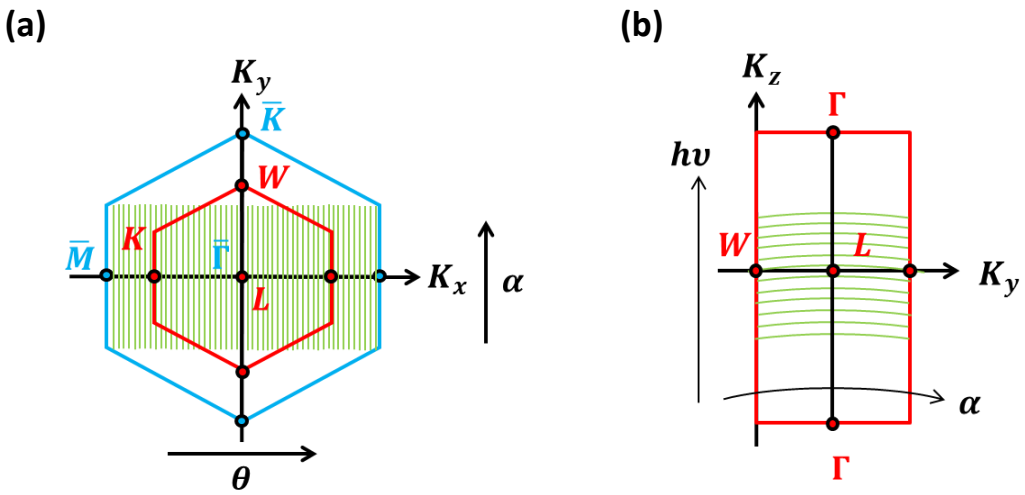

Figure 9: Measurement configurations for (a) in-plane analysis: α-resolved scans at different θ angles for a given incident photon energy (b) out-of-plane analysis: α-resolved scans at different incident photon energies for θ=0. The blue hexagon corresponds to the (111) Surface Brillouin Zone. The red hexagon and rectangles correspond to the bulk BZ.

III.B.1 In-plane wave vector measurements

Energy dispersion maps

Figure 10 presents the ARPES results obtained along the two high symmetry directions $\overline{\Gamma K}$ and $\overline{\Gamma M}$ for an incident photon energy of 32 eV and a p-polarization.

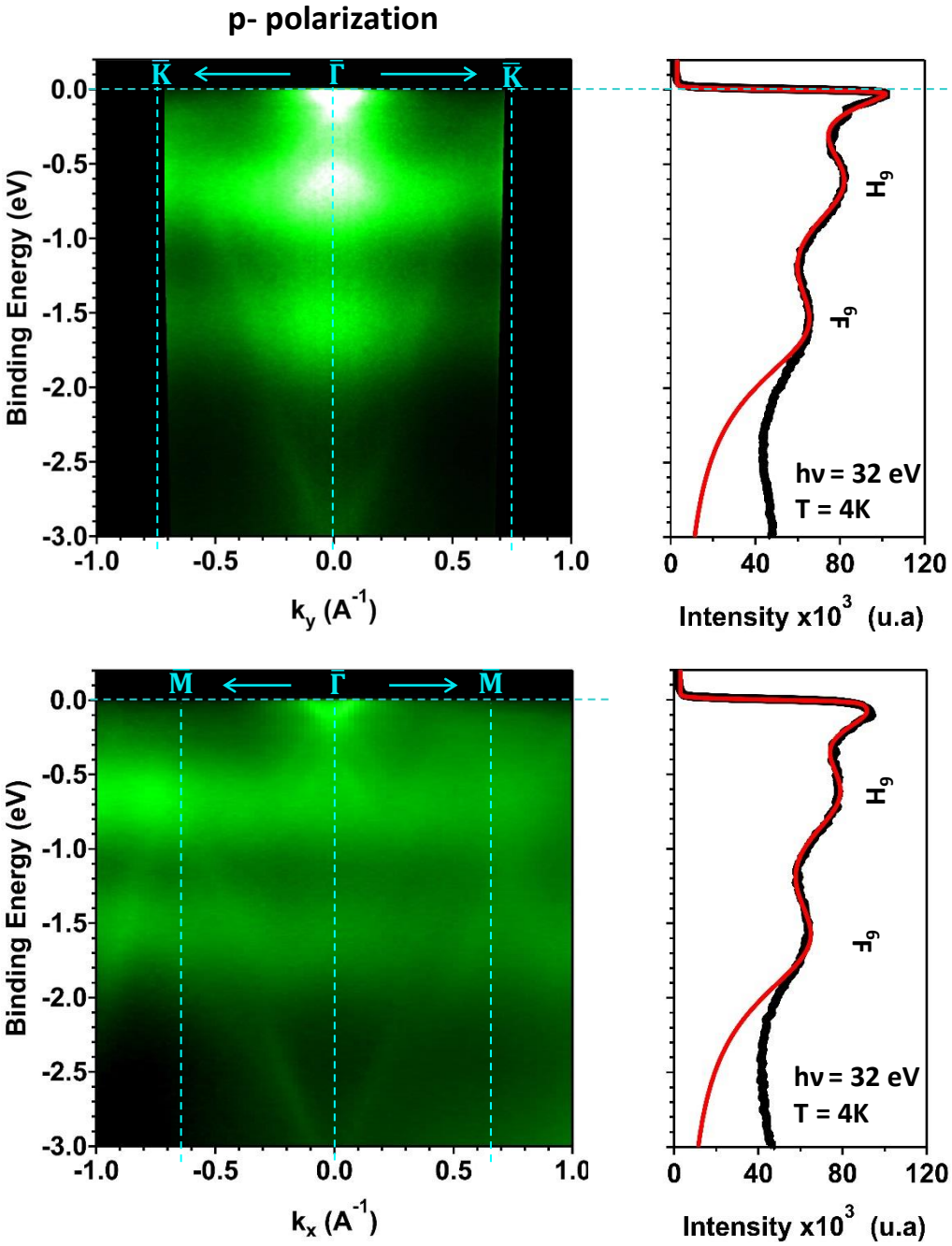

Figure 10: Left: $I(E_B, k_{//})$ maps along the high symmetry directions $\overline{\Gamma K}$ and $\overline{\Gamma M}$. Right: Energy Dispersion Curves (EDCs) at $\bar{\Gamma}$ point. The EDCs are adjusted (red curves) by three Lorentzians multiplied by the Fermi-Dirac function. The ARPES experiments have been performed at 4K, for a photon energy of 32 eV and a p-polarization.

Two non-dispersive contributions, localized around -0.6 eV and -1.6 eV, can be first observed along the two directions. They correspond to the Sm 4f divalent multiplets ^{6}H and ^{6}F respectively and are attributed to the divalent surface contribution (section III.A.). These relatively intense bands make the analysis of other less intense contributions difficult. They have been thus extracted from angle-integrated EDCs, fitted by two Lorentzian curves and subtracted from the intensity maps. The resulting maps after subtraction of the divalent contributions are shown in figures 11 (a) and (b) (p-polarization). Measurements along $\overline{\Gamma K}$ with an incident s-polarization are also presented (figure 11 (c)).

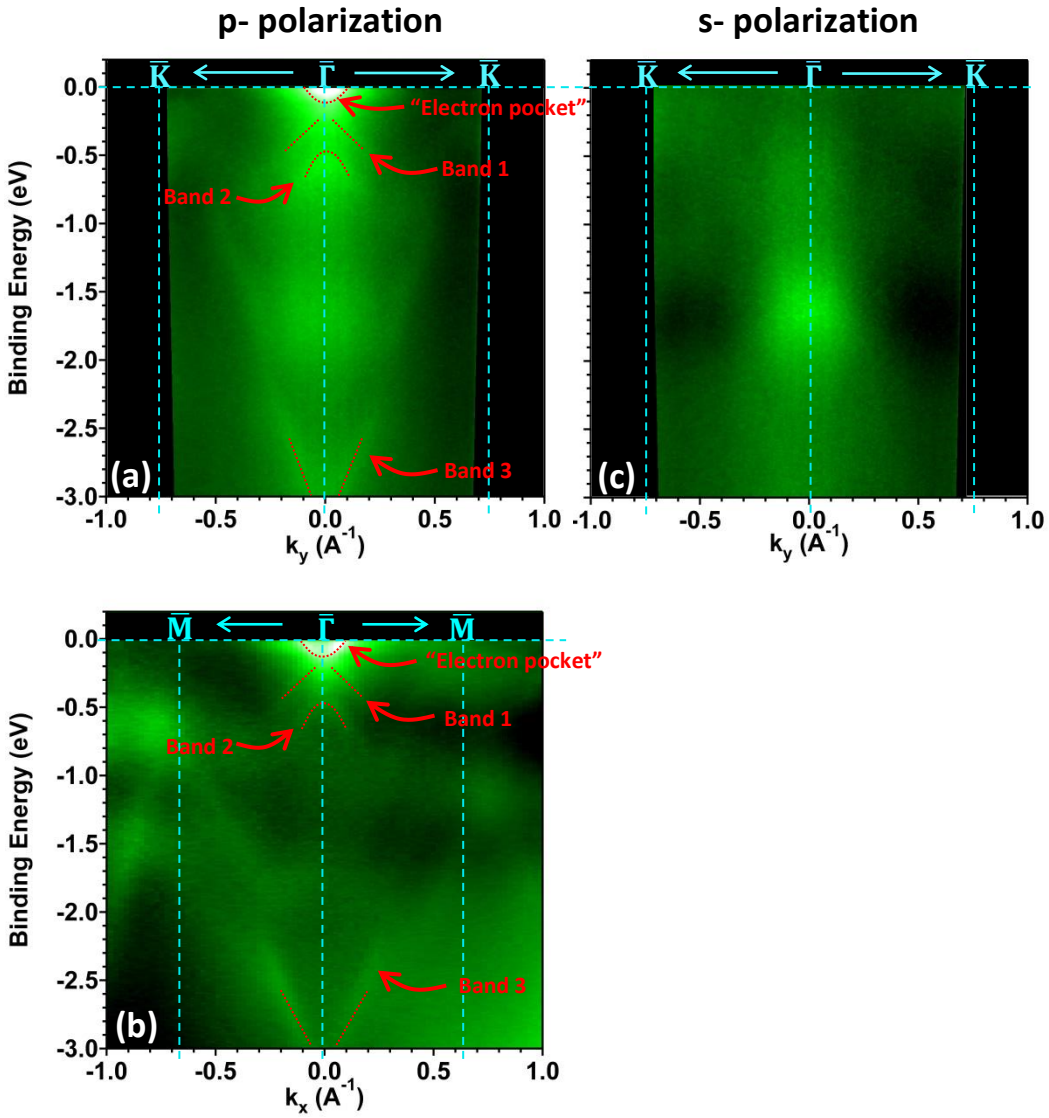

Figure 11: Intensity maps after subtraction of the two divalent contributions (measured at 4K for a photon energy of 32 eV) (a) and (b) along the high symmetry directions $\overline{\Gamma K}$ and $\overline{\Gamma M}$ for a p-polarized beam (c) along the high symmetry direction $\overline{\Gamma K}$ for a s-polarized beam.

After subtraction of the non-dispersive divalent contributions, the ARPES maps collected with p-polarization (figures 11 (a) and (b)) exhibit mainly three features that are actually observed along both directions, although the contrast is obviously better along $\overline{\Gamma M}$:

(i) An intense electron pocket, close to the Fermi level and strongly localized around the $\bar{\Gamma}$ point.
(ii) Two dispersive bands (bands 1 and 2) observed for binding energies up to -0.8eV
(iii) One dispersive band (band 3) for larger binding energies with a bottom around -3eV

The electron pocket contributes to the strong spectral weight measured close to E_f in the EDCs (figures 10). In these EDCs, the three contributions are well-adjusted (red curve) by three Lorentzians multiplied by the Fermi-Dirac function. The peak positions extracted from the fit are -1.63 eV and -0.63 eV for the ^{6}H and ^{6}F contributions respectively with a full width at half maximum of approximately 1 eV. The electron pocket is localized close to the Fermi level and exhibits a full width at half maximum of 0.22 eV. The difference in peak width for these two contributions (divalent and electron pocket) may result from different lifetimes of the hole and the photoelectron[30].

Energy dispersion

The in-plane energy dispersion curves of the various contributions have been fitted with a parabola $E = \hbar^2 k^2 / 2m^* + E_0$ where $\hbar$ is the Planck's constant divided by 2π, m* the effective mass and E_0 the energy at the $\bar{\Gamma}$ point. These fits, reported in figure 12, permit to extract the effective mass m* and E_0, as summarized in Table 2. The binding energy position of the electron pocket and the band 3 have been extracted from the fit of the Momentum Dispersion Curves (MDCs) (cut at constant E_B in the $I(E_B,k_y)$ map) by two Lorentzian functions whereas the binding energy positions of the bands 1 and 2 have been directly extracted from the map due to their weak spectral weight.

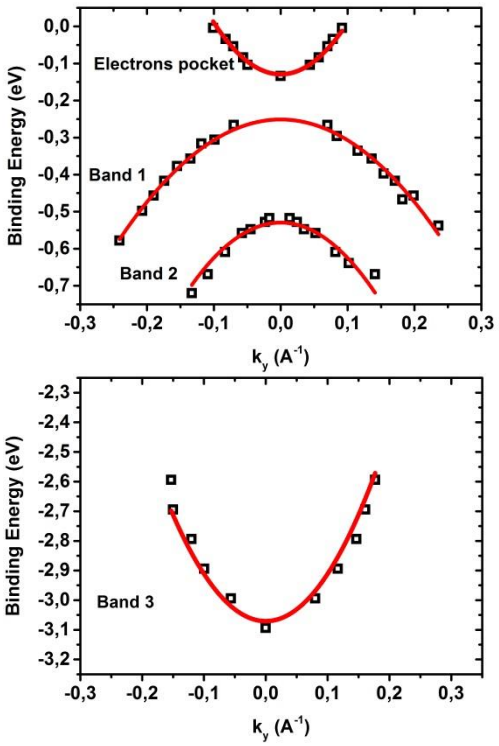

Figure 12: Energy dispersion curves along ky for the electrons pocket and the dispersive bands identified in figure 11 (a). The solid red curves are the parabolic fits using the relation $E = \hbar^2 k^2 / 2m^* + E_0$. The extracted effective mass m and E_0 are given in Table 2.*

Electronic structures	m^*/m_{e^-}	E_0 (eV)
Electron pocket	0.27	-0.13
Band 1	-0.68	-0.25
Band 2	-0.40	-0.53
Band 3	0.24	-3.07

Table 2: Effective mass m and E_0 extracted from the parabolic fits show in figure 12.*

The fitted parabolic dispersion curves match pretty well with the experimental data. The electrons pocket and the electronic band 3 have similar positive m^*/m_{e^-} ratio which may suggest a similar origin. The bands 1 and 2 present slightly larger negative m^*/m_{e^-} ratio related to their shapes with a maximum at the $\bar{\Gamma}$ point and a downwards energy dispersion.

Polarization analysis

The various electronic contributions have been further investigated via the study of their dependences on the incident photon beam polarization. As described in chapter 2 (I.C.), and as a result of the optical transitions for the photon-electron governed by the Fermi gold rules, only the initial states with the same symmetries as the electromagnetic field **E** can be excited in photoemission. Following the development proposed by J. Hermanson[31] for cubic crystals, the dipole-allowed initial symmetries for a (111) crystal face and for a normal emission are either Λ_1 or Λ_3 (irreducible representation in single group notation), depending on the direction of the optical electric field: Λ_1 for the electric field parallel to <111> and Λ_3 for the electric field in the (111) plane.

Two types of linear polarization are available on the CASSIOPEE beamline (figure 13): the s-polarization, where the electric field is perpendicular to the incident plane (defined by the incident photon beam and the normal to the surface), and the p-polarization, where the electric field lies in the incident plane. If the (Oz) axis refers to the [111] normal direction, $E_z = 0$ for the s-polarization and $E_z \neq 0$ for the p-polarization. It turns out that the Λ_1 symmetry should be allowed in the p-polarization and the Λ_3 symmetry should be allowed in the s-polarization.

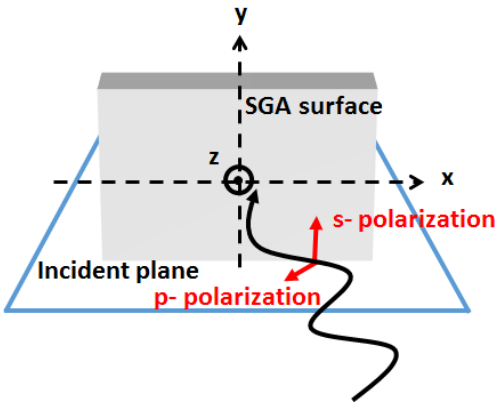

Figure 13: Sketch of s-polarization (perpendicular to the incident plane) and p-polarization (parallel to the incident plane). The incident plane is defined by the incident photon beam and the normal to the sample surface.

The $I(E_B, k_y)$ energy map obtained along the $\overline{\Gamma K}$ direction for an incident photon energy of 32 eV and a s-polarization is presented in figure 11 (c) and can be compared to figure 11 (a) obtained with a p-polarisation of the photon beam. The corresponding EDCs at the $\bar{\Gamma}$ point (after subtraction of the divalent contributions) are given in figure 14.

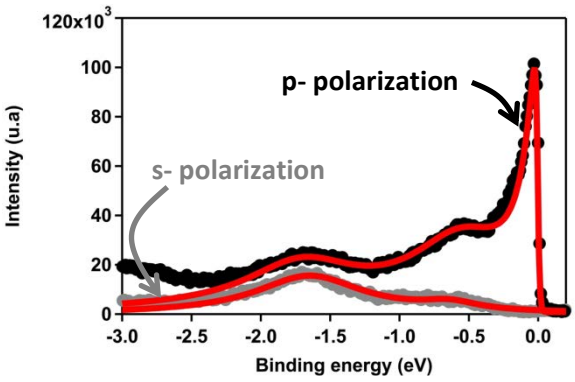

Figure 14: EDC curves at the $\bar{\Gamma}$ point for p-polarization (black circles) and s-polarization (grey circles) and after substraction of the divalent contributions. The measurements have been performed at 4K and for a photon energy of 32 eV. The red curves correspond to the fits by three Lorentzians multiplied by the Fermi function.

The energy map collected with s-polarization only exhibits some spectral weight at $\bar{\Gamma}$ point and in the vicinity of -1.6eV, which could be attributed to a residual divalent part (not fully subtracted, as it can be also seen for the p-polarization). The localized electron pocket, as well as the three dispersive bands, totally disappears when the electric field is perpendicular to the incident plane. This is also obvious in the EDCs where the spectral weight close to the Fermi level (electron pocket) and for binding energies above -2.5eV (band 3) is strongly reduced.

Given the development proposed by J. Hermanson about the allowed initial states for s- and p- polarizations, one can deduce that these various contributions exhibit a Λ_1 symmetry.

Iso-energy maps

In order to explore the shapes of the various electronic contributions, iso-energy (k_x,k_y) in-plane maps have been extracted from the ARPES measurements. The in-plane maps for zero binding energy (cuts of the Fermi surface) and for an incident photon energy of 32eV are given in figure 15 for both p- and s-polarizations.

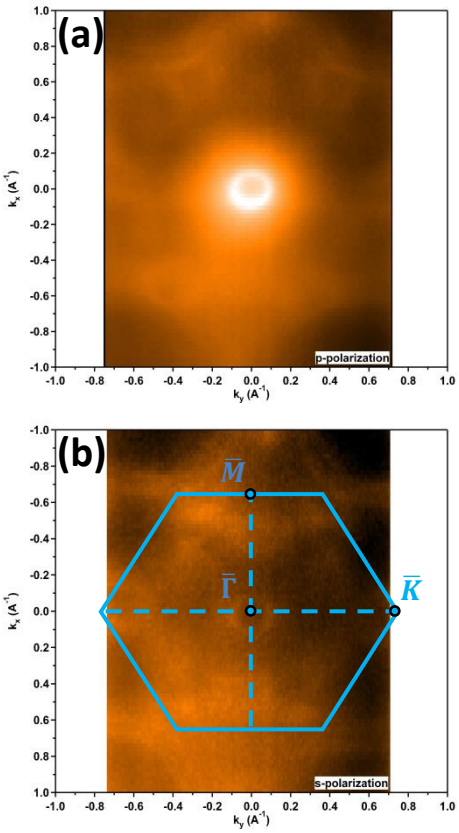

Figure 15: (k_x, k_y) cuts of the Fermi surface measured for an incident photon energy of 32eV and for (a) p-polarization and (b) s-polarization.

The in-plane cut of the Fermi surface for p-polarization (figure 15 (a)) reveals a nice ring shape associated to the electron pocket, localized around the $\bar{\Gamma}$ point of the Surface Brillouin Zone. This contribution is strongly reduced for a s-polarized photon beam, which enables the observation of a six-fold symmetry, in agreement with the (111) Surface Brillouin Zone, as sketched by the blue hexagon.

Iso-energy (k_x,k_y) maps for larger binding energies (figure 16) highlight the shape of the electron pocket, i.e. a paroboloid of revolution opening upwards. Its bottom is around -0.13eV and the curvature is related to the effective mass, extracted from measurements along the k_y direction (figure 12 and table 2).

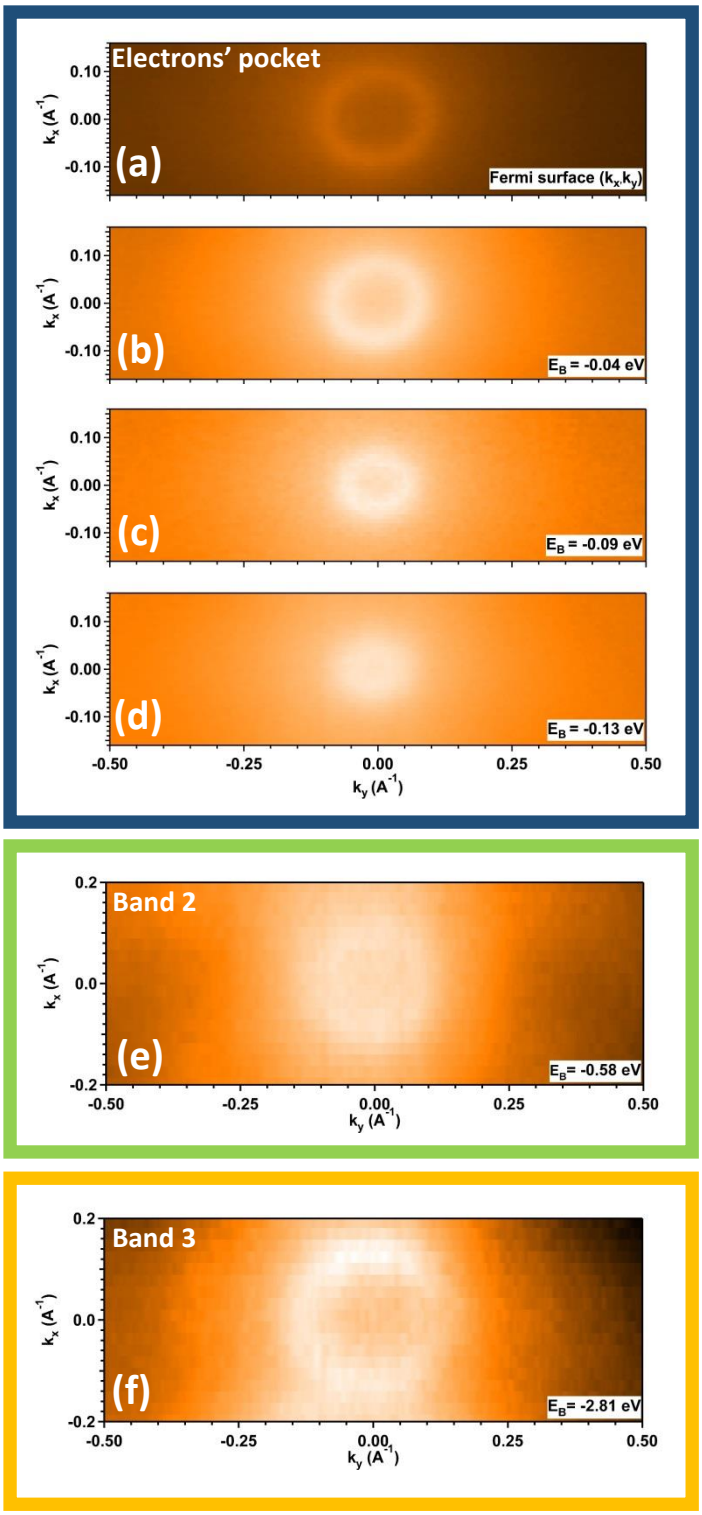

.

Figure 16: Iso-energy (k_x, k_y) maps measured for different binding energies at 4K for an incident p-polarized photon beam of 32eV. (a-d): electron pocket contribution (e) band 2 (f) band 3. The same intensity scale has been used, except for (a).

For larger binding energies in the energy ranges where other dispersive contributions have been observed (figure 16 (e) and (f)), the (k_x,k_y) maps also exhibit a similar ring shape for the so-called bands 2 and 3, revealing similar paraboloids of revolution. The separate analysis of bands 1 and 2 was not possible given the proximity (in space and energy) of these two contributions.

III.B.2 Out-of-plane wave vector measurements

The further exploration of the various contributions to the electronic structure requires investigating the influence of the incident photon beam. Changing the incident photon energy has namely two main effects:

(i) It may drive some resonance processes, as it has been described in the case of 4f contributions (section III.A.), and thus strongly enhance the photoemission intensity.

(ii) It changes the perpendicular component of the momentum **k**, and thus permits to probe the electronic structure in the k_z direction.
As described in chapter 2 (II.A.), in the case of normal emission (Θ = α = 0°):

$$k_z = \sqrt{2m_e(E_K + V_0)/\hbar^2} \qquad \textbf{(III-3)}$$

where E_K is the measured kinetic energy of the emitted photoelectrons (dependent on hν) and V_0 is the inner potential.

The EDCs at the $\overline{\Gamma}$ point (normal emission) for different photon energies ([20eV-50eV] range) and a p-polarized bean have been extracted from the $I(E_B; k_y)$ maps (detection over the detector acceptance angle for various incident energies). They are presented in figure 17 (b).

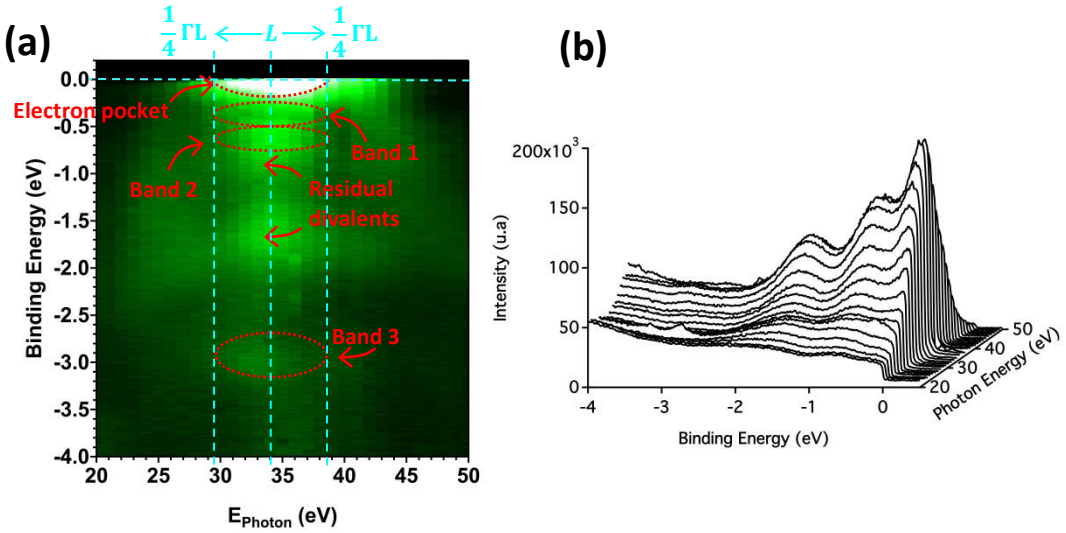

Figure 17: (a) : $I(E_B, h\nu)$ map and (b) corresponding EDCs, measured in normal emission at 4K and for a p-polarized photon beam.

The Sm divalent contributions (^{6}H and ^{6}F) are clearly visible in the EDCs for the whole photon energy range and thus partially mask the other electronic states identified in figure 11. Both divalent contributions exhibit little dispersion as a function of the photon energy, which is consistent with the localized character of 4f electrons and the surface nature of divalent contributions. As in the case of in-plane wave vector measurements, the divalent contributions have been subtracted from each $I(E_B, k_y)$ map in order to highlight the dispersion of other electronic states along the normal direction.

The $I(E_B, E_{photon})$ map at the $\overline{\Gamma}$ point deduced from this treatment is presented in figure 17 (a). Some residual divalent contributions are still visible but the in-plane dispersive bands (1-3) can be now better detected. The electron pocket and the other bands appear in a limited photon energy (k_z) range, approximately between 30eV and 39eV, with an obvious large dependence of the intensity

but small dependence of the binding energy. Since these various states are only visible for limited photon energies, the dispersion in binding energy is not suitable to properly discuss their possible two dimensional/three dimensional character. The analysis of the curvature, i.e. the effective mass, is likely more relevant.

For this purpose, as well as for the possible investigation of the bulk band structure and its comparison with calculation, it is necessary to determine the values of k_z corresponding to the various photon energies, which requires the knowledge of the inner potential V_0. V_0 is usually experimentally determined from the periodicity and/or specific features identified when varying the perpendicular component of the momentum. For metallic systems, V_0 is generally comprised between 11eV and 14eV and a value of 13.7eV has been determined from the symmetry of the Fermi surface in $YbAl_2$[7]. In the present case where the observed contributions are only present in a narrow photon energy range, the assumption was to localize the bottom of the electron pocket at one edge of the Brillouin Zone, i.e. at one point of special symmetry along the ΓL direction ($|\overline{\Gamma L}|$=0.685Å^{-1}). A value of V_0=15eV permits to localize the bottom of the electron pocket around a L point in the fifth BZ (k_z=5$|\overline{\Gamma L}|$=3.425Å^{-1}). This value is slightly larger than, but remains in reasonable agreement with, the ones reported in literature. An inner potential of 18.82eV is required for the band 3 that appears at larger binding energies. No quantitative information could be extracted for the bands 1 and 2, due to their weak spectral weight and their close proximity to the electron pocket and the residual divalent contributions.

The deduced (E_B, k_Z) perpendicular dispersion curves for the electron pocket and the band 3 are presented in figure 18, left. As for in-plane measurements, these curves have been fitted with the expression $E = \hbar^2 k^2/2m^* + E_0$ to determine the effective mass m* and the bottom energy E_0. The extracted values are reported in Table 3, where the values deduced from in-plane measurements are also recalled for comparison.

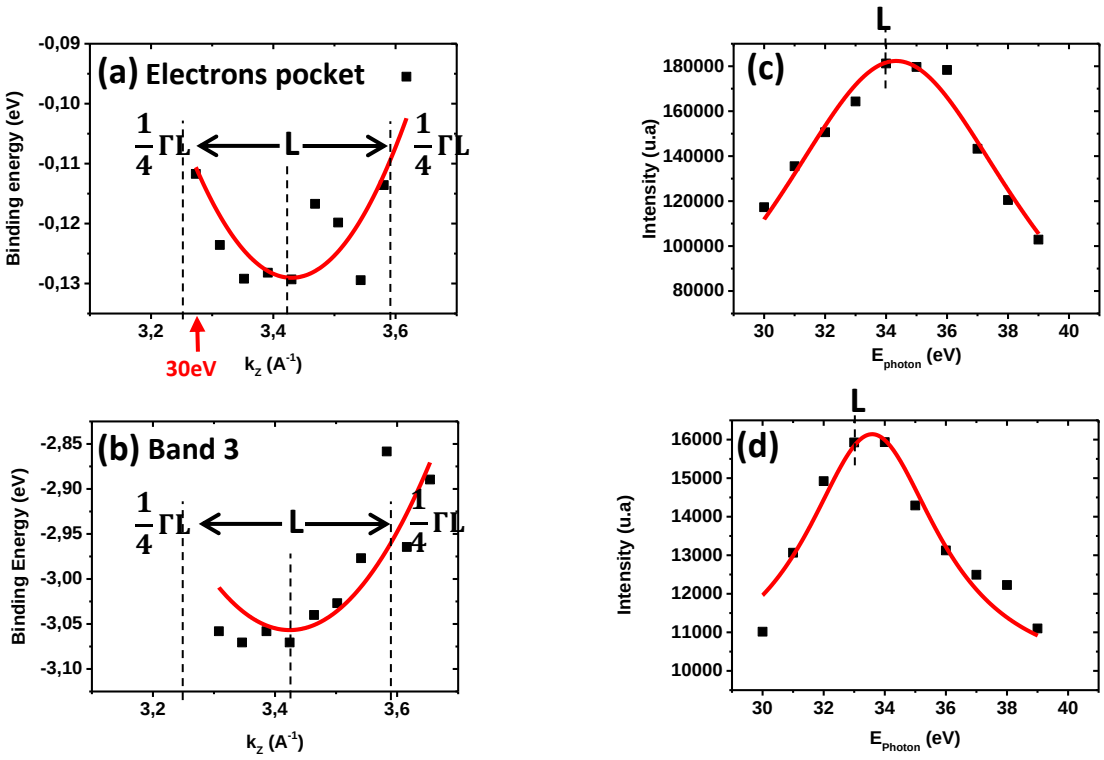

Figure 18: (a-b): Energy dispersion curves along the perpendicular [111] direction for the electrons pocket (top) and the band 3 (bottom) identified in figure 11 (a). The solid red curves are the parabolic fits using $E = \hbar^2 k^2/2m^* + E_0$. The extracted effective mass m and E_0 are given in Table 3. (c-d): Intensity versus the photon energy for the same contributions. The solid red curves are Lorentzian fits.*

Electronic structures	Electron pocket		Band 3	
Direction probed	k_y	k_z	k_y	k_z
m^*/m_{e^-}	0.27	5	0.24	1.08
E_0 (eV)	-0.13	-0.13	-3.07	-3.05

Table 2: Effective mass m and bottom energy E_0 extracted from the parabolic fits shown in figures 12 (along k_y) and 18 (along k_z).*

It appears that these contributions are very little dispersive in the perpendicular direction, especially the electron pocket, the effective mass of which is more than 20 times larger than in the plane. This feature is less obvious for the band 3 but it still exhibits a perpendicular effective mass 4.5 times larger than the in-plane one.

The intensities measured as a function of the photon energy are reported in figure 18, right. As mentioned previously, some spectral weight is detected only in a limited energy range. Both contributions approximately peak around the same photon energy of 34eV, which also corresponds to the k_z positions close to the L point. Although the quantitative analysis of the bands 1 and 2 was not successful, a close examination of $I(E_B; k_y)$ maps for different photon energies reveals the same tendency, i.e. a maximum intensity at 34 eV.

Iso-energy maps

As for in-plane wave vector measurements, iso-energy (k_z,k_y) out-of-plane maps have been extracted from the ARPES measurements collected for different photon energies. The (k_z,k_y) map for zero binding energy (Fermi surface mapping in the (k_z,k_y) plane) is given in figure 19, where the FS mapping in the (k_x,k_y) plane has been recalled for comparison. A sketch of the bulk fcc BZ permits to locate those FS mappings.

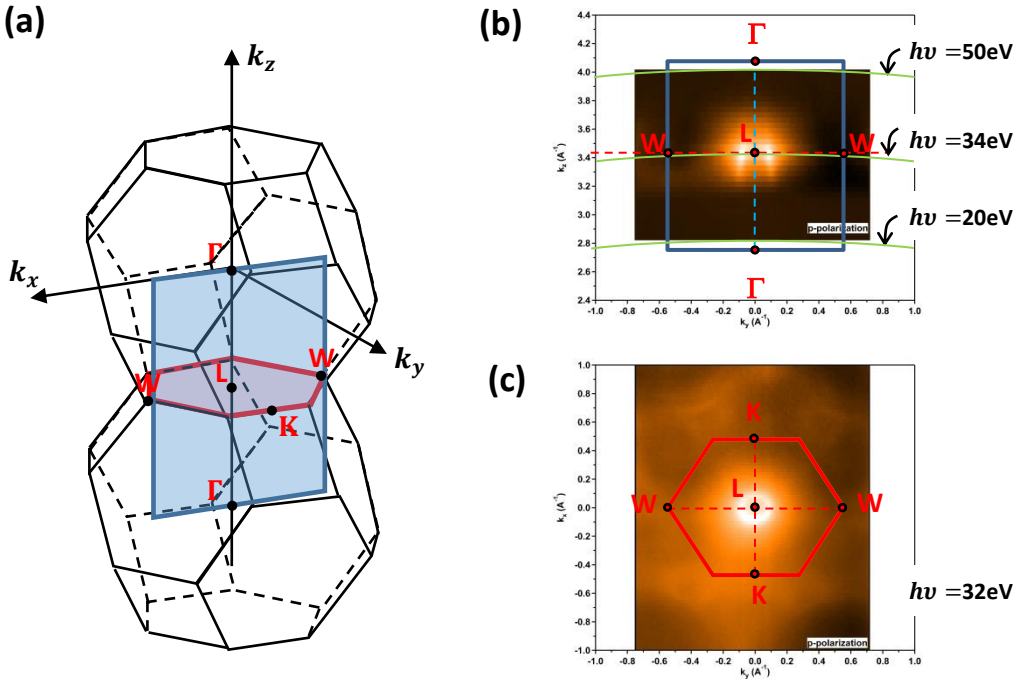

Figure 19: (a) Bulk BZ of SGA, in which k_z corresponds to the [111] direction of the fcc BZ (b) and (c) Fermi Surface mapping in the (k_z, k_y) and (k_x, k_y) planes, respectively (measured at 4K with p-polarized photon beam).

The main feature observed in the (k_z,k_y) plane and for a p-polarized photon beam is the so-called electron pocket, centred at the L point of the bulk BZ. Contrary to the ring shape observed in the (k_x,k_y) plane, the electron pocket exhibits an elongated shape, more or less like an ellipse, in agreement with the larger effective mass measured along k_z than along k_y.

One can also notice that, in contrast with the ring in the (k_x,k_y) plane, the spectral weight is not uniform along the ellipse. This is likely related to the variation of intensity versus the photon energy, as described in figure 18 (c). While in-plane measurements are collected at constant photon energy, out-of-plane measurements require namely the variation of photon energy, as it is shown on figure 19 (b) by the green curves. The region of high intensity corresponds to the data collected for photon energies close to 34eV, in agreement with figure 18 (c).

To summarize this experimental section:

1. Various contributions to the (111)SGA electronic structure have been brought out by the ARPES experiments: an intense and strongly localized electrons pocket, close to the Fermi level, and two sets of more dispersive bands: bands 1-2, opening downwards, for binding energies just below the electron pocket and up to -0.8eV and band 3, opening upwards, for larger binding energies with a bottom around -3eV.
2. These electronic states exhibit a Λ_1 symmetry.
3. Their spectral weight is largely enhanced for photon energy around 34eV.
4. They exhibit isotropic dispersion in the (k_x,k_y) plane, giving rise to dispersion sheets the shape of which are paraboloids of revolution.
5. Their dispersion appears to be significantly reduced in the perpendicular direction, especially for the electron pocket, the effective mass of which is increased by a factor of 20 (an increase by a factor 4.5 is measured for the band 3).

It remains now to try identifying these various contributions that could be either related to the bulk SGA electronic band structure, or resulting from the specific properties of the (111)SGA surface. This is the main goal of the following section.

III.B.3 Discussion on the nature of observed electronic states

As briefly mentioned in section I.C, some electronic states may specifically develop at the surface (so-called surface states) and can be identified thanks to photoemission-based spectroscopies. Various criteria are usually considered to conclude to the existence of a surface state:

(i) Because of its strongly localized character, a surface state should be totally delocalized in $k_\perp$, as a consequence of the Heisenberg uncertainty principle. Its binding energy thus doesn't depend on $k_\perp$, giving rise to a so-called "flat band" in this direction.

(ii) Pure surface states are located in an energy gap of the bulk band structure projected onto the two dimensional SBZ (Shockley surface state[32]). Resonant surface states coupled to bulk states (predicted by Tamm[33]) may however occur and these don't satisfy this condition.

(iii) Surface states are intrinsically highly sensitive to the surface conditions, especially the roughness and the chemical adsorption. The surface state intensity decreases or disappears with the surface contamination (oxygen or carbon for example) or surface disorders (ionic bombardment), more rapidly and more drastically than bulk states.

The surface emission being a one step process, one can also mention that excitation peaks associated to surface states are generally thinner than those associated to bulk states. The hole lifetime still contributes to the peak broadening.

In comparison with surface states, bulk states generally exhibit a significant dispersion in the $k_\perp$ direction and are less sensitive to surface contamination. One has however to keep in mind that some bulk states may also exhibit little dispersion along $k_\perp$ and that the degradation of the surface quality will of course affect the measurements of bulk states as well.

The distinction between surface and bulk states can thus be tricky and only the association of several strong indications can permit the clear distinction between those two. Electronic band structure calculations are often priceless to support experimental assumptions.

In the following, we will first review the various experimental observations that would tend to support the existence of surface states. We will then discuss these elements in comparison with other experimental results from literature and electronic band structure calculations.

Experimental observations supporting the existence of surface states.

1. The first important point is the morphology of the observed electronic states: the isotropic parabolic dispersion sheets in the surface plane with a small dispersion in the perpendicular direction. As already mentioned, this last feature is especially relevant for the electron pocket that exhibits a huge difference between parallel and perpendicular effective masses. This strongly points out a two-dimensional character of the electronic state. The observed ring shape of in-plane iso-energy maps is by the way commonly reported for surface states[34] and the values of m^*/m_{e^-} are close to the values extracted for surface states developing at the (111) surface of noble metals (Cu, Ag or Au)[35].

2. A second point is the dependence on the surface quality/contamination. Figure 20 presents the EDCs measured at the $\bar{\Gamma}$ point for a photon energy of 32 eV for various surface conditions: (a) and (b) correspond to two (111) SGA initial surfaces, just after similar but different preparation processes. (c) and (d) correspond to the same initial surface as (b), but during and after the PES experiments. The data are adjusted (red curves) by three Lorentzians (for the electron pocket and both divalent contributions) multiplied by the Fermi-Dirac function.

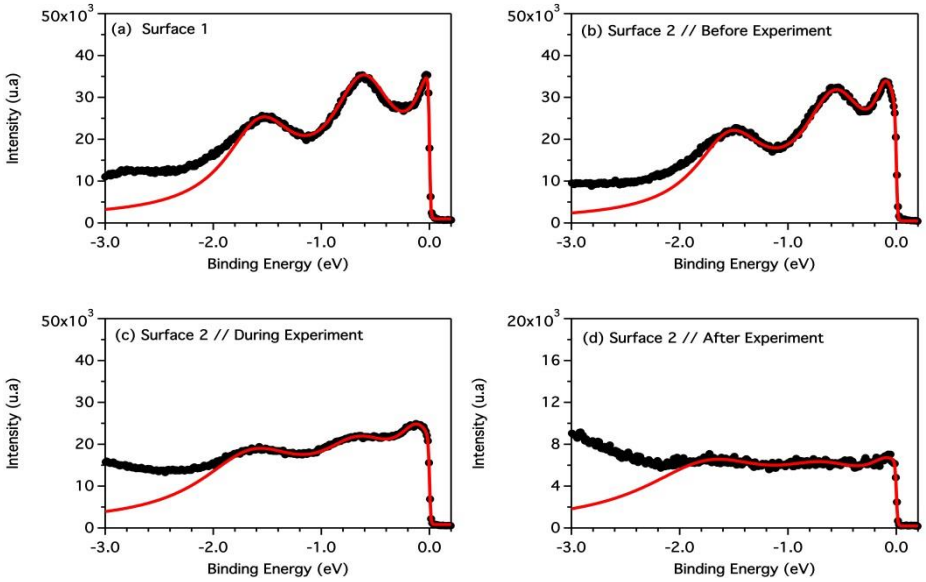

Figure 20: EDCs collected at the $\bar{\Gamma}$ point, at 4K and for a photon energy of 32 eV: (a) and (b) just after similar but different preparation processes; (c) and (d) same initial surface as (b) but during and after PES experiments respectively. The data have been adjusted by three Lorentzian multiplied by the Fermi-Dirac function (red curves).

Figures 20 (a) and (b) highlight the strong influence of the preparation on the localized feature close to the Fermi level. Despite identical preparation processes, the localized state is above the Fermi level (+0.03 eV) in one case and below (-0.09 eV) in the other case. This shift can be explained by a change in the surface stoichiometry, giving rise to a hole doping in (a) and an electron doping in (b). A residual oxygen contamination in (a) could pump electrons from the valence band (electronegative character of oxygen) and shift the localized peak above the Fermi level. Successive preparation processes tend to remove the residual oxygen contaminations and the peak then appears below the Fermi level.

The comparison of EDCs in (b), (c) and (d) shows that the electron pocket as well as the divalent contributions are strongly reduced (by a factor of approximately 6) at the end of the experiment (approximately 12 hours long). The surface obviously deteriorates during the experiments, likely due to some surface contamination despite the low base pressure (in the 10^{-10} mbar range) inside the photoemission chamber.

These various EDCs clearly prove that these three electronic states are very sensitive to the surface condition. An interesting point is that the decrease in spectral weight seems similar for the electron pocket and for the divalent contributions that are known to be localized at the surface. There is no clearly identified bulk state to compare how it would be influenced by the same surface characteristics. However, the decrease observed for the contribution at higher binding energy (band 3) appears to be comparatively smaller and slower.

One has to underline that these observations remain very qualitative. To investigate the sensitivity of electronic states to surface conditions, the thickness and nature of adsorbates are generally carefully controlled. The adsorption of [0.03-0.06] layers of oxygen[21],[36] typically results in a decrease of the surface state intensity, much faster than for bulk states [21] and larger than 50% of its initial value [21],[36].

3. The two previous remarks about the morphology/dispersion of electronic states and their sensitivity to surface characteristics belong to the common criteria to identify surface states. One can mention other elements that would be consistent with the occurrence of surface states.

The strong dependence of the spectral weight as a function of the photon energy may be attributed to a resonant process, as it has been described for Sm 4f contributions (section III.A.). In this photon energy range, a resonant process has been reported for the Gd 5d surface state (at 32eV) where the 5d emission is enhanced for incident photon energy tuned to the $5p \rightarrow 5d$ energy threshold[29]. The observed resonant-like behaviour at 34eV would tend to prove the 5d character of these electronic states. Whether this 5d state should be attributed to Gd or Sm remains an opened question, but the small Gd concentration and the reported resonant energy for Gd (32eV[29],[37] compared to 34eV in this study) would tend to rule out a Gd contribution. PES experiments on a (111) $SmAl_2$ surface (without Gd substitution) have been undertaken to clarify this point. Although a similar contribution seems present in the vicinity of the Fermi level, the poor quality of the data, related to difficulties in preparing the surface, unfortunately didn't allow drawing any definitive conclusion.

The observed electronic states exhibit a Λ_1 symmetry. The existence of a surface state with Λ_1 symmetry is common to the (111) surfaces of the noble metals Cu, Ag, Au and has been observed for Ni(111) [36] as well. A $5d_{z^2}$ symmetry has been reported for the (0001) Gd surface state[15].

The conjunction of these several features would thus suggest the existence of electronic surface states, especially for the electron pocket that exhibits the smallest perpendicular dispersion and the strongest sensitivity to surface conditions. One can underline that no surface states have been reported up to now for $SmAl_2$ or more generally for $REAl_2$ compounds in polycrystalline form. In the paper by C. Laubschat *et al.*[14], the authors reported the photoemission spectra around the 4f contribution of several $REAl_2$ compound (e.g. $SmAl_2$, $GdAl_2$, $DyAl_2$) and identified divalent

contribution as surface features. They didn't observe any additional contribution at the Fermi level, maybe due to higher incident photon energies (70-75 eV).

Electronic band structure calculation

Despite the various points reported above, the identification of the observed electronic states as surface states is not straightforward: the limited energy range where they are observed make the analysis difficult and the sensitivity of divalent contributions to the surface condition could also drive the decrease of the electron pocket spectral weight.

Moreover, as recalled in section I.A., electronic band structure calculations performed for YAl_2 [2] have evidenced the existence of small electrons pockets around L points that could explain our experimental results. A similar feature by the way also appears in the calculated Fermi surface for $YbAl_2$ (figure 1 (b) in [7]).

In order to try clarifying this point, electronic band structure calculations for $SmAl_2$ have been undertaken in collaboration with C. Tiusan (professor at the Technical University of Cluj-Napoca (TUCN), Roumania). They were performed in the Local Spin-Density Approximation incorporating the Hubbard parameter and the spin-orbit coupling (LSDA+U+SO). The Wien2k code, based on the Full Potential Linearized Augmented Plan Waves (FP-LAPW) method, was used. This approach is similar to the one developed by H.J. Gotsis *et al*[3] to calculate the electronic structure of $SmAl_2$ (section I.A). Gotsis'calculations were however performed for limited parts of the Brillouin Zone and some updates and corrections have been added to the code since their publication in 2003. This justifies the development of new calculations for bulk $SmAl_2$, over extended parts of the BZ. Further calculations have been also undertaken to analyze the possible role of the surface on the Density Of States.

Bulk band structure calculations

Calculations have ben first performed with a bulk cell crystallizing in the Fd-3m symmetry space group and with lattice constants equal to 7.912 Å (figure 21).

The Hubbart (U) parameter and the spin-orbit (SO) coupling have been chosen to get proper localization of the 4f trivalent contributions compared to the experiment (figure 7 (a)) and satisfactory values for spin and orbital moments (m_{orb} = -3.23 μ_B and m_{spin} = 2.95 μ_B).

The calculated electronic band structure for bulk $SmAl_2$ are presented in figure 22 along different directions of the bulk Brillouin Zone. The ΓL bulk direction (left part of the figure) is experimentally probed when changing the incident photon energy. The LK and LW bulk directions (right part of the figure) are experimentally probed via in-plane measurements along k_x and k_y respectively.

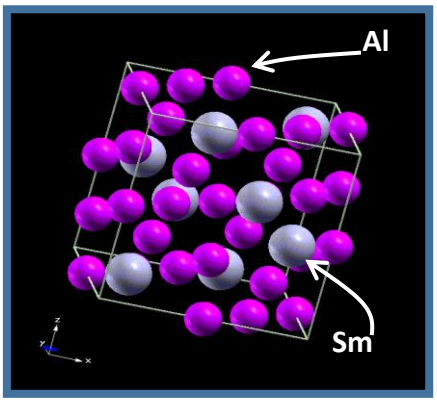

Figure 21: Bulk $SmAl_2$ cell used for the electronic band structure calculations.

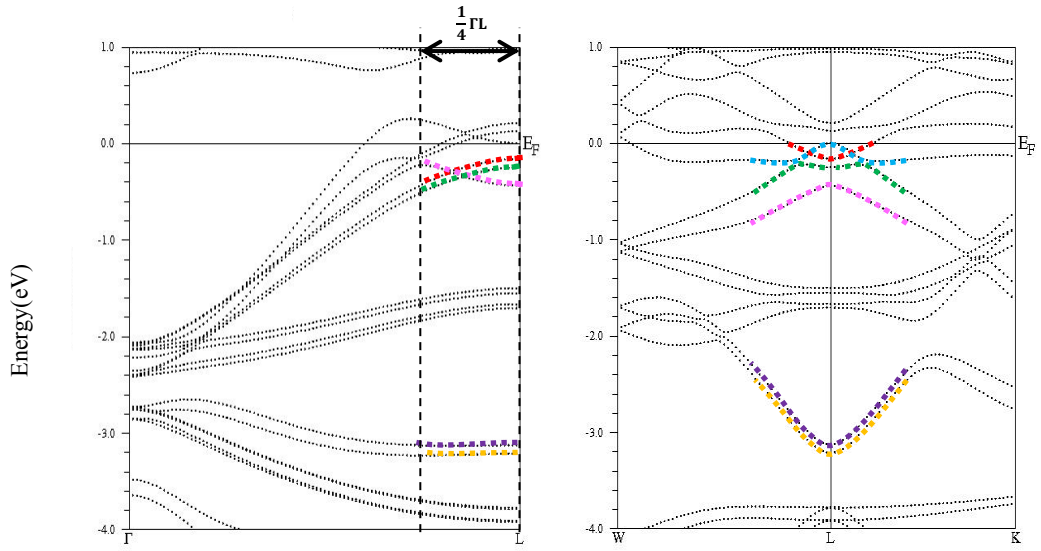

Figure 22: Electronic band structure calculated for bulk $SmAl_2$ (Wien2k code). The color dots are guides for the eyes.

The calculated electronic band structure along WLK (right part) presents several interesting features that are in relatively good qualitative agreement with in-plane experimental observations around the bulk L point, i.e. the surface $\bar{\Gamma}$ point (figures 11 (a) and (b)):

(i) Dispersive bands with positive effective mass and a bottom energy at approximately -3.2eV (purple/orange)
(ii) Dispersive bands with negative effective mass and a top energy around -0.4eV and -0.2eV (pink/green)
(iii) Localized spectral weight close to the Fermi level (red) with a minimum around -0.1eV at the L point and positive effective mass.
(iv) Some relatively flat and diffuse spectral weight around -1.6eV.

Experimental observations however didn't really evidence a contribution arising at the Fermi level and at the L point, as it is the case for the calculated "blue" electronic state. This may be masked by a much larger spectral weight for the localized electrons pocket (in red).

The calculated electronic band structure along ΓL (left part) has to be compared with the dispersion curves presented in figure 18 (a) and (b).

(i) The purple/orange bands starting at L at -3.2eV are flat around L. They only exhibit a small dispersion when increasing towards Γ points. The experimental dispersion that we have extracted in the explored ¼ ΓL range is slightly larger than the calculated behavior.
(ii) The red band exhibits a rather dispersive behavior with a decrease in binding energy towards Γ points. This is in disagreement with the large positive effective mass deduced for the electron pocket in the perpendicular direction. The calculation doesn't bring any evidence of a flat contribution close to the Fermi level along ΓL.

In summary, the conjunction of experimental observations and electronic band structure calculations would suggest that the localized electron pocket around $\bar{\Gamma}$ of the (111)SGA SBZ is a surface state with Λ_1 symmetry. This surface state, of 5d character, is likely built on the bulk state close to the Fermi level. The other dispersive bands that exhibit similar symmetry and 5d character would rather correspond to bulk states.

One can finally underline that the main characteristics of those calculated electronic bands are similar to those calculated in $LaAl_2$[1] and YAl_2[2]. In these papers, a Λ_1 symmetry is reported along ΓL for the band close to the Fermi level and the band with a bottom energy around -3.2eV, consistently with these experimental results.

Surface Density Of States

Calculations have been recently extended to explore the possible development of a surface state at the (111)SGA surface. For this purpose, a different supercell has to be built (figure 23 (a)) to consider the different possible environments for Sm: the samarium located in the bulk of the structure (bulk Sm), the samarium located at the surface (surf Sm) and the samarium located just underneath the surface when this latter is formed by Al atoms (sub-surf Sm). Because of the size of the supercell, computing times are much longer and it was not possible to calculate the electronic band structure and to take the U and SO parameters into account. Only Density of States without U and SO have been calculated.

No significant difference between bulk and surface environements (surface or sub-surface) have been detected in the Sm f-DOS. The results obtained for Sm d states are presented in figure 23 (b) and (c).

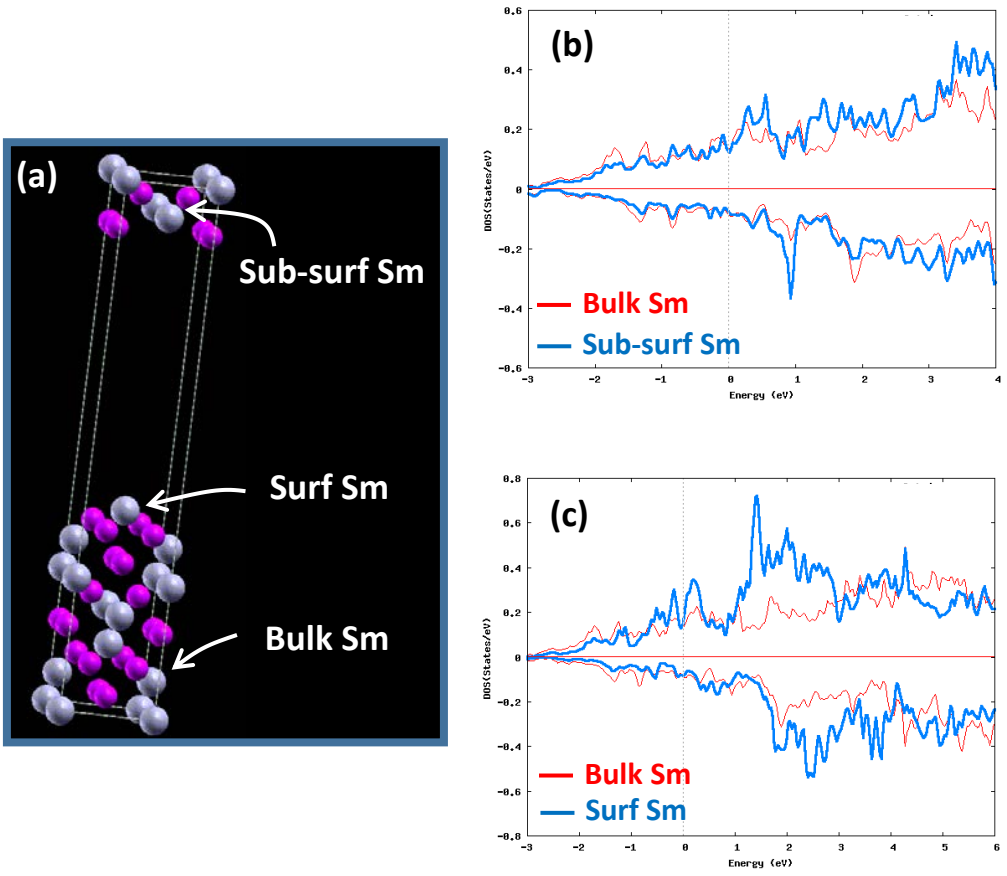

Figure 23: (a) Supercell used for the DOS calculation. Bulk Sm, surf Sm and sub-surf Sm denote the different Sm environments, respectively in the core of the crystal, at the Sm-terminated surface and just underneath the Al-terminated surface; (b) Calculated DOS for bulk Sm and sub-surf Sm; (c) calculated DOS for bulk Sm and surf Sm (Wien2k code).

The comparison between the bulk and the sub-surf Sm d-DOSs (figure 23 (b)) doesn't show any significant difference both in the majority and minority channels, indicating no Sm surface states for an Al terminated surface. The comparison between the bulk and the surf Sm d-DOSs (figure 23 (c)) does however highlight significant supplementary contributions in the surf Sm d-DOS, especially in the majority channel. This would suggest the development of Sm d surface states, only for a Sm-terminated surface; Sm electrons would be sensitive to the surface only when they are not covered by Al.

In the present experimental case, no specific information is available on the chemical nature of the SGA surface after the preparation process which has been developed. The observation of several supplementary features in the surf Sm d-DOS close to the Fermi level would be however consistent with our experimental results.

III.C. Spin Resolved analysis

The SRPES experiments can bring complementary information on the electronic properties of the (111)SGA valence band by probing the spin-polarization at the Fermi level. These measurements have been performed in the so-called "spin chamber" of the CASSIOPEE beamline and in the remanent state (zero applied magnetic field).

As mentioned in the chapter 2, a solution to get rid of possible differences between the detectors is to perform two sets of measurements in reversing the sample magnetization. Because of the huge coercivity in SGA films, this couldn't be achieved in reversing the applied magnetic field. Different field-cooling procedures (under +0.12T and under -0.12T) were required to stabilize two opposite magnetization states (up and down spin orientations) in the SGA film. Because of the long acquisition time in SRPES experiments, the SGA surface had to be "refreshed" following the protocol detailed in section II, *for each temperature and each magnetization state*. This is of course a drawback since the surface characteristics may slightly change between the two magnetization states but it appeared to be necessary due to the surface degradation. In summary, the process was the following (i) surface preparation (ii) transfer into the spin chamber at a temperature above the Curie temperature (125K) (ii) application of the magnetic field (+0.12T or -0.12T) (iii) Field-cooling down to the measurement temperature.

Moreover, experimental issues arose in the MBE chamber (pressure rising well above 10^{-8} mbar during the annealing process) during the SRPES synchrotron run, so that a lot of time has been spent to get a surface with the required quality, similar to the surfaces used for ARPES. Only two SRPES measurements have been thus performed, at 30K and 88K. 88K is the compensation temperature measured by SQUID for this SGA expitaxial film.

These results are presented in figure 24. The spin up and spin down density of states and the polarization have been calculated using the formalism detailed in F. Bonell's PhD work[30]:

$$\mathrm{P} = \left[\left(\sqrt{I_2^+ I_1^-} - \sqrt{I_2^- I_1^+}\right)/\sqrt{I_2^+ I_1^-} + \sqrt{I_2^- I_1^+}\right] \times (1/0.12) \qquad \textbf{(III-4)}$$

$$I_{up} = (I_{tot}/2) \times (1 + P) = \left[\left(2\sqrt{I_2^+ I_1^-} + 2\sqrt{I_2^- I_1^+}\right)/2\right] \times (1 + \mathrm{P}) \qquad \textbf{(III-5)}$$

$$I_{down} = (I_{tot}/2) \times (1 - P) = \left[\left(2\sqrt{I_2^+ I_1^-} + 2\sqrt{I_2^- I_1^+}\right)/2\right] \times (1 - P) \qquad \textbf{(III-6)}$$

where $I_i^{\pm}$ is the intensity collected by the detector *i* for the up (+) or down (-) spin orientation.

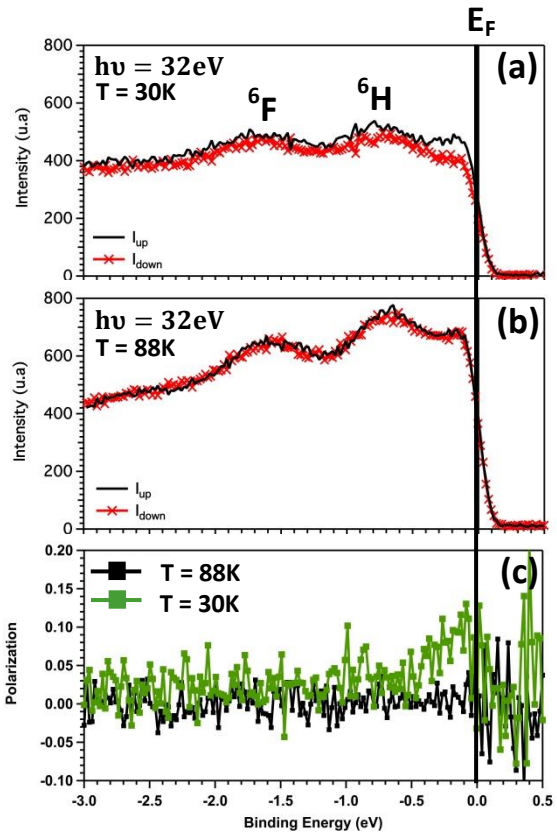

Figure 24: (a) and (b) Spin resolved intensities and (c) perpendicular to the plane polarization measured at 30K and 88K (hν = 32eV, p-polarized photon beam).

As previously reported, these EDCs exhibit at both temperatures several contributions, mostly the two divalent surface contributions and the electron pocket close to the Fermi level.

At 30K, a small positive polarization of approximately 13% could be extracted in the vicinity of the Fermi energy, whereas no spin polarization is observed at the magnetic compensation (88K). This later point is not consistent with transport measurements on SGA based magnetic tunnel junctions, that evidenced a finite Tunnel Magneto Resistance at the SGA compensation and thus a finite spin-polarization at the Fermi level[38]. This SRPES result would need to be reproduced and confirmed since some doubts have been emitted concerning the real temperature during the measurements. Complementary experiments are definitely required at several temperatures in order to investigate the temperature dependence of the spin polarization and to clearly determine the polarization in the compensated state.

The spin-polarization measured at low temperature is likely attributed to the 5d- based electronic state observed by ARPES. D. Wegner *et al.*[20] reported on a (0001) Sm surface state observed by Scanning tunnelling spectroscopy but their results strongly suggest its non-magnetic nature (unsplit contribution). The authors concluded that the topmost divalent Sm surface layer on (0001) Sm is nonmagnetic despite the magnetically ordered trivalent Sm core layer. The present results on (111)SGA would confirm the nonmagnetic nature of the divalent Sm surface contributions but rather suggest the occurrence of a spin polarized surface state. One can also underline that the measured positive polarization is consistent with calculation showing a surface state developed in the majority channel (figure 23 (c)).

However, as recalled previously, the experimental conditions were particularly difficult during this synchrotron run and complementary experiments are required before drawing any definitive conclusions on these various aspects.

IV. Electronic structure of (111)SGA/MgO

Following the study of electronic properties of a free (111) SGA surface, the next step was to investigate the SGA/MgO system, in order to explore how the (111) SGA electronic properties are affected by the presence of the MgO cover layer. This aspect is relevant for transport properties of SGA-based magnetic tunnel junctions where the SGA electrode is covered by the insulating barrier, typically MgO or Al_2O_3. This interface with the oxide layer may especially affect surface states, the spin polarization at the Fermi level and thus magneto transport properties. The aim of this section is to report on the electronic properties of this SGA/MgO system, where a special attention has been paid to the Sm 4f contributions and to the electron pocket discussed in the previous part. As for the free (111)SGA surface, the analysis of Al 2p multiplets was also used to analyze the oxidation of the SGA/MgO interface.

A 2 monolayers thick MgO film has been deposited at room temperature on the (111)SGA surface, right after the surface preparation process, in the CASSIOPEE MBE chamber. MgO has been evaporated from an electron gun, previously calibrated (before our synchrotron run) by using RHEED intensity oscillation. No observation of the Al 2p contributions has been performed between the surface preparation and the MgO deposit to minimize the risk of surface degradation.

IV.A. Interface oxidation

As presented in section II.C., the preparation process developed for the free (111)SGA surface permits to obtain a clean surface, where the observation of the Al 2p multiplets is the signature of the absence of oxygen contamination (figure 25 (a), open symbols). The deposit of a 2 ML thick MgO film drives strong modification of SGA at the interface, as evidenced by the appearance of a supplemental contribution at higher binding energy, attributed to oxidized Al (figure 25 (a), filled symbols). The two contributions for aluminum metal ($2p_{1/2}$ and $2p_{3/2}$) are however still clearly visible and present the same characteristics, i.e. spin-orbit coupling, intensity ratio, and width, as for the clean free SGA surface.

The observation of the typical Mg 2p peak reported for MgO[39] (figure 25 (b)) confirms the presence of MgO on the SGA surface.

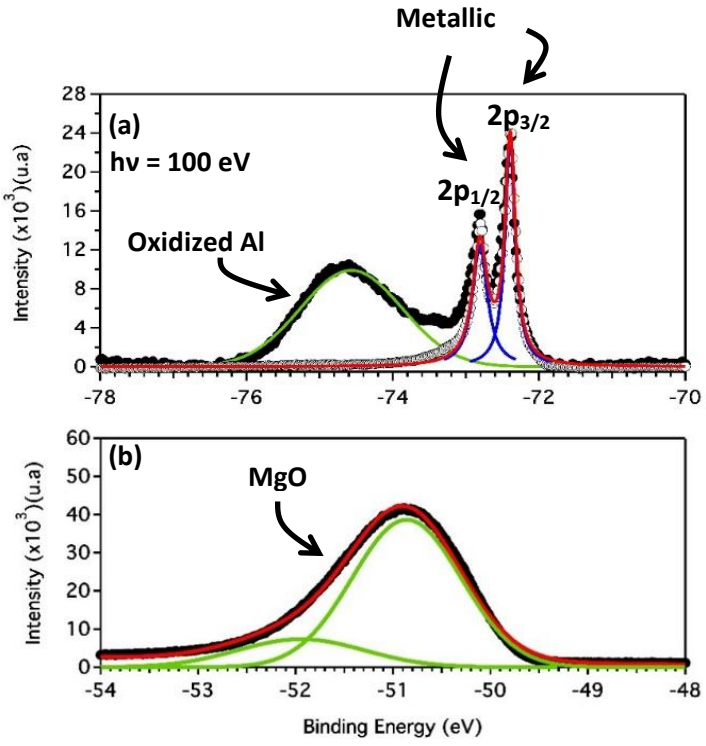

Figure 25: (a) XPS spectra around the Al 2p contributions measured at 4K and with a 100 eV photon energy for a free (open circles) and a MgO-covered (filled circles) SGA surface. The signal for the MgO-covered surface has been multiplied by a factor of 4.8. The metallic contributions can be well fitted by two Lorentzian (blue curves) and the oxide contribution by a Gaussian (green curve). (b) XPS spectrum around the Mg 2p contributions measured at 4K and with a 100 eV photon energy for the MgO-covered SGA surface.

The observation of both metallic and oxidized Al contributions reveals that the probed SGA volume is heterogeneous with oxidized and non-oxidized parts. The oxidized part likely corresponds to the surface (PES experiments performed at the IJL have shown that etching the MgO cover results in the decrease of the oxidized Al 2p contribution at the benefit of the metallic one). However these two parts may also coexist laterally, in the hypothesis of incomplete covering of SGA by MgO.

An inelastic mean free path of approximately 5Å is typically reported for a photon energy of 100eV[40]. The escape depth of electrons in the SGA layer must be however smaller when it is covered by MgO, as in the case of Cr/MgO[41] for example.

The oxidized SGA/MgO interface of course likely perturbs the surface electronic properties of SGA. This point is discussed in the following sub-sections by studying the Sm 4f multiplets and the valence band.

IV.B. Samarium 4f multiplets

Figure 26 presents the XPS spectra around the Sm 4f contributions measured at the Sm^{3+} and Sm^{2+} resonance (140eV and 134eV) and in normal emission for the MgO-covered SGA (black curve) and for the free SGA surface (grey curve). The emitted intensity for the free SGA surface has been normalized with respect to the ^5I peak intensity (divided by a factor 5 and 3 for the Sm^{3+} and Sm^{2+} resonance respectively) to allow an easier comparison. The weights and binding energies for the Sm^{3+} and Sm^{2+} multiplets calculated by F. Gerken *et al.*[25] are recalled by the red and blue bars respectively.

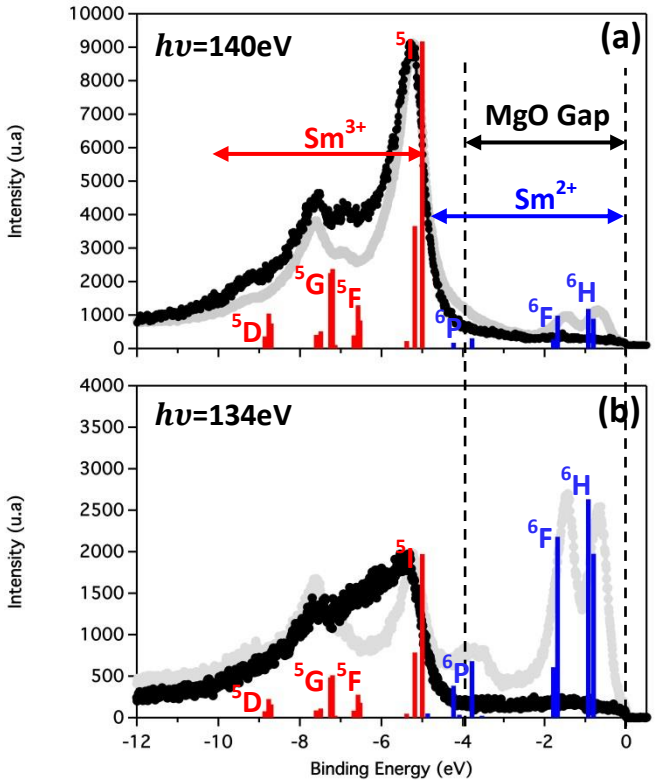

Figure 26: XPS spectra around the Samarium 4f contributions measured in normal emission with a photon energy of 140 eV (a) and 134eV (b) for the MgO-covered (black symbols) and free (grey symbols) SGA surfaces. The emitted intensity for the free SGA surface has been normalized with respect to the ^5I peak intensity (divided by a factor 5 and 3 for the Sm^{3+} and Sm^{2+} resonance respectively). The colored bars denote the calculated weights and binding energies for the trivalent (red) and divalent (blue) Sm contributions [25].

The spectrum collected for the MgO-covered SGA mainly exhibits the trivalent Sm contributions, already described in the part devoted to the free SGA surface. These contributions, attributed to the core of the layer, are largely attenuated by the MgO cover (by a factor of approximately 5), but their positions are identical to those measured for the free SGA surface. This reveals that the SGA part below the surface is not affected, i.e. not oxidized, by MgO. A chemical shift larger than 1 eV for the Sm^{3+} multiplets is indeed expected for oxidized Sm, as reported by G. Dufour *et al.*[42].

One can also notice that the Sm divalent contributions almost totally vanished; they are at least reduced by a much larger factor than the trivalent ones (approximatively by a factor 10). This is related to their surface state characteristics, which make them very sensitive to any cover or adsorbates. This observation would suggest a complete covering of the SGA surface by the MgO deposit.

As expected from the literature on MgO[43], no additional contribution from MgO are observed in this binding energy range. The MgO gap, extending down to 4eV below the Fermi level, especially allows the study of the underneath SGA valence band, provided a reasonably thin MgO cover layer.

IV.C. Valence band analysis

The valence band of the MgO-covered SGA has been analyzed via the measurements of the intensity in normal emission for both p- and s- polarizations (at 4K and for a photon energy of 32 eV). These EDCs are presented in figure 27 (a) and can be compared to those measured for the free SGA surface (figure 14). Figure 27 (b) presents an in-plane cut of the Fermi surface extracted from the ARPES measurements (with p-polarization).

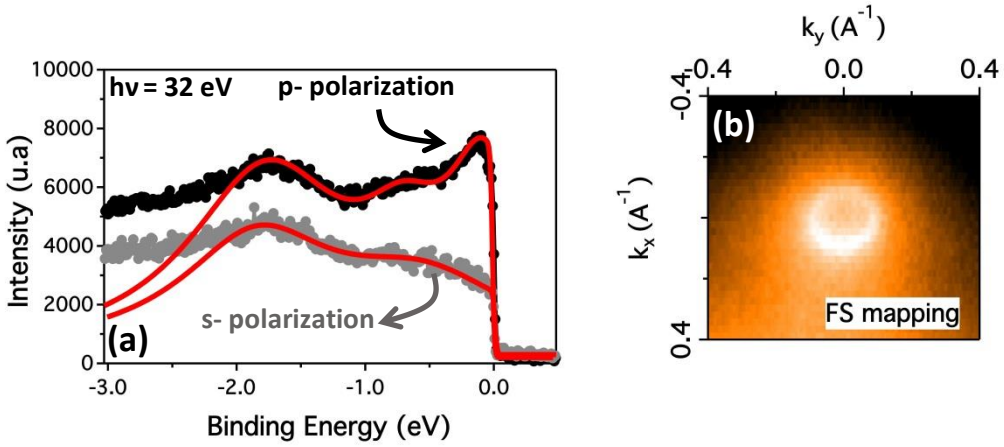

Figure 27: (a) EDCs measured in normal emission for the MgO-covered SGA (T=4K and hν=32eV) with a p-polarized (black circle) and s-polarized (open circle) beam. (b) in-plane cut of the Fermi surface extracted from ARPES measurements.

These results first show some residual broad divalent contributions. Their relative shapes and width, similar to what has been observed for a 'contaminated' surface, suggest that these persisting contributions originate from MgO-covered SGA rather than from uncovered SGA. The strong attenuation and change in their respectively weights would result from the change in the chemical environment at the SGA surface. There is no evidence of uncovered SGA like divalent contributions.

Interestingly, the electron pocket appears to survive at the SGA/MgO interface. It exhibits the same symmetry as for the free SGA surface (disappearance for the s-polarized beam) and a similar ring-shape in the in-plane FS mapping, signature of an isotropic paraboloidal shaped in-plane

dispersion sheet. From the fit of the in-plane energy dispersion curves using $E = \hbar^2 k^2 / 2m^* + E_0$, a ratio m^*/m_{e^-} of 0.32eV and a bottom of the band E_0 = -0.12 eV have been found. These values are very close to those determined for the free SGA surface. No out-of-plane measurements have been performed in this case, and thus no information can be brought about the perpendicular dispersion.

As divalent states that partially subsist below the 2 ML thick MgO cover, this other contribution appears to survive and presents similar characteristics at the SGA surface and at the SGA/MgO interface.

To summarize, the ARPES measurements on MgO-covered SGA have shown that the SGA/MgO interface is affected by the MgO cover with an oxidation localized at the SGA surface. Despite the interface oxidation and the MgO cover, the ARPES measurements have revealed the persistence of the electron pocket close to the Fermi level. This may be surprising for a contribution with surface state characteristics but divalent 4f surface states partially persist as well. Moreover, it is known that surface states as interface resonant states may survive the cover layer, as it is the case in Fe- based magnetic tunnel junctions with MgO barrier[44].

V. Conclusion

A few important points can be underlined to summarize this chapter:

(i) A specific preparation process has been developed to obtain clean and good quality (111)SGA surfaces, suitable for relevant ARPES experiments.

(ii) Photoemission experiments performed for incident photon energies in the [130eV-150eV] range enabled the observation of the multiplets originating from the Sm^{2+} and Sm^{3+} contributions, unambiguously identified by the resonant experiments. The divalent contribution is most likely related to surface atoms, as suggested by previous studies and by their binding energies, consistent with a divalent surface covering a trivalent crystal[10]. This result is in agreement with the stability diagram for $SmAl_2$ reported by C. Laubschat *et al.*[14].

(iii) ARPES experiments have permitted to perform an accurate analysis along various directions of the BZ and to extract relevant informations on the (111)SGA electronic structure. The conjunction of experimental observations and electronic band structure calculations would reveal the occurrence of a surface state with Λ_1 symmetry, appearing as a strongly localized electron pocket around $\bar{\Gamma}$ in the (111)SGA SBZ. This surface state, of 5d character, may be built on a bulk state close to the Fermi level. Other electronic states, with similar symmetry and similar d-character, would rather correspond to bulk bands.

(iv) First SRPES suggest a low temperature positive spin polarization at the Fermi level. These results have to be confirmed and completed, especially to analyse the temperature dependence of the spin polarization and eventually its value at the SGA magnetic compensation.

(v) The study of the MgO-covered SGA system revealed an oxidized SGA/MgO interface but the persistence of the localized electron pocket close to the Fermi level.

References

[**1**] A. Hasegawa *et al.*, J. Phys. F Met. Phys **10**, 847 (1980).
[**2**] A. Hasegawa *et al.*, J. Phys. F Met. Phys **10**, 2207 (1980).
[**3**] H. Gotsis *et al.*, Phys. Rev. B **68**, 224427 (2003).
[**4**] V. Kathirvel *et al.*, Phys. B Condens. Matter **404**, 2130 (2009).
[**5**] D. Paudyal *et al.*, J. Phys. Condens. Matter **25**, 396002 (2013).
[**6**] C. Laubschat *et al.*, Phys. Rev. B **33**, 6675 (1986).
[**7**] M. Matsunami *et al.*, Phys. Rev. B **87**, 165141 (2013).
[**8**] G.K. Wertheim *et al.*, Phys. Rev. Lett. **40**, 813 (1978).
[**9**] B. Johansson, Phys. Rev. B **19**, 6615 (1979).
[**10**] A. Rosengren *et al.*, Phys. Rev. B **26**, 3068 (1982).
[**11**] C.L. Chang *et al.*, Chinese J. Phys. **38**, 146 (2000).
[**12**] F. Strisland *et al.*, Phys. Rev. B **55**, 1391 (1997).
[**13**] Y. Nakayama *et al.*, Surf. Sci. **552**, 53 (2004).
[**14**] C. Laubschat *et al.*, Phys. Rev. B **33**, 6675 (1986).
[**15**] R. Wu *et al.*, Phys. Rev. B **44**, 9400 (2008).
[**16**] D. Li *et al.*, J. Magn. Magn. Mater. **99**, 85 (1991).
[**17**] B. Kim *et al.*, Phys. Rev. Lett. **68**, 1931 (1992).
[**18**] D. Wegner *et al.*, Phys. Rev. B **73**, 115403 (2006).
[**19**] G. Kaindl *et al.*, Phys. Rev. B **51**, 7920 (1995).
[**20**] D. Wegner *et al.*, Phys. Rev. B **79**, 140406(R) (2009).
[**21**] S.C. Wu *et al.*, Phys. Rev. B **44**, 720 (1991).
[**22**] M. Bodenbach *et al.*, Phys. Rev. B **50**, 14446 (1994).
[**23**] A. Avisou *et al.*, J. Magn. Magn. Mater. **316**, 317 (2007).
[**24**] A. Thompson *et al.*, *X-Ray Data Booklet* (Berkeley, 2001).
[**25**] F. Gerken *et al.*, J. Phys. F Met. Phys **13**, 703 (1983).
[**26**] M. Godlewski *et al.*, Synchrot. Radiat. Nat. Sci. 2 (2012).
[**27**] M. Richter *et al.*, Phys. Rev. A **40**, 7007 (1989).
[**28**] S. Lebègue and al, Phys. Rev. B **74**, 045114 (2006).
[**29**] P.A. Dowben *et al.*, J. Phys. Condens. Matter **1**, 6571 (1989).
[**30**] F. Bonell, thesis (2009).
[**31**] J. Hermanson, Solid State Commun. **22**, 9 (1977).
[**32**] W. Shockley, Phys. Rev. **56**, 317 (1939).
[**33**] I. Tamm, Phys. Z. Sov. Union **1**, 732 (1932).
[**34**] G. Nicolay *et al.*, Phys. Rev. B **65**, 033407 (2001).
[**35**] S.D. Kevan *et al.*, Phys. Rev. B **36**, 5809 (1987).
[**36**] F.J. Himpsel *et al.*, Phys. Rev. Lett. **41**, 507 (1978).
[**37**] P.A. Dowben *et al.*, J. Vac. Sci. Technol. A Vacuum, Surfaces, Film. **13**, 1549 (1995).
[**38**] M. Da Silva *et al.*, Appl. Phys. Lett. **98**, 232504 (2011).
[**39**] V. Fournier *et al.*, Surf. Interface Anal. **34**, 494 (2002).
[**40**] S. Tanuma and al, Surf. Interface Anal. **43**, 689 (2011).
[**41**] M.A. Leroy *et al.*, Phys. Rev. B **88**, 205134 (2013).
[**42**] G. Dufour *et al.*, Chem. Phys. Lett. **42**, 433 (1976).
[**43**] Y.N. Xu *et al.*, Phys. Rev. B **43**, 4461 (1991).
[**44**] P.J. Zermatten *et al.*, Phys. Rev. B **78**, 033301 (2008).

Chapter 4
Overview of the magnetic anisotropy in [Co/Pt] multilayers

I. Introduction to the magnetic anisotropy 72
I.A. Origin of magnetic anisotropy in thin magnetic films 72
I.A.1. Shape anisotropy 72
I.A.2. Magneto-crystalline anisotropy 73
I.A.3. Surface or interface anisotropy 73
I.A.4. Magneto-elastic anisotropy 74
I.B. Effect of the roughness and interface alloy 75
I.C. Experimental determination of Keff 75
I.D. Stoner-Wohlfarth model 76
II. Perpendicular Magnetic Anisotropy in [Co/Pt] multilayers 77
II.A. Influence of the crystallographic orientation and preparations 78
II.B. Deviation from the linear behavior 79
III. Conclusion 80
References 81

This chapter is divided in two main sections. The first section defines and identifies the different contributions to the magnetic anisotropy and reminds the magnetization reversal process in magnetic nanostructures. The second section gives an overview of the magnetic properties, especially the perpendicular magnetic anisotropy, in [Co/Pt] multilayers, as they can be found in the literature. It is shown how various parameters such as the deposition technique, the thickness or the nature of the buffer can influence the anisotropy.

I. Introduction to the magnetic anisotropy

Magnetic films with magnetization orientated perpendicular to film plane are currently the best candidates in magnetic storage devices with respect to the challenge to decrease the bit size. This technology is actually used in commercial hard drives with the highest storage densities. This phenomenon of having a preferential magnetization perpendicular to film plane is usually referred to as Perpendicular Magnetic Anisotropy (PMA). Magnetic anisotropy is characterized by an effective anisotropy constant (K_{eff}) that has a volume contribution K_V and a surface or interface contribution K_s. The magnetic anisotropy can be described as:

$$K_{eff} = K_V + \frac{1}{t}K_S \qquad \text{(I-1)}$$

where t is the thickness of the ferromagnetic layer.

In the following, a macrospin model sketched in figure 1 will be used to get an expression of the total magnetic anisotropy $E_A = K_{eff}.V$. The angle θ defines the angle between the external magnetic applied field **H** and the easy magnetization axis whereas φ defines the angle between the magnetization $\boldsymbol{M}$ and the easy magnetization axis. The magnetization $\boldsymbol{M}$ is defined as $M_s\boldsymbol{u}(\boldsymbol{r})$ with $M_s = |\boldsymbol{M}|$ the magnetization at saturation and $\boldsymbol{u}(\boldsymbol{r})$ the unit vector. The easy magnetization axis is defined perpendicular to film plane, along the z axis. This will be the case for our [Co/Pt] multilayers.

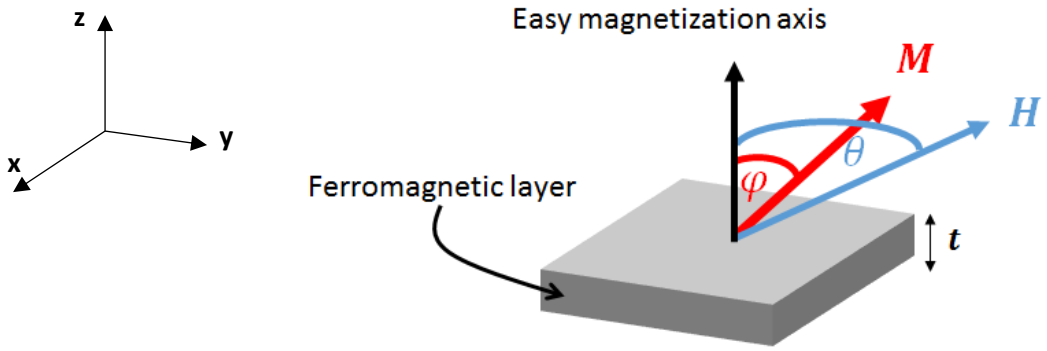

*Figure 1: Sketch of a ferromagnetic layer (FM) with its magnetization **M** making an angle φ with the easy magnetization axis whereas θ defines the angle between the external applied field **H** and the easy magnetization axis. The thickness of the ferromagnetic layer is equal to t.*

I.A. Origin of magnetic anisotropy in thin magnetic films

I.A.1. Shape anisotropy

The phenomena related to the magneto-statics in the matter are completely described by the Maxwell equations. In a magnetic material with homogenous magnetization, the projection of the magnetization at magnetic matter surfaces generates surface magnetization currents. These currents induce a local field, opposite to the magnetization, called demagnetizing field that will be labelled $\boldsymbol{H_d}(\boldsymbol{r})$ in the following. The demagnetizing energy E_d resulting from this field is given by:

$$E_d = -\frac{\mu_0}{2}\iiint \boldsymbol{M}.\boldsymbol{H_d}(\boldsymbol{r})dV = -\frac{\mu_0 M_S}{2}\iiint \boldsymbol{u}.\boldsymbol{H_d}(\boldsymbol{r})dV \quad \textbf{(I-2)}$$

with M_S the saturation magnetization and μ_0 the vacuum permeability.

Generally $\boldsymbol{H_d}(\boldsymbol{r})$ can be determined exactly only for second order geometries e.g. ellipsoidal or spherical geometries. However, making the hypothesis of a uniform magnetization in the considered volume, a demagnetizing tensor $\overline{\overline{N}}$ depending only on the geometry of the system can be calculated. Consequently, the demagnetizing field can be re-written as $\boldsymbol{H_d}(\boldsymbol{r}) = -\overline{\overline{N}}.\boldsymbol{M}$ and the demagnetizing energy as:

$$E_d = \frac{\mu_0 M_S^2}{2}\left(N_{xx}u_x^2 + N_{yy}u_y^2 + N_{zz}u_z^2\right) \times V \quad \textbf{(I-3)}$$

where N_{xx}, N_{yy} and N_{zz} are the diagonal components of the demagnetizing tensor. In the case of thin films with perpendicular anisotropy, it can be shown that $N_{xx} = 0$, $N_{yy} = 0$ and $N_{zz} = 1$ and consequently the demagnetizing energy can be written as:

$$E_d = -\frac{\mu_0 M_S^2}{2} sin^2\varphi \times V \quad \textbf{(I-4)}$$

I.A.2. Magneto-crystalline anisotropy

The microscopic origin of the magneto-crystalline anisotropy is the spin-orbit interaction and the crystal electric field. As a result of the interaction between the electronic orbital and the orbital moment, magnetization is favored along some crystallographic directions. Consequently, in a crystal, some directions are easier to be magnetized than others. These directions are called easy magnetization axis. In practical, the magneto-crystalline energy can be developed in series of cosine and sine of the angle between the magnetization and the crystallographic easy axis. For the case of cubic crystal (e.g. Ni or Fe crystals), the magneto-crystalline energy E_K is given by:

$$E_K = (K_1(\alpha_1^2\alpha_2^2 + \alpha_2^2\alpha_3^2 + \alpha_1^2\alpha_3^2) + K_2(\alpha_1^2\alpha_2^2\alpha_3^2 + \cdots)) \times V \quad \textbf{(I-5)}$$

where K_1 and K_2 are the first and second order anisotropy constants respectively, α_1, α_2, α_3 the direction cosines between the magnetization and the crystallographic axis.

For a uniaxial symmetry (in first approximation for hexagonal, rhombohedral and tetragonal crystals), the magneto-crystalline energy E_K can be expressed as:

$$E_K = [K_1 sin^2(\varphi) + K_2 sin^4(\varphi)] \times V \quad \textbf{(I-6)}$$

Generally, the second order term can be neglected and E_K can be simplified as $E_K = K_1 sin^2(\varphi) \times V$.

I.A.3. Surface or interface anisotropy

Surface or interface anisotropies have been predicted by Néel in 1954[1] and experimentally observed for the first time in 1968 by Gradmann and Muller[2]. It results from the broken symmetry at the interface or at the surface of the magnetic layers. The magnetic surface or interface anisotropy E_{K_S} is given by:

$$E_{K_S} = \left(\frac{K_S^1}{t} + \frac{K_S^2}{t}\right) sin^2(\varphi) \times V \quad \textbf{(I-7)}$$

where K_S^1 and K_S^2 are the anisotropy constants of both surfaces or interfaces, and t is the thickness of the ferromagnetic layer. For perpendicular magnetic anisotropy, K_S is positive.

I.A.4. Magneto-elastic anisotropy

As for the surface or interface anisotropy, the magneto-elastic anisotropy in multilayers appears when the thicknesses of the layers are thin, typically in the nanometer range. Strains can appear in those thin films before relaxation and may thereby alter the direction of the magnetization. These strains are due to the lattice mismatch between the different layers in [FM/NM] multilayers and also deposition techniques. Two regimes can be distinguished, below and above a critical thickness t_c.

Below the critical thickness, the magneto-elastic anisotropy is a volume contribution. The lattice parameters of the different layers are close, at an intermediary value between those of each layer, in order to minimize the energy. This regime, where the strains are constant, is called coherent regime and the magneto-elastic anisotropy energy E_{me} can be expressed as:

$$E_{me} = K_{V,me} sin^2(\varphi) \times V \quad \textbf{(I-8)}$$

where $K_{V,me}$ is the volume magneto-elastic anisotropy constant.

Above the critical thickness, the magneto-elastic anisotropy is a surface contribution. In this case, it becomes more favorable to introduce misfit dislocations and each layer of the multilayer adopts its own lattice parameter and strain relaxation occurs. This regime where the strain is proportional to 1/t is called incoherent regime and its magneto-elastic anisotropy energy E_{me} is given by:

$$E_{me} = \frac{1}{t}\left[K_{S,me} sin^2(\varphi)\right] \times V \quad \textbf{(I-9)}$$

where K_{Sme} is the surface magneto-elastic anisotropy constant and t is the thickness of the ferromagnetic layer.

Finally, the magnetic anisotropy energy E_A can be expressed as the sum of all the anisotropy contributions described previously:

$$E_A = \left[\left(K_1 + K_{V,me} - \frac{\mu_0 M_s^2}{2}\right) + \frac{K_S^1 + K_S^2 + K_{S,me}}{t}\right] sin^2(\varphi) \times V = K_{eff} sin^2(\varphi) \times V \quad \textbf{(I-10)}$$

Here, the effective anisotropy constant K_{eff} is divided in a volume contribution $K_V = K_1 + K_{V,me} - \mu_0 M_s^2/2$ and a surface contribution $K_S = K_S^1 + K_S^2 + K_{S,me}$. This expression is valid only for thin films where the magneto-crystalline anisotropy is uniaxial, the second order term in E_K neglected.

Making the hypothesis that the top and bottom ferromagnetic interfaces contribute equally to the surface anisotropy ($K_S^1 = K_S^2$), K_S can be re-written as $K_S = 2K_S^1 + K_{S,me}$.

I.B. Effect of the roughness and interface alloy

The effect of layer roughness on the perpendicular anisotropy has been studied by P. Bruno in reference[3],[4]. In the model, the roughness amplitude is σ and the lateral correlation length of the roughness is ζ. As a result from this model, a surface contribution to the magnetic anisotropy associated to the roughness has been derived and equals:

$$K_s = \frac{\mu_0 M_S^2}{2}\frac{3}{4}\sigma\left\{1 - f\left[2\pi\left(\frac{\sigma}{\zeta}\right)\right]\right\} \quad \text{(I-11)}$$

where f is a function of σ and ζ. The associated anisotropy energy contribution equals:

$$E_d = \frac{1}{t}\left[\frac{\mu_0 M_S^2}{2}\frac{3}{4}\sigma f\left(\frac{\sigma}{\zeta}\right) sin^2(\varphi)\right] \times V \quad \text{(I-12)}$$

It is a dipolar surface contribution which is always positive and so favors a perpendicular magnetization. The perpendicular anisotropy appears more intense when the roughness is stronger.

P. Bruno also studied the effect of roughness on the magnetic surface anisotropy predicted by Néel. He showed that roughness can reduce this contribution by:

$$\frac{\Delta K_S}{K_S} = -\frac{2\sigma}{\zeta} \quad \text{(I-13)}$$

The formation of interface alloys can contribute to modify and reduce the symmetry breaking at the interface between the layers and as a result to reduce the magnetic anisotropy predicted by Néel.

I.C. Experimental determination of K_{eff}

In practice, the effective anisotropy constant is extracted from M(H) loops by subtracting the areas between the M(H) loop along the hard and easy magnetization axis. This method called "area method" is based on electromagnetic considerations where the difference of areas corresponds to the energy needed to turn the magnetization from the easy magnetization axis to the hard magnetization axis:

$$K_{eff} = \mu_0\left(\int_{\text{Hard axis}} \vec{M}.d\vec{H} - \int_{\text{Easy axis}} \vec{M}.d\vec{H}\right) \quad \text{(I-14)}$$

The "area method" is always valid even for large and multi-domains structures[5] or tilted easy axis of magnetization. This is the case in several of our [Co/Pt] multilayers. Therefore, the determination of K_{eff} is always relevant and rigorous. On this basis, a plot of $K_{eff} \times t$ versus t where t is the thickness of the magnetic layer allows the determination of both the volume and the surface contributions, as it should vary as a linear function of t according to equation I-1. The slope corresponds directly to K_V and the intercept at zero thickness to K_s. Figure 2 gives an example in the case of [Co/Pt] multilayers.

The negative slope of the curve means that K_V is negative and favors an in-plane magnetization whereas the positive value for K_s favors a perpendicular magnetization. So the preferential magnetization direction results from the competition between the volume and surface contributions. Below a critical cobalt thickness (t_c), 1.1 nm in this example, the surface contribution

dominates the volume contribution which leads to a positive value of K_{eff} and a magnetization perpendicular to the film surface whereas for high cobalt thickness (larger than 1.1 nm), the volume contribution is dominant which leads to a negative value of K_{eff} and a in-plane magnetization. More details about the deviation from the linear behavior at low Co thicknesses will be given later.

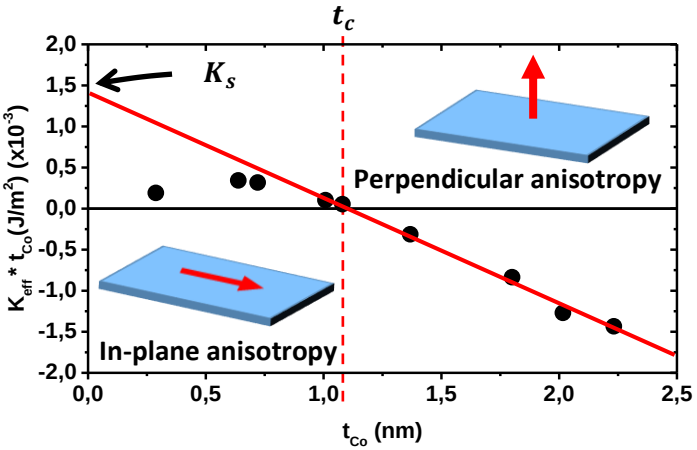

Figure 2: $K_{eff} \times t_{Co}$ versus t_{Co} where t_{Co} is the Cobalt thickness in [Co/Pt] multilayers. When K_{eff} is positive, PMA is obtained (sketch right, top); When K_{eff} is negative, in-plane anisotropy is favored (sketch left, bottom).

I.D. Stoner-Wohlfarth model

The Stoner-Wohlfarth model[6] is the simplest model to explain the magnetic behavior of nanostructures when submitted to a applied magnetic field. The model applies only for single domain nanostructures for which coherent magnetization reversal occurs. Consequently, the magnetization can be described as a macro-spin. The two contributions to the energy of the nanostructure are the Zeeman energy that tends to align the macrospin with the applied field and the anisotropy energy which tends to align the magnetic moments along the easy magnetization axis. As a result, the total energy of the system (E) corresponds to the sum of these two contributions and equals:

$$E = \left[-\mu_0 M_s \times H cos(\theta - \varphi) + K_{eff} sin^2(\varphi)\right] \times V \qquad \textbf{(I-15)}$$

with M_s the saturation magnetization, φ the angle between the magnetization and the easy axis of magnetization, θ the angle between the magnetic field and the easy axis of magnetization (defined in figure 1). The magnetic configuration is given by φ and is obtained by minimizing E with respect to φ, for given values of θ and H, taking only the stable equilibrium states into account. The M(H) loops when the magnetic field is applied along the easy and hard magnetization axis are shown in figure 3 (Right). When the magnetic field is applied along the easy magnetization axis (Θ = 0°), the magnetic response is a square and hysteretic loop. The field needed to get a zero magnetization along the applied field is called the coercive field and is labelled H_C. The remanent magnetization, i.e. the magnetization at zero applied field, is equal to M_S, the saturated magnetization. When the magnetic field is applied along the hard magnetization axis (Θ = 90°), the magnetic response is non-hysteretic with zero magnetization remanence. The magnetic field necessary to saturate the ferromagnetic material is called the anisotropy field, H_{Keff}, and is equal to:

$$H_{Keff} = \frac{2K_{eff}}{\mu_0 M_s} \qquad \textbf{(I-16)}$$

In the case of the Stoner-Wohlfarth model, the coercive and effective anisotropy fields are equal. In practice, this happens only for small nanostructures with nanometric lateral sizes. Usually, the coercive field is lower than the effective anisotropy field due to some defects in the sample which favor the nucleation of domains, their propagation leading to the magnetization switching. However, a good estimate of the effective anisotropy is obtained from H_{Keff}. Indeed, along the hard axis, the magnetization often rotates to saturation and is therefore well reproduced by the Stoner-Wohlfarth model. Finally, in the Stoner-Wohlfarth model, the H_C varies with Θ. An analytical expression can be derived and is given by:

$$H_C = \frac{2K_{eff}}{\mu_0 M_S} \frac{1}{\left(sin^{2/3}(\theta)+cos^{2/3}(\theta)\right)^{3/2}} \quad \text{(I-17)}$$

This is the well-known Stoner-Wohlfarth asteroid (figure 3 left).

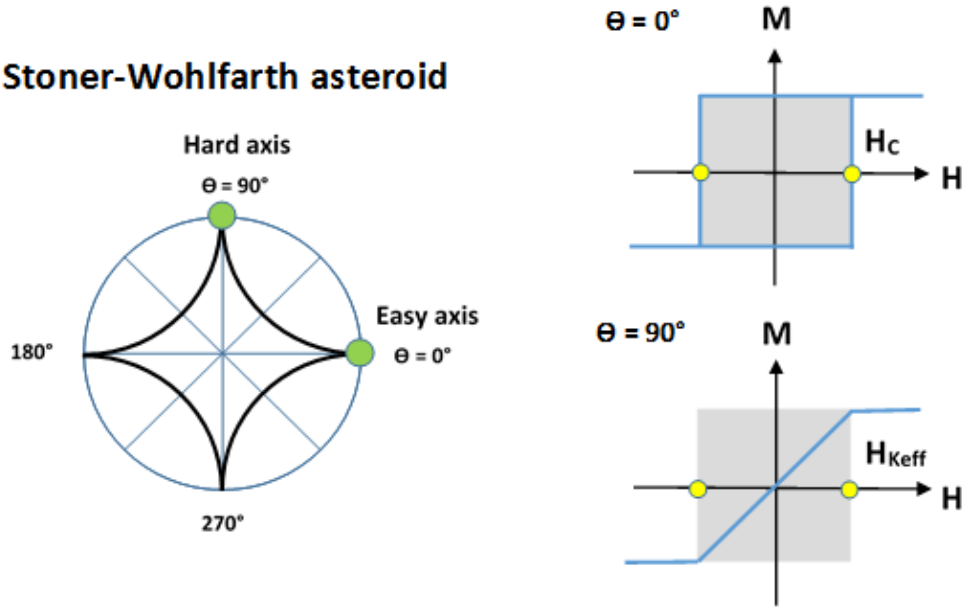

Figure 3: Left: Stoner-Wohlfarth asteroid. Right: M(H) loops for particular Θ angles of the Stoner-Wohlfarth asteroid.

II. Perpendicular Magnetic Anisotropy in [Co/Pt] multilayers

Multilayers with perpendicular anisotropy have several key advantages over multilayers with in-plane magnetization in spintronics and memory applications: higher thermal stability and smaller domain wall widths[7], lower threshold current for spin-transfer switching[7] and for current-induced domain wall motion[8]. According to the previous section on the magnetic anisotropy, the perpendicular anisotropy appears when the surface contributions overcome the volume contributions which are generally dominated by the shape anisotropy. However the origin of the surface contribution in multilayers remains an open question and depends on the control of the interface at the atomic level. It is generally attributed either to the surface anisotropy predicted by Néel or to the magneto-elastic strain[3],[9]. Since the discovery of the PMA in [Co/Pt] multilayers by P.F. Garcia *et al.*[10], it is known that the PMA is strongly related to the surface morphology of the [Co/Pt] multilayers[11],[12]. This can be understood from Bruno's models described in the previous section where it is reported that the roughness and inter-mixing can play a crucial role on the surface

anisotropy. Consequently, the surface anisotropy strongly depends on the preparation conditions (e.g. nature of the substrate, buffer layer, sputtering pressure, and thicknesses of the Co and Pt layers) and the growth techniques used (e.g. sputtering, evaporation, Molecular Beam Epitaxy). Despite the various parameters which can be tuned, some general trends for the PMA dependence can be extracted from the literature and are reported below.

II.A. Influence of the crystallographic orientation and preparations

A very complete review paper published by M.T Johnson *et al.*[5] on the perpendicular anisotropy in various [Co/X] multilayers with X = Pt, Pd, Au, Cu summarizes the different trends of the PMA dependences on the crystallographic orientation and the preparation conditions. This paper has been published in 1996 but remains an interesting reference to introduce and give an overview of the main parameters which drive the PMA in [Co/Pt] multilayers. Consequently, unless otherwise indicated, the different graphics and tables shown in this section are extracted from reference[5].

The dependence of the effective anisotropy constants times Co thickness versus Co thickness are reported in figure 4 for different crystallographic orientations and growth technique, i.e. Molecular Beam Epitaxy (MBE) or Sputtering (S). These permit to extract both volume and surface anisotropy constants.

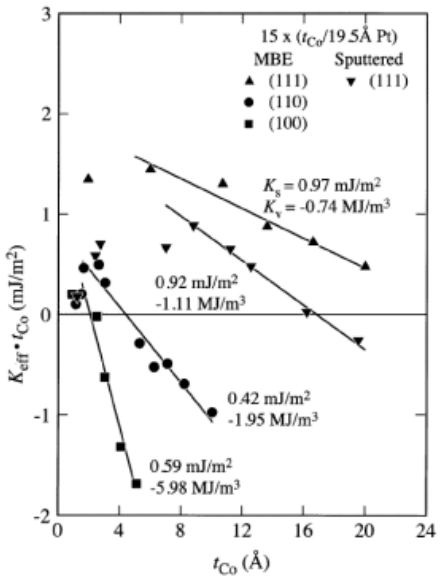

Figure 4: Dependence of the volume (K_V) and surface (K_S) anisotropy contributions in epitaxial and sputtered [Co/Pt] multilayers for different crystallographic orientations.

In figure 4, the negative slope indicates a negative volume anisotropy K_V driven by the shape anisotropy $(-\mu_0 M_S^2/2)$ and favoring an in-plane magnetization; the value at zero Co thickness reveals a positive interface anisotropy K_S favoring a perpendicular magnetization. All the [Co/Pt] multilayers experience a perpendicular to in-plane magnetization transition when the Co thickness increases. As described in section I.C, below a critical cobalt thickness (larger than 2.4 nm for (111) epitaxial [Co/Pt] multilayers), the surface contribution dominates the volume contribution and the magnetization is perpendicular to the multilayers plane (out-of-plane configuration) whereas for thicker cobalt layers, the volume contribution is dominant and the magnetization lies in the multilayer plane (in-plane configuration).

Whatever the growth technique used, the larger PMA is observed for the (111) crystallographic orientation where K_S is maximum and K_V minimum. The largest negative K_V value

(weak PMA) is observed when the [Co/Pt] multilayers are grown along the (100) direction in line with the large strains in these layers and the positive magnetostriction[5].

A summary of the values of K_V and K_S reported in literature (different substrates or buffers, deposition techniques) is given in Table 1[4].

Substrate buffer	Composition/ interface	K_s (mJ m^{-2})	K_v (MJ m^{-3})	Deposition technique
GaAs	$(Co/Pt(100))_n$	0.59	−5.98	MBE
Glass, Quartz, Si/Pt	$(Co/Pt(100))_n$	0.31	−1.00	E
GaAs	$(Co/Pt(110))_n$	0.42	−1.95	MBE
Glass, Quartz, Si/Pt	$(Co/Pt(110))_n$	0.37	−0.91	E
Glass, Quartz, Si/Pt	$(Co/Pt(111))_n$	0.76	−0.92	E
GaAs(111)	$(Co/Pt(111))_n$	0.82		MBE
GaAs	$(Co/Pt(100))_n$	0.20	−0.73	E
Glass,Si	$(Co/Pt(111))_n$	0.42	−0.68	E
Glass/Pt	$(Co/Pt(111))_n$	0.50, 0.58	−1.0, −0.7	E
Si	$(Co/Pt(111))_n$	0.27	−0.7	E
GaAs	$(Co/Pt(111))_n$	0.97	−0.74	MBE
	$(Co/Pt(111))_n$	0.92	−1.11	S
Pt(111)	Co/Pt	1.15	−0.77	MBE

Table 1: *K_V and K_S constants for different substrate natures and deposition techniques (MBE for Molecular Beam Epitaxy, E for Evaporation and S for Sputtering).*

The enhancement of the PMA for the (111) texture is confirmed whatever the growth technique, the substrate or the buffer. By changing the nature and the pressure of the gas during the sputtering of the [Co/Pt] multilayers, several studies have shown the close correlation between the (111) texture and the enhancement of the PMA[11–13]. The paper by C.-J Lin *et al.*[14] where the largest coercive field has been reported for multilayers with the best (111) texture has confirmed the crucial role of the (111) texture in the enhancement of the PMA. Moreover, as reported by Table 1 and in several papers[14-15], a (111) Pt buffer layer increases drastically the PMA by favoring the (111) texture. Consequently the [Co/Pt] multilayers are generally grown on thick (20-200 Å)[16-19] (111) textured Pt under-layer. However, a stronger PMA for [Co/Pt] multilayers growth on TaOx buffer than on Pt buffer with comparable crystallographic properties has been recently reported by S. Emori *et al.*[20].

II.B. Deviation from the linear behavior

In figure 4, a small deviation from the linear behavior of $K_{eff} \times t_{Co}$ can be observed at low Co thickness. Several other studies[14,21,22] have reported this deviation which can be better observed in figure 5 for [Co(d)/Pt(6.5nm)] sputtered sandwiches, extracted from the paper by M. Kisielewski *et al.*[22]

As mentioned in the previous section, several features such as the roughness, the intermixing and the magneto-elastic effects can explain this deviation at low Co thickness. With a mismatch of 10% between the Co and Pt, most authors have excluded a coherent growth at low Co thickness and attribute the decrease of PMA to a reduction of the surface anisotropy predicted by Néel, consistently with the second part of P. Bruno's model. This hypothesis has been experimentally confirmed by using different techniques. For example by studying the surface morphology of [Co/Pt] multilayers via atomic force microscopy experiments, J-H Kim *et al.*[13] have correlated the decrease

of K_S to an enhancement of the roughness induced by changing the Ar pressure during the sputtering of the [Co/Pt] multilayers. S. Hashimoto *et al*.[23] linked the decrease of effective anisotropy in [Co/Pt] and [Co/Pd] systems and the reduction of the X-ray diffraction intensity to the formation of an interface Co_xPt_y alloy. Complementary work on the magnetic anisotropy dependence on the structural properties of $Co_{50}Pt_{50}$ alloy on MgO buffer[24] has confirmed the decrease of K_u with the decrease of the order in the CoPt alloy.

Finally, it has been recently reported by S. Bandiera[25] that the insertion of a Cu layer in Pt/Co/Pt trilayers permits to limit the mixing between the Co and Pt and permits to restore partially the effective anisotropy.

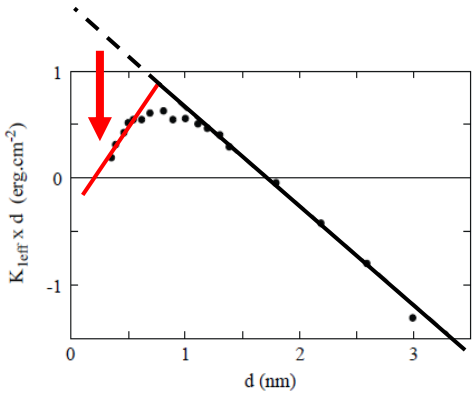

Figure 5: Variation of $K_{eff} \times d$ as a function of the Co thickness d in $Pt_{3.4nm}/Co(d)/Pt_{6.5nm}$ sandwiches.

III. Conclusion

To summarize, the first section of this chapter gives an overview of the origins of the magnetic anisotropies in thin films (i.e. shape, magneto-crystalline, surface and magneto-elastic anisotropy) and their main features. The Stoner-Wohlfarth model that allows describing the magnetization reversal in a nanostructure with uniform magnetization has been exposed. Two particular configurations have been identified, whether the applied field is along either the easy or the hard magnetization axis.

From the rich literature on the [Co/Pt] multilayers, it appears that the PMA is strongly dependent on the crystallographic orientation, the growth technique and the nature of the buffer layer. The strongest PMA is reported for the (111) textured [Co/Pt] multilayers grown on a (111) textured Pt buffer. Moreover, a deviation from the linear behavior for the $K_{eff} \times t_{Co}$ dependence as a function of the Co thickness is observed for small Co thicknesses. It likely results from the decrease of the Néel surface anisotropy which favors the PMA in [Co/Pt] multilayers. This decrease has been experimentally explained by the increase of roughness or inter-mixing with the possible formation of $Co_{1-x}Pt_x$ interface alloy when the Co thickness decreases. These would reduce the broken symmetry at the interfaces, as theoretically suggested by P. Bruno.

References

[**1**] L. Néel, J. Phys.Rad **15**, 225 (1954).
[**2**] U. Gradmann *et al.*, Phys. Status Solidi **27**, 313 (1968).
[**3**] P. Bruno *et al.*, J. Appl. Phys. **64**, 5736 (1988).
[**4**] P. Bruno, J. Appl. Phys. **64**, 3153 (1988).
[**5**] M.T. Johnson *et al.*, Reports Prog. Phys. **59**, 1409 (1996).
[**6**] E.C. Stoner *et al.*, Philos. Transations R. Soc. London A **240**, 599 (1948).
[**7**] S. Mangin *et al.*, Appl. Phys. Lett. **94**, 012502 (2009).
[**8**] S. Fukami *et al.*, J. Appl. Phys. **108**, 113914 (2010).
[**9**] B. Zhang *et al.*, J. Appl. Phys. **73**, 6198 (1993).
[**10**] P.F. Carcia *et al*, J. Appl. Phys. **63**, 5066 (1988).
[**11**] G.A. Bertero *et al.*, J. Magn. Magn. Mater. **134**, 173 (1994).
[**12**] P.F. Carcia *et al.*, J. Magn. Magn. Mater. **121**, 452 (1993).
[**13**] J. Kim *et al.*, J. Appl. Phys. **80**, 3121 (1996).
[**14**] C.-J. Lin *et al.*, J. Magn. Magn. Mater. **93**, 194 (1991).
[**15**] M. Hashimoto *et al.*, J. Magn. Magn. Mater. **88**, 211 (1990).
[**16**] Z. Liu *et al.*, Phys. Rev. B **79**, 024427 (2009).
[**17**] R. Shan *et al.*, J. Appl. Phys. **99**, 063907 (2006).
[**18**] Y. Nie *et al.*, Trans. Nonferrous Met. Soc. China **20**, 819 (2010).
[**19**] N. Nakajima *et al.*, Phys. Rev. Lett. **81**, 5229 (1998).
[**20**] S. Emori *et al.*, J. Appl. Phys. **110**, 033919 (2011).
[**21**] H. Stillrich *et al.*, J. Magn. Magn. Mater. **322**, 1353 (2010).
[**22**] M. Kisielewski *et al.*, J. Magn. Magn. Mater. **260**, 231 (2003).
[**23**] S. Hashimoto *et al.*, J. Appl. Phys. **66**, 4909 (1989).
[**24**] H. Sato *et al.*, J. Appl. Phys. **103**, 07E114 (2008).
[**25**] S. Bandiera, thesis (2011).

Chapter 5
Magnetic and structural properties in [Co/Pt] multilayers

I. Description of the [Co/Pt] multilayers 84
II. Structural properties of the [Co/Pt] multilayers 85
II.A. Generalities on X-ray diffraction 85
II.B. Experimental setup 86
II.C. Growth direction in the sputtered [Co/Pt] multilayers 88
II.D. Reflectometry analysis on [Co/Pt] multilayers 89
II.D.1. Co and Pt thicknesses 92
II.D.2. Co and Pt roughnesses 93
III. Magnetic properties in the [Co/Pt] multilayers 93
III.A. Experimental setup 93
III.B. Experimental results 94
III.B.1 Effective anisotropy 97
III.B.2. Saturation magnetization 99
III.B.3. Influence of temperature 102
IV. Conclusion 103
References 105

The knowledge of the magnetic properties in [Co/Pt] multilayers is a crucial step for the development of [Co/Pt]-based magnetic tunnel junctions. As detailed in the previous chapter, several parameters such as the crystallographic orientation or the buffer nature must be considered in order to achieve a strong perpendicular anisotropy in [Co/Pt] multilayers. In this chapter, we report on the study of various types of [Co/Pt] multilayers, where we focused on the influence of two main parameters: the Pt thickness and the nature of the buffer layer. This latter is all the more important in MTJs based on two [Co/Pt] electrodes since the top one has to be grown on the insulating barrier.

After the description of the investigated systems, the results are presented and discussed in two main sections. The first one is devoted to the structural investigation of the [Co/Pt] multilayers using high angles and low angles X-ray diffraction, to determine the growth direction, the layers' thicknesses and roughnesses. The second section is devoted to the magnetic properties of [Co/Pt] multilayers, especially the effective anisotropy and saturation magnetization, the variations of which have been related to the structural characteristics. The effect of temperature has been explored for a few specific samples to extract accurate and relevant parameters for low temperature micromagnetic simulations (next chapter).

I. Description of the [Co/Pt] multilayers

The goal of this study is to characterize the structural and magnetic properties of [Co/Pt] multilayers before their integration in magnetic tunnel junctions. A magnetic tunnel junction is defined by two magnetic electrodes (top and bottom electrodes) separated by an insulating barrier (a thin MgO or Al_2O_3 layer in our case). As reported in the previous chapter, the PMA of [Co/Pt] multilayers strongly depends on the buffer nature. Consequently, in order to accurately characterize the [Co/Pt] multilayers that will be used as the top and bottom electrodes in the magnetic tunnel junctions, several sets of [Co/Pt] multilayers have been studied, with various buffer and capping layers. The different sets are summarized in the Table 1.

	Buffer	[Co/Pt] stacking	Capping
Set A	**Ta/Pt**	**$[Co/Pt]_3/Co$**	**MgO**
Set B	**Ta/Pt/MgO**	**$[Co/Pt]_4$**	**Pt**
Set C	**Ta/Pt**	**$[Co/Pt]_3/Co$**	**Al_2O_3**
Set D	**$Ta/Pt/Al_2O_3$**	**$[Co/Pt]_4$**	**Pt**
Set E	**Ta/Pt**	**$[Co/Pt]_4$**	**Pt**
XRD sample	**Ta/MgO**	**$[Co/Pt]_{50}$**	**No capping**

Table 1: Description of the different [Co/Pt] multilayers investigated in this study.

The [Co/Pt] multilayers have been sputtered on a Silicon substrate (Si) covered by 100 nm of an amorphous Silicon oxide (SiO). In order to avoid the Si diffusion into the [Co/Pt] stacking and to favor the good adhesion of the 5 nm-thick Pt layer, a 5 nm-thick Tantalum layer has been first deposited. The nominal thickness of MgO or Al_2O_3 is equal to 2.5 nm and typically corresponds to the [2-3 nm] thickness range used for the insulating barrier in magnetic tunnel junctions.

Sets A and C, where the [Co/Pt] stackings are respectively covered with MgO and Al_2O_3, are similar to bottom electrodes ; Sets B and D, where the [Co/Pt] stackings are respectively grown on MgO and Al_2O_3, are similar to top electrodes. Sets A and B would thus constitute the bottom and top electrodes in MTJs with MgO barrier, whereas sets C and D would constitute bottom and top electrodes in MTJs with Al_2O_3 barrier. The sets A and D are all constituted of 4 Cobalt layers (the first or last one being in direct contact with the oxide layer) and 7 Co/Pt interfaces. Within each set, five samples with different Pt thicknesses have been sputtered in order to analyze their properties as a function of the non-magnetic spacer (see Table 2).

	Pt nominal thickness (nm)	Co nominal thickness (nm)
Set A,B,C and D	**0.90/1.13/1.35/1.58/1.80**	**0.58**
Set E	**1.80**	**0.29/0.72/1.01/1.10/1.37/1.80/2.02/2.23**
XRD sample	**0.97**	**0.50**

Table 2: Nominal thicknesses for the Pt and Co layers in the different [Co/Pt] multilayers investigated in this study.

According to the PMA dependence on the Pt and Co thicknesses reported in the literature[1],[2], a Pt thickness larger than 0.9 nm and a Co thickness in the [0.5 nm -0.6 nm] range should lead to a strong PMA. Since the PMA is very sensitive to various preparation/structural parameters, these trends must be however confirmed in our [Co/Pt] multilayers.

The choice of the number of Co layers (n = 4) has been motivated by two reasons:

- increasing the number of Co layers yields an increase of the PMA but also to a less abrupt magnetization reversal with the nucleation of domains. These features have been illustrated by C.J-Lin *et al.*[1] in [$Co_{0.3nm}/Pt_{1.0nm}$] multilayers where the number of Co layers have been increased from 5 to 80. So n = 4 should permit to stay in a regime where the [Co/Pt] reversal is mono-domain[1].

- n = 4 corresponds to the [Co/Pt] stacking used in perpendicular MTJs where a TMR of 8% has been reported by C. Ducruet *et al*[3]. This value is larger than the TMR of 6% observed in $L1_0$-ordered CoPt alloy based magnetic tunnel junctions[4].

The small thicknesses of the layers constituting the [Co/Pt] stackings and the presence of a thick Pt buffer make the analysis of the texture of sputtered [Co/Pt] multilayers difficult. The "XRD sample", with a larger number of [Co/Pt] repeats and without any Pt buffer/capping layer, has been fabricated to enable the characterization of the crystallographic orientation in [Co/Pt] multilayers. In this case, the $[Co/Pt]_{50}$ stacking has been sputtered on a Ta/MgO buffer.

The set E has been fabricated for the specific analysis of effective anisotropy versus the Co thickness, in comparison with previously published results (chapter 4).

II. Structural properties of the [Co/Pt] multilayers

II.A. Generalities on X-ray diffraction

The X-Ray Diffraction technique (XRD) is very commonly used for the structural analysis of thin films. It is a non-destructive approach that can easily bring valuable information: at large angles and in specular geometry, one can determine the average crystallographic orientation, the dispersion in this orientation, the inter-reticular distance between atomic planes parallel to the sample surface, the coherence length in the direction perpendicular to these atomic planes; at low angles, the so-called X-ray reflectometry gives access to the thicknesses, roughness and density of the different layers constituting the multilayer stack. The principle of XRD at large and low angles is sketched in figure 1 (a) and (b).

When incoming X-rays with a wavelength λ are scattered by the crystal lattice (*hkl* atomic planes parallel to the sample surface, as sketched in figure 1 (a)) constructive interferences occur when the Bragg's law given by $n\lambda = 2d_{hkl}\sin(\theta)$ is satisfied. d_{hkl} is the interplanar distance, n is an integer and θ is the angle between the incoming X-ray beam and the atomic planes.

In XRD experiments at high angles and in specular geometry, the wavelength λ is known and the sample rotates by Θ while the detector rotates by 2Θ. The intensity is collected as a function of the angle Θ, and Bragg reflections are thus observed when the conditions of diffraction are satisfied.

Contrary to the large angle XRD which occurs throughout the bulk and gives intensity for specific geometrical conditions, X-ray reflectometry (figure 1(b)) is based on the reflection of the incoming X-ray beam at the surface/interfaces and gives intensity at any angles in the low angle range generally up to approximately <5°. The reflection at the surface or interfaces correspond to different electron densities, i.e. to different refractive indexes (n), in the different layers which constitute the sample. Below a critical angle θ_C, related to the density of the material, the total external reflection occurs. Above θ_C, one part of the incoming intensity is reflected and one part is transmitted through the material.

In the very simplified picture where the system consists of a single layer, interference fringes (Kissing fringes) are observed with a period related to the total layer thickness and the decrease in intensity when increasing the angle θ is related to the layer roughness. However, a proper analysis of X-ray reflectometry results requires the adjustment of experimental data using the Fresnel or Parratt formalism or the matrix formalism as described in A. Gibaud book[5].

The X-ray reflectometry is thus a powerful tool to characterize a layered system, in particular to determine the layer thicknesses and to analyze surface/interface properties. It can especially bring information on the sharp, or not sharp, character of interfaces. However, since the reflectivity signal only depends on the electron density profile in the system, XRD at low angles and in specular geometry doesn't permit to distinguish between a rough and an inter-mixed interface with the possible formation of an alloy between neighboring layers. More details about the XRD at low angles can be found in the book of A. Gibaud[5].

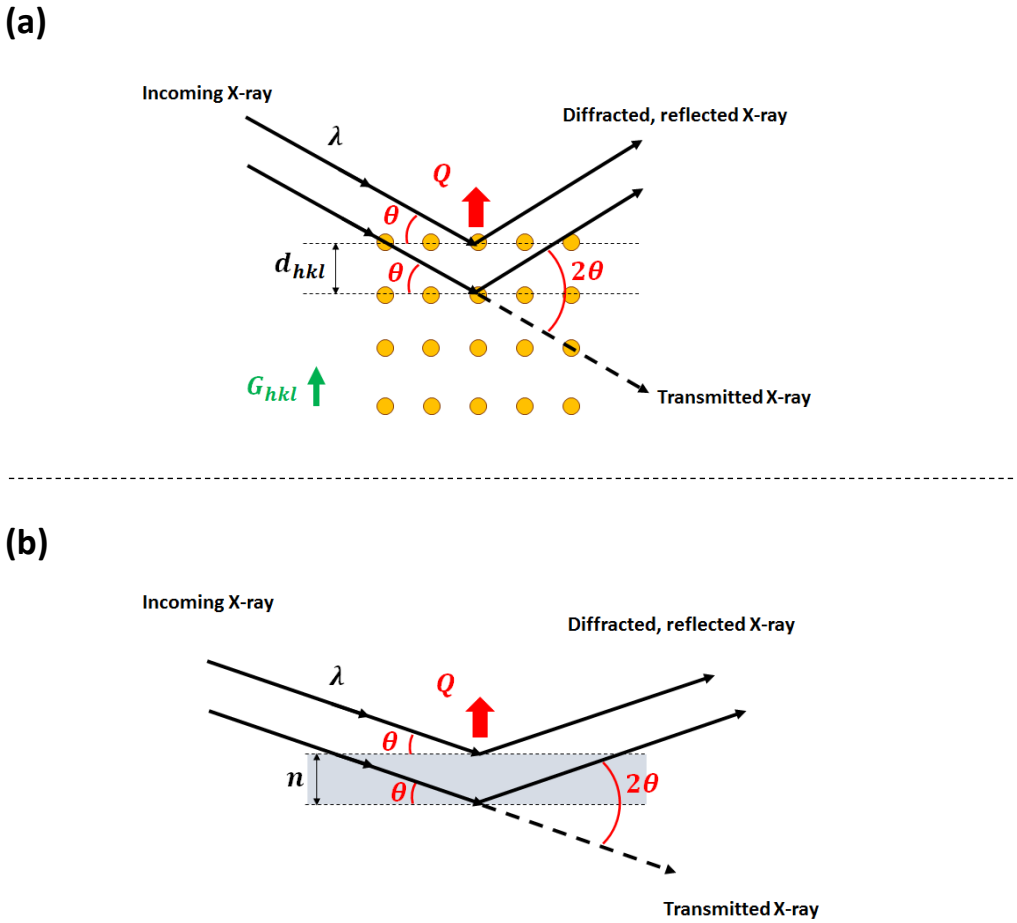

Figure 1: Sketches of the X-ray diffraction principles at large (a) and low (b) angles when incoming X-rays interact with the matter.

II.B. Experimental setup

The XRD experiments on [Co/Pt] multilayers have been performed in the Institute Jean Lamour using a PanAnalytical X'Pert Pro diffractometer (figure 2) and working with the wavelength λ = 1.54056 Å (electronic transition $K_{\alpha 1}$ of the copper anode). Thanks to the use of dedicated primary and secondary optical blocks (respectively mounted before the sample and before the detector), high resolution and high intensity XRD can be performed in the low and large angles ranges.

The primary optical block is composed of attenuator foils and slits. The multi-layer crystal converts a divergent beam projected by a line focus of an X-ray tube into a quasi-monochromatic and quasi-parallel beam of high intensity. The secondary optical block is composed of a Parallel Plate Collimator (PPC), a set of parallel plates configured to limit the angular divergence of the diffracted X-ray beam. Moreover, a PIXcel detector with extremely high dynamic range and low noise is used.

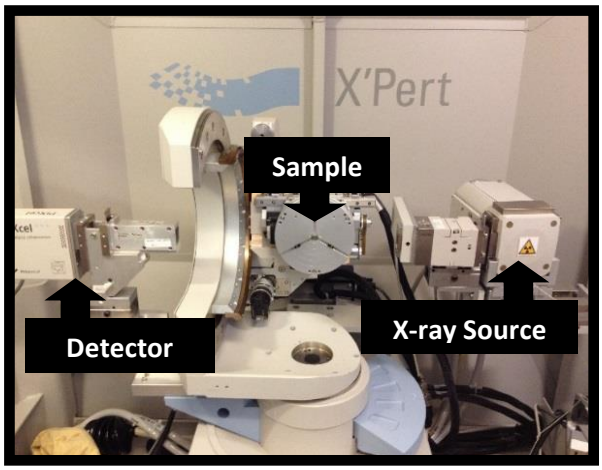

Figure 2: Picture of the PanAnalytical X'Pert Pro diffractometer used for the structural characterization of the [Co/Pt] multilayers.

The adjustments of the low angles XRD spectra have been made using the commercial X'pert Reflectivity software which uses the Parratt formalism[6]. Starting from the various initial parameters, i.e. thicknesses, roughnesses and densities of the layers, a segmented adjustment is realized: it consists in adjusting first the part of the curve close to the critical angle θ_C, and then in progressively adjusting the curve over the full angle range. The strategy used for the segmented adjustment was the following: (i) to determine the thicknesses of the layers by adjusting roughly the position of the Kissing fringes to the experimental reflected curve in keeping the densities fixed at their bulk values and the roughnesses at an arbitrary value (0.2 nm). (ii) When the thicknesses were more or less determined, the density and roughness parameters have been allowed to vary over a specific range. The upper boundaries for the density (resp. roughness) were the bulk values (resp. the thickness of the different layers). Except in some specific cases that will be mentioned in the manuscript, the different [Co/Pt] bilayers forming the stacking have been considered identical: the Co (resp. Pt) layers all exhibit the same density, thickness and roughness.

The roughness, defined by the deviation from the ideal sharp interface, is given by the parameter σ_j in figure 3: the probability to find the interface at $z_j+z(x,y)$ is given by the Gaussian distribution $P_j(z)$ with variance σ_j which characterizes the "degree of roughness", i.e. the larger σ_j the rougher the surface[5].

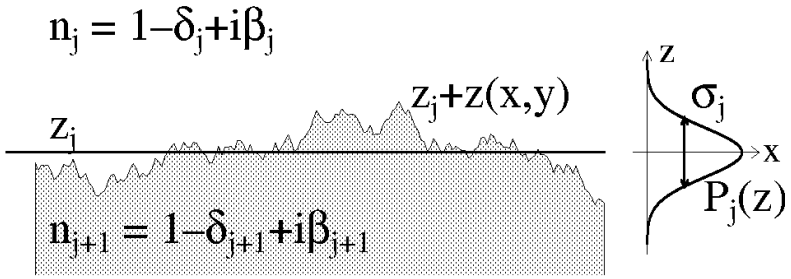

Figure 3: Interface with mean z-coordinate z_j and fluctuation z(x,y). n_j and n_{j+1} are the refractive indexes of the j and j+1 layers [7].

II.C. Growth direction in the sputtered [Co/Pt] multilayers

The crystallographic orientation of the [Co/Pt] multilayers has been studied using the "XRD sample" described in the first section (Tables 1 and 2). The XRD pattern recorded at high angles is presented in figure 4. The intensity is plotted in logarithm scale as a function of the scattering vector amplitude $\|\boldsymbol{Q}\|$ which is related to the angle Θ by:

$$\|\boldsymbol{Q}\| = \frac{4\pi}{\lambda}\sin(\theta) \qquad \text{(II-1)}$$

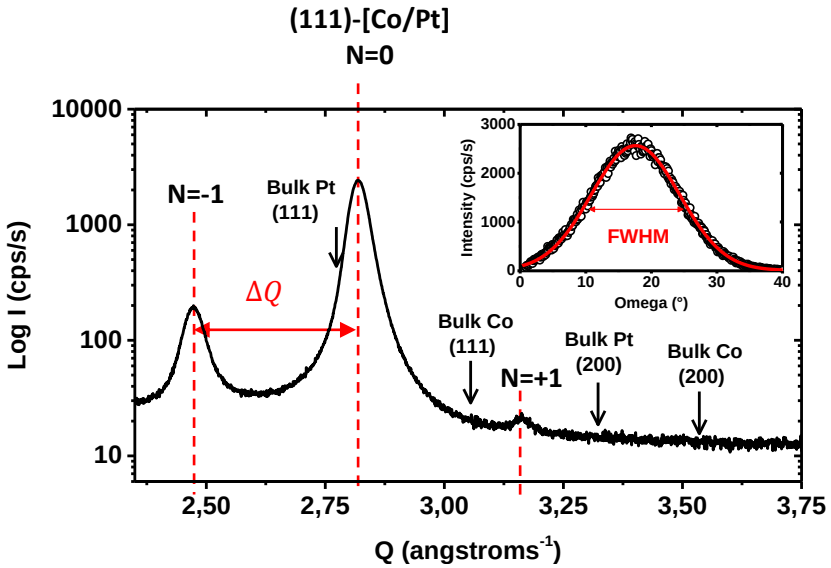

Figure 4: X-ray pattern collected at high angles for the "XRD sample". The positions of the N = -1, 0 and 1 Bragg peaks for the periodic $[Co_{0.97nm}/Pt_{0.5nm}]_{50}$ stacking are shown by the red vertical dash lines. Inset is the rocking curve measured across the (111)-[Co/Pt] multilayers Bragg peak (open circles) with a Gaussian adjustment (red line).

This pattern shows first the occurrence of an (111) average Bragg peak, located between the (111) reflections expected for bulk Co and Pt, and the absence of other Bragg reflections. The system is thus (111)-textured. The Full Width at High Maximum (FWHM) of the rocking curve measured across this peak (inset figure 4) reaches 13.5°, revealing a relatively large mosaicity, i.e. dispersion of the [111] direction around the growth axis. A FWHM of 9° has been reported in [Co/Pt] multilayers by D. Weller *et al.*[8].

The (111) Bragg peak is observed for a scattering vector $\|\boldsymbol{Q}_{exp}\| = 2.81$ Å^{-1}. This value can be compared with the calculated scattering vector obtained from the nominal Co and Pt thicknesses and the (111) interplanar spacings in bulk elements: $\|\boldsymbol{Q}_{cal}\| = 2.87$ Å^{-1}. This value is larger than the experimental one, which is likely related to imperfect calibration for the Co and Pt thickness and/or strains in the Co and Pt thin layers.

The (111) main Bragg peak (N = 0) for the [Co/Pt] multilayers is surrounded by N = -1 and N= +1 satellites due to the periodicity of the structure[9]. The ΔQ spacing between the main Bragg peak and its satellites permits to determine the [Co/Pt] bilayer thickness equal to 1.8 nm, i.e. approximately 22% larger than the 1.47 nm expected from the nominal Co and Pt thicknesses.

Figure 5 presents the X-ray pattern collected at low angles for the $[Co/Pt]_{50}$ multilayer (XRD sample) with the fit obtained using the X'Pert Reflectivity software and the fitting procedure described in the previous section.

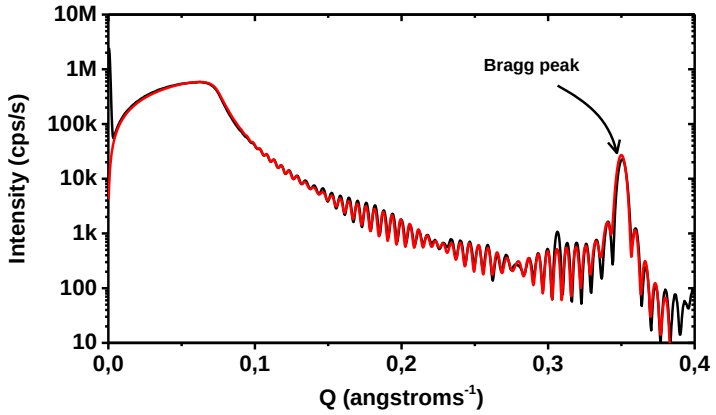

Figure 5: X-ray pattern collected at low angles for the "XRD sample" (black curve) and its fit with the X'Pert reflectivity software (red curve).

The position of the low angle Bragg peak $\|\boldsymbol{Q}\| = 0.35$ Å^{-1} reveals a [Co/Pt] bilayer thickness of 1.8 nm, in agreement with the value determined at large angles. The curve exhibits a small wavelength modulation related to the total thickness of the [Co/Pt] stacking. The periodicity of the so-called Kissing fringes reveals a [Co/Pt] total thickness of 94.6 nm (average on 10 modulations), i.e. approximately 5% larger than the total thickness expected from the 50 repetitions of 1.8 nm thick bilayers. The deviation in the total thickness can be due to some deviation in the Co and Pt flux during the [Co/Pt] multilayer sputtering.

In order to obtain a good agreement between the experimental reflectivity curve and the fit, the first [Co/Pt] bilayer had to be separated from the remaining $[Co/Pt]_{49}$ stacking, based on the assumptions that some deviations in thickness and roughness may occur at the beginning of the sputtering process. From the reflectivity adjustment (red curve in figure 5), the Co (Pt) thickness determined from the fit is 0.67 nm (1.83 nm) in the first [Co/Pt] bilayer and 0.61 nm (1.225 nm) in the remaining $[Co/Pt]_{49}$ multilayer. A total thickness of 92.5 nm has been determined, i.e. only 2.8% larger than the value expected from the 1.8 nm thick bilayer. The Co (Pt) roughness determined from the fit is 0.48 nm (0.25 nm) in the first [Co/Pt] bilayer and 0.42 nm (0.18 nm) in the remaining $[Co/Pt]_{49}$ multilayer. It appears than both layers are rougher in the first bilayer and that the Co roughness values are close to the Co thickness, which suggests very perturbed Co layers.

To summarize the structural analysis of the thick $[Co/Pt]_{50}$ stacking on Ta/MgO, the results have evidenced a (111) texture despite the absence of a 5nm thick Pt layer. This (111) texture thus likely occurs in all [Co/Pt] sets, in those similar to bottom electrodes as in those similar to top electrodes. The (111) texture is consistent with previous observations found in the literature[1],[8],[10] and should promote the PMA, as detailed in the previous chapter. The large mosaicity reveals however a pretty large dispersion of [111] axis which may be related to the growth on MgO. The large roughnesses, especially for Co layers, also point out a rather perturbed stacking.

II.D. Reflectometry analysis on [Co/Pt] multilayers

Figure 6 presents the X-ray reflectivity patterns collected for the set A (Pt buffer/MgO capping) and for the set B (MgO buffer/Pt capping). The X-ray reflectivity patterns for the set C (Pt buffer/ Al_2O_3 capping) and set D (Al_2O_3 buffer/Pt capping) are presented in the figure 7.

All the reflectivity curves have been fitted (red curves) using the X'pert reflectivity software and following the procedure reported in the section II.B.

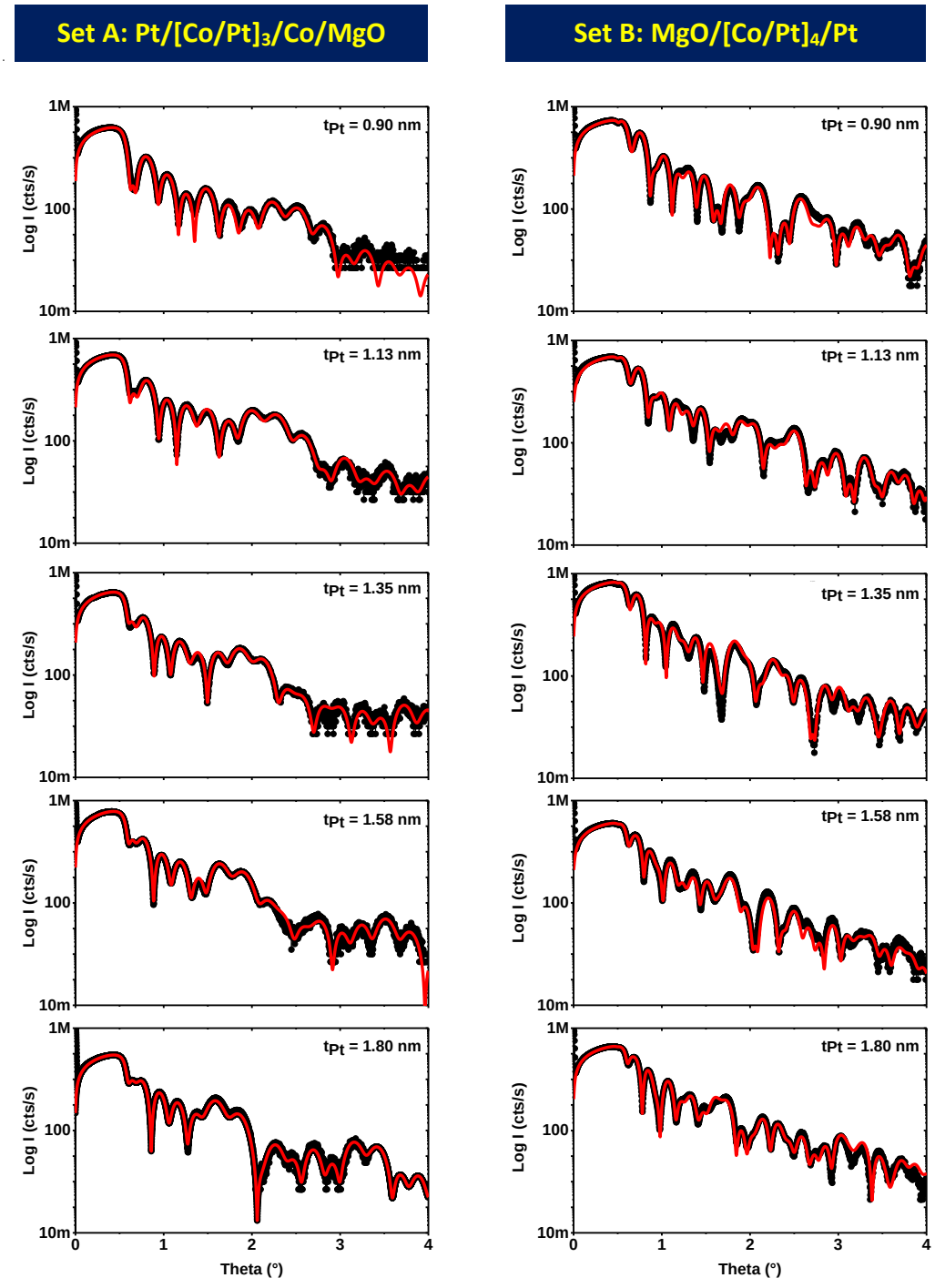

Figure 6: X-ray reflectivity spectra (black curves) and their fits using X'pert Reflectivity (red curves) for the sets A (Left) and B (Right). The reported Pt thicknesses are the nominal ones.

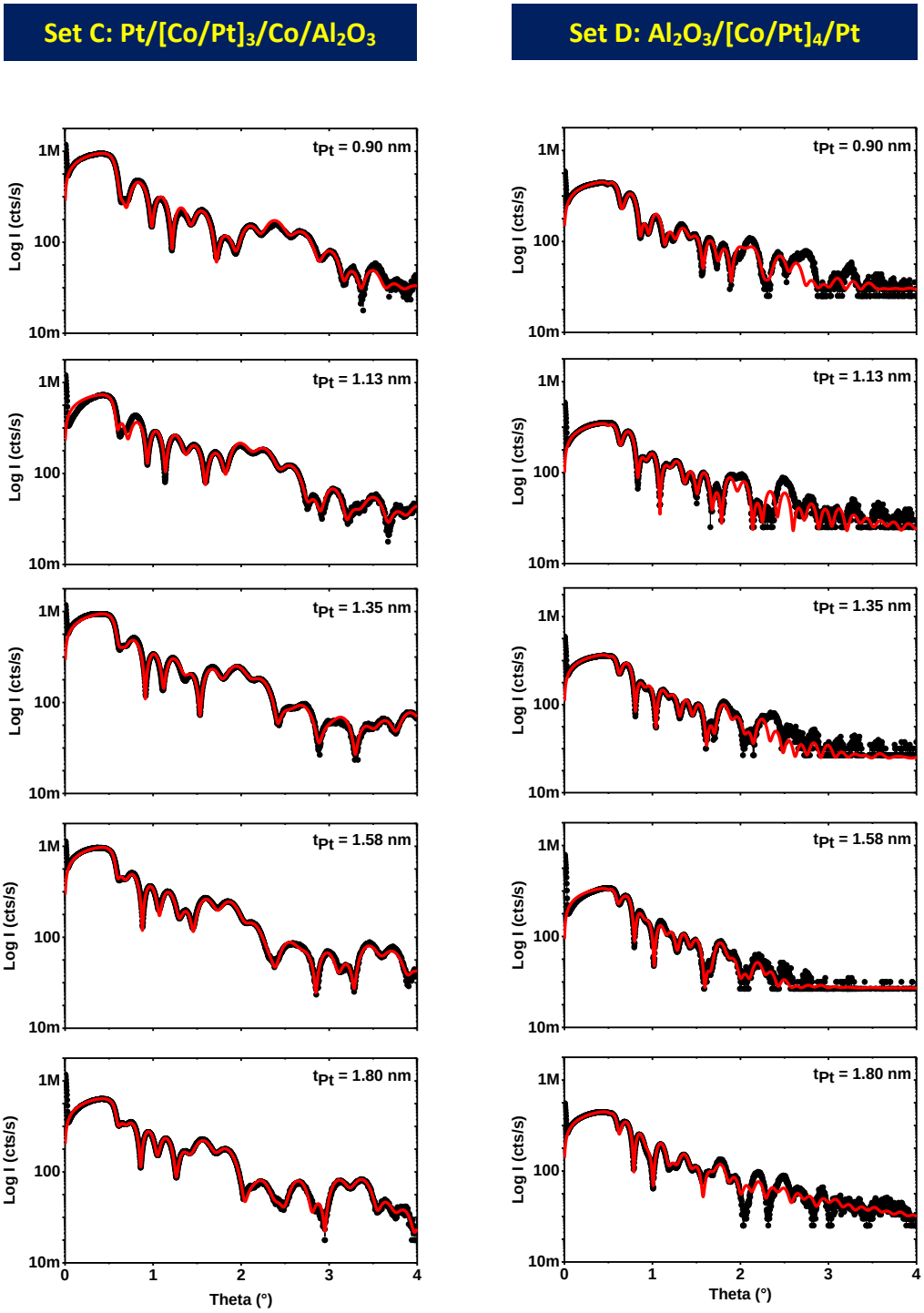

Figure 7: X-ray reflectivity spectra (black curves) and their fits using X'pert Reflectivity (red curves) for the sets C (Left) and D (Right). The reported Pt thicknesses are the nominal ones.

Despite the rather high complexity of these layered systems, an excellent agreement is obtained between experimental reflectivity curves and the results of the fitting process for the sets A, B and C. In the case of the set D (Al_2O_3 buffer), the counting statistics is not so good and a satisfactory agreement between experimental data and adjustment is only obtained in a reduced angle range, approx. up to 2°. Above this value, the reflectivity signal is too noisy and more or less embedded in the background.

The fits have permitted to determine with a relatively high degree of confidence the thicknesses and roughnesses for the Co and Pt layers in the [Co/Pt] stackings. These are successively presented and discussed in the two following paragraphs.

II.D.1. Co and Pt thicknesses

The Co and Pt thicknesses extracted from the reflectivity fits are presented in figures 8 (a) and (b) respectively.

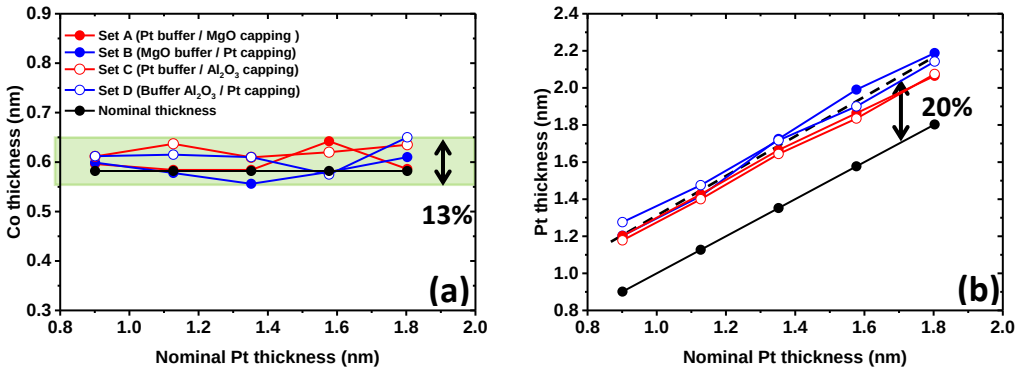

Figure 8: Evolution of the Co and Pt thicknesses extracted from the X-ray reflectivity fits versus the nominal Pt thickness.

Note: *in the case of the sets A and C, the Co thickness reported correspond to the average of the Co thickness (roughness) between the* $[Co/Pt]_3$ multilayers and the Co layer deposited on the top of $[Co/Pt]_3$ stacking.

In agreement with the constant Co nominal thickness (0.58 nm) in the four sample sets, no significant changes in the fitted Co thickness can be observed for the different samples. The average of the Co thickness for the multilayers sputtered on Pt and Al_2O_3 is 0.61 nm whereas it is equal to 0.58 nm for the multilayers sputtered on MgO. These results reveal a dispersion of approximately 13% between the different sets and a maximum shift of less than 11% compared to the nominal value.

Concerning the Pt thickness, the fitted values exhibit smaller dispersion with a maximum of 6% difference between different sets for a given Pt nominal thickness. However, the fitted values are significantly larger than the nominal thickness, by roughly 20%. This shift can be explained by an imperfect calibration of the Pt flux.

Despite a significant difference between the Pt thicknesses and the nominal values, the relatively small dispersions for the Co and Pt thicknesses between the different sets prove the good reproducibility in the sputtering process, especially for the [Co/Pt] multilayers in each set. Given the high quality and consistency of reflectivity adjustments, the Pt and Co thicknesses obtained from the fits will be used instead of the nominal thicknesses in the following paragraphs.

II.D.2. Co and Pt roughnesses

The roughnesses obtained from the reflectivity fits for the Co and the Pt layers are presented versus the Pt thickness in figures 9 (a) and (b) respectively ($\sigma/2$ is reported for an easier comparison with the layers' thicknesses).

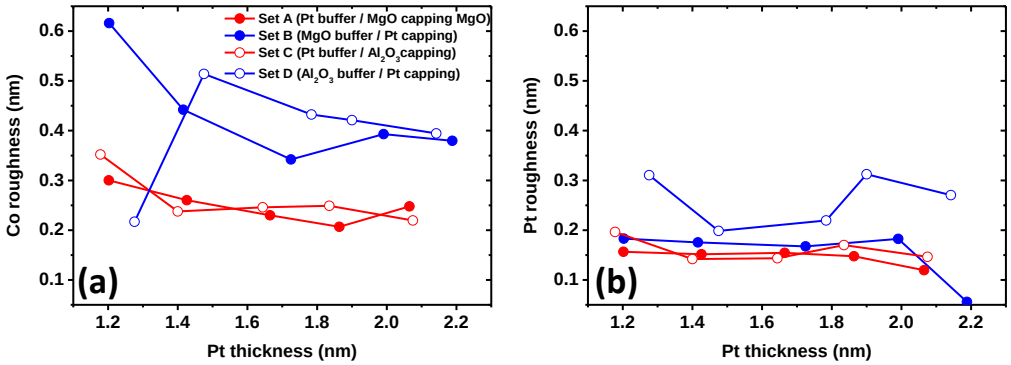

Figure 9: Evolution of the Co and Pt roughnesses extracted from the Reflectivity fits versus the Pt thickness.

Note: *The Co roughness reported for the sets A and C correspond to the average of the Co roughness between the* $[Co/Pt]_3$ multilayers and the Co layer deposited on the top of $[Co/Pt]_3$ stacking.

For both the Co and Pt layers, the general trend is a decrease of the roughness when the Pt thickness increases, although the effect is more pronounced for Co layers than for Pt ones. This trend is observed for each set but the results obtained for the set D (Al_2O_3 buffer) are obviously more scattered, which is likely related to the poorer quality of the fits.

[Co/Pt] multilayers sputtered on a Pt buffer (red symbols) exhibit smaller roughnesses than those on MgO and Al_2O_3 buffers (blue symbols). The use of the Al_2O_3 buffer appears to particularly damage the quality of interfaces. The difference is significant for Co layers, the roughness of which is increased by nearly 50% in the case of MgO and Al_2O_3 buffers. Given the small thickness of the Co layers, such values of roughness mean that the Co/Pt interfaces are not well defined with high degree of roughness and/or inter-mixing. The situation is better for Pt layers, the larger thickness of which probably helps in smoothing the interface, but higher roughness are still obtained on the Al_2O_3 buffer.

In summary, better interfaces are formed when using a Pt buffer, i.e. in the case of bottom electrode- like multilayers. The use of MgO, and worst Al_2O_3 buffers, leads to increased roughnesses, i.e. more perturbed interfaces in the case of top electrode– like multilayers. In both cases, increasing the Pt thickness tends to improve the interface quality. Finally, Co/Pt and Pt/Co interfaces appear to be significantly different, with a higher degree of roughness and/or intermixing for the formers than for the latters.

III. Magnetic properties in the [Co/Pt] multilayers

III.A. Experimental setup

The magnetic measurements of [Co/Pt] multilayers have been performed in the Institut Jean Lamour at room temperature by using a Vibrating Sample Magnetometer (VSM) and at low

temperature by using a Superconducting Quantum Interference Device (SQUID). Pictures of both devices are shown in figure 10. The field range available for VSM (resp. SQUID) measurements is ±2.5T (resp. ±7T). All the "magnetization versus field" (M(H)) loops have been recorded for an applied field perpendicular and parallel to the sample surface.

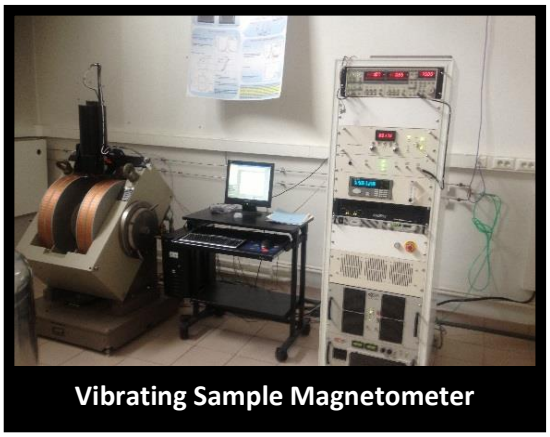

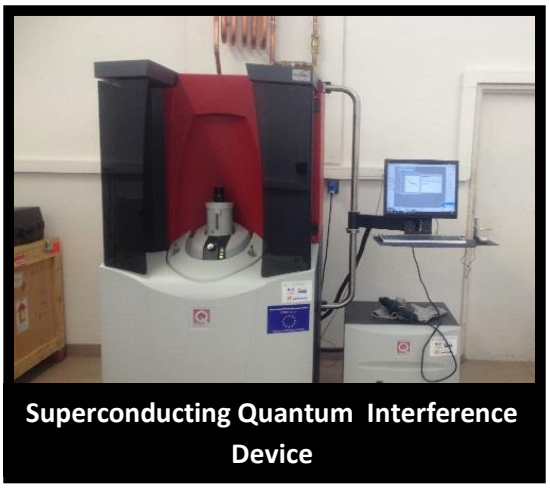

Figure 10: Pictures of the experimental setups for the magnetic measurements on Co/Pt multilayers. The VSM and SQUID are respectively shown in top and bottom parts (courtesy of C.C magnetism-IJL).

III.B. Experimental results

Figure 11 presents the M(H) loops collected for the sets A and B (MgO as respectively capping and buffer layers) with the external field applied perpendicular (⊥) and parallel (//) to the sample surface. Figure 12 presents the M(H) loops collected for the sets C and D (Al_2O_3 as respectively capping and buffer layers) with the external field applied perpendicular (⊥) and parallel (//) to the sample surface.

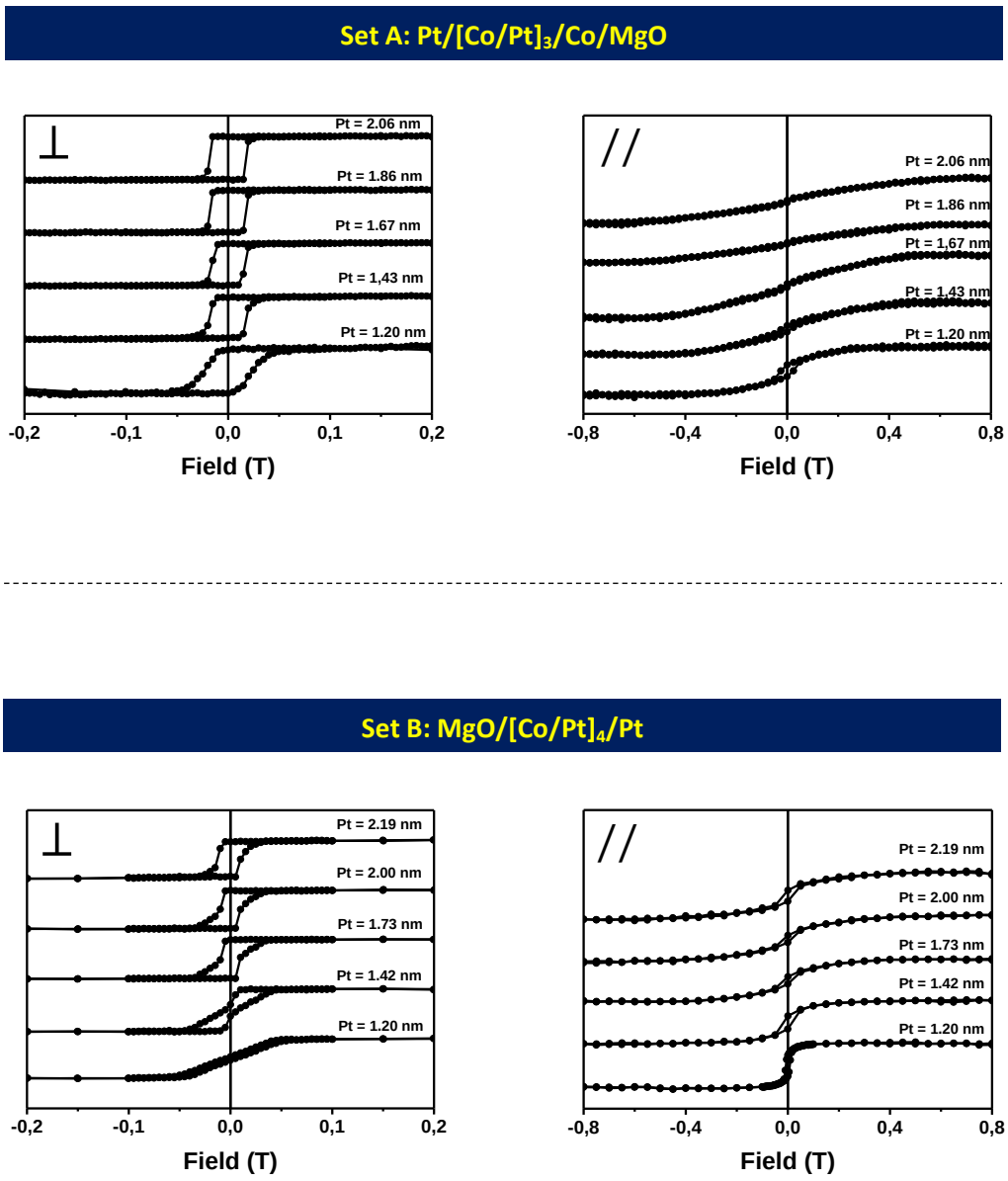

Figure 11: M(H) loops for the out-of-plane (left) and in-plane (right) configurations measured at room temperature for the sets A (top) and B (bottom).The reported Pt thicknesses are the fitted ones.

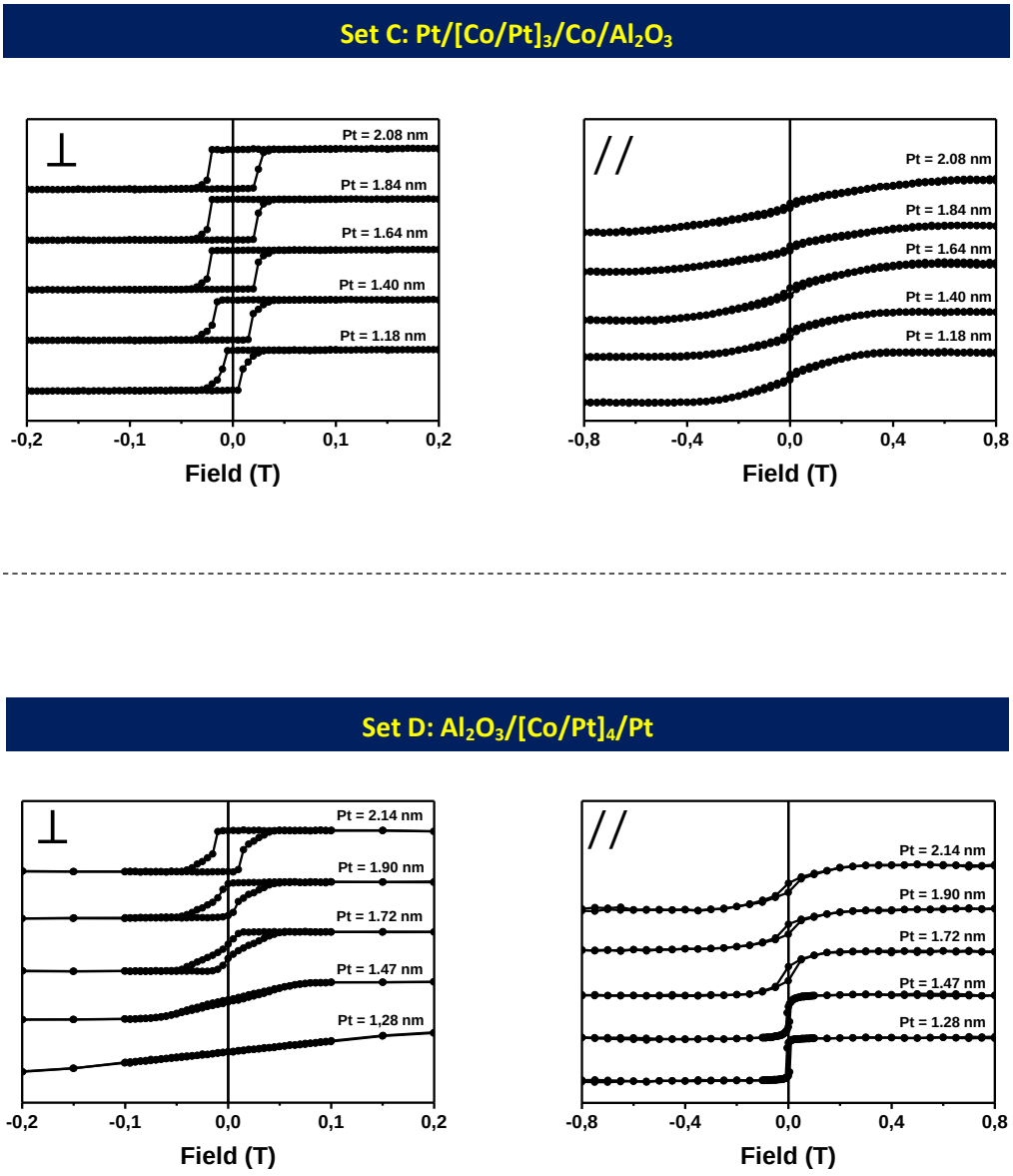

Figure 12: M(H) loops for the out-of-plane (left) and in-plane (right) configurations measured at room temperature for the sets C (top) and D (bottom). The reported Pt thicknesses are the fitted ones.

These results first permit to determine the easy magnetization axis in the various [Co/Pt] multilayers. In comparing the shapes of M(H) loops for perpendicular and parallel applied fields, it is obvious that the easy magnetization direction is perpendicular to the sample surface for [Co/Pt] sputtered on the Pt buffer (sets A and C), in the whole Pt thickness range: the M(H) loops measured with the perpendicular applied field are more or less "square" with a strong hysteretic behavior and equal remanence and saturation values. The more linear and non-hysteretic behavior observed for parallel applied field is consistent with a magnetically hard direction. The [Co/Pt] multilayers sputtered on MgO and Al_2O_3 buffers (sets B and D) both exhibit a transition from in-plane to perpendicular-to-the-plane easy axis when increasing the Pt thickness.

The Table 3 summarizes the perpendicular or in-plane character of the magnetic anisotropy as a function of the Pt thickness (average of the Pt thickness extracted from reflectometry adjustment and detailed in section II.D) for the different sample sets.

<table>
<tr><th>Pt thickness (average)</th><th colspan="2">Pt buffer</th><th>MgO buffer</th><th>Al_2O_3 buffer</th></tr>
<tr><th>(nm)</th><th>MgO capping (set A)</th><th>Al_2O_3 capping (Set C)</th><th>Pt capping (Set B)</th><th>Pt capping (set D)</th></tr>
<tr><td>1.21</td><td rowspan="5">Perpendicular</td><td rowspan="5">Perpendicular</td><td>In-plane</td><td rowspan="2">In-plane</td></tr>
<tr><td>1.43</td><td rowspan="4">Perpendicular</td></tr>
<tr><td>1.69</td><td rowspan="3">Perpendicular</td></tr>
<tr><td>1.90</td></tr>
<tr><td>2.11</td></tr>
</table>

Table 3: Perpendicular or in-plane character of the magnetic anisotropy versus the Pt thickness for the different sample sets.

Beyond these first qualitative observations, a more quantitative analysis can be undertaken (i) to explore the dependence of magnetic anisotropy via the determination of the effective anisotropy constant and (ii) to investigate the magnetization amplitude in these various systems, and see how both anisotropy and magnetization could be linked to the Pt thickness and/or structural properties.

These are the objects of the two following paragraphs.

III.B.1 Effective anisotropy

The effective anisotropy constants have been extracted from the M(H) loops via the "area method" described in the previous chapter. Figures 13 (a) and (b) present the effective anisotropy constant and coercive field dependence on the Pt thickness for the four different sample sets. Figure 13 (c) presents the effective anisotropy multiplied by the Co thickness versus the Co thickness for the set E. This sample set corresponds to $[Co/Pt]_4$ multilayers with 1.8 nm thick Pt layers and different Co layers thicknesses, sputtered on a Pt buffer (Tables 1 and 2).

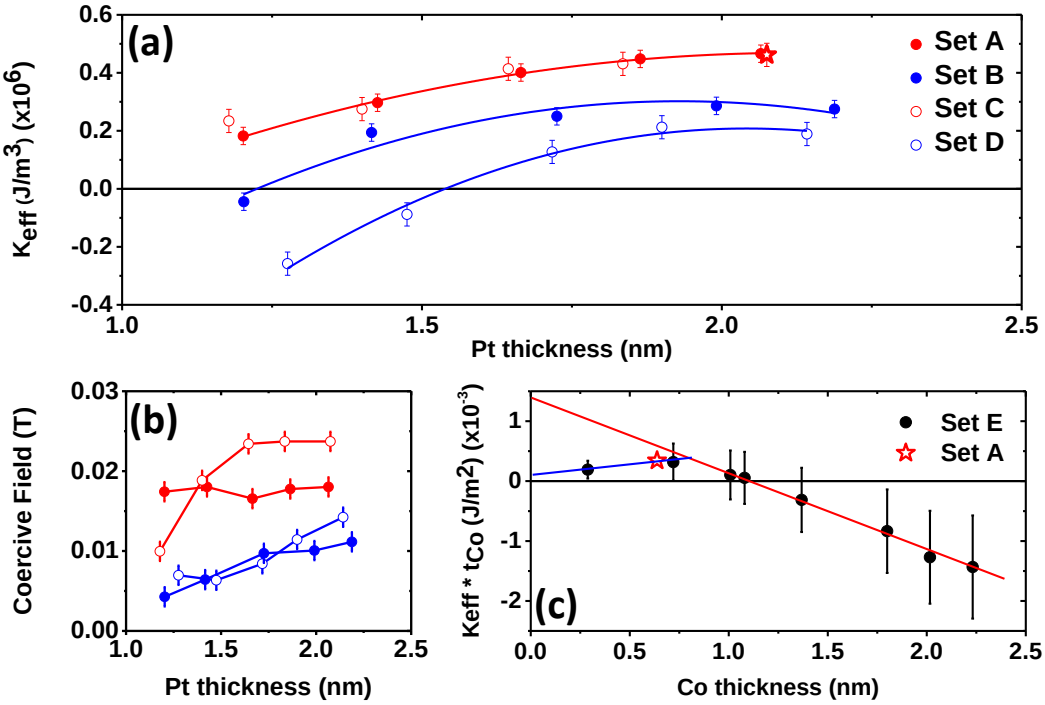

Figure 13: Variations of the effective anisotropy constants (a) and coercive fields (b) with the Pt thickness for the four different sample sets. (c) Effective anisotropy multiplied by the Co thickness versus the Co thickness for the set E. The red star corresponds to the value extracted from the set A and for the largest Pt thickness (2.06 nm). The lines are guides for the eyes.

Figure 13 (a) first shows that all sample sets exhibit an increase of the effective anisotropy constant with the Pt thickness, with stabilization around 2 nm. By comparing the various sets, one can observe that the effective anisotropy constants are similar and the highest for the sets on Pt buffer (A and C), but significantly reduced for the sets on MgO (B) and Al_2O_3 (D) buffers, the reduction being more important on the Al_2O_3 buffer. For these two sets, the negative values of effective anisotropy constants obtained for small Pt thicknesses are the signature of the in-plane anisotropy.

The effective anisotropy constant increase with the Pt thickness is in agreement with previous results reported by C.-J. Lin *et al.*[1] in [Co(0.3 nm)/Pt(x nm)] multilayers (x ∈ [0.2 - 2] nm) where a stabilization of the effective anisotropy constant around 1.2 nm is reported. It can be noted that our values for the effective anisotropy constant (larger than 0.2 MJ/m^3 on Pt buffer) are larger than the values reported in their paper (K_{eff} = 0.1 MJ/m^3 for Pt thickness larger than 1.2 nm) but can be well understood by the factor 2 between our and their Co thickness and the number of Co layers (4).

Figure 13 (c) obtained from the measurements of the sample set E permits us to extract the surface contribution K_S and the volume contribution K_V defined as $K_{eff} \times t_{Co} = K_V \times t_{Co} + 2K_S$ (see (I-10) in chapter 4). The intercept at zero Co thickness corresponds to $2K_S$ whereas the slope of the linear part gives us directly K_V. It turns out that K_S = 0.72 mJ/m^2 and K_V = -1.3 MJ/m^3. These values are in the range of the surface and volume anisotropy constants reported in the literature for (111) textured [Co/Pt] multilayers (see chapter 4).

Moreover, two regimes with the Co thickness can be distinguished. For t_{Co} > 1.1 nm, the demagnetizing field, the main contribution to the volume anisotropy, is larger than the interface anisotropy and tilts the magnetization towards the sample plane. For t_{Co} < 1.1 nm, the interface anisotropy is dominant and drives the easy magnetization direction towards the perpendicular to the

sample plane. As mentioned in the literature devoted to [Co/Pt] multilayers, a deviation of the PMA from the linear behavior is observed at low Co thickness. This reduction in effective anisotropy likely originates from the reduction of surface anisotropy due the degradation of the interfaces when decreasing the Co thickness.

Discussion on the PMA in connection with structural properties

The larger effective anisotropy for [Co/Pt] sputtered on Pt can be first explained by a likely better (111) texture which is known to promote the PMA as reported in the literature (see chapter 4). This hypothesis is strengthened by the results reported in figure 13 (b), where larger coercive fields are also observed for the [Co/Pt] multilayers grown on a Pt buffer, suggesting the reduction of domains nucleation and consistently with the more abrupt magnetization reversal (figures 11 and 12). Beyond the effect of (111) texture, our structural analysis has evidenced a significant difference in roughness, especially for Co layers, between the samples grown on Pt and those grown on MgO or Al_2O_3. The roughness is the highest for samples on Al_2O_3, those exhibiting the smallest effective anisotropy.

As reported in the previous chapter, roughness, interdiffusion, and magneto-elastic effects, can namely lead to the decrease of the PMA. The mismatch of 10% between the Co and Pt eliminates the hypothesis of a coherent growth for the [Co/Pt] multilayers and thus rules out possible magneto-elastic surface contribution. Bruno's model shows that an increasing roughness may: (i) promote the PMA if only the dipolar surface anisotropy is considered (ii) reduce the PMA due to the weaker broken symmetry associated to the Néel surface anisotropy. In our case, the increased roughness appears to reduce the effective anisotropy, in agreement with the second part of Bruno's model.

Based on this model, the effect of roughness can also account for the variation of effective anisotropy versus the Pt thickness presented in figure 13 (a). A similar trend for $K_{eff}(t_{Pt})$ has been reported by C.-J Lin *et al*.[1] but no really explained. Our structural analysis has shown that the Co roughness decreases when increasing the Pt thickness (figure 9) and that this decrease is stronger for [Co/Pt] multilayers sputtered on MgO or Al_2O_3, those for which the increase in effective anisotropy is also more important.

As mentioned previously, our X-ray reflectometry study in specular geometry doesn't permit to distinguish between roughness and intermixing effect at the interfaces. The formation of an interface Co_xPt_{1-x} alloy can also lead to the reduction of the PMA by limiting the broken symmetry at the Co/Pt interfaces.

III.B.2. Saturation magnetization

The variation of the magnetization with the Pt thickness is reported in figure 14 for the four different sample sets. Those magnetization values have been calculated at saturation and per Co cm^3 via the Co thicknesses obtained from X-ray reflectivity adjustments and the determination of the samples area. The main source of error in the magnetization calculation comes from the error on sample area that can be estimated to ± 1 mm^2.

`

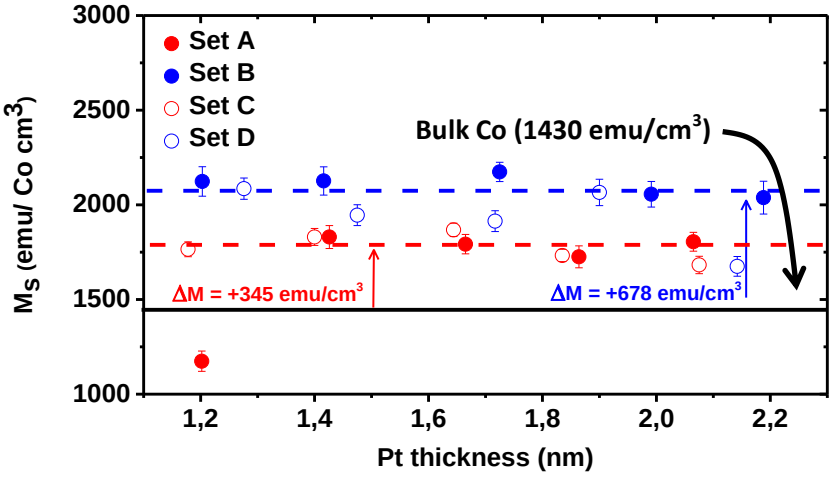

Figure 14: Magnetization versus the Pt thickness for the different sample sets. The black horizontal line corresponds to bulk Co (1430 emu/cm^3) and the dash lines are guides for the eyes.

For all sample sets, the magnetization is obviously larger than for bulk Cobalt (1430 emu/cm^3) and this increased magnetization appears to depend on the buffer layer: An enhancement of approximately 24% (ΔM = +345 emu/cm^3) is observed for [Co/Pt] stackings sputtered on Pt (sets A and C) and an enhancement of 47% (ΔM = +678 emu/cm^3) is observed for [Co/Pt] stackings sputtered on MgO (set B) and Al_2O_3 (set D) buffers. The values determined for sets A and C are similar, showing no influence of the capping layer on the [Co/Pt] multilayers magnetization.

Two main contributions to this magnetization enhancement could be obviously considered: the enhancement of the Co magnetic moment and the appearance of an induced magnetic moment on Pt atoms. It is well known from previous studies on various Co-based and Pt-based systems that both phenomena are likely to occur, specifically at the Co/Pt interfaces. Any definitive conclusion on the origin of this magnetization enhancement would thus require an element-selective and even better, an element-selective and depth-resolved analysis. It is however instructive to discuss the amplitude of ΔM and its dependence on the Pt thickness in comparison with previously reported results.

An enhancement of the interfacial Co orbital moment in [Co/Pt] multilayers has been evidenced and quantified by D. Weller *et al.*[11] by XMCD measurements: Δm_{orb} = +0.07 μ_B/ Co atoms. The results were confirmed by Nakajima *et al.*[12] who have unambiguously shown (XMCD measurements at room temperature): (i) the enhancement of the Co orbital moment (Δm_{orb} = +0.064 μ_B/at.), essentially localized in a single atomic interface layer (ii) a close connection between the enhanced Co orbital moment and the Co 3d - Pt 5d hybridization. More recently, M. Gottwald *et al.*[13] have reported on the enhancement of both Co effective spin and orbital moments at the Co-Ni interfaces. In sputtered systems, those enhancements are determined to be $\Delta m_{spin\text{-}eff}$ = +0.1 μ_B/at. and Δm_{orb} = +0.07 μ_B/at. In our case, the measured enhanced magnetization would correspond to approximately +0.7μ_B/Co at. for sets B and D and +0.35μ_B/Co at. for sets A and C. These values appear to be much too large to be exclusively attributed to the increased Co moment and suggest a large induced polarization on Pt atoms, as previously reported by several authors.

A large magnetization enhancement has been namely reported in [Co/Pt] multilayers[1],[10],[14],[15], and attributed to the Co induced spin-polarization on the neighboring Pt atoms, explained by the Co 3d- Pt 5d hybridization. The presence of heavy metals like Pt in [Co/Pt] multilayers induces a strong hybridization between the Co 3d and the Pt 5d orbitals, which shifts the Pt 5d bands towards the Co majority spin and induces a Pt spin moment parallel to the Co moment. A

large Pt orbital moment aligned parallel to the Co magnetic moment results from the strong spin-orbit coupling in Pt and contribute to the enhanced total magnetic moment compared to bulk Co.

Induced Pt magnetic moments have been calculated to be + $0.37\mu_B$ in $Co_{50}Pt_{50}$ alloy and +$0.08\mu_B$ in [$Co_{0.4nm}$/$Pt_{1.8nm}$] multilayers[16]. Experimentally, room temperature spin absorption measurements performed at the Pt L_3 edge for [Co/Pt] multilayers ([Co(0.4nm)/Pt(x nm)] with x ∈ [0.9 - 4] nm)[17] have proved that Pt atoms at the interface with Co are spin-polarized with an average moment decreasing from 0.15 to 0.03 μ_B when increasing x. A few years later, The use of a depth-resolved technique (resonant X-ray reflectometry) has permitted to analyze the Pt magnetization depth profile at a single $Co_{2.6nm}$/$Pt_{6.2nm}$ interface: the authors reported an induced Pt 5d magnetic polarization of 0.21 μ_B/atom at the rough interface (roughness of 0.7 nm) followed by an exponential decay within 1 nm [18]. More recently, based on magnetometry measurements at room and low temperatures for [Co(0.4 nm)/Pt(x nm)] multilayers with x ∈ [0.8 - 8] nm, J.W. Knepper *et al.*[14] have suggested that: (i) Pt atoms in thin Pt layers can be polarized by Co atoms on both sides of the Pt layer (ii) the thickness over which Pt atoms are polarized at the Co/Pt interface increases when decreasing temperature and can reach 3nm at low temperature.

In the present case, if one considers that the excess in magnetization ΔM only originates from the induced Pt polarization, the average induced Pt magnetization M_{Pt} and the total effective thickness where Pt atoms are polarized t_{Pol} are related by the following expression:

$$M_{Pt} \times t_{Pol} = \Delta M \times 4t_{Co} \qquad \textbf{(III-1)}$$

Given the 1nm value reported for the room temperature Pt polarized thickness at a Co/Pt interface, on can assume that the thin Pt layers in the present samples are fully polarized. The effective polarized part would thus correspond to the three Pt layers surrounded by Co layers and to an approximate 1 nm thick layer in the first (last) bottom (top) Pt ($t_{Pol} = 3t_{Pt} + 1$). This permits to calculate a rough estimation of the average Pt induced moment for the various samples (figure 15).

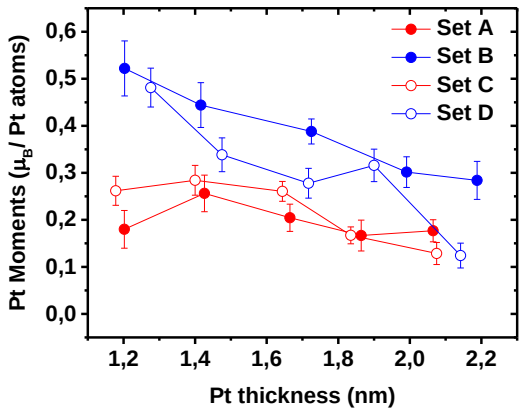

Figure 15: Calculated induced Pt moment versus the Pt thickness for the different sample sets (see text for more details).

These induced moments are similar[14] or slightly higher than those generally reported for similar systems. In contrast to a single Co/Pt interface or to relatively distant interfaces, the close Co/Pt interfaces in present samples with thin Pt layers likely promote larger induced moments. Pt atoms at one Co/Pt interface are namely polarized by the closest Co atoms but also by the Co atoms on the other side of the Pt layer[14].

Figure 15 highlights a larger induced Pt moment in the [Co/Pt] stackings sputtered on MgO and Al_2O_3 buffers (set B and D) than in stackings sputtered on Pt (sets A and C), by a factor of almost 2. As for the effective anisotropy constant, this difference likely originates from different interface morphologies, as attested by the different Co roughnesses (figures 9). Roughness and/or inter-mixing increase the quantity of Pt atoms in direct contact with Co atoms and thus likely increase the average Pt induced moment, and consequently the magnetization of the [Co/Pt] multilayers.

In this hypothesis where Pt layers are fully polarized, the average induced Pt moment appears to decrease when increasing the Pt thickness. This can be first explained by (i) the decay of the Pt moment when going further from the Co/Pt interface (ii) the increased distance between consecutive Co/Pt interfaces so that Pt atoms close to one interface are less polarized by the second further interface. But one could also invoke (iii) the decrease in Co roughness when increasing the Pt thickness (figure 9). If this change in morphology affects the induced Pt moment, as it is obvious from the difference observed between the sets grown on Pt on those grown on the oxide layers, the decrease in roughness when increasing the Pt thickness should also contribute to the reduction in Pt induced moment. A more accurate evaluation of these three possible effects would require a depth-sensitive analysis of the induced Pt moment.

III.B.3. Influence of temperature

The magnetic properties versus temperature have been studied for three samples belonging to the set B: with 1.42 nm, 1.73 nm and 2.19 nm – thick Pt layers. The temperature dependence of M_S and K_{eff} are reported in figure 16 (a) and (b). These values will be later used as parameters in micro-magnetic simulation (OOMMF), in order to calculate the different magnetic behaviors of the top electrode at different temperatures (chapter 6).

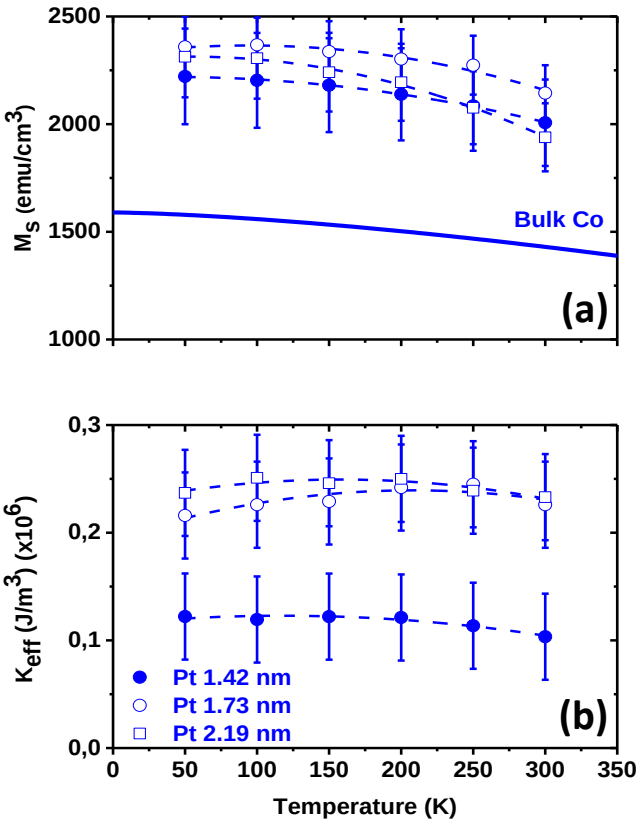

Figure 16: Magnetization (a) and effective anisotropy constant (b) versus temperature for three different [Co/Pt] multilayers on MgO buffer (set B). The solid line corresponds to the variation of bulk Co magnetization.The dash lines are guides for the eyes.

For the three Pt thicknesses, the magnetization slightly increases when the temperature decreases. Given the weak bulk Co magnetization variation with temperature in this temperature

range (solid line), this increase cannot be attributed to Co atoms, but rather to an increase of the Pt induced magnetic moment and/or of the polarized Pt thickness, as suggested by T. Sugimoto *et al.*[19]. A similar behavior has been reported by P.J. Bloemen *et al.* on [$Co_{0.6nm}$/Pt] multilayers with Pt thicknesses varying in the [0.9nm-4nm] range[20]. The study by J.W. Knepper *et al.*[14] on [Co(0.4nm)/Pt(x nm)]$_8$ multilayers with x up to 8 nm concludes that the Pt polarization can extend to 3 nm from the Co/Pt interface at 25K. This leads to an increase in saturation magnetization with Pt thickness at low temperature, while it decreases at room temperature because of the increased distance between Co/Pt interfaces.

In the present case where the three Pt layers surrounded by Co are likely fully polarized at room temperature, the increase of the polarized thickness at low temperature is essentially due to the last top Pt layer: $t_{Pol}(50K) = 3t_{Pt} + 3 = t_{Pol}(300K) + 2$[11]. In the hypothesis where the average Pt moment doesn't change with temperature in the thickness $t_{Pol}(300K)$, one can calculate the average Pt moment in the supplementar polarized 2nm at low temperature: it comes 0.11μ_B/at. for samples with 1.42 nm and 1.73 nm Pt layers, and 0.42μ_B/at. for the sample with 2.19 nm thick Pt layers. This latter especially high value would suggest that the increase in magnetization in the third sample should be partly attributed to an increase of the Pt average moment inside the Pt layers surrounded by Co. In this sample where Co/Pt interfaces are distant by 2.19 nm across Pt layers, the increase of polarized thickness at low temperature may likely explain a larger polarization on Pt atoms that become more and more sensitive to both interfaces. An increase of 35% compared to the room temperature result together with the supplementar 2nm polarized at the top interface (0.11μ_B/at) can account for the low temperature magnetization value. The effect of increased polarized thickness inside the Pt layers surrounded by Co could be also responsible for the larger increase in magnetization when decreasing temperature for this particular sample (figure 16 (a)), in agreement with Ref[11].

Concerning the effective anisotropy constant, no significant variation is observed with temperature (figure 16 (b)). This result is somehow surprising since the increase in magnetization should namely lead to an increase of the dipolar anisotropy term $-\mu_0 M_S^2/2$ which contributes to tilt the magnetization towards the sample plane, and thus to reduce the PMA. The constant effective anisotropy suggests the occurrence of a positive contribution that would counterbalance the increase in dipolar anisotropy, i.e an increase of Néel surface anisotropy and/or magneto-elastic effect[16]. Magneto-elastic contributions have been proposed to account for the temperature dependent anisotropy in [Co/Au] multilayers[21] but don't appear to be relevant in [Co/Pt] multilayers that exhibit different variation of K_s versus temperature[22]. The origin of the PMA dependence on temperature in [Co/NonMagnetic] multilayers actually remains an open question.

IV. Conclusion

The first goal of this thorough study of [Co/Pt] stackings was to provide an accurate structural and magnetic characterization of the magnetic systems potentially used as bottom and top electrodes in Magnetic Tunnel Junctions. The aim was to especially focus on the link between their magnetic and structural properties, and to pay a specific attention to the influence of the Pt thickness, an aspect which is seldom developped in the numerous previous studies.

(111) [Co/Pt] multilayers with a good reproducibility of the deposited thicknesses have been sputtered on various buffers: Pt (with MgO or Al_2O_3 capping, for bottom electrode), MgO and Al_2O_3 (with Pt capping, for top electrode).

The structural and magnetic properties of the [Co/Pt] multilayers are qualitatively summarized in the Table 4. For each quantity in the left column, the green arrows sketch the

tendency (constant/increase/decrease) observed when increasing the Pt thickness; the yellow stars symbolize the relative amplitudes.

	Pt buffer				MgO buffer		Al_2O_3 buffer	
	MgO capping (set A)		Al_2O_3 capping (set C)		Pt capping (set B)		Pt capping (set D)	
Roughness	↘	★	↘	★	↘	★★	↘	★★★
Magnetization	→	★	→	★	→	★★	→	★★
Coercive Field	→	★★	↗	★★★	↗	★	↗	★
Effective Anisotropy	↗	★★★	↗	★★★	↗	★★	↗	★

Table 4: *Qualitative summary of the different structural and magnetic parameters for the four sample sets*

No significant difference could be noticed between the sets A and C, revealing no effect of the capping layer for the same Pt buffer. Strong differences have been however observed between the systems grown on Pt (A and C) and those grown on MgO (B) or Al_2O_3 (D):

1. The Co/Pt interfaces are more perturbed when grown on MgO and Al_2O_3 than on Pt, with however a significant decrease in Co roughness when increasing the Pt thickness.
2. The systems grown on Pt exhibit higher effective anisotropy, although PMA is observed for all sets for Pt thickness above 1.5 nm. The effective anisotropy increases when increasing Pt thickness.
3. The increase in magnetization compared to bulk Co is twice more important in the systems grown on MgO or Al_2O_3, although all sets exhibit a largely increased magnetization due to Pt induced polarization.

The comparison between those different sets tends to highlight the prominent role played by the layer roughness, especially by Co layers roughness in the present case. It appears that rough interfaces contribute to the reduced PMA, in agreement with Bruno's model describing how the roughness limits the Néel surface anisotropy. This effect is also observed for a given sample set since the smoothing of interfaces (in increasing the Pt thickness) tends to improve PMA. Simultaneously, rough interfaces contribute to the enhanced magnetization via the polarization of Pt atoms in direct contact with Co. This effect on magnetization may also indirectly drive the reduction of PMA via the increase of the dipolar anisotropy contribution which favors in-plane magnetization.

Finally, the effect of temperature has been analyzed for one of the sample sets: it appears that decreasing temperature has a very limited effect on the effective anisotropy, despite the increase observed for the saturation magnetization (increase of the Pt induced moment and/or polarized Pt effective thickness). In order to account for this constant effective anisotropy, a supplementary contribution favoring PMA and opposing the low temperature increase of the dipolar contribution has to be taken into account. This contribution remains to be clearly identified.

Concerning now our first interest in these [Co/Pt] stackings as future electrodes in MTJs, these investigations have proved that the different systems are suitable for integration in [Co/Pt]-based MTJs. Bottom and top electrodes both present satisfactory structural characteristics that enable the stabilization of Perpendicular Magnetic Anisotropy. Since the top electrodes exhibit however reduced quality, especially when using the Al_2O_3 buffer, our choice was to focus on MTJs with [Co/Pt] electrodes separated by an insulating MgO barrier.

References

[**1**] C.-J. Lin *et al.*, J. Magn. Magn. Mater. **93**, 194 (1991).
[**2**] M. Kisielewski *et al.*, J. Magn. Magn. Mater. **260**, 231 (2003).
[**3**] C. Ducruet *et al.*, J. Appl. Phys. **103**, 07A918 (2008).
[**4**] G. Kim *et al.*, Appl. Phys. Lett. **92**, 172502 (2008).
[**5**] A. Gibaud *et al.*, *X-Ray and Neutron Reflectivity: Principles and Applications* (Springer, 1999).
[**6**] L.G. Parratt *et al.*, Phys. Rev. **95**, 359 (1954).
[**7**] K.M. Zimmermann *et al.*, Advanced Analysis Techniques for X-Ray Reflectivities : Theory and Application Dissertation, 2005.
[**8**] D. Weller *et al.*, J. Appl. Phys. **89**, 7525 (2001).
[**9**] P.F. Fewster *et al.*, Reports Prog. Phys. **59**, 1339 (1996).
[**10**] S. Emori *et al.*, J. Appl. Phys. **110**, 033919 (2011).
[**11**] D. Weller *et al.*, Phys. Rev. B **49**, 888 (1994).
[**12**] N. Nakajima *et al.*, Phys. Rev. Lett. **81**, 5229 (1998).
[**13**] M. Gottwald *et al.*, Phys. Rev. B **86**, 014425 (2012).
[**14**] J. Knepper *et al.*, Phys. Rev. B **71**, 224403 (2005).
[**15**] C.L. Canedy *et al.*, Phys. Rev. B **62**, 508 (2000).
[**16**] G. Schütz *et al.*, J. Appl. Phys. **67**, 4456 (1990).
[**17**] S. Rüegg *et al.*, J. Appl. Phys. **69**, 5655 (1991).
[**18**] J. Geissler *et al.*, Phys. Rev. B **65**, 020405 (2001).
[**19**] T. Sugimoto *et al.*, J. Magn. Magn. Mater. **104-107**, 1845 (1992).
[**20**] P.J.H. Bloemen *et al.*, J. Magn. Magn. Mater. **93**, 105 (1991).
[**21**] C.H. Lee *et al.*, Phys. Rev. B **42**, 1066 (1990).
[**22**] H.Y. Zhang *et al.*, IEEE Trans. Magn. **29**, 3376 (1993).

Chapter 6
Magnetic Tunnel Junctions with [Co/Pt]-based electrodes

I. Introduction 108
I.A. MTJ's structure 108
I.B. Micromagnetic simulations and magnetic parameters of the materials 109
II. Magnetic properties in MTJs full stack 111
II.A. Magnetization reversal 111
II.B. Magnetic configurations 114
II.B.1. Influence of the applied magnetic field 114
II.B.2. Influence of the temperature 117
II.B.3. Calculated (H,T) phase diagram for the hard electrode 118
III. Transport properties in nano-patterned MTJs 119
III.A. Common features in perpendicular MTJs 119
III.A.1. Tunnel characteristics 119
III.A.2. R(H) characteristics 122
III.B. Phase diagrams in nano-patterned MTJs 124
III.B.1. Duplication of domains from the hard to the soft electrode 126
III.B.2. Spring magnet and exchange bias behavior 130
III.C. Coupling through the MgO barrier 131
IV. Conclusion 134
References 135

The [Co/Pt] multilayers, the structural and magnetic properties of which were discussed in the previous chapter, have been integrated as electrodes in magnetic tunnel junctions. This chapter, devoted to the [Co/Pt]-based MTs, is divided in two main sections. The first section presents the magnetic properties of MTJs full stacks, before nano-structuration. A specific attention is paid to the role of the hard electrode, constituted of a [Co/Pt] stacking magnetically hardened by a CoTb layer. The influence of the Pt thickness and temperature are especially investigated, both experimentally and via micromagnetic simulations.

The second section is devoted to the magneto transport properties of patterned MTJs, mostly driven by the magnetic layers in contact with the tunnel barrier. The transport measurements are focused on the tunnel characteristics and on the major and minor R(H) loops. These enable to study the effective tunnel polarization, to determine the Curie temperature in the [Co/Pt] multilayers (next chapter) and to analyze the coupling through the MgO barrier. The experimental (field, temperature) diagrams for R(H) characteristics highlight distinct behaviors closely related to the hard electrode magnetic response and original phenomena like domains' duplication and spring magnet behavior.

Thanks to the magnetic parameters extracted in the previous chapter, all magnetic behaviors can be reproduced and explained by micromagnetic 3D OOMMF simulations.

I. Introduction

I.A. MTJ's structure

The structure of the MTJs studied in this work is sketched in figure 1. The bottom and top electrodes consist in $[Co/Pt]_3/Co$ multilayers, separated by a 2.5nm thick MgO insulating barrier (the MgO thickness is the same for all the MTJs discussed in this chapter). The thickness of the Co layers is the same for all samples, equal to 0.6 nm. The thickness of the Pt layers varies between 0.49 nm and 2.19 nm. These electrodes are thus similar to the samples belonging to the sets A and B, previously discussed in chapter 5.

The top $[Co/Pt]_3/Co$ electrode has been magnetically hardened by a 20nm thick $Co_{86}Tb_{14}$ layer (referred to as CoTb in the following), an alloy that has been extensively investigated during M. Gottwald's PhD work[1]. Given its high anisotropy, the CoTb is used to pin one electrode by exchange coupling, so that it should be possible to get separate reversal for both electrodes and thus to obtain the total Tunnel Magneto Resistance value. After the growth, a 3 steps optical lithography process is used to pattern 30µmx30µm junctions and to take electrical contacts (Ta(5nm)/Pt(150nm) bilayer) on both sides of the MgO tunnel barrier.

Note: *During my PhD, I did not take part to the nano-patterning of the magnetic tunnel junctions. Therefore, no explanation about the nano-patterning process is given in this chapter but more details can be found in several other PhD manuscripts*[2,3].

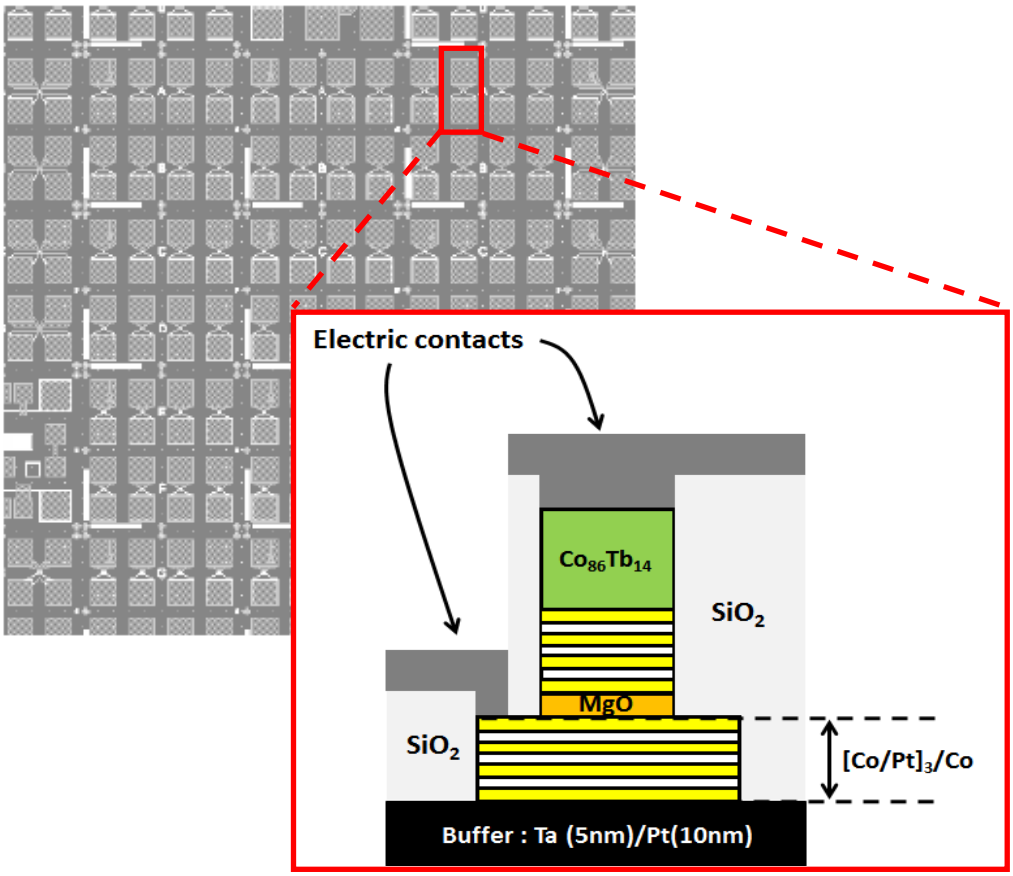

Figure 1: Sketch of the Magnetic Tunnel Junction with the bottom and top $[Co/Pt]_3/Co$ electrodes.

In the case where the tunneling of electrons through the barrier is only composed of a spin polarized tunneling channel, the effective tunnel polarization of the [Co/Pt] multilayers in contact with MgO ($P_{[Co/Pt]/MgO}$) can be extracted from the experimental TMR value using the Jullière's model[4]:

$$P_{[Co/Pt]/MgO} = \sqrt{\frac{TMR}{2+TMR}} \quad \text{(I-1)}$$

As it was shown in several previous studies, and especially in the paper by F. Montaigne *et al.*[5], the extracted polarization is not only related to the band structure of the electrode material but rather to the system electrode/barrier. The parabolic band model shows indeed that all the characteristics of the barrier have to be taken into account to define the polarization of an electrode, especially in the case of thin and low height tunnel barriers. But equation I-1 remains valid. Furthermore, the picture of separated electrodes is limited to resistive enough junctions. For low resistive junctions, it is necessary to consider the tunnel junction as a single entity. Therefore, to ensure separate electrodes, a 2.5 nm thick MgO barrier has been chosen with barrier heights above 1 eV.

I.B. Micromagnetic simulations and magnetic parameters of the materials

The magnetic response of the hard CoTb/$[Co/Pt]_3$/Co electrode has been simulated using the 3D OOMMF micromagnetic code. In order to reduce calculation time, a pillar of 50 nm x 50 nm has been considered with a cell size of 50 nm x 50 nm x 1 nm. The demagnetization field was not taken into account for this calculation. The multilayer stack used in the micromagnetic calculations is sketched in figure 2.

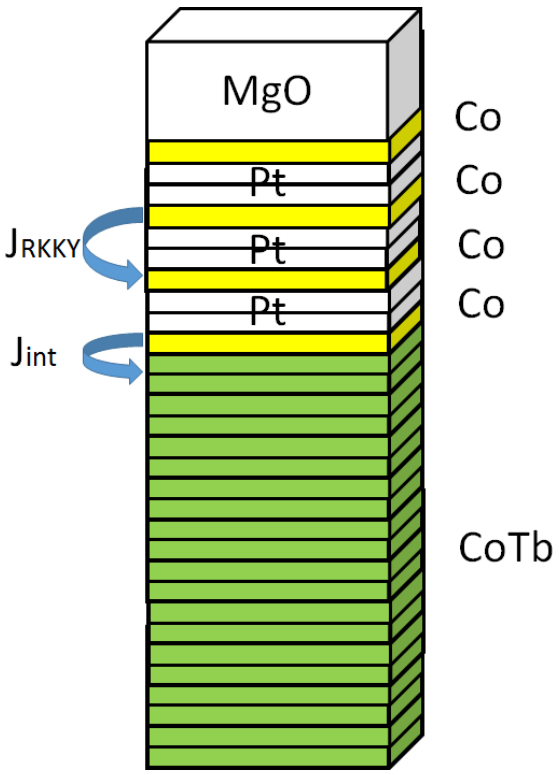

Figure 2: Multilayer stack used in the micromagnetic calculations.

As it has been mentioned, the magnetic properties of the CoTb alloy have been extensively studied in M. Gottwald's PhD work[1]. The exchange constant has been chosen equal to 6×10^{-12} J/m[1], and independent of temperature. While the saturation magnetization is known[1], the evaluation of the effective anisotropy is difficult since the magnetic fields to saturate the CoTb films in plane exceed the maximum fields available in our setups. It could be evaluated at room temperature but its variation with temperature has been inferred from the magnetic response of the CoTb/$[Co/Pt]_3$/Co multilayer and from literature[6]. The variations of CoTb saturation magnetization and effective anisotropy with temperature are given in figures 3 (a) and (b).

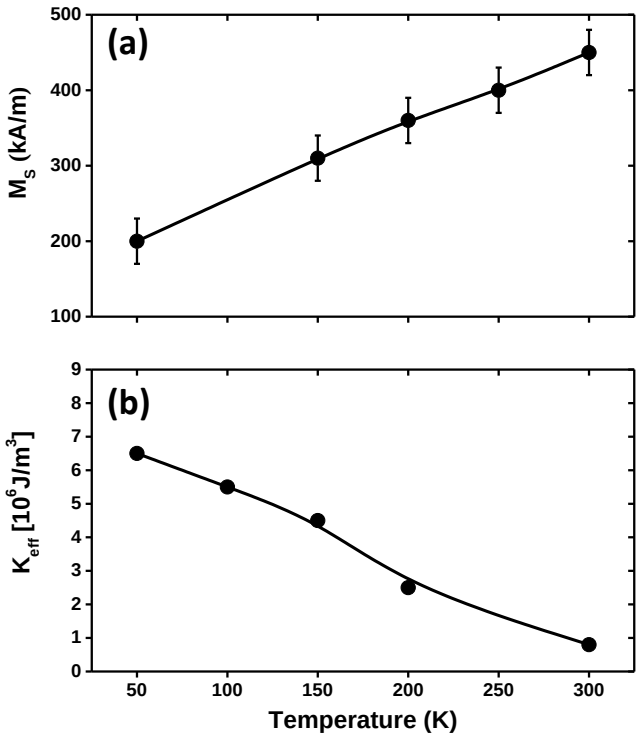

Figure 3: Magnetic properties of the $Co_{86}Tb_{14}$ alloy. (a) M_s measured as a function of temperature. (b) Effective anisotropy constant measured at room temperature and inferred at lower temperature from the magnetic response of the CoTb/$[Co/Pt]_3$/Co bilayer.

The [Co/Pt] multilayer was treated as 1 nm thick Co layers (i.e. thickness of one cell) coupled by a RKKY interaction through the Pt layers. The exchange constant in the Co layers has been chosen equal to 30×10^{-12} J/m, the usual parameter used in OOMMF, and independent of temperature. The saturation magnetizations and effective anisotropy fields have been extracted from measurements (see previous chapter). The RKKY exchange constant (J_{exch}) could be determined for the thickest Pt layers (i.e. 1.73 nm and 2.19 nm) from the shift of the $[Co/Pt]_3$ reversal observed by transport measurements of the nano-structured MTJs; this will be presented later in the chapter. For the thinnest Pt layers (i.e. 1.42 nm), the coupling constant has been deduced from the exchange spring response of the CoTb/$[Co/Pt]_3$/Co multilayer. Those exchange constants J_{exch} and their variations with temperature for the different Pt thicknesses are given in figure 4.

Finally, the temperature-independent exchange constant at the Co/CoTb interface J_{int} has been chosen equal to 15×10^{-12} J/m, an average value between the exchange constant in the CoTb and in the Co layers.

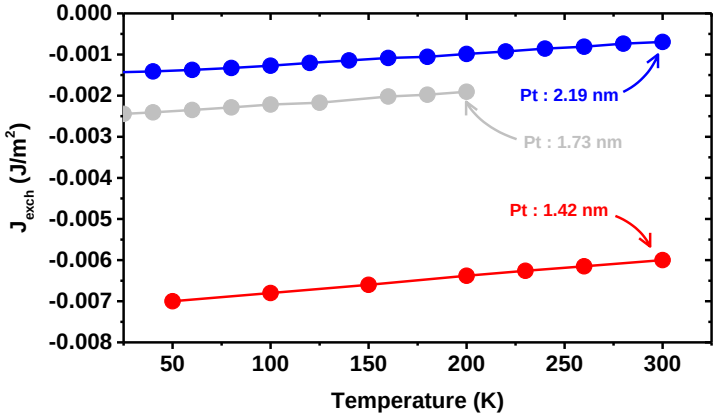

Figure 4: Temperature dependence of the RKKY interaction constant between Co layers through Pt for different Pt thicknesses (deduced from the magnetic response of the CoTb/[Co/Pt]$_3$/Co bilayer for the Pt thicknesses equal to 1.73 nm (grey) and 2.19 nm (blue) ; deduced from the exchange spring response of the CoTb/[Co/Pt]$_3$/Co multilayer for the Pt thickness of 1.42 nm (red)).

II. Magnetic properties in MTJs full stack

Before the lithography process, the magnetic response of the MTJs full stack has been studied using conventional magnetometry via the measurements of M(H) loops with the magnetic field applied perpendicular to the surface (the easy magnetization axis) and for temperatures between room temperature and 4K. This is an important step to understand the behavior of the multilayer stack. In the case of electronic transport measurements in MTJs, the results are indeed mainly or exclusively related to the magnetic response of the electrodes in contact with the tunnel barrier. The use of magnetometry brings information on the magnetic behavior of the whole system. Some particularly interesting features, observed for the CoTb/[Co/Pt]$_3$/Co hard electrode, turn out to be essential in the understanding of transport properties. These are reported below.

II.A. Magnetization reversal

Typical M(H) loops measured at room temperature with the magnetic field applied perpendicular to film plane are presented in figure 5 for Pt thicknesses smaller (top left) and larger (bottom left) than 1.73 nm.

These hysteresis loops are first typical of measurements along the easy magnetization axis, confirming the strong perpendicular anisotropy in these MTJs (in both [Co/Pt]$_3$/Co and CoTb layers). Several jumps and steps are observed during the field sweep corresponding to different magnetic configurations for the soft and hard electrodes. They are sketched in figure 5 (Right) in Ⓐ, Ⓑ, Ⓒ, Ⓓ and detailed below.

The magnetic behavior of the [Co/Pt]$_3$/Co multilayer in the soft electrode has been discussed in the chapter 5. Its magnetization reversal occurs in a single magnetic switch of the multilayer stack, whatever the Pt thickness, and is observed at low fields (switch from step Ⓐ to Ⓑ).

The magnetic response of the CoTb/[Co/Pt]$_3$/Co hard electrode however depends on the Pt thickness, as observed in figure 5 (Left). For Pt thicknesses smaller than 1.73 nm (top left), a single step is also observed (from Ⓑ to Ⓓ), corresponding to the total magnetization reversal of the hard electrode. For Pt thicknesses larger than 1.73 nm (bottom left), the hard electrode magnetization reversal occurs in two distinct steps (from Ⓑ to Ⓒ and from Ⓒ to Ⓓ). A close look at the jump

between Ⓑ and © reveals an amplitude of ¾ of the $[Co/Pt]_3/Co$ magnetization, suggesting a partial reversal of the $[Co/Pt]_3/Co$ in the $CoTb/[Co/Pt]_3/Co$ electrode: only three Co layers switch, the last Co layer being pinned by CoTb (sketch ©). Increasing the negative applied field finally drives the simultaneous reversal of the last Co layer in $[Co/Pt]_3/Co$ and of the CoTb layer.

From these two different behaviors in the hard electrode, it appears that the MTJs may exhibit different magnetic configurations depending on the Pt thickness: For Pt thicknesses smaller than 1.73 nm, the magnetizations of the electrodes are either parallel (Ⓐ and Ⓓ) or antiparallel (Ⓑ) depending on the applied magnetic field. For Pt thicknesses larger than 1.73 nm, there exists an (intermediary state where the magnetization in the hard layer becomes inhomogeneous and breaks in different parts: the magnetizations directly above and below the tunnel barrier are likely parallel, although the magnetization reversal in the hard layer is not completely achieved.

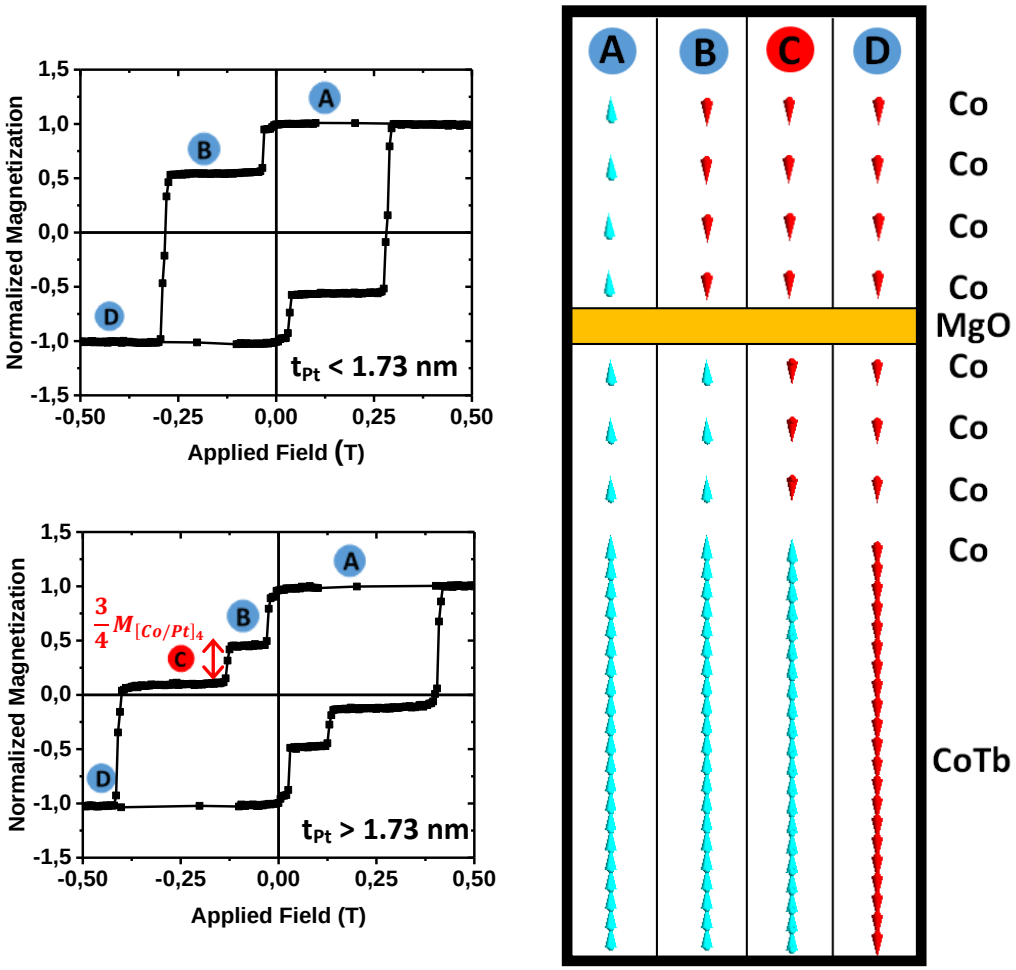

Figure 5: Left: M(H) loops measured at room temperature and with the field perpendicular to the plane for MTJs full stack with Pt thicknesses smaller (top) and larger (bottom) than 1.73 nm. Right: sketch of the different magnetization configurations for the soft and hard electrodes (micromagnetic calculations): Ⓐ parallel configuration, Ⓑ anti-parallel configuration with the reversal of the soft electrode, © intermediary step with the reversal of the $[Co/Pt]_3$ multilayers in the hard electrode, Ⓓ back to parallel configuration.

Discussion

The above results permit to get important information on the magnetization reversal in the hard electrode. (i) The $[Co/Pt]_3/Co$ multilayers cannot be considered neither as a uniform single magnetic layer nor as a single macro spin. The multilayer has to be modeled by four Co layers, ferromagnetically coupled by RKKY interaction, as it has been presented in section I.B. This conclusion is in agreement with the macrospin model developed in the chapter 4 and extended to the case of multilayers considering that each Co layer are independent and obey to the same law. It will play a crucial role in the micromagnetic simulations detailed later. (ii) The simultaneous reversal of the $[Co/Pt]_3/Co$ and CoTb magnetizations in the hard electrode depends on the strength of the coupling between the Co layers in the $[Co/Pt]_3/Co$ multilayer.

For "thin" Pt layers, the coupling between Co layers is strong. The reversal of the $[Co/Pt]_3/Co$ multilayer is complete and its reversal leads to the reversal of the CoTb layer. This is reproduced by the micromagnetic calculations in figure 6 (Pt thickness of 1.42 nm).

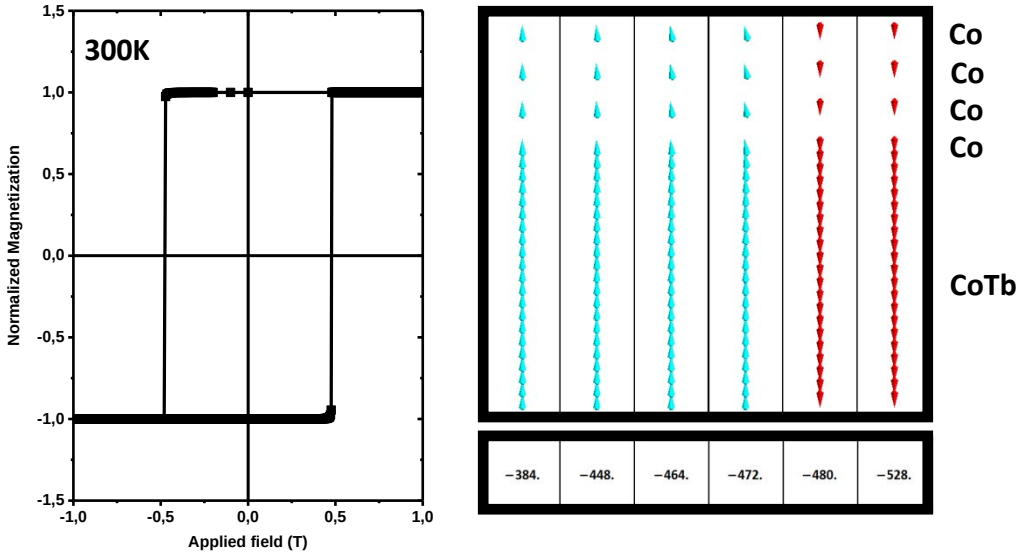

Figure 6: Left: Calculated M(H) loop for the CoTb/$[Co/Pt]_3/Co$ multilayer with 1.42 nm thick Pt layers. Right: magnetic configurations calculated for different applied fields in mT.

For "thick" Pt layers, as a result of the rapid decrease of the coupling when increasing the Pt thickness, only ¾ of the $[Co/Pt]_3/Co$ multilayer is reversed while the Co layer in contact with the CoTb is pinned along the CoTb magnetization. The Zeeman energy leads to the reversal of the three Co layers in the [Co/Pt] multilayers, the last Co layer switching with the CoTb layer at higher applied field. This behavior is also reproduced by the micromagnetic calculations of figure 7 (2.2 nm thick Pt layers). If the reversal is stopped for a field between -320 mT and -520 mT, while the CoTb layer has not switched, an exchange bias behavior could be observed.

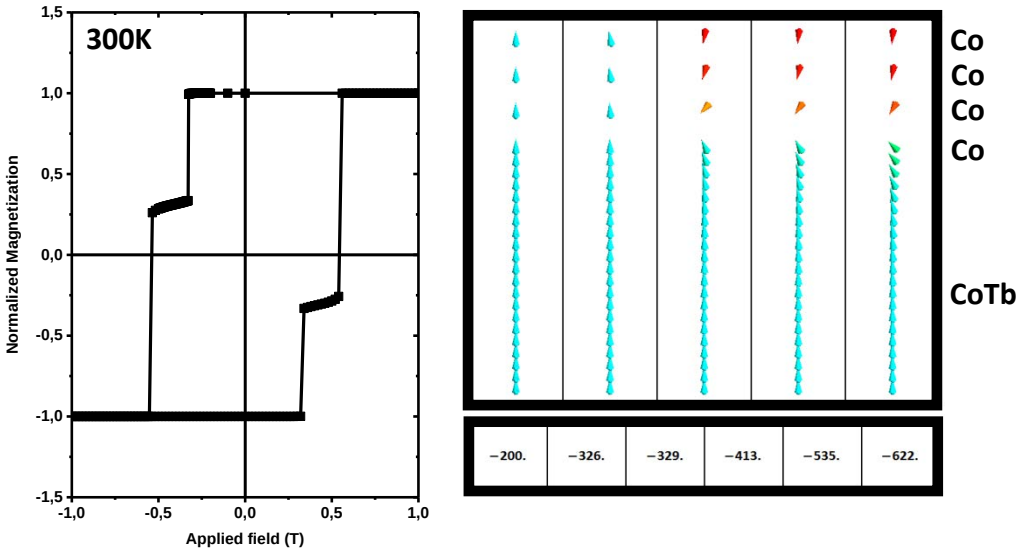

Figure 7: Left: Calculated M(H) loop for the CoTb/[Co/Pt]$_3$/Co multilayer with 2.19nm thick Pt layers. Right: magnetic configurations calculated for different applied fields in mT.

For all Pt thicknesses, using the amplitude of the magnetization reversal in the soft electrode (figure 5) and in either the hard electrode (figure 6) or the Co/CoTb multilayer (figure 7), it was possible to extract a CoTb saturation magnetization of 395 emu/cm^3. This value is close to the one measured and reported in figure 3.

II.B. Magnetic configurations

As we have seen, different types of magnetization reversal can be observed depending on the Pt thickness. In the following, we will show that, for a given Pt thickness, minor loops can lead to complex magnetic configurations. Starting from saturation under positive field, we will report on the influence of the maximum negative applied field value (in the following called H_{rev}) on the minor loop. We will also show that the temperature can strongly affect the magnetic properties of the MTJs full stack.

The results presented in this section are obtained for the $[Co_{0.6nm}/Pt_{1.42nm}]_3/Co_{0.6nm}$ based MTJ. This is a typical example and the different behaviors with H_{rev} and temperature can be extended to the whole studied Pt thickness range.

II.B.1. Influence of the applied magnetic field

The effect of a partial reversal of the hard electrode has been explored in measuring minor loops, i.e. in reversing the field before the complete reversal of the $[Co_{0.6nm}/Pt_{1.42nm}]_3/Co_{0.6nm}/CoTb_{20nm}$ electrode. After positive saturation, the field is decreased, reversed to negative values, stopped at H_{rev} before saturating the system under positive field again. Typical minor loops measured at room temperature are presented in figure 8 (a). For the sake of clarity, only two values of H_{rev} during the hard electrode reversal have been chosen here.

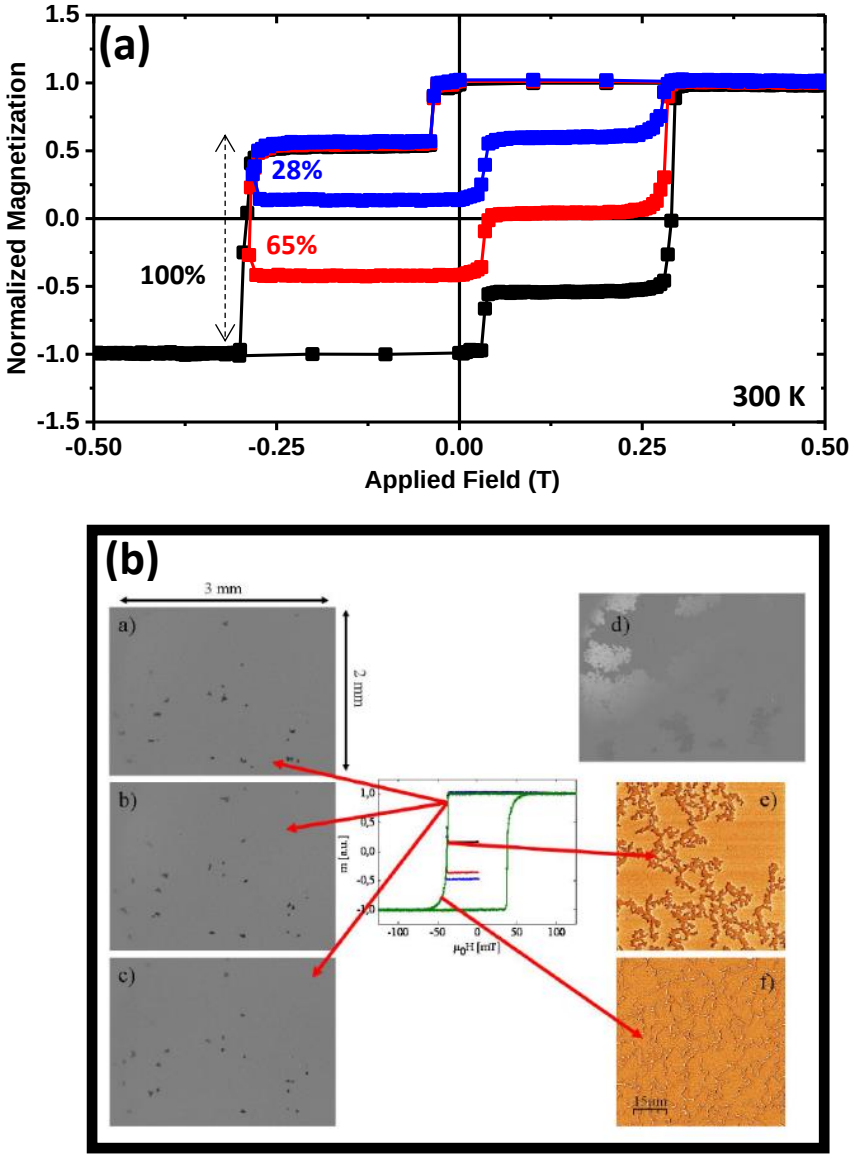

Figure 8: Top: M(H) loops measured at 300K for H_{rev} = -0.5 T (black squares), -287.5 mT (red squares) and -282.5 mT (blue squares). Bottom: Domains structure at remanence imaged by Kerr microscopy and MFM in a single $Co_{88}Tb_{12}$ layer[1].

The value of H_{rev} = -0.5 T is sufficient to observe the total reversal of both electrodes, leading to a symmetric M(H) loop, as it is presented in figure 5.

However, for smaller H_{rev} chosen during the reversal of the hard electrode, an intermediate magnetization state corresponding to this partial reversal is stabilized. The amplitude of the second jump gives a ratio of approximately 65% and 28% of reversed magnetization for H_{rev} = -287.5 mT and H_{rev} = -282.5 mT respectively. This ratio is conserved in the remanent state, i.e. after switching off the applied field. This specific property for the $CoTb_{20nm}$ /$[Co_{0.6nm}/Pt_{1.42nm}]_3/Co_{0.6nm}$ electrode is likely driven by the reversal mechanism in the CoTb layer. As shown in M. Gottwald PhD work, switching off the applied field during the reversal process freezes the magnetic configuration in a 20 nm thick $Co_{88}Tb_{12}$ layer, as illustrated in figure 8 (b). The domain structure persists at the remanence and is therefore responsible for the stabilization of the intermediary magnetization step in the CoTb M(H) loop.

The nucleation process in the hard electrode has been simulated using micromagnetic calculations. Using the room temperature parameters for 1.42 nm thick Pt layers, the calculation shows that the reversal starts in the top Co layer and propagates into the entire $[Co_{0.6nm}/Pt_{1.42nm}]_3/Co_{0.6nm}$ and $CoTb_{20nm}$ layers (figure 9).

The proposed scenario is thus first a nucleation in the top Co layer and a propagation into the $[Co_{0.6nm}/Pt_{1.42nm}]_3/Co_{0.6nm}$ and $CoTb_{20nm}$ layers with the formation of lateral domains. When the negative field is stopped before complete reversal and is switched back to zero, those domains are stabilized in the CoTb layer and in the $[Co_{0.6nm}/Pt_{1.42nm}]_3/Co_{0.6nm}$ multilayer in contact with CoTb.

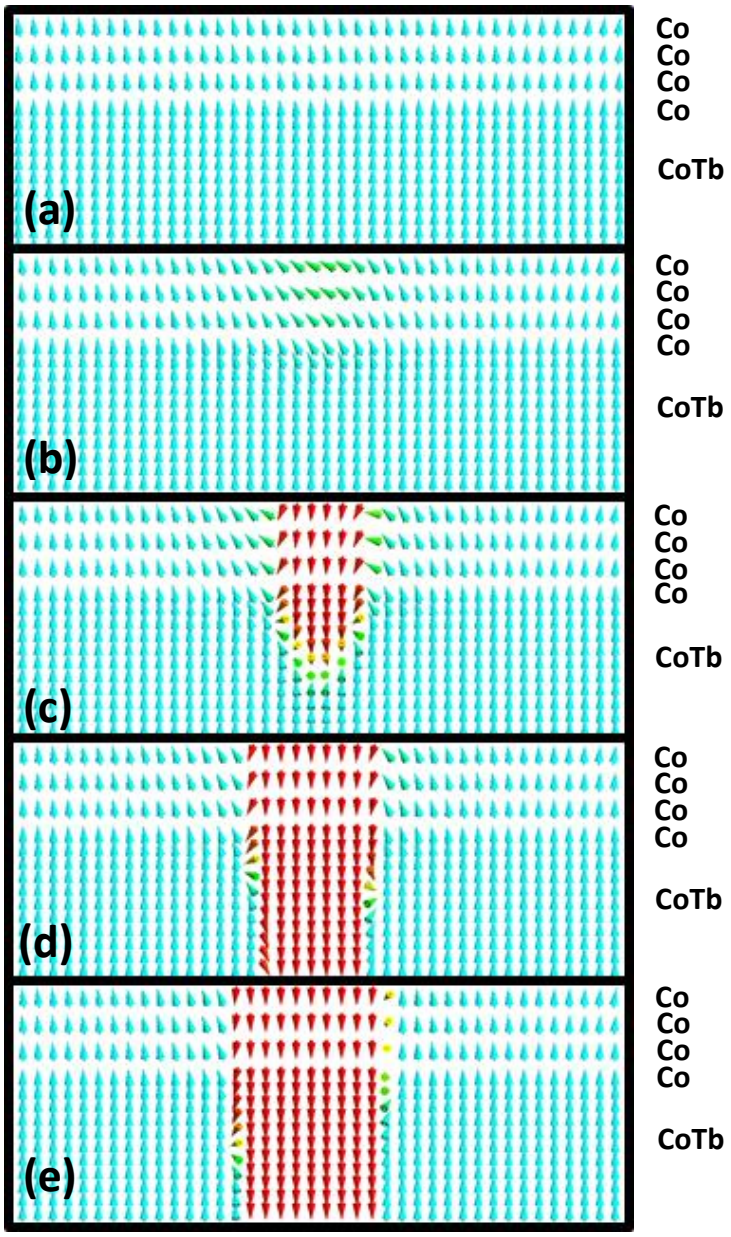

Figure 9: Nucleation of a reversed domain in the $CoTb_{20nm}$ /$[Co_{0.6nm}/Pt_{1.42nm}]_3/Co_{0.6nm}$ electrode. This simulation has been done on a 400 nm x 400 nm pillar with 5 nm x 5 nm x 1 nm cell size, taking the demagnetization energy into account (the nucleation thus occurs at the center of the pillar). The reversal starts in the top Co layer (b) and propagates into the entire $[Co_{0.6nm}/Pt_{1.42nm}]_3/ Co_{0.6nm}$ and $CoTb_{20nm}$ layers. (b), (c), (d) and (e) are obtained for the same applied field, as a function of time.

II.B.2. Influence of the temperature

The influence of temperature on the M(H) loops for the MTJs full stack has been studied between 300K and 45K. At 300K, the magnetization reversal for the MTJ with 1.42 nm thick Pt layers occurs in two steps associated to the two electrodes (figure 5 top): the hard electrode reverses as a single block since the $[Co_{0.6nm}/Pt_{1.42nm}]_3/Co_{0.6nm}$ multilayer is strongly coupled to $CoTb_{20nm}$ by direct exchange. When decreasing the temperature down to 150K and below, the reversal process in the hard electrode changes significantly, with the occurrence of two successive steps (figure 10 (a)). The smooth part (labeled C_i) suggests the creation of a spring magnet configuration in the $[Co_{0.6nm}/Pt_{1.42nm}]_3/Co_{0.6nm}$ multilayer in contact with CoTb. This was confirmed by micromagnetic calculations, as shown in figure 10 ((b) and right part).

This change in magnetic behavior of the hard electrode at low temperature is driven by the magnetic properties of the CoTb layer with temperature. When the temperature decreases, the $Co_{86}Tb_{14}$ magnetization decreases and its anisotropy increases[1]. In our case, the main consequences are a drastic increase of the effective anisotropy and of the coercive field in the CoTb layer, leading to its reversal for higher negative field values and to a higher restoring force when the $[Co_{0.6nm}/Pt_{1.42nm}]_3/Co_{0.6nm}$ multilayer magnetization starts reversing. This results in the formation of a spring magnet configuration.

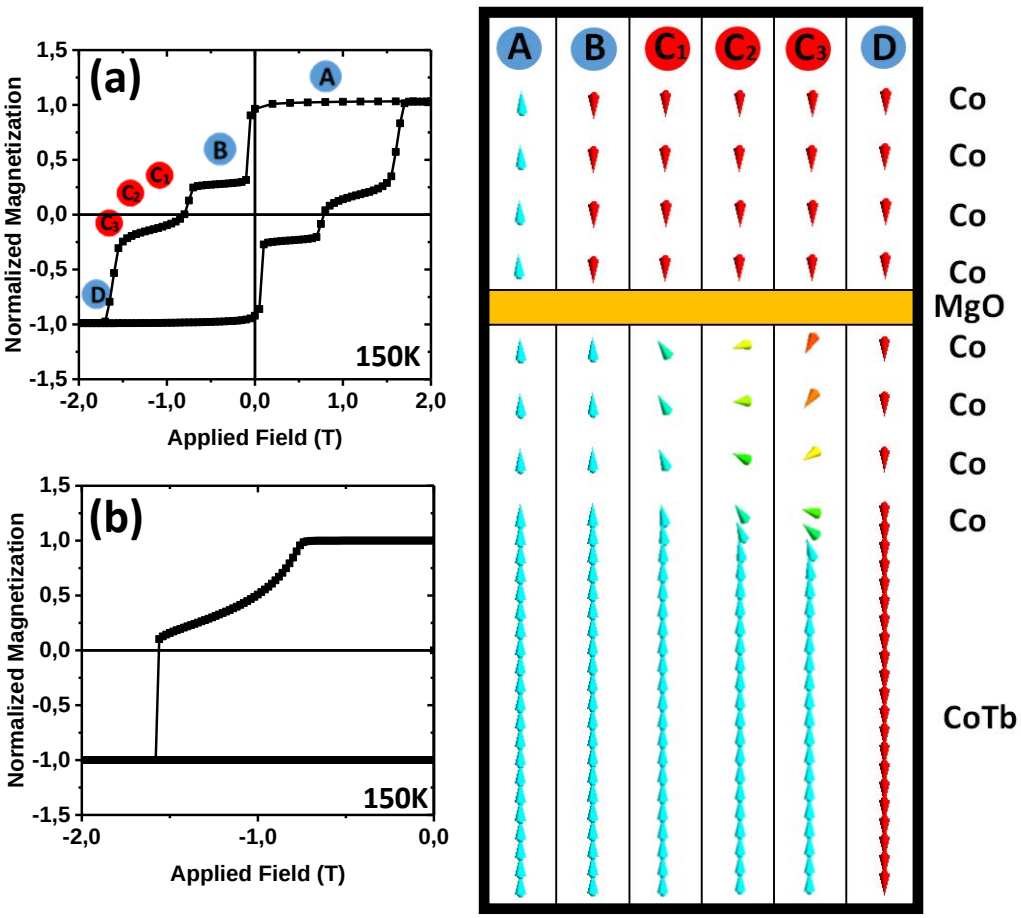

Figure 10: Left: (a) M(H) experimental loop for the MTJ full stack measured at 150K. (b) M(H) calculated for the $CoTb_{20nm}/[Co_{0.6nm}/Pt_{1.42nm}]_3/Co_{0.6nm}$ hard electrode at 150K. Right: Magnetic configurations for the soft and hard electrodes: Ⓐ parallel configuration, Ⓑ anti-parallel configuration after reversal of the soft electrode, Ⓒ 1, 2 and 3 reversal of the $[Co/Pt]_3/Co$ multilayer in the hard electrode by the creation of a spring magnet Ⓓ back to a parallel configuration.

II.B.3. Calculated (H,T) phase diagram for the hard electrode

The magnetic response calculated for the hard electrode can be summarized in a phase diagram as a function of temperature and applied field for a given Pt thickness. The calculated phase diagrams for the $CoTb_{20nm}/[Co_{0.6nm}/Pt_{1.42nm}]_3/Co_{0.6nm}$ and the $CoTb_{20nm}/[Co_{0.6nm}/Pt_{2.19nm}]_3/Co_{0.6nm}$ multilayers are reported in figure 11 top and bottom respectively. Those Pt thicknesses have been chosen because they are characteristic of the two main behaviors observed for the hard electrode in the present MTJs, as shown in the section II.A.

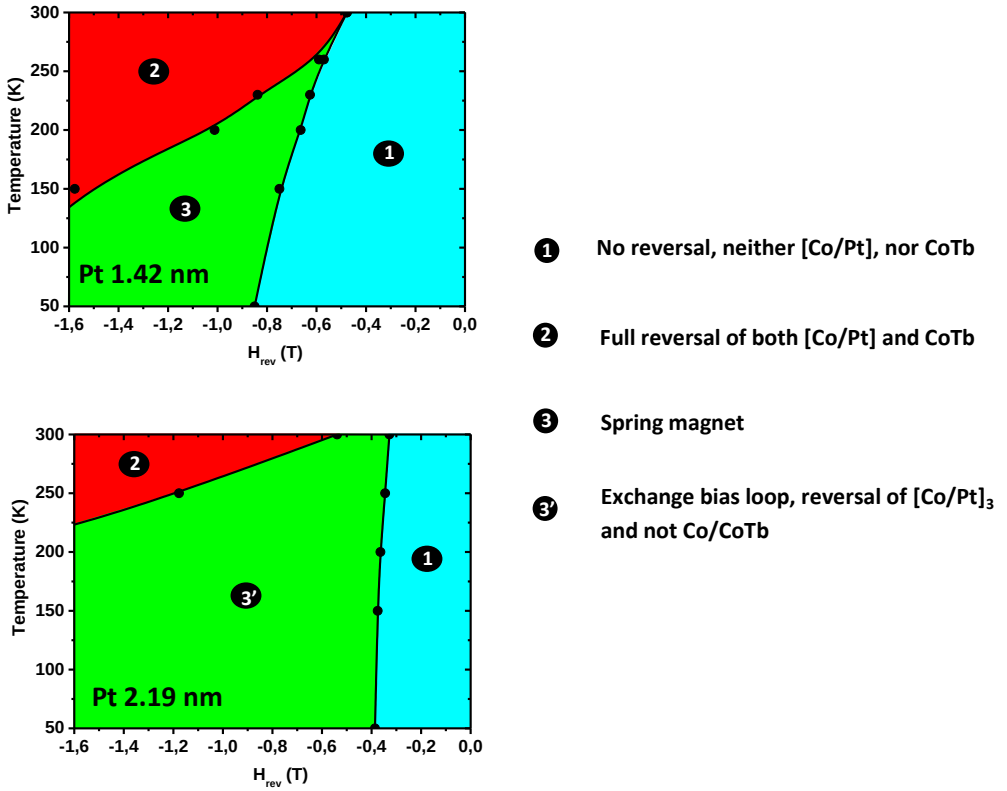

Figure 11: Calculated phase diagrams for the hard electrode with (top) 1.42 nm thick and (bottom) 2.19 nm thick Pt layers (micromagnetic calculations using the magnetic parameters of $[Co_{0.6nm}/Pt_{1.42nm}]_3/Co_{0.6nm}$ and $[Co_{0.6nm}/Pt_{2.19nm}]_3/Co_{0.6nm}$ multilayers reported in the chapter 5).

Both phase diagrams exhibit several different areas presented in different colors (blue, red and green) and with different numbers (1,2 and 3 or 3') which correspond to the different magnetic behaviors of the hard electrode described in the previous sub-sections.

In the "blue" areas (small H_{rev}), the magnetic field is not strong enough to reverse neither the $[Co/Pt]_3/Co$, nor the CoTb layer of the hard electrode. The full $CoTb/[Co/Pt]_3/Co$ magnetization resists to the applied field. In the MTJ, this should lead to a symmetric minor M(H) loop corresponding to the reversal of the soft electrode only.

In the "red" areas (large H_{rev} and high temperature), the magnetic field is strong enough to reverse both the $[Co/Pt]_3/Co$ and the CoTb layer of the hard electrode. The full $CoTb/[Co/Pt]_3/Co$ multilayer reverses, which should lead to a symmetric major M(H) loop with complete reversal of both hard and soft electrodes in the MTJ structure.

The "green" areas (middle range H_{rev} and low temperature) correspond to a magnetic configuration where the CoTb didn't reverse and the $[Co/Pt]_3/Co$ multilayer partially reversed. This

results from the strong increase of the anisotropy constant and from the decrease of the saturation magnetization of the CoTb layer when the temperature decreases (figure 3). Depending on the Pt thickness, two different magnetic behaviors, labeled as 3 and 3', are predicted. For "thin" Pt layers (green area 3), the total reversal of the CoTb/$[Co/Pt]_3$/Co hard layer occurring at room temperature is replaced at low temperature by a progressive and reversible reversal of the $[Co/Pt]_3$/Co multilayer. Considering the strong RKKY interaction in the $[Co/Pt]_3$/Co multilayer, the cost in exchange energy is distributed all over the multilayer and an exchange spring behavior is predicted (figure 10). For "thick" Pt layers (green area 3'), the reversal of the CoTb/$[Co/Pt]_3$/Co hard electrode occurs in two steps as a result of the rapid decrease of the RKKY coupling between the Co layers in $[Co/Pt]_3$/Co. The $[Co/Pt]_3$ part reverses first, followed, if the applied field is sufficient, by the Co/CoTb part (figure 7). The cost in exchange energy is located at one Co/Pt interface. The magnetic reversal of the $[Co/Pt]_3$ part is then not reversible and an exchange bias behavior can be predicted.

III. Transport properties in nano-patterned MTJs

In previous sections (chapters 5 and 6), the magnetic properties of the soft and hard electrodes have been studied by magnetometry both as single independent systems and in the MTJs full stack. Micromagnetic simulations performed in using magnetic parameters extracted from experiments could nicely reproduce experimental observations.

The next step consists in exploring the magneto-transport properties in patterned MTJs. The aim is first to investigate how the various magnetic behaviors described in section II could affect the transport properties and give rise to interesting and original features. The magneto-transport properties are also a fine probe of the magnetic configurations in direct contact with the insulating barrier, and thus constitute a powerful tool to complement magnetometry and micromagnetic simulations. Finally, in the general context of this work, a specific attention has been paid to determine the tunnel polarization of the [Co/Pt] based electrodes. This last aspect will be developed in further details in the next chapter.

The electronic transport characteristics have been measured in using an "home made" setup controlled by a Labview interface and composed of a cryostat for the low temperatures measurements (down to 20K), a two probes device for the electrical measurements and an electromagnet that can deliver a magnetic field of ±1.8T.

III.A. Common features in perpendicular MTJs

III.A.1. Tunnel characteristics

As a first step to characterize the MTJs, the conductance (G) versus voltage (V) characteristics have been measured and fitted using a polynome of V:

$$G = A + B \cdot V \quad + C \cdot V^2 \qquad \textbf{(I-2)}$$

Thanks to the Brinkman's model[7], the different parameters of the tunnel barrier, especially its thickness, height and height asymmetry, can be extracted from the A, B and C constants. The fit is limited to low applied voltages since the Brinkman's model is valid only in the case of trapezoidal barrier and for low voltages compared to the height of the barrier. Figure 12 presents the G(V) characteristic measured at room temperature for the $[Co_{0.6nm}/Pt_{1.73nm}]_3/Co_{0.6nm}$ based MTJ and the fit using equation (I-2). The trend reported here for one tunnel junction is the general trend observed for all MTJ's, independently on the Pt thickness.

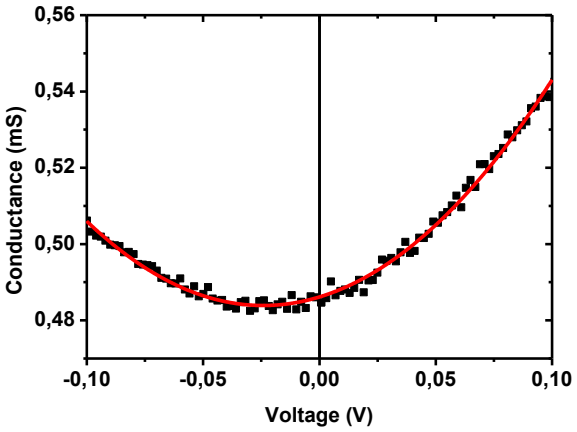

Figure 12: Conductance versus voltage characteristic extracted from current versus voltage characteristic at room temperature (black squares) and its fit using equation (I-2) (red curves). The electrodes are made with a $[Co_{0.6nm}/Pt_{1.73nm}]_3/Co_{0.6nm}$ multilayer.

The non-linearity of the current versus voltage characteristics is a prerequisite of a tunnel behavior for the electrons[8]. The barrier average parameters extracted from the Brinkman's model applied to several tunnel junctions are the following: thickness $d = 1.6\ nm$; mean barrier height $< \phi >= 1.05\ eV$ and barrier asymmetry $\Delta\phi = 0.5\ eV$. As a result, and for all the tunnel barriers, the barrier's shape is trapezoidal at zero applied voltage, with a barrier height at the bottom interface ($\Phi_b = 1.3\ eV$) higher than the barrier height at the top interface ($\Phi_t = 0.8\ eV$).

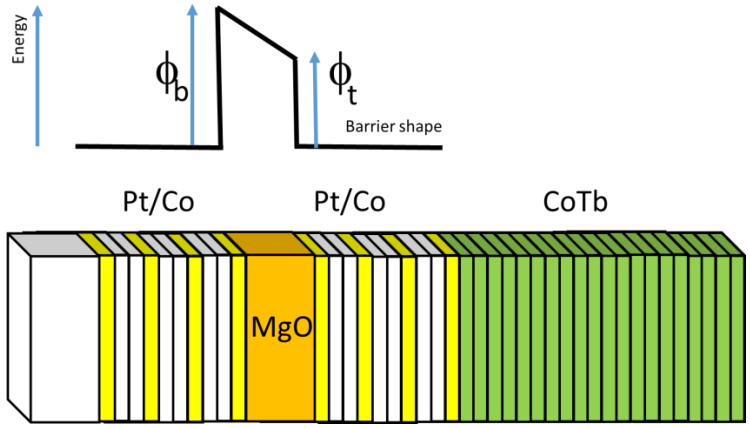

Figure 13: Potential energy seen by the electrons during the tunnel process and corresponding multilayer stack. The potential through the barrier is trapezoidal with the highest potential at the bottom interface.

The origin of the strong asymmetry $\Delta\phi$ in the height of the barrier is not clear and somehow surprising. It could be justified either by different crystalline structures for the Co layers below and above the MgO barrier, by a different density of states at both interfaces or by different work functions for the two electrodes (we can expect that Co is not continuous when deposited on MgO, see chapter 5).

In order to use equation (I-1) to determine the effective tunnel polarization of the [Co/Pt] stacking in contact with MgO, the temperature dependence of spin-polarized tunneling has to be investigated to extract the non-polarized contribution to the conductance G_{SI}. We use the formalism developed by C. H. Shang *et al.*[9] who showed that the total conductance can be expressed by:

$$G(\theta) = G(T)\{1 + P_1(T)P_2(T)\cos(\theta)\} + G_{SI}(T) \quad \textbf{(III-3)}$$

where θ is the angle between the magnetization directions of the two electrodes, $P_1(T)$ and $P_2(T)$ are the effective tunneling electron spin polarizations of the ferromagnetic electrodes, $G_{SI}(T)$ is the non-polarized contribution to the conductance and $G(T)$ is the direct elastic tunneling prefactor defined as:

$$G(T) = G_0 \, {}^{CT}/_{\sin(CT)} \quad \textbf{(III-4)}$$

where G_0 is a constant and $C = \frac{d}{\sqrt{\phi}} 1.387 \times 10^{-4}$ with d the barrier thickness in angstroms and ϕ the barrier height in eV.

The dominant part of conductance is elastic, spin-polarized tunneling between the two ferromagnetic electrodes, each with an electron polarization *P* that decreases with increasing *T* due to thermally excited spin waves. The variation of the electron polarization was expected to follow the Bloch law $P_{eff}(T) = P_0(1 - \alpha T^{3/2})$, where α is the material dependent constant and P_0 the spin polarization at 0K[9]. The second part of conductance is due to assisted, spin-independent tunneling, that can vary with temperature.

In a first step, the parameters related to the spin-polarized part of G can be determined in fitting:

$$\Delta G = G(180°) - G(0) = 2G(T)P_1(T)P_2(T) \quad \textbf{(III-5)}$$

G(180°) and G(0°) are the conductances measured for respectively antiparallel and parallel orientations of magnetizations in the ferromagnetic electrodes. The plot of ΔG for different voltages and their fits are reported in figure 14.

The fitting process was first to let the β exponent in $P_{eff}(T) = P_0(1 - \alpha T^{\beta})$ a free parameter and to keep G(T) constant. The result of the fit was β=3/2 showing that the Bloch law is followed in our case. β was then fixed to 3/2 and it turned out that the extracted G(T) is constant. This result is somehow surprising. Indeed, using the parameters extracted from the Brinkman fit and equation (III-4), a variation of 5% is predicted. For a Pt thickness of 1.73nm, $\alpha = 5.086 \times 10^{-5} \, K^{-3/2}$, which corresponds to a T_c = 653.5 K if $\alpha = 1/T_C^{3/2}$.

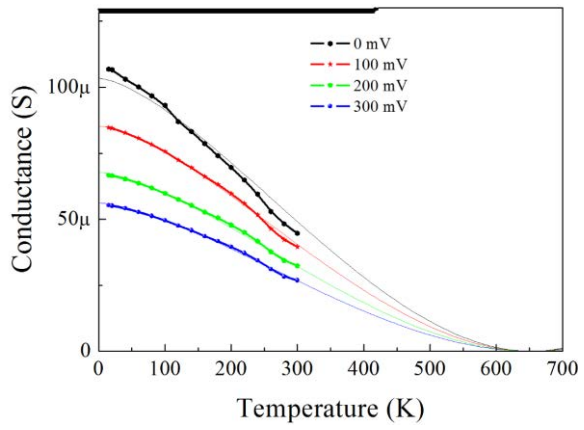

Figure 14: Temperature dependence of ΔG for different applied voltages. The experimental points are represented using dots connected with bold lines. The fits are represented by thin lines. (The electric characteristics have been made on $[Co_{0.6nm}/Pt_{1.73nm}]_3/Co_{0.6nm}$ multilayer based magnetic tunnel junctions).

Using the parameters deduced from the first step, the second step consisted in extracting the non-polarized contribution to the conductance by fitting: $G(0°) = G(T)\{1 + P_1(T)P_2(T)\} + G_{SI}(T)$ and $G(180°) = G(T)\{1 - P_1(T)P_2(T)\} + G_{SI}(T)$ (figure 15). The $G_{SI}(T)$ contribution was well reproduced and fitted using a T^2 variation law. This variation was predicted by L.I. Glazman *et al.*[10] in an inelastic tunneling process through a single localized state when the electron-phonon interaction is weak but sufficient to enlarge the tunneling resonance peak. It exists thus a non-polarized inelastic channel, the conductance of which varies between 0% at low T and 10% at room T of the elastic, spin-polarized tunneling channel.

The experimental TMR value in the Jullière's model[4] has to be modified accordingly:

$$P_{[Co/Pt]/MgO} = \sqrt{\frac{TMR\left(1+{}^{G_{SI}(T)}/_{G(T)}\right)}{2+TMR\left(1+{}^{G_{SI}(T)}/_{G(T)}\right)}} \qquad \textbf{(III-6)}$$

In the case of the present MTJs, considering that G_{SI} equals zero yields an under-estimation of the spin polarization of the ferromagnetic electrode at room temperature by 5% to 10%. Another consequence is the overestimation of the value of α.

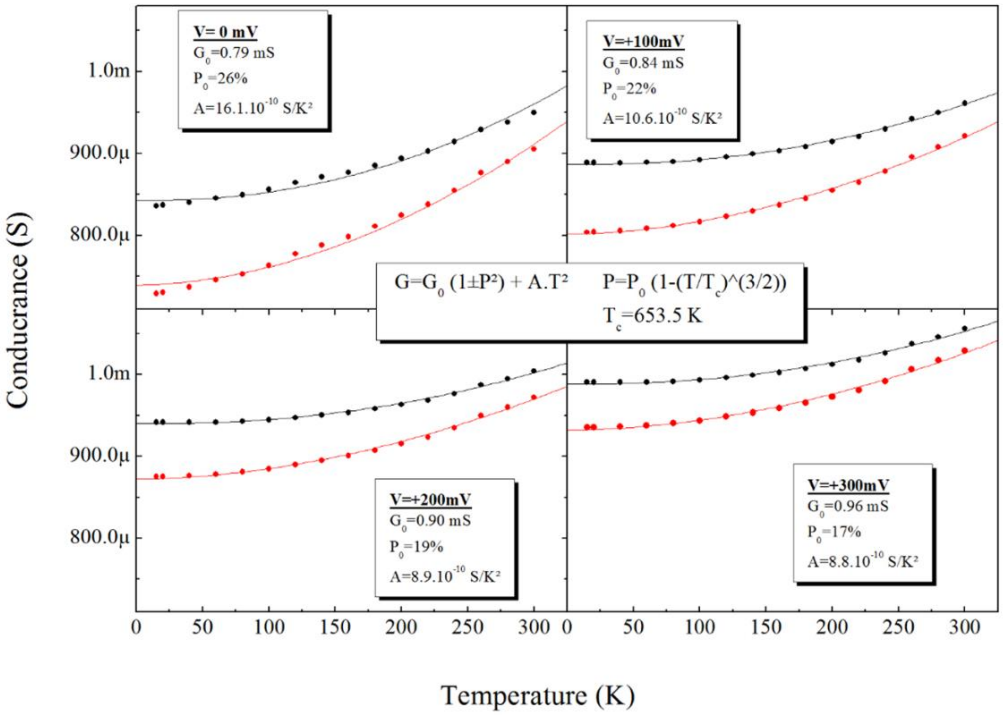

Figure 15: Temperature dependence of G(0°) (black curves) and G(180°) (red curves) for different applied voltages. The dots represent the experimental points and the lines represent the numerical fits. (The electric characteristics have been measured on $[Co_{0.6nm}/Pt_{1.73nm}]_3/Co_{0.6nm}$ multilayer-based magnetic tunnel junctions).

III.A.2. R(H) characteristics

The R(H) characteristics were measured with the applied field along the easy magnetization axis (perpendicular to the MTJs' plane). The R(H) curves measured at room temperature for the $[Co_{0.6nm}/Pt_{1.42nm}]_3/Co_{0.6nm}$ based MTJ are presented in figures 16 left (a) and (b), respectively for H_{rev} = -0.5 T and H_{rev} = -0.2 T. The different magnetic configurations calculated for the soft and hard electrodes are sketched in figure 16 right.

Several steps and jumps are observed in figure 16 (a) and can be correlated to the magnetization jumps observed in figure 5 (top left) for the MTJ full stack. For the high positive applied field values, the low resistance state corresponds to a parallel configuration for the magnetization of both electrodes (sketch Ⓐ). When decreasing the applied field to negative values, a first jump is observed and corresponds to the reversal of the soft electrode (sketch Ⓑ). The magnetizations of both electrodes are antiparallel and thus the resistance becomes high. A further increase of the negative applied field leads to the reversal of the hard electrode and the MTJ goes back to a low resistance state (sketch ©). The symmetric behavior is observed when sweeping the field from negative to positive values.

If the magnetic field is stopped after the first resistance jump and switched back to positive values, the system stays in a high resistance state until the positive field is high enough to drive back the magnetization reversal in the soft electrode. Only the reversal of the soft electrode is observed (figure 16 (b)).

These two main behaviors, major and minor R(H) loops, have been observed at room temperature for all the measured MTJs, whatever the Pt thickness and the reversal mechanism in the hard electrode. Consequently, the parallel and antiparallel states are well defined, the TMR can be measured and the effective [Co/Pt]/MgO polarization can be extracted using the Jullière's model.

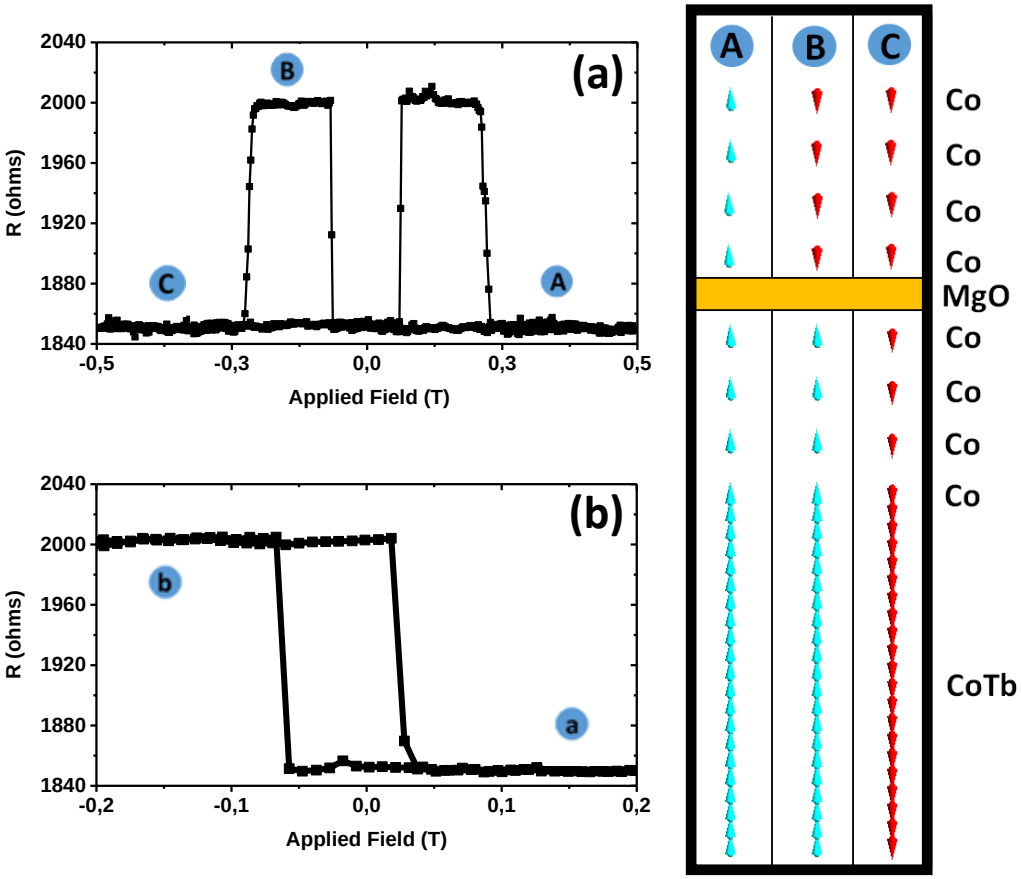

Figure 16: Left: R(H) characteristics measured at room temperature for a reversed field H_{rev} of (a) -0.5 T and (b) -0.2 T. Right: magnetic configurations of the soft and hard electrodes: Ⓐ parallel state, Ⓑ reversal of the soft electrode (anti-parallel state), © back to a parallel state with the reversal of the hard electrode.

Note: *During the nano-patterning via the lithography process, the MTJ full stack is exposed to temperature up to 180°C. It is well known that the RE-TM compounds are sensitive to the temperature annealing*[11] *and therefore the magnetic properties of the hard electrode are modified. In the case of CoTb alloys, the PMA is kept but a decrease of the coercive field is reported*[1]*. This decrease in CoTb coercive field leads to the decrease of the coercive field of the hard electrode in the nano-patterned MTJs. This difference between full stack and patterned MTS can be observed between the M(H) loops in figure 5 and the R(H) loops in figure 16.*

III.B. Phase diagrams in nano-patterned MTJs

The magnetic properties and magnetic parameters in independent [Co/Pt] multilayers could be determined in the chapter 5. These permitted to partly explain the magnetic response of MTJs full stack (chapter 6, section I). Then, a specific attention has been paid to the complex hard electrode for which the Pt thickness and temperature may strongly affect the magnetization reversal. Calculated (H,T) phase diagrams of the magnetic configurations in the hard electrode for different Pt thicknesses could predict the magnetic behaviors in MTJs full stack.

Similar (H_{rev},T) phase diagrams have been experimentally measured for nano-patterned MTJs by systematic R(H) transport measurements on the $[Co_{0.6nm}/Pt_{1.42nm}]_3/Co_{0.6nm}$, $[Co_{0.6nm}/Pt_{1.73nm}]_3/Co_{0.6nm}$ and $[Co_{0.6nm}/Pt_{2.19nm}]_3/Co_{0.6nm}$ based magnetic tunnel junctions. These are reported in figure 17 (left part). A close agreement between experimental (left) and calculated (right) phase diagrams is observed.

As predicted in the calculated phase diagram, several distinct behaviors are experimentally observed and correspond to different R(H) characteristics as a function of temperature and H_{rev}. For the three Pt thicknesses, the phase diagrams present the usual common R(H) characteristics presented in figures 16 (a) and (b), i.e. the symmetric major and minor loops observed in the “red” and “blue” areas respectively. The “green” areas have been also predicted. In these field and temperature ranges, the CoTb magnetization does not reverse, leading to the occurrence of a spring magnet or exchange bias loop, as it will be described in further details in section III.B.2.

However, two new areas (“orange” and “yellow”) appear in the MTJs’ experimental phase diagrams. These were not predicted in calculated phase diagrams for the hard electrode and should be thus specific to tunnel properties and/or to the MTJ’s structure. The “orange” area appears between “red” and “blue” areas while the “yellow” area appears between “red” and “green” areas. As reported in figure 8, stopping and reversing the field during the magnetization reversal of a single CoTb layer leads to the stabilization of domains at zero applied field. The density of reversed domains depends on the maximum negative applied field H_{rev} after positive saturation. Such a phenomenon likely occurs during the reversal of the hard electrode, generating a non-homogeneous stray field on the soft electrode. This results in the occurrence of original behaviors in these “orange” and “yellow” areas, as described in the following paragraphs.

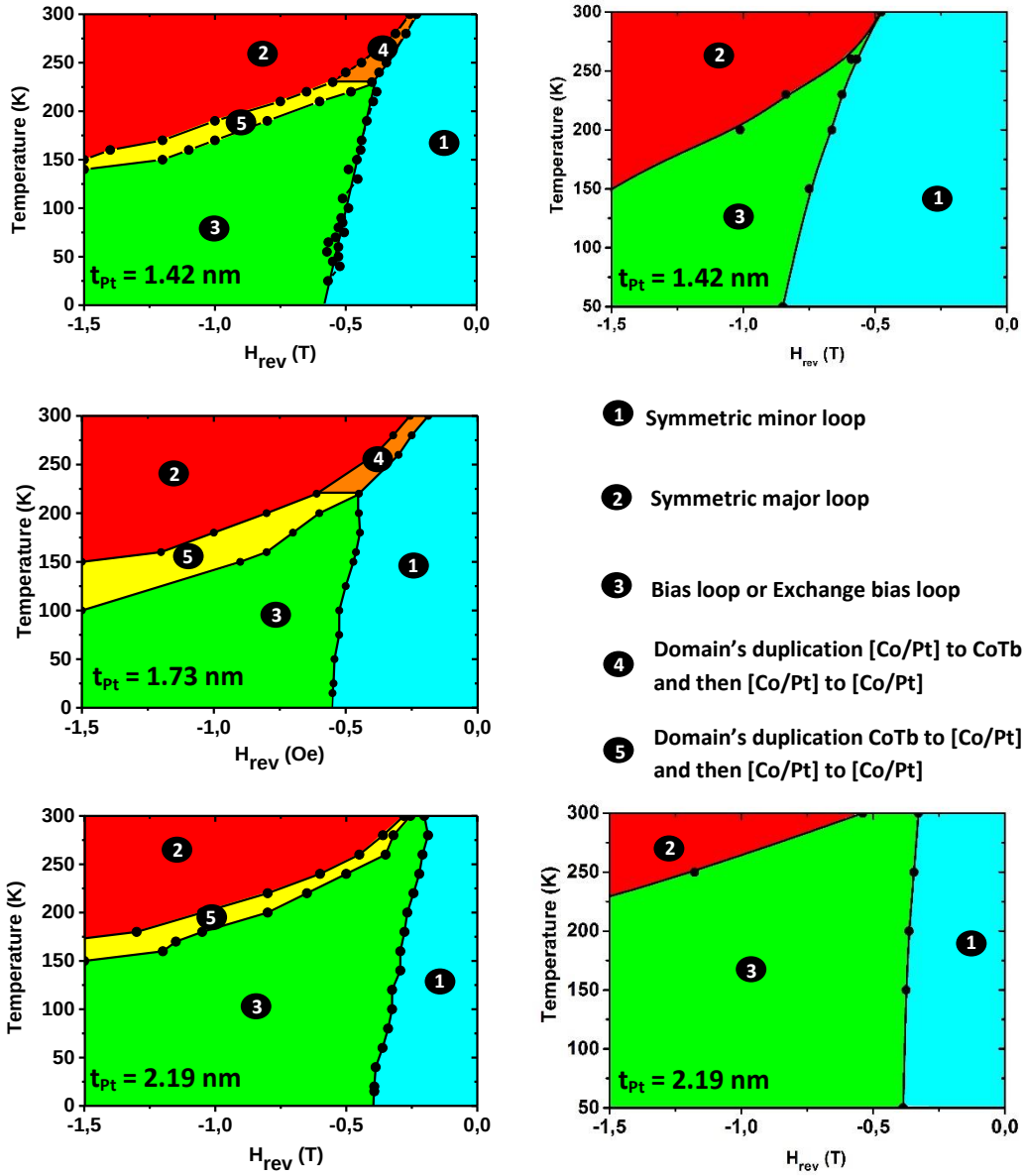

Figure 17: Left: Experimental phase diagrams of the [$Co_{0.6nm}$/$Pt_{1.42nm}$], [$Co_{0.6nm}$/$Pt_{1.73nm}$] and [$Co_{0.6nm}$/$Pt_{2.19nm}$] based MTJs (R(H) behavior versus temperature and H_{rev}). Right: Calculated phase diagrams of the [$Co_{0.6nm}$/$Pt_{1.42nm}$] and [$Co_{0.6nm}$/$Pt_{2.19nm}$] based hard electrodes (M(H) behavior versus temperature and H_{rev}).

III.B.1. Duplication of domains from the hard to the soft electrode

The accurate investigation of the R(H) behaviors in the orange and yellow areas (figure 18 (a) and (b) respectively) has permitted to identify a specific phenomenon corresponding to the duplication of magnetic domains from the hard electrode to the soft electrode. Such an effect has been previously reported only in the case of in-plane magnetized spin-valves and MTJs[12]–[14].

Two different domain duplication processes have been identified, depending on the Pt thickness and temperature (figures 18 (a) and (b) for orange and yellow areas respectively). For the sake of clarity, only the symmetric major loop (black) and the loop measured for one value of H_{rev} (red) are reported. These measurements have been performed at 300K and 190K for the $[Co_{0.6nm}/Pt_{1.42\ nm}]_3/\ Co_{0.6nm}$ based MTJs.

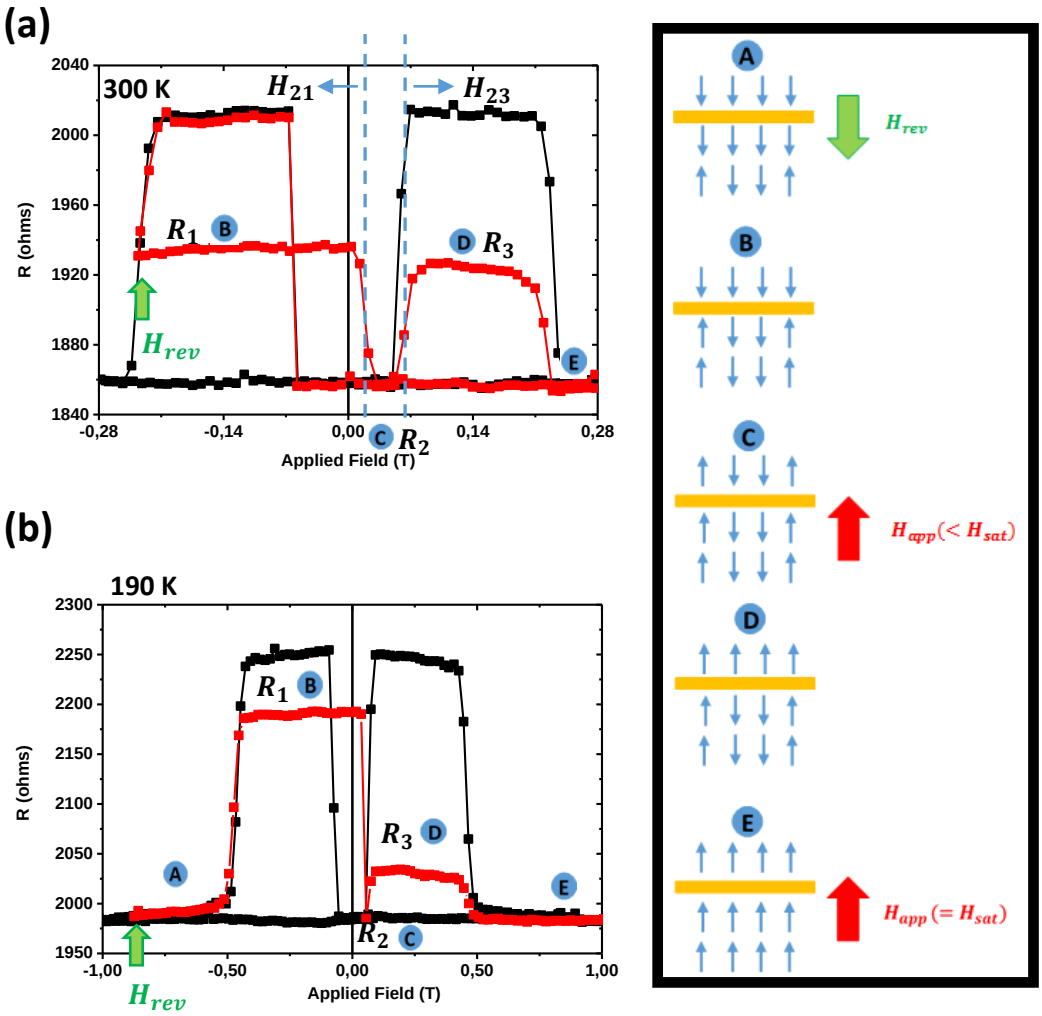

Figure 18: Major loops (black squares) and minor loops (red squares) measured for the $[Co_{0.6nm}/Pt_{1.42\ nm}]_3/Co_{0.6nm}$ based MTJ at (a) T=300K and H_{rev} = -0.236T and (b) T= 190K and H_{rev} = -0.877T. The magnetic configurations for the different resistance steps are sketched in Ⓐ, Ⓑ, Ⓒ, Ⓓ, Ⓔ and detailed in the text.

Several resistance steps and jumps are observed in figures 18 (a) and (b), and correspond to different magnetic configurations of the soft and hard electrodes. In Ⓐ, Ⓒ and Ⓔ, the low resistance state reveals a parallel configuration of both electrodes magnetizations. In Ⓑ and Ⓓ, the intermediate resistance states are signature of coexisting parts where the electrodes magnetizations are either in a parallel or antiparallel configuration.

Domains' duplication process in the "orange" area

Once the MTJ magnetization is saturated under a magnetic field of +1.5T, the applied field is decreased to zero and reversed. Increasing the negative applied will leads first to the reversal of the soft [Co/Pt] magnetization.

When H_{rev} enters in the field range where the reversal of the hard electrode occurs, magnetic domains form in the $[Co/Pt]_3/Co$ multilayer in contact with CoTb and propagate into the CoTb layer in a dynamical process (figure 9 and figure 18 (a), sketch Ⓑ). The magnetization in these domains is parallel to the magnetization of the soft electrode and as a result, increasing the value of H_{rev} progressively reduces the junction resistance to the low resistance measured when the magnetizations of both electrodes are parallel.

However, if H_{rev} is chosen during the hard electrode reversal and the applied field is brought back to zero, the junction resistance is kept at an intermediate value R_1, the resistance measured under the applied field H_{rev}. As the single CoTb layer, the $CoTb/[Co/Pt]_3/Co$ multilayer obviously keeps the domain structure stabilized at H_{rev}. When the applied magnetic field is reversed to positive values, the magnetic moments of the $[Co/Pt]_3/Co$ soft electrode are submitted to a space-dependent magnetic field.

The magnetization of the soft electrode under regions where the magnetization of the hard electrode is oriented along the applied field is submitted to an effective field equal to the applied field plus the magnetic stray field of the hard layer: those regions reverse first for a magnetic field H_{21}. In this state Ⓒ, the MTJ resistance goes back to the low value R_2 proving that the multi-domain structures of both electrodes are perfectly parallel (sketch Ⓒ) and suggesting that the domain walls don't contribute to the TMR, as it will be discussed later. This phenomenon where the multi-domain structure of the hard electrode is "printed" to the soft electrode is called domains' duplication.

The magnetization of the soft electrode under regions where the magnetization of the hard electrode is oriented antiparallel to the applied field is submitted to an effective field equal to the applied field minus the magnetic stray field of the hard layer: those regions will reverse in a second step, for a larger applied field H_{23}. The magnetic configuration of the soft electrode turns to be perfectly mono-domain again, whereas the domain structure persists in the hard electrode. This results again in coexisting areas where both electrodes magnetizations are either parallel or anti-parallel (sketch Ⓓ), giving rise to another intermediary resistance state R_3 in the positive field region.

Finally, by further increasing the positive applied field, the domain structure in the hard electrode disappears and the MTJ recovers its low, parallel resistance state (sketch Ⓔ).

Note: *The amount of reversed and non-reversed domains in the* hard *electrode and, as a result, the resistance amplitude R_1 in the (H_{rev},0) branch of the R(H) loop depends on H_{rev}. When H_{rev} is too small, the magnetization of the* hard *electrode is not affected by the field, and a minor R(H) loop for only the soft electrode reversal is measured ("blue" area). When H_{rev} is large enough to drive the full magnetization reversal in the hard electrode, a major R(H) loop is measured ("red" area). When H_{rev} drives a partial reversal of the magnetization in the* hard *electrode, magnetic domains appear and domain duplication occurs. The "orange" area emerges between the "blue" and the "red" areas.*

Domains' duplication process in the "yellow" area

The "yellow" area appears at low temperatures and separates the "red" area from the "green" area. In the green area, the $[Co/Pt]_3/Co$ multilayer in contact with CoTb layer is reversed (exchange biased M(H) loop for thick Pt layers) or partially reversed (spring magnet behavior for thin Pt layers) while the CoTb layer is not affected by the field (high anisotropy and low magnetization). In these two cases, the parts of the magnetic layers in contact with the tunnel barrier are in a parallel configuration, resulting in a low tunnel resistance. When increasing H_{rev}, the applied field becomes large enough to drive the partial reversal of the CoTb layer and this corresponds then to the "yellow" area: a domain state starts to nucleate in the CoTb layer (figure 18, sketch Ⓐ). Then, when reducing the field towards zero, the domain state of CoTb duplicates into the $[Co/Pt]_3/Co$ in contact with CoTb, leading to the intermediate resistance value R_1 (figure 18 (b) and sketch Ⓑ)). From this state, the same domains duplication process as the one described for the "orange" area occurs from the hard electrode to the soft electrode.

As shown in figure 17 (bottom left), this phenomenon is already observed at room temperature for "thick" Pt layers. In this case where the hard electrode magnetization reversal occurs in two separate steps (Figure 5 bottom left), it is possible to choose a value of H_{rev} where the $[Co/Pt]_3/Co$ layer has reversed and where the CoTb partial reversal starts with the formation of domains. This domain structure then duplicates into the $[Co/Pt]_3/Co$ in contact and further into the soft electrode. In the case of "thin" Pt layers, the "yellow" area appears for temperatures lower than 225K, when the magnetization reversals in the CoTb and $[Co/Pt]_3/Co$ layers are no more simultaneous but occur for different magnetic fields, as a consequence of the CoTb increased anisotropy.

Domains walls' contribution to the TMR

It has been shown in figure 18 that, for applied magnetic fields between H_{21} and H_{23}, the MTJ's resistance is the resistance of the parallel magnetizations state. The magnetizations of both electrodes are thus locally parallel, on both sides of the tunnel barrier. This also suggests that the domain walls, labeled as DWs in figure 19, contribute as a resistance of parallel magnetizations state as well.

In order to discuss this point, we will first assume that the magnetizations of the domain walls are *antiparallel* on both sides of the tunnel barrier (as shown in figure 19) and calculate, in this hypothesis, their total surface S_w over the tunnel junction.

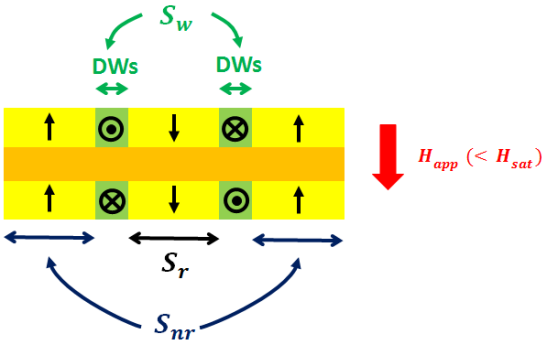

Figure 19: Sketch of the DWs in perpendicular MTJ. S_{nr} (S_r) is the surface of domains with magnetizations oriented (opposite) along the positive applied field, S_w the surface of domains walls.

The DWs constitute a tunnel channel in parallel with the tunnel channel of the domains. Then, the conductances of both channels can be added to have the total conductance of the MTJ. Let's now consider the total conductance of the MTJ and its variation along the R(H) loop, i.e. for different magnetic configurations. The conductances $G_1 = 1/R_1$, $G_2 = 1/R_2$ and $G_3 = 1/R_3$ are

those corresponding to Ⓑ, © and Ⓓ states in figure 18 (a). The variation of the conductance jump amplitudes $\Delta G_{21} = G_2 - G_1$ and $\Delta G_{23} = G_2 - G_3$ measured at H_{21} and H_{23} and the sum of these two conductance jumps $\Delta G = \Delta G_{21} + \Delta G_{23}$ are reported in figure 20.

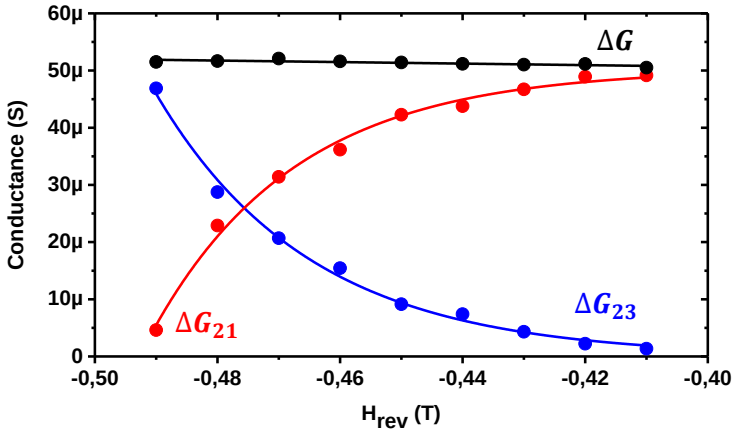

Figure 20: Variation of the conductance amplitude jumps measured at H_{21} (red) and at H_{23} (blue) as a function of the negative field H_{rev} at which the field is reversed. The black filled circles correspond to the sum of the two conductance jumps. The lines are guides for the eyes. (Measurements on $[Co_{0.6nm}/Pt_{1.42\ nm}]_3/Co_{0.6nm}$ based MTJ at 240K).

Increasing H_{rev} towards negative values leads to a decrease (increase) of ΔG_{21} (ΔG_{23}), whereas ΔG exhibits a constant behavior with H_{rev}. If the DWs contribute a local conductance with *antiparallel* magnetizations, it has been shown by P. Rottländer *et al*.[13] that:

$$\Delta G_{21} = \frac{S_{nr}}{S}(G_P - G_{AP}) + \frac{S_w}{S} G_{AP} \qquad \textbf{(III-7)}$$

$$\Delta G_{23} = \frac{S_r}{S}(G_P - G_{AP}) + \frac{S_w}{S} G_{AP} \qquad \textbf{(III-8)}$$

Where S_{nr} (S_r) is the surface of domains with magnetizations oriented along (opposite) to the positive field direction, S_w is the surface of the DWs, S is the total surface of the MTJ ($S = S_w + S_{nr} + S_r$), G_P (G_{AP}) is the conductance of the MTJ when the magnetizations of the electrodes are in a parallel (anti-parallel) configuration.

Given the experimental variations of ΔG_{21} and ΔG_{23} (figure 20), equations III-7 and III-8 show that the increase of H_{rev} toward the negative values leads to a decrease (increase) of the surface of domains with magnetizations parallel (opposite) to the positive starting saturating field.

The sum of the two conductance jumps can be expressed as:

$$\Delta G = \Delta G_{23} + \Delta G_{21} = \left(\frac{S_r}{S} + \frac{S_{nr}}{S}\right)(G_P - G_{AP}) + 2\frac{S_w}{S} G_{AP} \qquad \textbf{(III-9)}$$

And the area density of domains walls is given by[13]:

$$\Delta_w = \frac{S_w}{S} = \left(\frac{1}{R_P} - \frac{1}{R_2}\right)\left(\frac{1}{R_P} - \frac{1}{R_{AP}}\right)^{-1} \qquad \textbf{(III-10)}$$

In the present MTJs, $R_2 = R_P$ (low resistance state after the duplication process) and consequently $\Delta_w = S_w = 0$ for all fields. If DWs contribute to an antiparallel magnetizations configuration channel,

their surface is thus equal to zero. The result contrasts with in-plane magnetized MTJs where a maximum area density of 8% has been estimated[13].

Since those domain walls do really exist, as proved by the observed duplication process, either their surface is negligible (low density of domain walls and low lateral extension, typically 2 to 5 nm for perpendicular magnetization), either the magnetization inside the DW on both sides of the tunnel barrier are parallel. Considering the ferromagnetic coupling observed through the MgO barrier in these MTJs (see section III.C), the parallel orientation on both sides of the barrier is highly probable.

III.B.2. Spring magnet and exchange bias behavior

Figure 21 (a) presents the R(H) curves measured in the "green" area (T=60K) of figures 17 for $[Co_{0.6nm}/Pt_{1.42nm}]_3/Co_{0.6nm}$, $[Co_{0.6nm}/Pt_{1.73nm}]_3/Co_{0.6nm}$ and $[Co_{0.6nm}/Pt_{2.19nm}]_3/Co_{0.6nm}$ based magnetic tunnel junctions. The magnetic behavior of the MTJ full stack measured at 65K for the "thin" Pt layer is recalled in figure 21 (b).

These R(H) characteristics can be easily understood from the magnetic properties of the hard electrode and more especially of the CoTb layer. Because of the increase in anisotropy and decrease in magnetization when decreasing temperature, the CoTb magnetization reversal occurs at higher and higher fields, exceeding 4T at 65K (figure 21 (b)). Consequently, in the entire H_{rev} range allowed by the experimental setup, the CoTb is pinned and its magnetization remains in a single domain state, parallel to the positive field direction. H_{rev} is however large enough to reverse the $[Co/Pt]_3/Co$ multilayer in contact with CoTb. The magnetization being thus parallel on both sides of the MgO barrier (sketch Ⓐ), the system is in the low resistance state.

By increasing the field back towards the positive value, the exchange coupling between the CoTb layer and the $[Co/Pt]_3/Co$ multilayer in contact leads to the first reversal of the $[Co/Pt]_3/Co$ multilayers of the hard electrode (sketch Ⓑ). The magnetization on both sides of the tunnel barrier being opposite, the resistance state of the system becomes high. The soft electrode finally switches when increasing the applied field further (sketch ©) and the system goes back to its low resistance state.

Two limit cases for the R(H) characteristics have been identified in figure 21 (a): they correspond to the two magnetic behaviors, i.e. spring magnet or exchange bias, of the hard electrode, observed and reproduced using micromagnetic calculations.

For "thin" Pt layers (filled squares in figure 21 (a)), the reversal of the $[Co/Pt]_3/Co$ multilayer of the hard electrode is perfectly reversible and reproducible creating a spring magnet configuration as experimentally observed in MTJs full stack between approx. -1.5T and -4.5T (figure 21 (b)). For "thick" Pt layers, the reversal of the $[Co/Pt]_3/Co$ multilayer of the hard electrode is a typical bias loop. As observed in the MTJs full stack (figure 5 bottom left), only three $[Co/Pt]_3$ multilayers switch, the last Co layer being pinned by the CoTb. The ferromagnetic exchange coupling through the Pt layer leads to the horizontal shift of the magnetization reversal observed in figure 21 (a). The magnitude of this horizontal shift allows extracting the exchange coupling constant J_{exch} that has been used in the micromagnetic calculations (figure 4).

These different results obtained by transport measurements are perfectly in agreement with (i) the magnetic behavior of the hard electrode as a function of Pt thickness and temperature detailed in the section II (ii) the predicted phase diagram obtained by micromagnetic calculations using the magnetic parameters of the $[Co/Pt]_3/Co$ multilayer determined in the previous chapter.

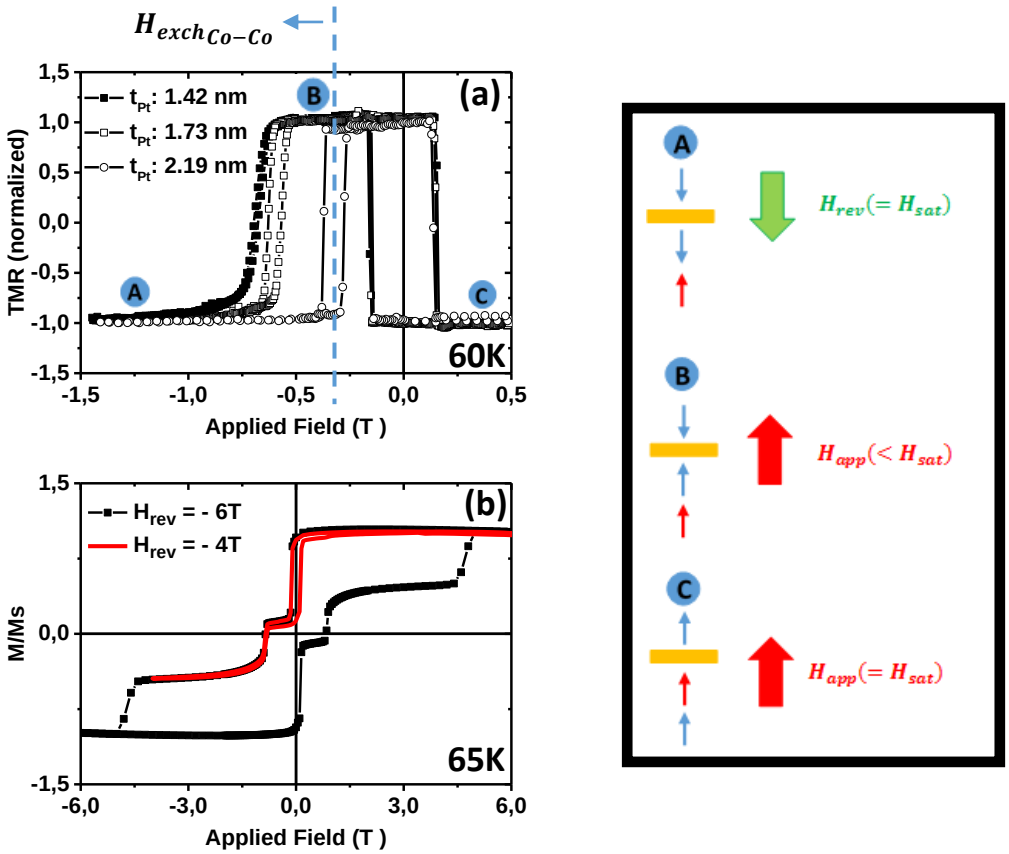

Figure 21: Left: (a) Normalized TMR versus applied field measured at 60K for MTJs with Pt thicknesses equal to 1.42nm (filled squares), 1.73 nm (open squares) and 2.19 nm (open circles). (b) M(H) loops measured at 65 K for H_{rev} =-6T (black squares) and H_{rev} chosen before the reversal of the CoTb layer (red line) for the MTJ with Pt thickness equal to 1.42 nm. Right: Sketches of the magnetic configurations of the bottom and top electrodes.

III.C. Coupling through the MgO barrier

This last section presents the results concerning the magnetic coupling between the electrodes through the MgO tunnel barrier. The coupling between electrodes leads to the horizontal shift of the minor loop associated to the soft electrode reversal. The amplitude of this shift is directly related to the exchange coupling between electrodes[15],[16]. The field shift of the [Co/Pt] soft electrode reversal has been extracted from R(H) minor loops and plotted as a function of temperature for the different Pt thicknesses (figure 22).

For temperatures in the 4K-300K range and for all studied Pt thicknesses, the coupling is found to be ferromagnetic (negative field shift). It decreases when the temperature decreases which is an unusual behavior. Indeed, if the coupling is related to the magnetization of the films, since magnetization increases when temperature decreases, coupling should increase. At low temperatures and for several points, a cross to weak antiferromagnetic coupling is observed. The field shift is larger for smaller Pt thickness and exhibits a stronger variation as a function of temperature.

When two ferromagnetic electrodes are separated by an insulating barrier, mainly two types of coupling can occur: interlayer coupling of RKKY-type predicted by P. Bruno[17] and/or magnetostatic coupling (according to the orange peel coupling observed and generalized by J.C.S Kools *et al* in spin-valves devices[18]). Contrary to the case of ferromagnetic electrodes separated by a

metallic spacer, where the RKKY coupling oscillates with the spacer thickness, the 'tunnel' RKKY coupling through an insulating barrier decreases exponentially when the barrier thickness increases. Interestingly, this coupling decreases with temperature, which would be in agreement with our results. However, both theoretical predictions based on P. Bruno's calculations[17] and experimental results published by J. Faure-Vincent *et al.*[19] report that the RKKY coupling through an insulating layer is negligible for thickness larger than 2 nm. With a 2.5nm thick MgO layer, the RKKY coupling between the [Co/Pt] multilayers of the soft and hard electrodes can be reasonably excluded.

The field shift reported in figure 22 is thus likely driven by the orange peel coupling between both electrodes through the MgO insulating barrier.

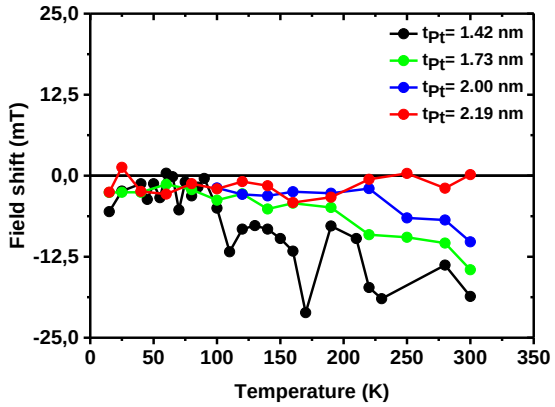

Figure 22: Temperature dependence of the field shift for R(H) minor loops (soft electrode reversal) for different Pt thicknesses : 1.42 nm (black), 1.73 nm (green), 2.00 nm (blue) and 2.19 nm (red).

The orange peel coupling between ferromagnetic layers with perpendicular magnetization separated by a non-magnetic spacer has been modeled by J. Moritz *et al.*[20] . In their model, illustrated in figure 23, J. Moritz *et al.* consider two ferromagnetic layers F_1 and F_2, each of thickness t, separated by a non-magnetic-metallic spacer (NM) of thickness b. M_1 and M_2 are the magnetizations of F_1 and F_2 respectively whereas 2h and T represent the peak-to-peak amplitude of the roughness and its spatial wavelength respectively. The angles Θ and ψ are defined as the angle between the normal to the interface (n) and the z-direction (perpendicular to the multilayer) and as the angle between the direction of the magnetization m and the z-direction.

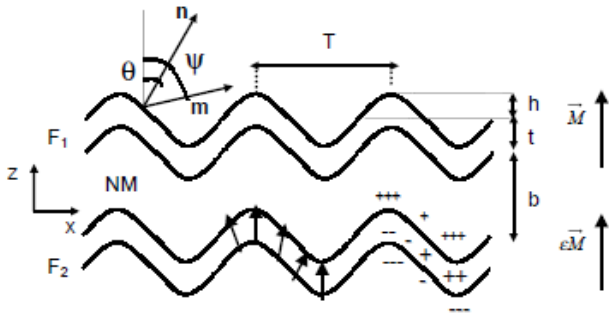

Figure 23: Sketch of magnetic layers F_1 and F_2 separated by a non-magnetic spacer NM. The '+' and '-' represent the effective magnetic charges responsible for the magnetic coupling between the layers[20].

In this model, the roughnesses of the layers are correlated and the anisotropy axis is always locally normal to the interface. J. Moritz *et al.* calculate analytical expressions for the magnetostatic, the exchange and the anisotropy energies[20]. The total energy is given by the sum of the three contributions; by minimizing the energy with respect to ψ both in the parallel and anti-parallel magnetizations configurations, it has been possible to extract the magnetic configuration and the resulting magnetostatic coupling, labelled ΔE. A positive (negative) sign of ΔE means an anti-ferromagnetic (ferromagnetic) coupling between both ferromagnetic layers.

The model proposed by J. Moritz *et al*. has been tested for the current perpendicular MTJs in using the experimental magnetic parameters of the [Co/Pt] multilayers grown on MgO (chapter 5). The results are shown in figure 24 left, presenting the dependence of ΔE on K_u, the uniaxial anisotropy, for different roughnesses.

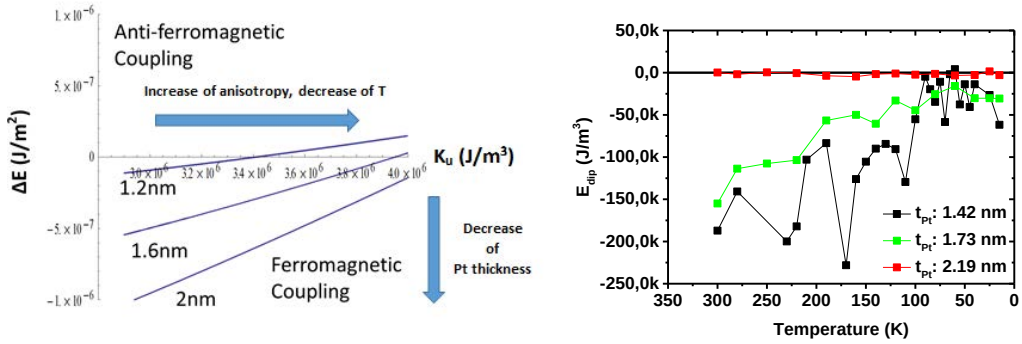

Figure 24: Variation of ΔE with the uniaxial anisotropy of the ferromagnetic layer in contact with the NM layer in the Moritz model. The structural and magnetic parameters used for the calculation are: peak to peak roughness = 1.2 nm, 1.6 nm and 2 nm; t=0.6 nm; T=7 nm (typical grain size); b=2.5 nm and the magnetic parameters of the [Co/Pt] multilayers deposited on MgO.

Discussion

Depending on the multilayer parameters, the calculation shows that the coupling can be either ferromagnetic or antiferromagnetic. For a given roughness, the ferromagnetic coupling constant decreases when Ku increases and can change to antiferromagnetic. The slope of the variation decreases when the roughness decreases. For a small value of K_u, a strong decrease of the ferromagnetic coupling through NM is predicted when the roughness decreases. On the other hand, for high values of K_u, a transition from a ferromagnetic to an anti-ferromagnetic coupling can be observed.

To compare the simulation with experimental data, one has to keep in mind that the uniaxial anisotropy ($K_u = K_{eff} + \mu_0 M_s^2/2$) is mainly driven by the saturation magnetization that increases when the temperature decreases. An increase of Ku in the simulation is thus synonymous of a decrease of temperature in the experiments. Moreover, the structural analysis of [Co/Pt] stackings (chapter 5) has shown that increasing the Pt thickness leads to a significant decrease of the layers roughnesses. The calculated variation of ΔE versus K_u for different roughnesses (figure 24 left) can be thus compared to the experimental temperature dependence of the field shift for different thicknesses (figure 22 and 24 right).

It appears that experiments and calculations are in good agreement with each other. Most of the experimental features described above are consistent with the evolution of the coupling energy reported in figure 24: (i) the coupling is mainly ferromagnetic (ii) it decreases when the temperature decreases, i.e. when K_u increases (iii) it increases when the Pt thickness decreases, i.e. when the roughness increases.

The experimental variations of the exchange coupling between the electrodes through the insulating MgO barrier would therefore confirm that it is essentially due to orange peel coupling.

IV. Conclusion

The magnetic properties of MTJs full stack reveal several interesting features, mainly driven by the magnetic properties of the hard electrode. Since the strength of the coupling between the Co layers through the Pt spacer decreases rapidly when the Pt thickness increases, two reversal modes of the hard electrode have been highlighted at room temperature. For thin Pt thicknesses, the simultaneous reversal of the $[Co/Pt]_3/Co$ multilayer and of the CoTb layers is observed whereas for large Pt thicknesses, the reversal occurs in two steps (first reversal of the $[Co/Pt]_3$ multilayer followed by the Co/CoTb reversal for larger applied fields). At low temperatures, the drastic increase of the anisotropy and the decrease of the saturation magnetization in CoTb prevents its reversal, leading either to a spring magnet behavior for thin Pt thicknesses or to an exchange bias behavior for large Pt thicknesses. Finally, by playing with the field history, it is possible to stabilize a remanent intermediate magnetization state with the persistence of domains in the hard electrode. The different magnetic behaviors observed by magnetometry have been reproduced by micromagnetic calculations using the magnetic parameters of the $[Co/Pt]_3/Co$ and CoTb individual multilayers, and summarized in original phase diagrams. Those can account for the magnetic properties observed in MTJs full stack.

The magneto-transport properties of patterned MTJs have been explored to investigate how the various magnetic behaviors could affect the transport properties and give rise to interesting and original features. Their analysis also constitutes a powerful complementary tool for the study of magnetic configurations, especially at the MgO interface. Beyond the usual cases where the applied field can reverse both electrodes (major symmetric loop) or only the soft one (biased minor loops), the resistance versus magnetic field characteristics have highlighted two interesting behaviors for magnetic fields in the range of the hard electrode magnetization reversal: (i) if the magnetic field is large enough to reverse the [Co/Pt] multilayer in the hard electrode but not the CoTb layer, the R(H) loops exhibit some common characteristics with M(H), associated to the [Co/Tb] reversal: an exchange biased loop or a reversible spring magnet behavior. This last property is very attractive and could be used in the development of magneto-resistive sensor at room temperature and high fields; (ii) if the magnetic field is large enough to reverse the [Co/Pt] multilayer in the hard electrode and a part of the CoTb layer, the development of magnetic domains in the hard electrode gives rise to a domains duplication phenomenon from the hard to the soft electrode. This is nicely observed via the occurrence of a low resistance intermediate state. The analysis of the conductance has shown that the domains walls in perpendicular MTJs don't contribute to the TMR, thus contrasting with the results obtained for in-plane MTJs.

Finally, the ferromagnetic coupling between both electrodes through the MgO tunnel barrier has been found to decrease with decreasing temperature and increasing Pt thickness. These results have been successfully explained using the theoretical model developed by J. Moritz *et al*. [20] based on a stray field interaction between perpendicularly magnetized layers separated by a non-magnetic spacer.

References

[**1**] M. Gottwald, thesis (2011).
[**2**] F. Montaigne, thesis (1999).
[**3**] D. Lacour, thesis (2002).
[**4**] M. Julliere *et al.*, Phys. Lett. **54A**, 225 (1975).
[**5**] F. Montaigne *et al.*, J. Appl. Phys. **91**, 7020 (2002).
[**6**] P. Hansen *et al.*, J. Appl. Phys. **66**, 756 (1989).
[**7**] W.F. Brinkman *et al.*, J. Appl. Phys. **41**, 1915 (1970).
[**8**] J.G. Simmons, J. Appl. Phys. **35**, 2655 (1964).
[**9**] C.S. He *et al.*, Phys. Rev. B **58**, R2917 (1998).
[**10**] L.. Glazman *et al.*, Sov.Phys. JETP **67**, 163 (1988).
[**11**] Y.J. Wang *et al.*, Phys. Rev. B **41**, 651 (1990).
[**12**] M. Hehn *et al.*, Phys. Rev. B **61**, 643 (2000).
[**13**] P. Rottländer *et al.*, Phys. Rev. B **69**, 064430 (2004).
[**14**] D. Lacour *et al.*, J. Appl. Phys. **89**, 8006 (2001).
[**15**] J. Faure-Vincent *et al.*, J. Appl. Phys. **93**, 7519 (2003).
[**16**] L.E. Nistor *et al.*, Phys. Rev. B **81**, 220407 (2010).
[**17**] P. Bruno *et al.*, Phys. Rev. B **49**, 13231 (1994).
[**18**] J.C.S. Kools *et al.*, J. Appl. Phys. **85**, 4466 (1999).
[**19**] J. Faure-Vincent *et al.*, Phys. Rev. Lett. **89**, 107206 (2002).
[**20**] J. Moritz *et al.*, Europhys. Lett. **65**, 123 (2004).

Chapter 7
Spin-polarization in [Co/Pt]- and SGA- based magnetic tunnel junctions

I. TMR and effective polarization in [Co/Pt] based-MTJs 138
I.A. Effective polarization of [Co/Pt]: more than an interface phenomenon? 138
I.B. Bloch low and Curie temperature 141
II. TMR and spin-polarization in SGA/AlO_x/[Co/Pt] MTJs 143
II.A. Tunnel characteristic 143
II.B. Finite magneto-resistance tunnel at the magnetic compensation 144
II.C. Discussion 146
III. Preliminary results on SGA/MgO/[Co/Pt] MTJs 146
III.A. SGA surface preparation 148
III.B. Common features in perpendicular SGA-based MTJs 149
III.B.1. Tunnel conductance versus voltage 149
III.B.2. Tunnel conductance versus temperature 150
III.B.3. Resistance versus applied field characteristics 151
III.C. Discussion 151
IV. Conclusion 152
References 153

This chapter is devoted to the integration of the SGA compound in magnetic tunnel junctions, to build hybrid MTJs in which the spin-polarization of one electrode (the [Co/Pt] multilayer) is already known. The aim is then to determine the spin-polarization of the SGA/MgO system. Chapters 5 and 6 allowed getting a perfect knowledge of the magnetism and the electronic transport properties of [Co/Pt]-based magnetic tunnel junctions. So, the [Co/Pt] multilayer has been chosen as a reference material with perpendicular magnetization to constitute the free electrode.

This chapter follows from magneto-transport results detailed in the chapter 6. In a first section, the effective tunnel polarization in [Co/Pt]-based magnetic tunnel junctions is presented. Its dependence on the Pt thickness is discussed in considering the Pt induced moment in [Co/Pt] multilayers (chapter 5). Its dependence on temperature permits to extract the Curie temperature and to discuss the T_c variation with Pt thickness in comparison with the variation of the inter layer coupling. The second section gathers the magneto-transport results obtained in SGA-based MTJs with an AlO_x insulating barrier and underlines the specific features that motivated further investigation, especially with a MgO barrier. The preliminary results obtained with a MgO insulating barrier during this PhD work are finally presented and discussed in the last section.

I. TMR and effective polarization in [Co/Pt] based-MTJs

I.A. Effective polarization of [Co/Pt]: more than an interface phenomenon?

As a reference for hybrid SGA/MgO/$[Co/Pt]_4$ MTJs, the effective polarization of the [Co/Pt] multilayers (Pt thicknesses ranging from 0.49nm to 2.19nm) was first determined from TMR values measured in [Co/Pt]-based MTJs. The results are shown in figure 1, for three different temperatures.

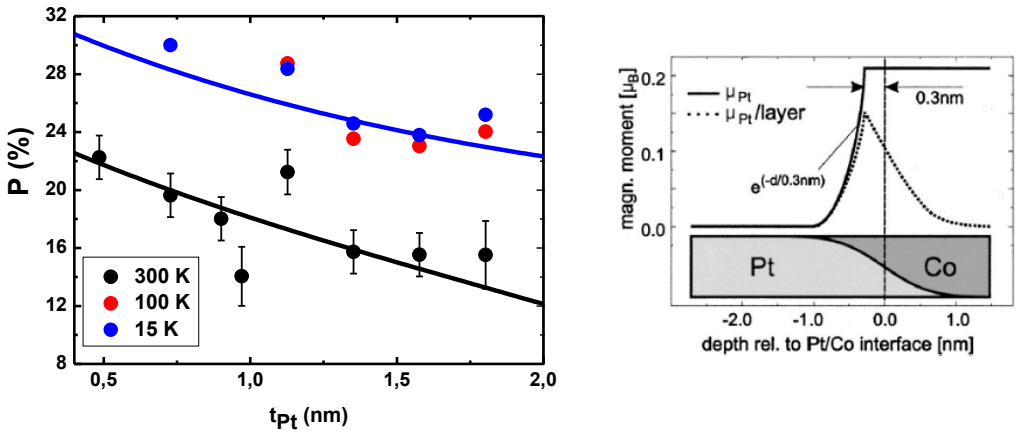

Figure 1: Left: Effective tunnel polarization versus Pt thickness measured at 15K (blue dots), 100K (red dots) and 300K (black dots). The blue line is a fit of the data measured at 15K (see text). The black line is the expected variation from the fit at 15K and including the variation of polarization with temperature from the Bloch law. Right: Pt induced magnetic moment profile in a [Co/Pt] bilayer[1].

As shown in chapter 6, the effective polarization is extracted from the TMR value using a modified expression of the Jullière's model:

$$P_{[Co/Pt]/MgO} = \sqrt{\frac{TMR\left(1+{}^{G_{SI}(T)}/_{G(T)}\right)}{2+TMR\left(1+{}^{G_{SI}(T)}/_{G(T)}\right)}} \qquad \text{(I-1)}$$

At low temperatures, G_{SI} equals zero ($G_{SI} \propto T^{\gamma}$)[2] and the extracted polarization reflects the effective polarization of the [Co/Pt]/Co/MgO interface. The result is plotted at 15K and 100K in blue and red respectively. A decrease of the effective tunnel polarization with increasing the Pt thickness is observed. At first glance, this result is somehow surprising, since spin-polarized tunneling is usually considered as an interface phenomenon in sputtered MTJs, and thus no dependence on the Pt thickness is expected. This decrease suggests that the induced polarization in the Pt layers should be taken into account.

As discussed in chapter 5, in the hypothesis where Pt layers are fully polarized, the average induced Pt moment appears to decrease when increasing the Pt thickness. This can be first explained by (i) the decay of the Pt induced moment when going further from the Co/Pt interface (ii) the increased distance between consecutive Co/Pt interfaces so that Pt atoms close to one interface are less polarized by the second further interface. Finally, it has been shown by J. Geissler and al[1] by resonant X-ray reflectometry in a [$Co_{2.6nm}/Pt_{6.2nm}$] bilayer that the Pt induced polarization profile follows an exponential decay (figure 1, right).

Based on this study and experimental observations, a model (sketched in the figure 2 and detailed in the next paragraph) is proposed to qualitatively explain the behavior of the effective polarization with the Pt thickness.

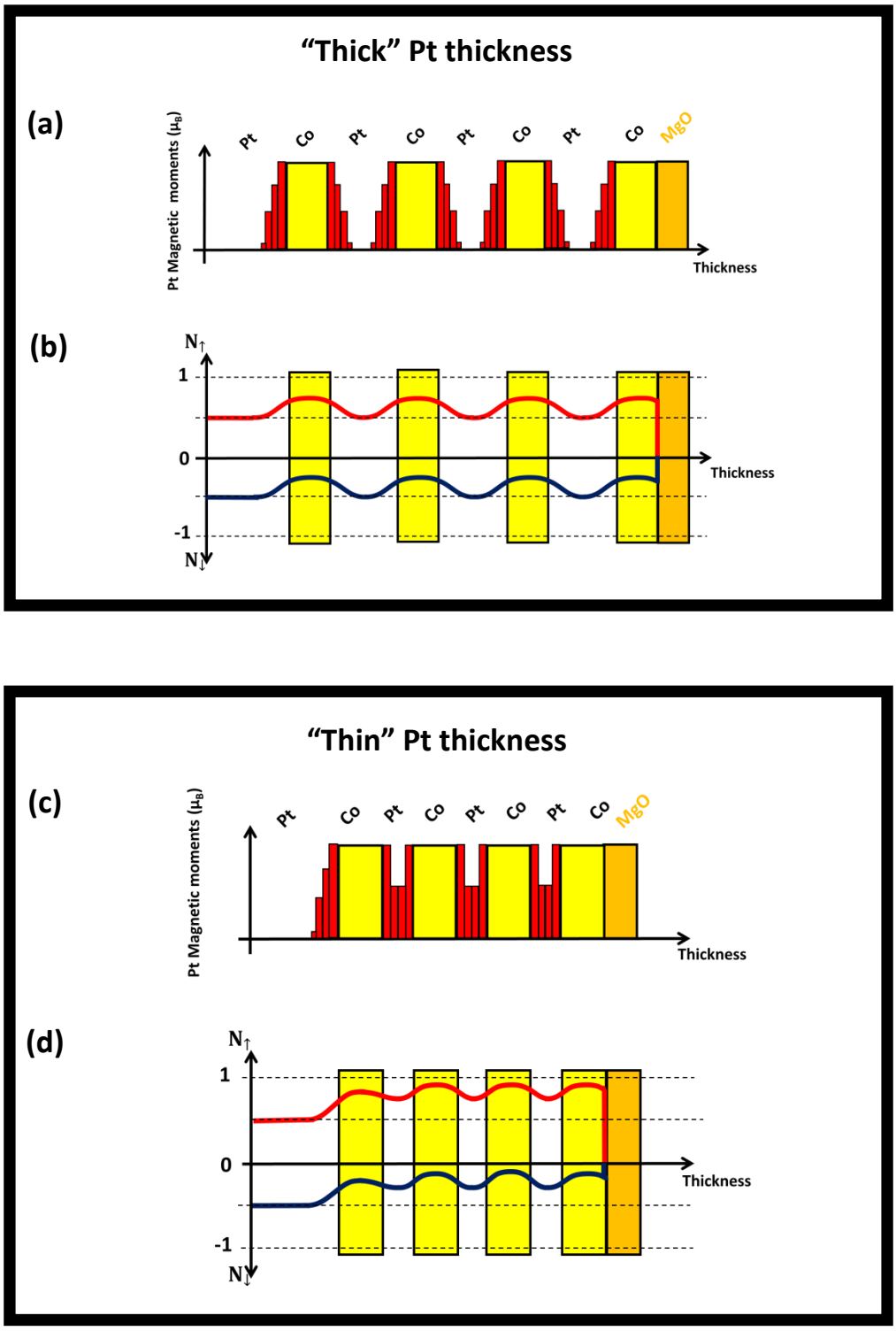

Figure 2: (a) and (c) Sketches of the Pt magnetic moment distribution with the Pt thickness (red vertical bars) in [Co/Pt] multilayers. (b) and (d) Sketches of the spin up and spin down polarization densities through the Co and Pt layers.

For “thick” Pt layers, the first Pt atomic planes are polarized at the Co/Pt interfaces (sketch (a)) and the polarization is reduced to zero in the middle of the Pt layers. Consequently, at the Co/MgO interface, the effective tunnel spin polarization of only the Co thin layer will be measured (sketch (b)). In the case of “thin” Pt layers, the Pt induced magnetic moment doesn’t reach zero in the multilayer (sketch (c)). As a result, at the Co/MgO interface, the effective tunnel spin polarization of the Co thin layer in contact with MgO is “reinforced” by the spin polarization of the nearest Co/Pt interface. Then, the effective tunnel spin polarization will be enhanced (sketch (d)) and a higher TMR value than in the case of “thick” Pt layers is measured.

In this model, considering the exponential decay of the Pt induced moment from the interface[1], the effective tunnel spin polarization should vary as:

$$P_{eff}(t_{Pt},\ 0K) = P_{Co}\left(1 + exp\left(-\frac{t_{Pt}}{\Lambda}\right)\right) \qquad \textbf{(I-2)}$$

The fit of the experimental data led to P_{Co} = 17.3% and Λ = 1.63 nm (figure 1, blue line). The characteristic decay length Λ at low temperature is in agreement with the reported experimental values between 1 and 3nm. The polarization is also in agreement with the value expected for such thin Co layers where a polarization P_0 between [9-20]% have been reported by spin polarized photoemission at room temperature for Co thickness between [1-9] ML[3].

At room temperature, the effective tunnel spin polarization has been corrected using equation (I-1). The value of G_{SI}/G is known (see chapter 6) and different from zero, considering that the MgO tunnel barriers are of same quality (made in the same run, in the same sputtering chamber). The results presented in figure 1 (black dots) show a similar decrease as a function of the Pt thickness. The effective tunnel spin polarization can be written as:

$$P_{eff}(t_{Pt},T) = P_{Co}\left(1 + exp\left(-\frac{t_{Pt}}{\Lambda}\right)\right)\left(1 - \alpha(t_{Pt})T^{3}/_{2}\right) \qquad \textbf{(I-3)}$$

where the α parameter of the Bloch law ($(1/T_c)^{3/2}$) depends on the Pt thickness, as presented in the next paragraph. Equation (I-3) has been plotted in figure 1 (black line) without any free parameters, using P_{Co} = 17.3% and Λ = 1.63 nm (from the low temperature measurements), and $\alpha(t_{Pt}) = \left(\frac{1}{778-136t_{Pt}}\right)^{3/2}$ (from the temperature dependence of polarization, paragraph I.B.). A close agreement with the experimental data is observed.

In conclusion, the variation of the effective spin polarization at room temperature results from the exponential decay of the induced magnetic moment in the Pt layers and from the reduction of the polarization of the Co layer predicted by the Bloch law. In our knowledge, these results have not been reported before in [Co/Pt] multilayers based MTJs.

Generally, in addition to the elastic tunneling electron channels introduced in the Jullière’s model, other inelastic spin independent channels resulting from magnetic excitations (e.g. excitation of magnons[4]) must be considered in the TMR expression and thus in the effective polarization (the spin independent channel has been removed). The present results thus show that the direct elastic tunneling with a Bloch’s law dependent polarization is the main contribution to the TMR dependence on temperature.

I.B. Bloch low and Curie temperature

The [Co/Pt]/Co/MgO effective tunnel spin polarization dependence on temperature has been studied and reported in figure 3 (a) for the different Pt thicknesses. As shown for the 1.73nm thick Pt layers (chapter 6), this variation could be accurately fitted using the following expression:

$$P_{eff}(T) = P_0\left(1 - \alpha T^{\frac{3}{2}}\right) \quad \textbf{(I-4)}$$

The fits of experimental data are given by the solid lines in figure 3 (a).

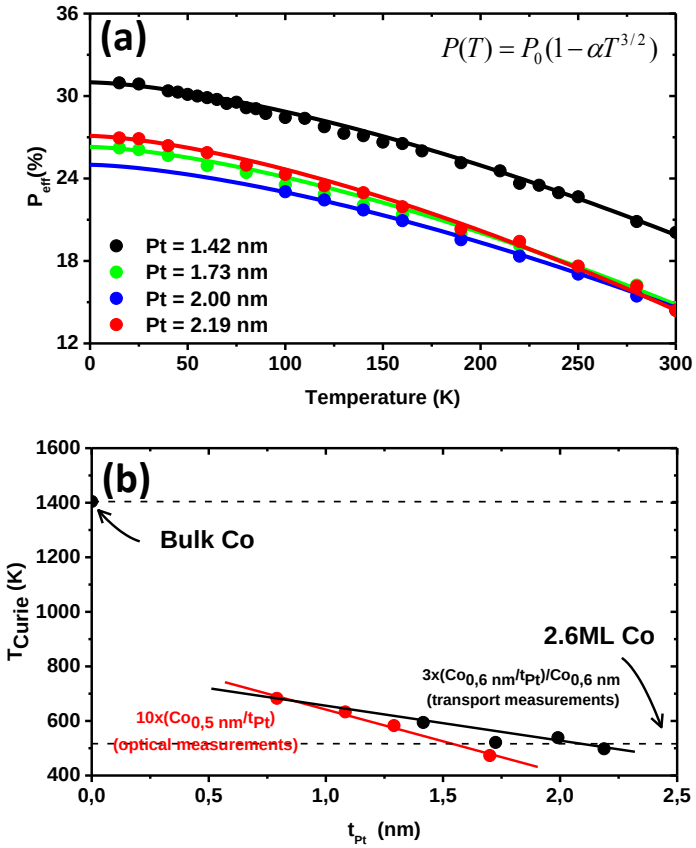

Figure 3: Effective [Co/Pt]/Co/MgO polarization dependence on temperature in [Co/Pt]-based MTJs (dots). The data were fitted using the Bloch's law (solid lines). (b) Curie temperature dependence on the Pt thickness extracted from transport measurements (black dots) [this study] and from optical experiments (red dots)[5]. The solids lines are guides for the eyes.

The Curie temperatures, deduced from the Bloch coefficients ($\alpha = (1/T_c)^{3/2}$) obtained from the fits, are presented in figure 3 (b) (black dots) as a function of the Pt thickness. T_c decreases with increasing the Pt thickness and can be satisfactorily fitted with a linear variation ($T_C = 778 - 136t_{Pt}$). The T_c values, drastically reduced compared to bulk Co, are in agreement with those extracted from optical measurements[5] (red dots) for [Co/Pt] multilayers with similar Co and Pt thicknesses. For thick Pt layers, the values are also close to the T_c measured on single 2.6ML thick Co layers[6],[7].

In order to explain this Pt thickness dependence of the Curie temperature, the role of the interlayer coupling between the Co layers in the [Co/Pt] multilayers was taken into account. The

interlayer coupling should namely play a role in the ferromagnetic order and must be considered in the expression of the Curie temperature. By simple considerations, S. Bandiera[8] determined the following relation:

$$T_c = \frac{(J+1)\mu_0 M_s(0)^2(\langle A\rangle+2\langle A'\rangle)}{3JNk_B} \quad \text{(I-5)}$$

with A and A' the couplings between the Co atoms in a single layer and between Co atoms from two different Co layers separated by Pt respectively; J is the total angular momentum (**J** = **L** + **S**) and N is the number of magnetic moments per unit volume. If the coupling A' decreases, for example by increasing the Pt layer thickness, the Curie temperature should decrease, in agreement with the T_c behavior observed in the figure 3 (b).

The coupling A' must be, by the way, closely related to the RKKY coupling. From the model developed by S. Bandiera[8], the ratio A'/A can be extracted:

$$\frac{T_c - T_C^0}{2T_C^0} = \frac{\langle A\prime\rangle}{\langle A\rangle} \quad \text{(I-6)}$$

where T_C^0 is the Curie temperature when A' equals zero. Considering that A' equals zero for the thickest Pt layer (which is not exactly the case since RKKY interaction is not zero), the values for $\frac{T_c - T_C^0}{2T_C^0}$ and the RKKY coupling (from chapter 6, average value over the total temperature range,) are reported in figure 4 versus the Pt thickness. A close correlation is namely observed. For the smallest Pt thickness, A' is 10% of A, the coupling between Co atoms inside the layer. Increasing the Pt thickness to 1.7nm reduces A' to 2% of A. This reduction by a factor 5 also appears in the RKKY coupling when going from the thinnest to the thickest Pt layers.

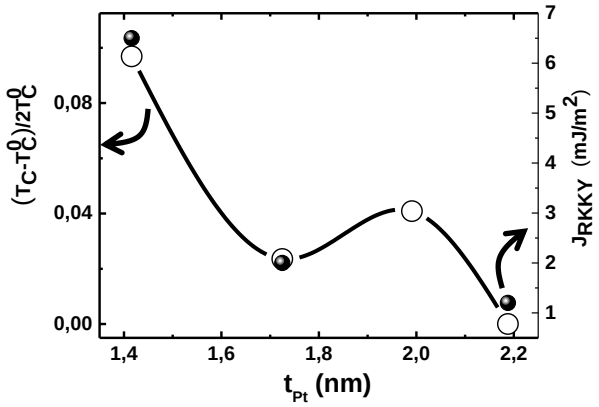

Figure 4: open symbols: relative variation of Tc with the Pt thickness (considering that A' is equal to zero for t_{Pt}=2.2nm). Filled symbols: variation of the RKKY coupling as a function of the Pt thickness.

As suggested by Bruno and studied in the paper[9], another explanation to the decrease of Tc when increasing the Pt thickness may be the formation of Co_xPt_{1-x} alloy, resulting from the inter-mixing between the Co and Pt atoms at the interface. However, in this Pt thickness range, the reflectometry studies (chapter 5) have shown *a decrease* of the Co and Pt roughnesses and/or inter-mixing when increasing the Pt thickness. This explanation to the decrease of T_c can thus be excluded in the present case.

II. TMR and spin-polarization in SGA/AlO_x/[Co/Pt] MTJs

The use of SGA as an original electrode in MTJs with an AlO_x insulating barrier has been first undertaken in our group by M. Da Silva *et al.*[10]. This study proved that SGA can simultaneously exhibit a zero-magnetization and provide spin polarized conduction electrons, being thus able to give rise to a spin-polarized current in the magnetic compensated state. In this section, we will remind the main features observed in SGA based-magnetic tunnel junction with AlO_x insulating barrier. Consequently, this section is largely inspired from the published work by M. Da Silva *et al.*; additional non-published data that partly motivated this PhD work are also added.

The details of the SGA growth using MBE have been given in chapter 1. In order to grow the insulating tunnel junction, the sample has been first covered by 2nm of Al (MBE) and then exposed to air during 12h for natural oxidation. As mentioned in reference[10], natural oxidation is an uncontrolled process compared to other oxidation methods such as Ar/O_2 plasma oxidation or as pure oxygen oxidation. However, TMR effects could be observed and have been previously reported using this growth method[11],[12]. On top of the 2nm-thick AlO_x insulating barrier, a $[Co_{0.2nm}/Pt_{0.65nm}]_5$ multilayer has been sputtered in order to form the top electrode. The [Co/Pt] multilayer has been chosen because of its perpendicular magnetic anisotropy, since SGA exhibits a perpendicular to film plane easy magnetization axis (see chapter 1).

As for the [Co/Pt]-multilayer based MTJs, the electrical and transport characteristics have been measured with a "home-made" experimental setup consisting of a two probes station at room temperature, and a cryostat at low temperature. A ±0.15T magnetic field is available.

II.A. Tunnel characteristic

Figure 5 presents the low temperature conductance versus applied voltage measured on a 10µmx10µm magnetic tunnel junction after field-cooling under +0.15T down to 15K.

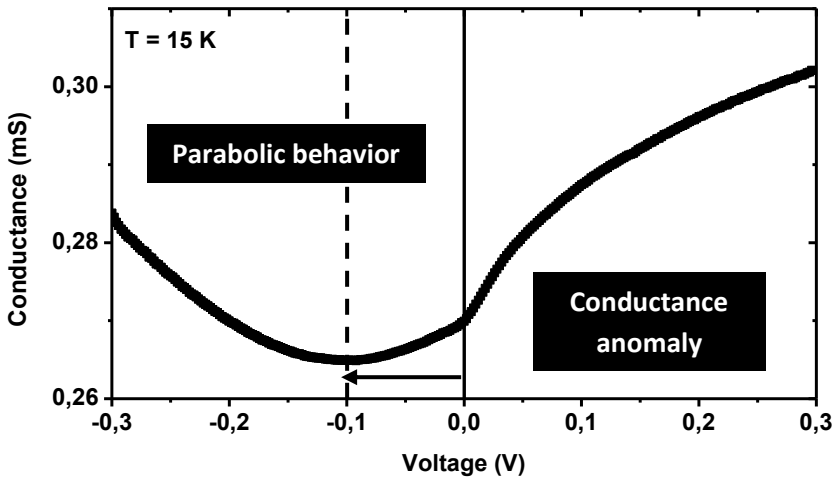

Figure 5: Conductance versus Voltage characteristic extracted from Current versus Voltage characteristic measured at 15K on a 10µmx10µm magnetic tunnel junction after a field-cooling process under + 0.15T. The dash vertical line denotes the horizontal shift of the conductance minimum.

Several anomalies are clearly visible in the G(V) characteristic. First of all, the minimum of the conductance is not localized at 0 V but for a negative voltage (approximately -0.1 V). Then, for

positive applied voltages, the behavior largely deviates from the parabolic behavior. This kind of electric response can result from an oxygen gradient in the insulating barrier, which leads to an asymmetry in the tunnel barrier height; but it can also reflect the electronic band structure of SGA and/or SGA/MgO interface. Similar asymmetries in the G(V) characteristics have been indeed reported in Fe/MgO/Fe magnetic tunnel junctions in the presence of surface state[13] that dramatically affect the tunnel conductance behavior. The G(V) anomaly observed in SGA-based MTJs could be thus consistent with the volume/surface localized state close to the Fermi level observed by ARPES for the SGA/MgO system (chapter 3). This hypothesis must be nevertheless confirmed for SGA/MgO/$[Co/Pt]_5$ hybrid MTIJs, the results of which are presented later in this chapter.

In order to investigate the possible effect of an oxygen gradient in the AlO_x tunnel barrier on the observed conductance anomalies, some attempts have been made during this PhD work with a better controlled process: plasma oxidation (Ar/O_2) of the Al layer. High resistive junctions that don't exhibit any TMR effect have been obtained, possibly related to an over-oxidation of the Al layer. Further experiments are required to improve the control of the oxidation process and explore that way.

II.B. Finite magneto-resistance tunnel at the magnetic compensation

Figure 6 recalls the magnetization and transport measurements at 15K after a +0.15T field cooling process for the SGA/AlO_x/$[Co/Pt]_5$ magnetic tunnel junction.

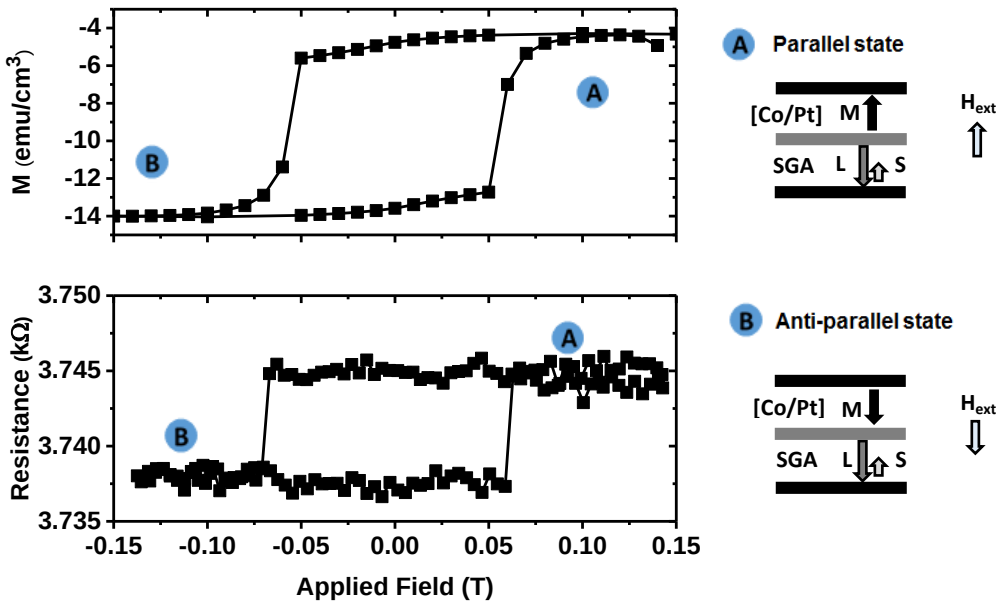

Figure 6: (a) Magnetization and (b) Resistance loops versus applied magnetic field measured at 10 mV and at 15 K, after a +0.15T field-cooling process for SGA/AlO_x/$[Co/Pt]_5$ MTJ. The letters Ⓐ and Ⓑ denote the magnetizations configurations of both electrodes, as sketched in the right part.

Considering the huge coercivity in SGA epitaxial films at low temperatures (see chapter 1), only the magnetization reversal of the $[Co/Pt]_5$ multilayer is observed in the explored field range (figure 6 (a)). This reversal is accompanied by an abrupt change in resistance (figure 6 (b)) that proves the existence of a TMR effect in SGA/AlO_x/$[Co/Pt]_5$. A TMR of 0.2% at 15K has been extracted from figure 6 (b). The attribution of parallel and anti-parallel magnetic configurations to the high and low resistance states respectively will be discussed latter.

The key point of the study by M. Da Silva *et al*. consists in showing that the TMR is not zero at the SGA magnetic compensation. The temperature dependences of the SGA magnetization (single layer) and of the TMR (SGA/AlO_x/$[Co/Pt]_5$ MTJ) at different voltages are presented in figure 7 (a) and (b) respectively.

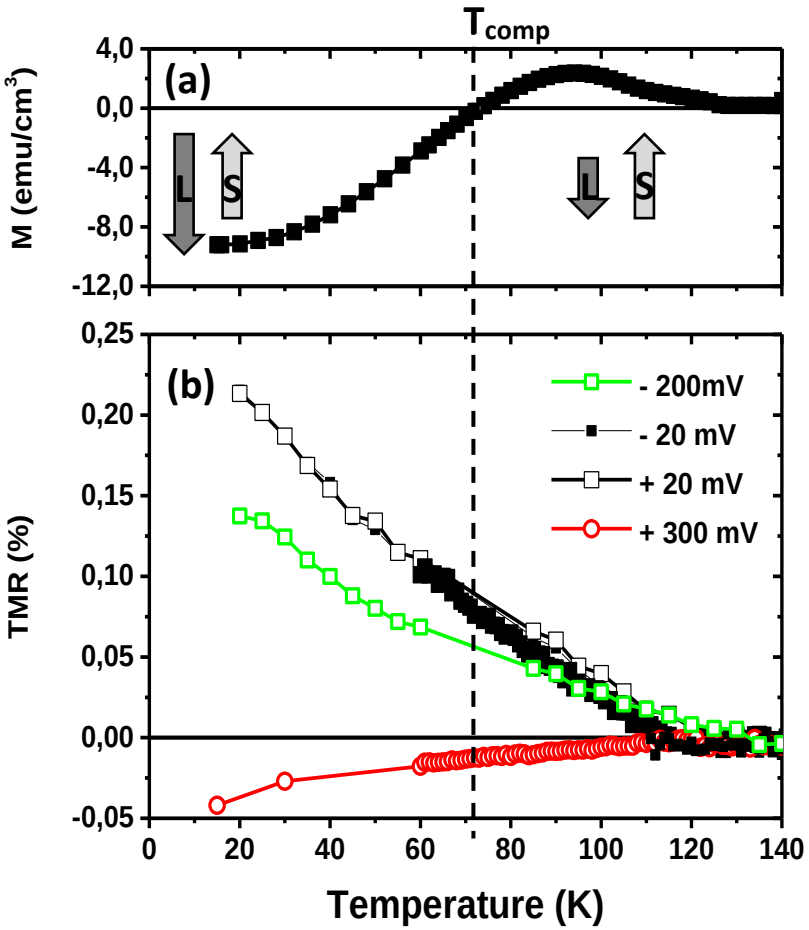

*Figure 7: Temperature dependences of: (a) the SGA magnetization (measured for a single layer in increasing temperature under zero-applied field after field-cooling under +7 T). The magnetic **L** and **S** contributions in SGA are sketched with the dark and light grey arrows respectively. (b) the TMR in a SGA/AlO_x/$[Co/Pt]_5$ MTJ for different voltages.*

The observation of a finite TMR value at the magnetic compensation is the proof that SGA can simultaneously exhibit a zero-magnetization and a polarization of the conduction electron, being thus able to give rise to a spin-polarized current in the magnetic compensated state.

Contrary to the RE-TM alloys-based magnetic tunnel junctions where a sign inversion is observed and results from the reversal of the dominant contribution (**L** to **S** crossing T_{comp})[14], a monotonic decrease of the TMR with temperature without sign inversion is observed for SGA/AlO_x/$[Co/Pt]_5$ MTJs. This is consistent with the magnetic orientation of the spin and orbital moments in the SGA layer. As detailed in the chapter 1, the **S**-up configuration is stabilized during the cooling process from above T_{comp} and persists down to low temperature in SGA epitaxial films. The monotonic variation of TMR thus shows that this effect is related to the relative spin orientations (not the magnetization orientations) of both electrodes. Consequently, for the positive applied fields,

the high resistance state observed in figure 6 corresponds to a parallel configuration for the spins of both electrodes (sketch Ⓐ), whereas for the negative applied fields, the low resistance state corresponds to an anti-parallel configuration for the spins of both electrodes (sketch Ⓑ).

Based on the positive spin polarization associated to the electronic structure of Co/Al_2O_3[15] and the observation of a larger resistance for the parallel spins state, M. Da Silva *et al.* suggest that the spin polarization of SGA should be negative.

Another interesting feature reported in figure 7 is the sign inversion of the TMR occurring for high voltages. This suggests an inversion of the spin-polarization with the voltage for one of the two electrodes, most likely the SGA electrode. This inversion appears when the additional contribution to the conductance is activated (figure 5).

II.C. Discussion

Beyond the proof that SGA can simultaneously exhibit a zero-magnetization state and a polarization of the conduction electrons[10], other interesting features such as the anomaly in the conductance characteristic and the inversion in the sign of the TMR for high voltages have been observed in the $SGA/AlO_x/[Co/Pt]_5$ MTJs.

The photoemission experiments described in the chapter 3 have shown the persistence of an electronic state at the SGA/oxide interface which could be consistent with the observation of these different features. The SRPES experiments however suggested a positive spin-polarization, which differs from the negative polarization deduced from the TMR measurements.

Two hypotheses can be made at this stage:

- First, the nature of the insulating barrier can lead to different electronic properties at the metal/oxide interface. Several papers [15],[16] have namely demonstrated the crucial role played by the metal/oxide interface in the determination of the spin-polarization of the tunneling electrons. The nature of the bonding at the metal/oxide interface can especially influence the character of the tunneling electrons and consequently the sign of the spin-polarization. In the present study, the electronic properties probed by photoemission correspond to the SGA/MgO interface, whereas the electronic properties probed by transport measurements correspond to the SGA/AlO_x interface.
- Second, as shown in figure 7, a sign inversion of the TMR occurs when the additional contribution to conductance is activated. Then, for +300mV, the sign of the SGA polarization likely changes and becomes positive, in agreement with the photoemission experiments.

As a result, the anomaly in the conductance and the change in sign of the TMR could be explained by the activation of the localized electronic state measured by photoemission, as it has been previously reported for Fe/MgO/Fe. However, preliminary electronic structure calculations performed for a SGA surface (chapter 3) show that no surface states should develop for an Al-terminated surface. This would suggest that the G(V) anomaly observed in MTJs with an AlO_x tunnel barrier would rather originate from electronic bulk states.

The elaboration and investigation of SGA/MgO/[Co/Pt] magnetic tunnel junctions appeared to be crucial to get a deeper understanding of the transport properties in SGA-based magnetic tunnel junctions.

III. Preliminary results on SGA/MgO/[Co/Pt] MTJs

The first step in the study of SGA-based magnetic tunnel junctions consists in the growth of SGA, a challenging point especially concerning its crystallographic structure and the control of the Gd

concentration. To achieve a Gd substitution smaller than 3% (necessary to generate a compensation temperature), the deposition rate of Gd has to be small and very well controlled. For the study by M. Da Silva *et al*. on SGA/AlO_x/[Co/Pt] MTJs, the SGA films have been fabricated in a dedicated MBE chamber. Unfortunately, during this PhD work, several technical issues resulted in a long period where no new samples could be produced. This strongly limited the number of SGA-based samples that could be fabricated. Furthermore, this MBE chamber is not connected to the sputtering set-up used to grow the [Co/Pt] multilayers.

Consequently, two main strategies have been developed to grow the SGA/MgO/[Co/Pt] MTJs:

- *Hybrid MBE/sputtering deposition process*

In this case, the SGA epitaxial film is optimally grown in the dedicated MBE chamber, covered by Nb to prevent the surface from further oxidation in air and then brought into the MPGA setup (figure 8) where:

1- The Nb layer is etched using an Ar gun with Auger analysis to ensure the total removal of the material. The sample is then transferred under UHV in the connected MBE chamber to perform a thermal annealing followed up by RHEED analysis.
2- The MgO barrier is grown either by MBE or by sputtering, once the sample is brought back (under UHV) to the sputtering chamber.
3- The [Co/Pt] multilayer is finally made by sputtering.

Most of the SGA-based MTJs investigated during this PhD work have been obtained using this strategy. The results are presented in the following. Those systems are also the closest to those investigated by ARPES and SRPES (capped SGA grown by MBE in Nancy, etched and annealed in the CASSIOPPE MBE chamber).

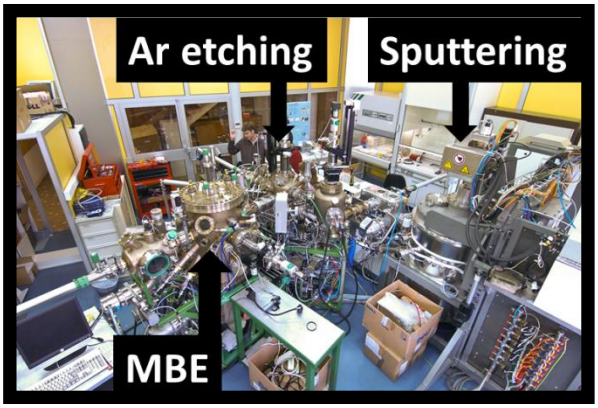

Figure 8: Picture of the MPGA setup at IJL used to prepare the MgO/[Co/Pt] part of the MTJs.

- *All sputtering deposition process*

In order to avoid the transfer between various deposition setups and the etching/annealing process of the SGA layer, all in-situ SGA(Sputtering)/MgO(Sputtering)/[Co/Pt](Sputtering) can be made using the MPGA set up.

The structural and magnetic properties of SGA films made by sputtering have been studied. However, as suspected, the main bottleneck was to control the Gd stoichiometry, to generate the magnetic compensation. All the attempts to get a low enough Gd content failed, even when keeping the target shutter closed… Despite satisfactory structural characteristics ((111) texture after annealing), this pathway has thus been given up.

In conclusion, SGA/Nb layers have been grown in the dedicated MBE chamber where an optimal control of the SGA deposition can be achieved. Similar layers have been used for the

photoemission experiments and as starting blocks to fabricate SGA-based MTJs (MgO and [Co/Pt] grown by sputtering in the MPGA setup).

III.A. SGA surface preparation

As explained in the previous paragraph, the growths of the MgO and [Co/Pt] multilayers have required (i) the transfer of the capped SGA epitaxial film into another deposition setup and most of all (ii) the SGA surface preparation. The same procedure as the one developed for the photoemission experiments on the CASSIOPEE beamline has been followed: (i) protection of the sample surface by a thick Nb capping layer (ii) etching of the capping layer (iii) annealing of the free SGA surface.

A typical Auger spectrum collected at the end of the etching process (IJL) is presented in figure 9 (red curve). An Auger spectrum collected for a SGA surface prepared in the CASSIOPEE MBE chamber is recalled for comparison in figure 9 (black curve).

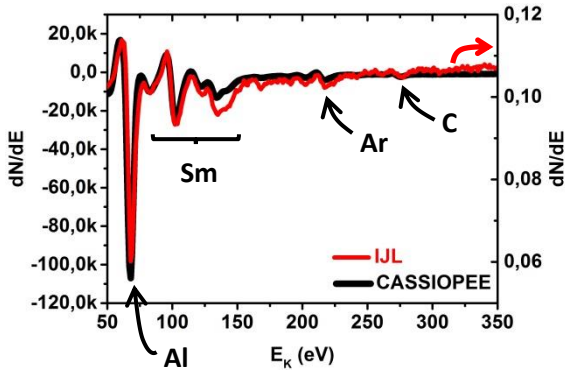

Figure 9: Auger spectra collected at the end of the etching process of (111)SGA surface performed at the IJL (red curve) and in the CASSIOPEE MBE chamber (black curve).

The Auger peaks identified as Al and Sm can be observed at the same kinetic energy and with the same ratio for both (111)SGA surfaces. These results suggest the same stoichiometry for both SGA surfaces prepared at IJL and in the CASSIOPEE MBE chamber. The presence of Carbon and Argon contaminations is observed in both cases.

The RHEED patterns collected at the IJL before and after annealing are presented in figures 10 (a) and (b), respectively. The RHEED patterns collected in the CASSIOPEE MBE chamber are recalled in figures 10 (c) and (d). One has to underline that the annealing processes are significantly different: a 90min annealing at 500°C (achieved by thermal radiation) in the IJL and a 15 minutes flash annealing at higher temperature (not known, achieved by electronic bombardment) in the CASSIOPEE MBE chamber.

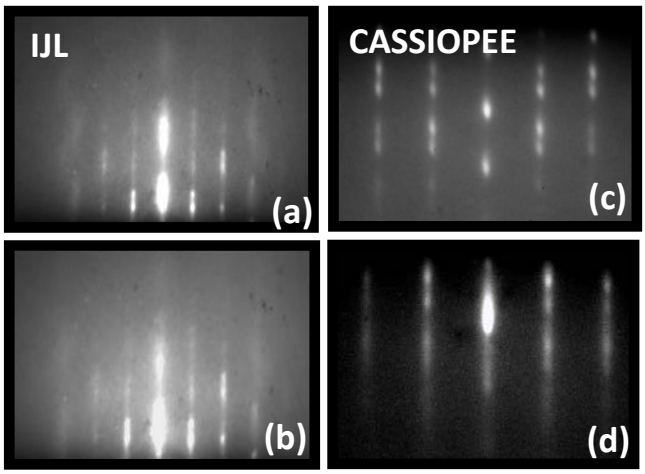

Figure 10: RHEED patterns obtained at the IJL (a,b) and in the CASSIOPEE MBE chamber (c,d) before (a,c) and after the different annealing processes along the $[11\bar{2}]$ azimuthal direction of the Nb-free SGA layer.

The diffraction patterns collected just after the etching (figures 10 (a) and (c)) clearly exhibit spotty streaks, resulting from a rough (111)SGA surface. The comparison with initial RHEED patterns collected in the MBE chamber just after the SGA growth (figure 4, chapter 3) reveals that such roughness is induced by the etching process. The effects of the annealing processes appear to be significantly different: the slow and long annealing at 500°C (IJL, figure 10 (b)) has relatively little effect on the SGA surface morphology, while the flash annealing at higher temperature (CASSIOPEE, figure 10 (d)) significantly smooth the surface, as evidenced by the appearance of more continuous streaks.

Recently, a new annealing process at slightly higher temperature (550°C) has been tested at the IJL (figure 11). The continuous streaks observed after the annealing at 550°C unambiguously reveal a much smoother SGA surface, the characteristics of which become very similar to the as-grown SGA film.

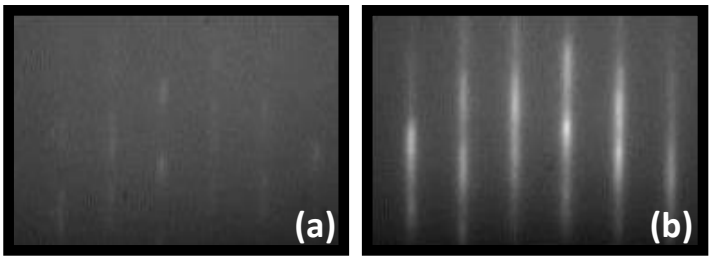

Figure 11: RHEED patterns collected at the IJL for a free SGA surface before (a) and after (b) annealing at 550°C.

These results suggest that an annealing temperature equal to or higher than 550°C is required to get a smooth SGA surface. It can be noticed that this temperature corresponds to the deposition temperature for SGA epitaxial films. MTJs have been grown on this optimally prepared SGA surface but low resistances have been measured suggesting some problems during the lithography, cut or bonding processes of the MTJs. The precise reasons remain to be identified.

The transport measurements reported below have been performed on MTJs grown on 500°C annealed SGA surfaces.

III.B. Common features in perpendicular SGA-based MTJs

III.B.1. Tunnel conductance versus voltage

Similar electronic transport measurements as for the [Co/Pt]-based MTJs (chapter 6) have been performed for SGA-based MTJs. The first step to characterize the MTJs has been to analyze the conductance (G) versus voltage (V). Fitting the experimental variation with a polynomial law of V permits to extract the parameters of the tunnel barrier thanks to the Brinkman model (chapter 6).

The SGA/MgO/[Co/Pt] MTJs appeared to be much more breakable than their analogue [Co/Pt]/MgO/[Co/Pt] MTJs, which has greatly limited the number of measurements that could be done. The origin of this issue could be linked to the quality of the tunnel barrier, the technological process, the sample cutting or the bonding process. Figure 12 presents the G(V) characteristic measured at 80K for SGA/MgO/$[Co_{0.58nm}/Pt_{1.8nm}]_4$ MTJs (10µm x 10µm).

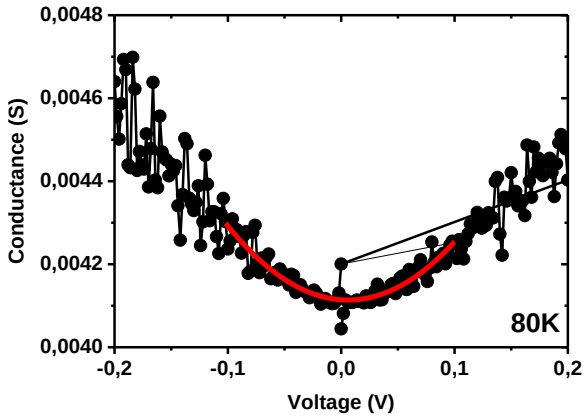

Figure 12: Conductance versus voltage characteristic extracted from current versus voltage measurements at 80K on a 10µm x10 µm SGA/MgO/[$Co_{0.58nm}$/$Pt_{1.8nm}$]$_4$ MTJ after a field-cooling of 0.3T. The red curve is a parabolic fit.

The parabolic behavior of G(V) is a first sign of a tunnel behavior for the electrons and results from the non-linearity of the current versus voltage characteristic. The barrier parameters extracted from the Brinkman's model are $d = 1.21$ nm, $\phi = 1.16\ eV$, $\Delta\phi = -0.11\ eV$, R = 241 ohms for the barrier thickness, barrier height, barrier asymmetry and resistance, respectively. In comparison with [Co/Pt]/MgO/[Co/Pt] MTJs, the tunnel barrier appears thinner, its height is quite the same, and its asymmetry is strongly reduced. While the reduced MgO thickness could be linked to a change in the MgO deposition flux, the change of the barrier asymmetry is difficult to comment on the basis of the poor statistics of the measurements on SGA/MgO/[Co/Pt]. It could be linked to the roughness of the SGA layer, as inferred from RHEED measurements.

III.B.2. Tunnel conductance versus temperature

The resistance or conductance dependence on temperature is another "good" criterion to assert the tunnel conduction through the magnetic tunnel junction. The conductance dependence on temperature in SGA-based MTJ is reported in figure 13 (black dots). The conductance obviously decreases when the temperature decreases, which confirms the tunnel character of the conductance and excludes a metallic character of the SGA-based magnetic tunnel junction (e.g. due to pinholes that lead to an increase in conductance when the temperature decreases[17]).

The tunnel characteristic is however not conventional. A linear behavior of conductance with temperature is namely observed for low applied voltage bias. For comparison, elastic tunnel conductance curves expected from the parameters extracted from the Brinkman fit are added to the figure 13 (black or blue lines). These cannot reproduce the experimental data. A non-spin-polarized conductance contribution has then been fitted using a T^{Υ} law[2],[18] (red line). The fitted value for Υ=1.036 doesn't correspond to any conduction contribution identified in literature up to now[2],[18].

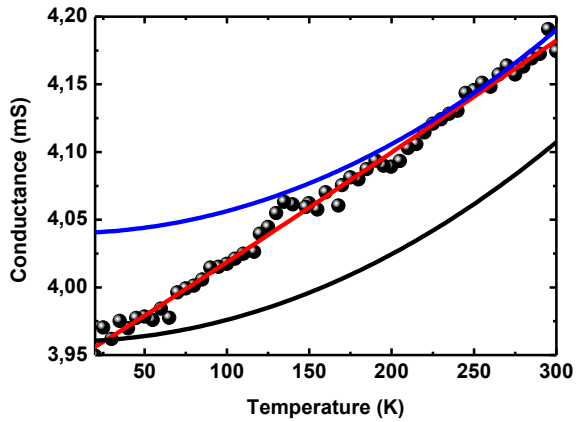

Figure 13: Variation of the conductance with temperature (black dots) for a SGA/MgO/[Co/Pt] MTJ (measurements performed at 10mV and under a magnetic field of 0.3T). The black and blue solid curves denote the variations expected from the parameters extracted from the Brinkman fit. The red solid curve is a fit using a T^{Υ} law.

Because of the limited number of measurements, no definitive explanation could be given for this behavior. One possibility would be however the oxidation of the bottom electrode. As previously observed in over oxidized Al_2O_3 tunnel junctions[19],[20] and references therein, the oxidation of the bottom electrode can induce charge localization or can increase the effective thickness of the tunnel barrier at low temperatures.

III.B.3. Resistance versus applied field characteristics

The R(H) characteristics were measured with the magnetic field applied along the easy magnetization axis (perpendicular to the MTJs' plane). The R(H) curves measured at 100K, 80K, 50K and 35K for SGA/MgO/$[Co_{0.58nm}/Pt_{1.8nm}]_4$ MTJs are presented in figure 14.

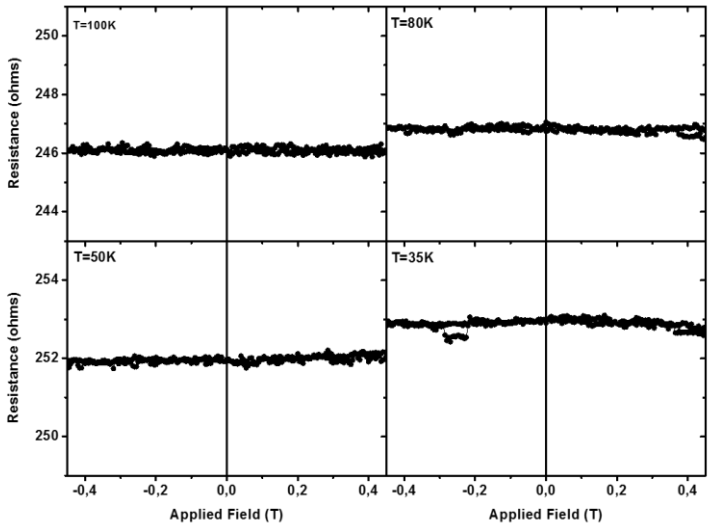

Figure 14: R(H) characteristics measured at 100K, 80K, 50K and 35K for SGA/MgO/$[Co_{0.58nm}/Pt_{1.8nm}]_4$ MTJs (10µm x 10µm)

No change in resistance versus the applied magnetic field can be observed in the explored field range (±0.45T) and consequently, no TMR and spin-polarization values for SGA can be extracted from these experiments. A first hypothesis would be to invoke the non-reversal of the [Co/Pt] multilayers. This is however highly unlikely, given previous results on SGA-based MTJs with Al_2O_3 barrier[10] and on [Co/Pt] multilayers-based MTJs (chapter 6) showing that the [Co/Pt] multilayers reversal is achieved for (±0.3T).

III.C. Discussion

In this PhD work, the studies have been mostly focused on SGA-based MTJs with MgO tunnel barriers that relax the constrains linked to the oxidation of an Al layer to make a tunnel barrier. The successive deposits of SGA and MgO/[Co/Pt] in two different deposition chambers constitute however another strong drawback. The results obtained on SGA-based magnetic tunnel junctions with an MgO insulating barrier significantly differ from the previous results obtained with an AlO_x insulating barrier: no anomaly has been observed in the G(V) characteristic and no TMR has been detected in the applied field range allowed by the experimental setup.

The study of the tunnel junctions has been completed by photoemission studies on SGA and MgO-covered SGA that still allow drawing the following conclusions:

- The quality of the SGA surface strongly depends on the annealing process after removal of the capping layer. While the annealing process at CASSIOPEE resulted in a SGA surface where band structures expected from calculations could be observed, the annealing process used up to now at IJL is not optimal. The surface roughness, stoichiometry (etc…) may not be suitable to get the electronic transport features seen in tunnel junctions with AlO_x barrier, where the quality of the SGA/AlO_x interface was not altered by any chemical or physical treatment.
- The SGA surface oxidizes when covered by MgO (chapter 3). The band structure can be thus altered in comparison with AlO_x tunnel barriers. In this latter case, the SGA surface was likely not oxidized thanks to the 2nm thick Al layer and the soft natural oxidation process. The SGA interface oxidation may lead to an additional contribution to the tunnel barrier at low temperature.
- A localized electronic state, possibly a surface state, exists at the Fermi level when the surface is optimally prepared. This surface state persists even after the deposition of MgO.

In summary, tunnel junctions with an improved SGA/MgO interface have to be definitely prepared. A first step will be the preparation of the SGA surface at higher annealing temperatures. A second, likely more promising, will be of course the successive depositions of both SGA and MgO in the same dedicated MBE chamber. The SGA/MgO system can be then relatively safely transferred in air to the sputtering chamber for the [Co/Pt] deposition. Moreover, the IJL project consisting in connecting various analysis and deposition chambers under UHV will greatly improve the fabrication conditions of such challenging hybrid systems.

IV. Conclusion

The careful analysis of [Co/Pt]-based MTJs has shown that the effective [Co/Pt]/MgO polarization depends on the Pt thickness and is linked to the induced polarization of the Pt layers. This conclusion is sustained by a simple model based on the polarization of Pt atoms at the Co/Pt interfaces that decreases with the Pt thickness. The effective polarization dependence on temperature can be well adjusted by a Bloch's law and permits to extract the Curie temperature as a function of the Pt thickness. This evolution is shown to be linked to the variation of the RKKY coupling between the Co layers in the [Co/Pt] multilayer. As a result, the room temperature variation of the effective [Co/Pt]/MgO polarization versus the Pt thickness originates from the variation of the intrinsic Pt polarization and from the variation of Tc.

The transport measurement on SGA-based magnetic tunnel junction with an AlO_x insulating barrier have proved that SGA can simultaneously exhibit a zero-magnetization and polarized a spin current. Interesting features such as an anomaly and asymmetry in the G(V) characteristic, a sign inversion in the TMR with the voltage have been highlighted and could be explained by the electronic properties of SGA/Oxide interface where a localized electronic state with 3d character has been detected at the SGA/MgO interface (ARPES).

SGA-based MTJs with MgO insulating barrier have been consequently fabricated in order to explore these aspects. Nevertheless, the first G(V) characteristic on SGA-based MTJs with MgO has revealed neither asymmetry nor anomaly, and no TMR effect could be observed. These results are likely explained by the difficulties to get a "good enough" SGA/MgO interface. Tunnel junctions with improved SGA/MgO interface should be elaborated in the next future in: (i) increasing the annealing temperature of the SGA surface preparation during the hybrid MBE/sputtering deposition process, (ii) developing the all-MBE deposition process in the SGA dedicated MBE chamber, to prevent the sensitive SGA surface from any chemical/physical treatment.
First tests to explore those two research directions are already in progress.

References

[**1**] J. Geissler *et al.*, Phys. Rev. B **65**, 020405 (2001).
[**2**] C.S. He *et al.*, Phys. Rev. B **58**, R2917 (1998).
[**3**] D. Pescia *et al.*, Phys. Rev. Lett. **58**, 933 (1987).
[**4**] S. Zhang *et al.*, Phys. Rev. Lett. **79**, 3744 (1997).
[**5**] S. Hashimoto *et al.*, J. Appl. Phys. **67**, 2136 (1990).
[**6**] C. M. Schneider *et al.*, Phys. Rev. Lett. **64**, 1059 (1990).
[**7**] P. Bruno *et al.*, J. Magn. Soc. Jpn **15**, 15 (1991).
[**8**] S. Bandiera, thesis (2011).
[**9**] A.S. Darling *et al.*, Platin. Met. Rev . **7**, 96 (1963).
[**10**] M. Da Silva *et al.*, Appl. Phys. Lett. **98**, 232504 (2011).
[**11**] Y. Suezawa *et al.*, J. Magn. Magn. Mater. **126**, 524 (1993).
[**12**] M. Sato *et al.*, IEEE Trans. Magn. **33**, 3553 (1997).
[**13**] P.-J. Zermatten *et al.*, Phys. Rev. B **78**, 033301 (2008).
[**14**] C. Kaiser *et al.*, Phys. Rev. Lett. **95**, 047202 (2005).
[**15**] J. M. De Teresa *et al.*, Science. **286**, 507 (1999).
[**16**] M. Sharma *et al.*, Phys. Rev. Lett. **82**, 616 (1999).
[**17**] J.M. Teixeira *et al.*, J. Appl. Phys. **106**, 073707 (2009).
[**18**] R.J.M. van de Veerdonk, thesis (1990).
[**19**] F. Montaigne, thesis (1999).
[**20**] S. Joo *et al.*, Appl. Phys. Lett. **100**, 172406 (2012).

General conclusion and future projects

The aim of this PhD work was first to extend and strengthen the investigation of surface/interface magnetic and electronic properties of SGA epitaxial thin films. In a second step, this ferromagnetic material, that exhibits zero magnetization at the compensation temperature, has been integrated in magnetic tunnel junctions to further explore its electronic properties and test its potential interest for spintronics studies and applications. The investigation of SGA-based MTJs has motivated the previous accurate analysis of MTJs based on two similar [Co/Pt] electrodes and of [Co/Pt] multilayers.

Synchrotron-based angle-resolved photoemission spectroscopy has been used to study the surface/interface electronic properties of (111) SGA epitaxial thin films. Those experiments have permitted to explore (i) the samarium valence stability with the identification of the samarium divalent and trivalent contributions localized at the surface and in the bulk of the thin film; (ii) the electronic states along various directions of the surface and bulk Brillouin Zones. The conjunction of experimental observations and electronic band structure calculations revealed the occurrence of a resonant surface state with Λ_1 symmetry, appearing as a strongly localized electron pocket close to the Fermi level and around $\bar{\Gamma}$ in the (111)SGA SBZ. This surface state, of 5d character, is likely built on the bulk electron pocket developing around L points close to the Fermi level. Interestingly, this electronic state is still observed for a MgO-covered surface and its signature should thus be detected in the transport properties of magnetic tunnel junctions. ARPES experiments have highlighted other electronic states with similar Λ_1 and 5d-character but larger in-plane dispersion that would correspond to bulk contributions, as obtained from band structure calculation. First SRPES experiments have been undertaken to get a direct estimation of the spin polarization at the Fermi level. Those preliminary results suggest that the Sm^{2+} divalent contributions identified as surface features are not polarised and that the resonant surface state is polarized at low temperature.

The next step towards the integration of SGA in magnetic tunnel junctions consisted in the study of structural and magnetic properties of the second electrode of the MTJ: [Co/Pt] multilayer with perpendicular magnetization. The combined structural and magnetic analysis permitted to highlight the prominent role played by the layer roughness, especially the roughness of the Co layers. It appeared that rough interfaces contribute to the reduced PMA, in agreement with Bruno's model describing how the roughness limits the Néel surface anisotropy. This effect is limited by increasing the Pt thickness that can smooth the interfaces and tends to improve PMA. Simultaneously, rough interfaces contribute to the enhanced magnetization via the polarization of Pt atoms in direct contact with Co. This effect on magnetization may also indirectly drive the reduction of PMA via the increase of the dipolar anisotropy contribution which favors in-plane magnetization. The effect of temperature has been finally analyzed: Decreasing the temperature appeared to have a very limited effect on the effective anisotropy, despite the increase in saturation magnetization. In order to explain this constant effective anisotropy, an additional contribution favoring PMA in decreasing temperature has to be taken into account but remains to be identified.

The [Co/Pt] multilayers have been then integrated in [Co/Pt]/MgO/[Co/Pt] magnetic tunnel junctions. The goals of this intermediate step were (i) to check the magnetic behavior of [Co/Pt] multilayers inserted in MTJ and their magnetic behavior when hardened by a CoTb pinning layer (ii) to study the effective spin polarization of the [Pt/Co]/MgO interface which is essential for the determination of the effective spin polarization of SGA/MgO and the comparison with direct photoemission measurements.

Several interesting features, mainly driven by the magnetic properties of the CoTb/[Co/Pt] hard electrode and the magnetic history of the sample, have been observed. When the magnetization of the CoTb layer is not reversed, exchange biased loops or reversible spring magnet behaviors could be generated. This last property is very attractive and could be used in the development of magneto-resistive sensor at room temperature and high fields. When the magnetization of the CoTb layer is partially reversed, the stabilization of magnetic domains in the hard electrode gives rise to a domains duplication phenomenon from the hard to the soft electrode. This is nicely observed via the occurrence of low resistance intermediate states. The analysis of the conductance showed that the domain walls in perpendicular MTJs do not contribute to the TMR, thus contrasting with the results obtained for in-plane MTJs. All these features have been well reproduced by micromagnetic calculations using the magnetic parameters of the different [Co/Pt] multilayers determined by VSM and/or SQUID measurements. Finally, the ferromagnetic coupling between both electrodes through the MgO tunnel barrier has been found to decrease with decreasing temperature and increasing Pt thickness. These results have been successfully explained using the theoretical model developed by J. Moritz *et al*. based on a stray field interaction between perpendicularly magnetized layers separated by a non-magnetic spacer.

The observation of well-defined parallel and anti-parallel states allowed the determination of the [Pt/Co]/MgO effective tunnel spin polarization as a function of both the Pt thickness and temperature. This analysis has shown that the effective [Pt/Co]/MgO polarization is linked to the induced polarization in the Pt layers. This conclusion is sustained by a simple model based on the polarization of Pt atoms at the Co/Pt interfaces that decreases with the Pt thickness. The effective polarization dependence on temperature can be adjusted by a Bloch's law and permits to extract the Curie temperature as a function of the Pt thickness. This evolution is shown to be related to the variation of the RKKY coupling between the Co layers in the [Co/Pt] multilayer. As a result, the room temperature variation of the effective [Co/Pt]/MgO spin polarization versus the Pt thickness originates from both the variation of the intrinsic Pt polarization and from the variation of Tc.

Finally, SGA/MgO/[Co/Pt] MTJs have been grown and their magneto-transport properties have been studied. While G(V) showed tunnel characteristics, especially an increase of resistance at low temperature, no TMR effect could be measured. This contrasts with the encouraging results previously obtained on SGA/AlO_x/[Co/Pt] MTJs. With our knowledge of the system, this difference may likely be explained by the difficulties to get a suitable controlled SGA/MgO interface, either due to the SGA roughness or oxidation state.

This PhD work has thus significantly contributed to a deeper understanding of magnetic and electronic properties in SGA epitaxial films, [Co/Pt] multilayers and in SGA- and [Co/Pt]-based MTJs. However, several important features remain to be clarified, several interesting questions have emerged and further experimental work would be definitely required to address those issues.

The analysis of the [Co/Pt] multilayers and of the role of the Pt thickness would benefit from an accurate investigation of the Co/Pt interface by High Resolution Transmission Electron Microscopy (HRTEM) and Nuclear Magnetic Resonance (NMR). These would help extracting the roughness and intermixing of the layers, which is difficult via only X-Ray experiments. The Pt induced magnetic moment could be also evaluated with element-selective spin-dependent X-ray absorption and even better resonant magnetic X-ray reflectivity to extract a Pt magnetic profile between the Co layers. Spin-resolved photoemission spectroscopy experiments could be also considered to directly analyze the spin polarization of [Co/Pt] multilayers at the Fermi level and to explore the role of the Pt thickness on this spin polarization, in comparison with the information that have be extracted from the Jullière's model.

[Co/Pt]-based MTJs exhibit several specific features that would require further investigation: The origin of the shift observed in the G(V) characteristic towards negative voltage is for example worth studying in possible connection with the MgO insulating barrier. The (111) texture for MgO obtained by sputtering should be confirmed and the G(V) behavior for epitaxial (111)MgO insulating barrier should be analyzed. Complementary information on the morphology of the Co layers at the interface with MgO, i.e. the structure of the system, could be brought by TEM observation. The effect of annealing, that is expected to smooth the Co/MgO/Co interfaces and increase the (111) texture in [Co/Pt] multilayers, could be also studied on the G(V) behavior and TMR values.

Another point of interest would be the optimization of the spring magnet behavior at room temperature, in order to develop a new generation of sensors where cooling is not necessary to achieve the required properties.

As far as SGA is concerned, new spin-resolved photoemission experiments are definitely required to determine the spin polarization dependence on temperature and to directly extract its value at the compensation temperature. Scanning Tunneling Spectroscopy experiments could also bring complementary information on the electronic band structure of (111)SGA surface. Electronic band structure calculations have to be developed (i) to calculate iso-energetics maps that could be compared to the experimental results (ii) to explore the influence of the surface in taking the Hubbart parameter into account. The first calculations have revealed the absence of surface states for Al-terminated surface. New ARPES experimental data on (111)SGA surface covered by Al_2O_3 would be thus interestingly compared with those obtained on MgO-covered SGA.

Concerning SGA-based MTJs, the main progress are first expected from a better control/quality of the SGA/MgO interface. The short-term projects are thus: (i) to increase the annealing temperature during SGA surface preparation of the hybrid MBE/sputtering deposition process, (ii) to develop the all-MBE deposition process in the SGA dedicated MBE chamber, in order to prevent the sensitive SGA surface from any chemical/physical treatment. Besides, new sets of MTJs could be fabricated with an AlO_x insulating barrier (natural oxidation process) and with different SGA Gd concentrations, in order to explore the possible role of the Gd content in the conductance anomaly reported in SGA/AlO_x/[Co/Pt] MTJs. Since the position in energy of the Fermi level will be changed, different G(V) behaviors are expected. Finally, test of spintorque experiments are planned with SGA/AlO_x/[Co/Pt] MTJs, especially in the compensate magnetic state where the SGA zero-magnetization should enhance the spintorque efficiency.

Des propriétés électroniques de $Sm_{1-x}Gd_xAl_2$ aux jonctions tunnel comportant des électrodes $Sm_{1-x}Gd_xAl_2$ et/ou des multicouches de [Co/Pt] : vers l'intégration de ferromagnétique sans aimantation dans de nouveaux dispositifs

Le contexte général de ce travail est le développement et l'intégration de nouveaux matériaux magnétiques ayant des propriétés originales et d'intérêt potentiel pour la spintronique. En tant que matériau ferromagnétique d'aimantation nulle, le composé $Sm_{1-x}Gd_xAl_2$ (SGA) attire une attention particulière, puisqu'il est capable, dans son état magnétique compensé, de polariser en spin un courant d'électrons.
Les études réalisées au cours de cette thèse ont tout d'abord apporté des informations pertinentes sur les propriétés électroniques de (111)SGA. Des expériences de photoémission résolues en angle sur synchrotron ont permis d'effectuer une analyse précise selon diverses directions de la zone de Brillouin. Les observations expérimentales associées à des calculs de structure de bandes électroniques suggèrent l'existence d'un état de surface résonant de symétrie Λ_1, apparaissant comme une poche d'électrons fortement localisée autour du point $\bar{\Gamma}$. Cet état, de caractère 5d, s'appuie sur un état du volume près du niveau de Fermi, et semble persister lorsque la surface SGA est couverte par MgO. Les autres états électroniques observés, de même symétrie et de même caractère d, correspondraient à des bandes de volume. Les premières expériences polarisées en spin ont été entreprises pour obtenir une estimation directe de la polarisation de spin au niveau de Fermi.
En vue de l'intégration de SGA dans des jonctions tunnel magnétiques, une attention particulière a été portée aux multicouches [Co/Pt] et aux JTMs à base de [Co/Pt]. Les multicouches [Co/Pt] constituent la seconde électrode des JTMs à base de SGA. Leurs propriétés magnétiques (en particulier l'anisotropie perpendiculaire et l'aimantation à saturation) ont été soigneusement étudiées en fonction de l'épaisseur de Pt et de la nature de la couche tampon (Pt, MgO ou Al_2O_3), et en liaison avec leurs caractéristiques structurales. Les résultats mettent en évidence le rôle joué par la rugosité des couches, qui contribue à réduire l'anisotropie perpendiculaire et à augmenter l'aimantation via la polarisation du Pt.
Dans les JTMs à base de [Co / Pt], les propriétés magnéto-électriques ont tout d'abord permis de déterminer la polarisation tunnel de [Co/Pt], essentielle pour obtenir une estimation quantitative de la polarisation du SGA à partir des propriétés des JTMs. Le comportement magnéto-tunnel est également une sonde puissante de la configuration magnétique d'interface et a révélé des propriétés originales telles que la duplication de domaines ou un comportement de type « spring magnet ». Ces phénomènes, liés à diverses interactions dans et entre les électrodes, sont bien expliqués et reproduits par les simulations micromagnétiques. Malgré la première observation d'une TMR finie dans SGA/AlOx/[Co/Pt], les tentatives pour observer un effet TMR dans SGA /MgO/[Co/Pt] ont été malheureusement infructueux jusqu'à présent, comme cela est finalement présenté et discuté.

From $Sm_{1-x}Gd_xAl_2$ electronic properties to magnetic tunnel junctions based on $Sm_{1-x}Gd_xAl_2$ and/or [Co/Pt]-electrodes: towards the integration of Zero Magnetization ferromagnets in spintronic devices

The general context of this work is the development and integration of new magnetic materials with original properties of potential interest for spintronic applications. In this field, the $Sm_{1-x}Gd_xAl_2$ (SGA) compound drives a particular attention, as a Zero-Magnetization ferromagnet that can exhibit a spin polarization in its magnetic compensated state.
The studies carried out during this PhD thesis have first brought relevant information on the (111)SGA electronic properties. Synchrotron-based Angle Resolved PhotoEmission Spectroscopy experiments have permitted to perform an accurate analysis along various directions of the Brillouin Zone. The conjunction of experimental observations and electronic band structure calculations would reveal the occurrence of a resonant surface state with Λ_1 symmetry, appearing as a strongly localized electron pocket around $\bar{\Gamma}$ in the (111)SGA SBZ. This surface state, of 5d character, may be built on a bulk state close to the Fermi level, and interestingly survives in a MgO-covered SGA surface. Other observed electronic states, with similar symmetry and similar d-character, would rather correspond to bulk bands. First SRPES experiments have been undertaken to get a direct estimation of the spin polarization at the Fermi level.
Towards the integration of SGA in magnetic tunnel junctions, a special attention has been the paid to [Co/Pt] multilayers and to [Co/Pt]-based MTJs. The [Co/Pt] multilayers would constitute the second electrode in SGA-based MTJs. Their magnetic properties (esp. perpendicular anisotropy and saturation magnetization) have been carefully investigated as a function of Pt thickness and nature of the buffer layer (Pt, MgO or Al_2O_3), and in close connection with structural characteristics. The results highlight the prominent role played by the layers roughness, which contributes to reduce the perpendicular anisotropy and enhance the magnetization via the Pt polarization.
In [Co/Pt]-based MTJs, magneto-electric properties could first be used to determine the [Co/Pt] tunnel polarization and its dependence on the Pt thickness, essential to get a quantitative estimation of the SGA polarization from SGA-based MTJs properties. The magneto-tunnel behavior is also a powerful probe of the interface magnetic configuration under field and revealed original properties such as domains duplication or spring magnet behavior. These phenomena, related to various interactions in and between electrodes, could be nicely explained and reproduced by micromagnetic simulations. Despite the first observation of a finite TMR in SGA/AlOx/[Co/Pt], the attempts to observe a TMR effect in SGA/MgO/[Co/Pt] MTJs have been unfortunately vain up to now, as it is finally presented and discussed.